Radial evolution of the solar wind electrons : simulations and preparation of the Solar orbiter and Parker solar probe observations

Laura Berčič

To cite this version:

Laura Berčič. Radial evolution of the solar wind electrons : simulations and preparation of the Solar orbiter and Parker solar probe observations. Astrophysics [astro-ph]. Université Paris sciences et lettres; Università degli Studi di Firenze, 2020. English. NNT : 2020UPSLO003 . tel-03273683

HAL Id: tel-03273683
https://theses.hal.science/tel-03273683
Submitted on 29 Jun 2021

RADIAL EVOLUTION OF SOLAR WIND ELECTRONS

LAURA BERČIČ

Supervised by

MILAN MAKSIMOVIĆ
SIMONE LANDI
LORENZO MATTEINI
FILIPPO PANTELLINI

President of the jury: LAURENCE RÉZEAU

September 29 2020

Laboratoire d'études spatiales et
d'instrumentation en astrophysique
L'Observatoire de Paris

Ecole Doctorale Astronomie et
Astrophysique d'Ile de France

Università degli Studi di Firenze
Dipartimento di Fisica e Astronomia

ABSTRACT

The solar wind electrons, as the lightest constituents of the solar wind, have not been as widely studied as the heavier solar wind protons and other positive ions, carrying nearly all of the solar wind mass and momentum. In contrast, electrons are important for the global dynamics of the solar wind precisely due to their low mass that allows high electron thermal speeds, which already in the solar corona reach way above the escape speed of the Sun. These fast electrons are responsible for part of the solar wind acceleration exerted on the positive charged solar wind species through the ambipolar electric field, which preserves the quasi-neutrality of the interplanetary plasma.

During the solar wind expansion, an interplay between Coulomb collisions, ambipolar electric field, magnetic moment conservation and electro-magnetic field-particle interactions, shapes the solar wind particle velocity distribution functions (VDFs), which often depart from a simple Maxwellian VDF. Electron VDFs in the solar wind are usually modelled by three components: a dense *core* present at lower electron energies, and a close to isotropic *halo* and a beam-like *strahl*, which both dominate higher electron energies. The goal of this thesis is to investigate the behaviour of these separate electron populations in order to gain new insight on the physical phenomena taking place during the solar wind expansion, as well as on the state of the solar corona. For this purpose, we have revisited data from the Helios mission, alongside the analysis of the novel Parker Solar Probe (PSP) data. To be able to relate the in-situ solar wind data to the conditions at its origin, we additionally make use of a numerical approach, a fully kinetic model of the solar wind accounting for magnetic moment conservation, ambipolar electric field, and binary collisions between particles (BiCoP).

We focused especially on the fast streaming strahl electrons, which are, due to their high anti-sunward directed velocities, believed to preserve the information about the solar corona. Expanding in a weaker interplanetary magnetic field (IMF), the strahl electrons experience focusing with increasing radial distance. This focusing is however counteracted by various scattering mechanisms. In the near-Sun PSP observations we found a solar wind type, where the strahl electrons could be scattered solely by Coulomb collisions, thus allowing a direct comparison between the experimental VDFs and the numerical VDFs. The model runs assuming a Maxwellian corona were found to better re-

produce the observed VDFs, which showed no signs of Kappa-like energy tails. The strahl parallel temperature ($T_{s,\|}$) was found to increase slightly due to Coulomb collisions during expansion, therefore reaching up to 15 % above the temperature of the electron in the solar corona.

RÉSUMÉ

Les électrons du vent solaire, dont ils sont les composants les plus légers, n'ont pas été étudié d'une manière aussi poussée que les protons et autres ions positifs bien plus massifs, qui représentent la quasi totalité de la masse du vent solaire, transportant la plus grande partie de sa quantité de mouvement. Mais précisément de par leur faible masse, les électrons sont d'une grande importance pour la dynamique global du vent solaire. Cette faible masse leur permet d'atteindre de grandes vitesses thermiques, qui dés la couronne solaire dépassent largement la vitesse de libération du Soleil. Ces électrons très rapides sont responsables d'une part de l'accéleration du vent solaire, en accélérant les espèces positivement chargées via le champ électrique ambipolaire, qui préserve la quasi-neutralité du plasma interplanétaire.

Durant l'expansion du vent solaire, les effets cumulés des collisions Coulombiennes, du champ électrique ambipolaire et des interactions entre particules et champs électromagnétiques façonnent les fonctions de distribution des vitesses (FDV) des particules, qui le plus souvent diffèrent d'une simple distribution Maxwellienne.Les FDV des électrons du vent solaires sont habituellement modélisées à l'aide de trois composantes: le *coeur*, dense, présent à faible énergie, le *halo*, quasi-isotrope et le faisceau du *strahl*, tout deux dominant les électrons de plus haute énergie. Cette thèse a pour objectif d'étudier le comportement de ces populations d'électrons, dans le but d'améliorer notre compréhension des phénomènes physiques se produisant lors l'expansion du vent solaire, ainsi que notre connaissance de la couronne solaire. Dans ce but, les données expérimentales de la mission Helios ont été revisitées, en parallèle de l'analyse des données récentes de la sonde Parker Solar Probe (PSP). En outre, de manière à interpréter les conditions du vent solaire à son origine, basé sur ses données in-situ, nous utilisons une approche numérique, un modèle intégralement cinétique du vent solaire tenant compte des collisions binaires entre particules (BiCoP).

Nous nous concentrons particulièrement sur les électrons rapides de la composante du strahl, qui de par leur importante vitesse dans la direction opposée au Soleil pourraient préserver l'information qu'ils ont à leur origine à propos de la couronne solaire. S'écoulant dans un champ magnétique interplanétaire plus faible, ces électrons composant le strahl sont focalisés à mesure que la distance au Soleil augmente, une focalisation à laquelle s'opposent cependant différents mé-

canismes de dispersion. Dans les données collectées dans l'environement proche du Soleil par la sonde PSP, nous trouvons un type de vent solaire pour lequel les électrons du strahl peuvent être disperés uniquement par les collisions Coulombiennes, nous permettant une comparaison directe entre les FDV expérimentales et les FDV simulées par le modèle BiCoP. Les résultats de ce dernier lorsque les électrons de la couronne solaire sont distribués selon une Maxwellienne reproduisent plus fidèlement les FDV obervées expérimentalement, qui ne présentent aucune queue de distribution de type Kappa. Dans les résultats numériques, la température parallèle du strahl ($T_{s,||}$) augmente légèrement en raison des collisions Coulombiennes durant l'expension, atteignant jusqu'à 115 % de la température des électrons dans la couronne solaire.

RIASSUNTO

Gli elettroni del vento solare, in quanto costituenti più leggeri del vento solare, non sono stati studiati così a fondp come i protoni e gli altri ioni positivi che trasportano la gran parte della massa e quantità di moto del vento solare. Tuttavia gli elettroni sono importanti per la dinamica del vento solare proprio per la sua piccola massa: nella corona solare la loro velocità termica è così elevata da permettergli di sfuggire facilmente alla attrazione gravitazionale del sole. La loro evaporazione produce un campo elettrico (detto campo elettrico ambipolare) necessario a preservare la neutralità del plasma del mezzo interplanetario il quale imprime un'accelerazione agli ioni positivi del vento solare.

Durante l'espansione del vento solare, la combinazione tra collisioni Coulombiane, campo elettrico ambipolare, conservazione del momento magnetico e interazioni tra campi elettro-magnetici e particelle modella le funzioni di distribuzione di velocità (VDF) delle specie osservate nel vento solare che spesso si discostano significativamente dalla distribuzione di equilibrio termodinamico. In particolare, le VDF degli elettroni mostrano spesso tre distinte popolazioni: per basse energie cinetiche si ha un *core*, mentre ad energie più alte si osserva una componente quasi isotropa detta *halo*. Infine, ad alte energie e lungo il campo magnetico in direzione uscente dal sole è presente un fascio di elettroni collimati, chiamato *strahl*.

L'obiettivo di questa tesi è stato lo studio delle proprietà di queste popolazioni e di come esse evolvano durante l'espansione del vento solare. Ciò è stato fatto sia rivisitando i dati delle missioni Helios, sia analizzando i dato della recente missione Parker Solar Probe (PSP). Questo ha permesso di incrementare le nostre conoscenze sulle proprietà degli elettroni del mezzo interplanetario e di dedurre informazioni delle stesse prorietà nella corona solare. Per permettere di correlare le osservazioni in-situ del vento solare con le condizioni fisiche alla loro origine ci siamo avvalsi di simulazioni numeriche di un modello completamente cinetico del vento solare che tien conto sia delle collisioni coulombiane, sia degli effetti del campo elettrico ambipolare e della conservazione del momento magnetico.

In lavoro si è concentrato in particolare sulla popolazione strahl che, essendo debolemente o per nulla soggetta a colliosioni, si ritiene conservi informazioni sulla funzione di distribuzione degli elettroni nella

corona. L'espansione sferica in un campo magnetico che decresce con la distanza, comporta una sempre maggior collimazione di questa popolazione che è eventualemente controbilanciata da meccanismi di diffusione.

Nelle osservazioni PSP, più vicine al sole, nelle condizioni di vento solare osservato, la collimazione del fascio di elettroni può essere spiegata dal solo effetto delle collisioni coulombiane. Usando il modello cinetico abbiamo confrontato le VDF misurate in-situ con quelle ottenute dalle simulazioni. Il confronto risulta migiore assumendo che nella corona solare le funzioni di distribuzione siano Maxwelliane, dato che le VDF osservate in situ non mostrano evidenze di code in eccesso alle alte energie. Le simulazioni hanno anche mostrato un aumento della temperatura parallela al campo magnetico dello strahl direttamente correlato alle collisioni che comporta un aumento della temperatura fino al 15% rispetto a quella assunta nella corona solare.

PUBLICATIONS

First-authored:

Berčič, Laura, Milan Maksimović, Simone Landi, and Lorenzo Matteini (2019). "Scattering of strahl electrons in the solar wind between 0.3 and 1 au: Helios observations." In: *Monthly Notices of the Royal Astronomical Society* 486.3, pp. 3404–3414. ISSN: 0035-8711. DOI: `10.1093/mnras/stz1007`.

Berčič, Laura et al. (Apr. 2020). "Coronal Electron Temperature Inferred from the Strahl Electrons in the Inner Heliosphere: Parker Solar Probe and Helios Observations." In: *The Astrophysical Journal* 892.2, 88, p. 88. DOI: `10.3847/1538-4357/ab7b7a`. arXiv: `2003.04016 [astro-ph.SR]`.

Co-authored:

Behar, E., F. Sahraoui, and L. Berčič (2020). "Resonant whistler-electron interactions: MMS observations vs. test-particle simulation." In: *Journal of Geophysical Research: Space Physics*. DOI: `10.1029/2020JA028040`.

Jagarlamudi, Vamsee Krishna, Olga Alexandrova, Laura Berčič, Thierry Dudok de Wit, Vladimir Krasnoselskikh, Milan Maksimovic, and Štěpán Štverák (July 2020). "Whistler Waves and Electron Properties in the Inner Heliosphere: Helios Observations." In: *The Astrophysical Journal* 897.2, 118, p. 118. DOI: `10.3847/1538-4357/ab94a1`.

Macneil, Allan R., Mathew J. Owens, Laura Berčič, and Adam J. Finley (Sept. 2020). "Parker Solar Probe Observations of Suprathermal Electron Flux Enhancements Originating from Coronal Hole Boundaries." In: *Monthly Notices of the Royal Astronomical Society*. DOI: `10.1093/mnras/staa2660`. arXiv: `2009.01558 [astro-ph.SR]`.

Maksimovic, M. et al. (Feb. 2020). "Anticorrelation between the Bulk Speed and the Electron Temperature in the Pristine Solar Wind: First Results from the Parker Solar Probe and Comparison with Helios." In: *The Astrophysical Journal, Supplement Series* 246.2, 62, p. 62. DOI: `10.3847/1538-4365/ab61fc`.

Malaspina, David M. et al. (Feb. 2020). "Plasma Waves near the Electron Cyclotron Frequency in the Near-Sun Solar Wind." In: *The Astrophysical Journal, Supplement Series* 246.2, 21, p. 21. DOI: `10.3847/1538-4365/ab4c3b`. arXiv: `1912.06793 [physics.space-ph]`.

Stansby, D., L. Matteini, T. S. Horbury, D. Perrone, R. D'Amicis, and L. Berčič (Feb. 2020). "The origin of slow Alfvénic solar wind at solar minimum." In: *Monthly Notices of the Royal Astronomical Society* 492.1, pp. 39–44. DOI: `10.1093/mnras/stz3422`. arXiv: `1907.02646 [physics.space-ph]`.

ACKNOWLEDGEMENTS

First, I would like to show my gratitude to my supervisors Milan, Simone and Lorenzo. This thesis would not have been possible without your guidance and support. Thank you for the numerous discussions, and for sharing your enthusiasm and passion for the solar wind research with me. For making me a part of your collaborations, and giving me all the possibilities to succeed as a researcher in the future. I really feel honoured and lucky to have been your PhD student.

I am extremely grateful to Davin and Phyllis, for making me a part of their team, and warmly welcoming me at SSL, UC Berkeley. My PSP data analysis would not have been possible without your help.

I would also like to thank all the people at LESIA who helped me along the way, Arnaud, Olga, Filippo, Karine, Goran, Sonny, Denis and Mingzhe. And the ping-pong team at Arcetri, Roberto, Jianchao, Mattia, Emanuele and others, who cheered up the everyday life in Garbasso building.

Vamsee and Kristina, Valentin, Riccardo and the rest of the quantum physicists, thank you for your friendships, you really made my time in Paris and Firenze special and meaningful.

Merci Etienne, for your help and support in many different ways, since the beginning till the end. Your scientific work was an inspiration all along the way.

Finally, I would like to thank my parents, for standing by my side and supporting me on every step.

Thank you!

CONTENTS

1

INTRODUCTION

The interplanetary space is filled with a continuous flux of magnetised plasma, which escapes from the hot solar corona in the centre of our solar system. It was named the *solar wind* by Eugene Parker (1958), a young scientist at the time, who was the first to propose a physical solution for the nature of this flow, as we know it now.

The solar wind was first measured by the three Luna spacecrafts sent to the Moon (Gringauz et al., 1960), only providing a measure of the proton density. Parker's prediction of continuous supersonic hydrodynamic flow was not confirmed until the Mariner-2 mission designed to flyby Venus reached the solar wind in 1962 (Neugebauer and Snyder, 1962). Ever since, the solar wind has been continuously measured and extensively studied. Due to its expansion over ~ 94 astronomical units (au) (the location of the measured termination shock by Voyager 1 spacecraft (Stone et al., 2005)) it is marked by high gradients and a broad range of spatial and temporal scales.

A global model for the propagation of magnetic field from the Sun to the interplanetary space was proposed already by Parker (1958). A combination of the Sun's rotation, and the magnetic field, *frozen in* the radially expanding solar wind, in the ecliptic plane results in a *Parker spiral* shape of the magnetic field lines (Levy, 1976; Mariani et al., 1978, 1979).

An important quantity for understanding the plasma dynamics is the ratio between thermal and magnetic pressure, referred to as the plasma β:

$$\beta_\alpha = \frac{8\pi n_\alpha k_B T_\alpha}{B^2}. \tag{1}$$

Letter n stands for the density, and T for the temperature of a plasma species α, k_B is the Boltzmann constant and B the magnetic field strength. In the solar corona plasma beta is typically much smaller than one ($\beta << 1$), and the magnetic field controls the plasma flow, forcing it to rotate with the Sun.

At farther distances B decreases, and the control is taken by the dynamic pressure of the accelerating plasma flow, which pulls the magnetic field lines radially outward, making them bend in a spiral. The angle of the Parker spiral changes with radial distance:

$$\phi(r)_B = \frac{B_\phi}{B_r} = \frac{\Omega_S \sin\theta}{u_p} \cdot (r_{eff} - r), \tag{2}$$

where Ω_S is the angular speed of the Sun's rotation, θ the polar angle, u_p the solar wind proton speed, and r_{eff} the distance at which the plasma flow starts to dominate the dynamics. This distance was estimate to be ~ 10 R_S for fast solar wind and ~ 20 R_S for slow solar wind (Bruno and Bavassano, 1997). Magnetic field strength decreases with radial distance with:

$$B(r) \propto \frac{\sqrt{1+\tan^2\phi(r)_B}}{r^2}. \tag{3}$$

One of the most basic properties of the solar wind is its variability, which is strongly related to the conditions at its origin. The fast solar wind with velocities of about 500 to 800 km/s and low densities is believed to originate in the *coronal holes*, the regions in the solar corona exhibiting open magnetic field lines. These regions appear darker in the UV and X-ray images of the Sun, as the plasma densities there are lower and the temperatures cooler. The the exact origins of the more variable slow solar wind (300 to 500 km/s) are still a subject of research and discussion. Generally, the slow solar wind appears to originate from regions with more complex magnetic field configuration, consisting of open and closed magnetic field lines (magnetic loops) (Phillips et al., 1995; McComas et al., 1998, 2000; McComas, 2003). A sub-type, called slow Alfvénic solar wind, is due to the Alfvénic nature of its magnetic and velocity fluctuations, believed to originate from small equatorial coronal holes (Stansby et al., 2020). The terminal speed of the solar wind is highly dependent on the conditions in the solar corona, like amount of turbulence and electromagnetic fluctuations, as well as on the temperature and the shape of the velocity distribution functions there. Protons in the coronal holes, the source regions of fast solar wind, are believed to be hotter, and electrons to be colder than in the solar streamer belt region. This information is preserved in the solar wind through a correlation / anti-correlation between the proton / electron temperature and the solar wind speed (Neugebauer, 1976; Marsch et al., 1982; Marsch and Goldstein, 1983; Kasper et al., 2008; Halekas et al., 2019; Stansby et al., 2020; Maksimovic et al., 2020).

More than 60 years has passed since the solar wind discovery, however, some relevant enigmas remain. One, which is also a subject of this thesis work, is the energy balance of the solar wind acceleration. First, how much thermal energy is required in the solar corona to account for the observed properties of the solar wind, and how is it distributed over particle species? And second, how is this thermal energy converted to the solar wind kinetic energy? While both, fluid and kinetic approaches (discussed further in Sec. 1.2), are able to produce slow solar wind, they can not explain the acceleration of the fast solar wind without assuming extreme boundary conditions or ad-hoc heating. By boundary conditions we refer to the properties of coronal velocity distribution functions. For example, the presence of *suprathermal electrons*, an excess of high energy electrons with respect to the Maxwellian distribution in the solar corona, has a strong influence on the solar wind electron heat-flux and on its final speed (Maksimovic et al., 1997a; Lamy et al., 2003; Zouganelis et al., 2005). The shape of electron VDF in the solar corona can unfortunately not be measured in-situ, but can be inferred either from remote sensing instruments, or from the field aligned, fast steaming electrons which in the solar wind represent the electron *strahl* population. Due to their fast speed the strahl electrons have limited time to interact with their environment on their way from the Sun, and even at the location of our spacecrafts preserves some information about the state of the electron VDF in the solar corona.

The radial evolution of the solar wind is a product of concurrent action of Coulomb collisions, adiabatic expansion, heat-flux, global and local electro-magnetic fields and turbulence. In this work we address the solar wind acceleration from the kinetic point of view. We focus on the solar wind electrons in acceleration region in absence of electro-magnetic fluctuations, and quantify their contribution to the global dynamics of the solar wind. In Sec. 1.1 we summarise the current knowledge on the solar wind electrons, and in Sec. 1.2 the evolution of the kinetic solar wind models. The following, Sec. 1.3, presents the plasma kinetic description with velocity distribution functions, and Sec. 1.4 reveals the expectations about the focusing of the strahl from a simple collisionless focusing model.

1.1 SOLAR WIND ELECTRONS

The solar wind expanding through our solar system with a radius larger than 20 thousand R_S originates from a small spherical surface of the hot solar corona with a radius of just a few R_S. The plasma conditions inside the solar corona, so deterministic for the solar wind properties, can not be measured *in-situ*. However, plasma moments like density and temperature can be inferred from *remote* observations using spectroscopy (David et al., 1998; Cranmer, 2002; Mercier and Chambe, 2015). The recent works by Hahn et al. (2011) and Saqri et al. (2020) present the spatial an temporal evolution of coronal density and temperature in a polar and equatorial coronal holes, put into perspective with the quiet-Sun regions. The obtained density is lower in the coronal holes ($\sim 10^8 \mathrm{cm}^{-3}$), the regions marked with open magnetic field lines allowing efficient acceleration of plasma. In the quiet-Sun regions, where magnetic field topology is more complex, the density was observed to be from 10 to 50 times larger. The same trend was found for the coronal electron temperature spanning between 0.6 and 1 MK (52 and 86 eV) in the coronal holes, and reaching above 2 MK (172 eV) in the quiet-Sun regions. The presented temperature values were calculated assuming a Maxwellian shape of coronal VDF, however, both cited works report an existence of a second, less dense and hotter electron population inside the coronal holes, with temperature ~ 1.5 MK (129 eV). Furthermore, Dzifčáková et al. (2018) show, that assuming a Kappa distribution in the solar corona accounts well for the spectroscopic observations of a solar flare.

The hot and dense coronal plasma is governed by strong magnetic fields and collisions. Due to their small mass, most of the electrons in, for example, 1 MK corona with thermal speed of 5504 km/s, are fast enough to escape the Sun, whose escape velocity is 618 km/s. However, this is not the case for the 1836-times heavier coronal protons, with thermal speed of 131 km/s. To assure the charge neutrality of the solar wind, and prevent the charging of the Sun, an electric field emerges pointing radially away from the Sun, transferring kinetic energy from electrons to the protons. This is the *ambipolar electrostatic field*, one of the key components of the solar wind acceleration.

As soon as the solar wind starts to accelerate and expand, great gradients arise in all the plasma parameters. Due to the rapid decrease of magnetic field strength, the *mirror effect* takes place. The conservation of first adiabatic invariant, the magnetic moment μ:

$$\mu = \frac{mv_\perp^2}{2B}, \tag{4}$$

results in the focusing of the electrons and protons along magnetic field B. The observed gradients of B would quickly give rise to extremely anisotropic distribution functions, if there were no relaxation mechanisms, like Coulomb collisions, or plasma instabilities. The electron focusing in the collisionless approximation is further discussed in Sec. 1.4.

Solar wind electrons are usually modelled with three components. Most of the electron density belongs to the *core* population present at lower energies, and well represented by a bi-Maxwellian. This population was found to be regulated by Coulomb collisions, and experiences only low anisotropy ($< 20\%$) (Štverák et al., 2008). A correlation between electron *collisional age*, a measure of the number of collisions experienced by the expanding solar wind electrons, and isotropy of the electron VDFs was shown using Wind measurements by Salem et al. (2003). The Coulomb collision cross-section is dependent on the relative velocity between colliding particles and decreases with v^4. Consequently collisions are only efficient at isotropising the thermal electron population, the electron core, and have much smaller or no effect on higher energy electrons.

Higher energy electrons belong to the *halo* population present at all pitch angles, and a magnetic field-aligned, beam-like population called the *strahl*. The supra-thermal populations have been modelled with Maxwellian- and Kappa-like distributions, and especially at large distances from the Sun (~ 1 au), appear to be well represented by a bi-Kappa distributions (Feldman et al., 1975; Pilipp et al., 1987a; Hammond et al., 1996; Maksimovic et al., 1997b; Maksimovic et al., 2005; Štverák et al., 2008, 2009; Tao et al., 2016; Wilson et al., 2019a,b; Macneil et al., 2020). A study of the Coulomb scattering of the strahl electrons using kinetic theory is presented in works by Horaites et al. (2018, 2019), who provide an analytical expression relating the *strahl pitch-angle width* (PAW) to the energy and density of solar wind electrons. PAW was found to decrease with electron energy, at 1 au affecting electrons below ~ 300 eV.

The effect of the collisions on the electron core and strahl is investigated in the scope of this thesis project using a numerical model simulating a radially expanding solar wind under the presence of binary Coulomb collisions (BiCoP) (Landi and Pantellini, 2001, 2003). The results are gathered in Chapter 3 and in Article C.

While the observed radial profiles of electron core temperature and density have been explained by models accounting for Coulomb collisions (Phillips et al., 1989; Phillips and Gosling, 1990; Lie-Svendsen et al., 1997), we still do not completely understand the evolution of the supra-thermal electron components. Against the expectation of focusing with radial distance, strahl has been observed to scatter during expansion between 1 and 3.5 au (Ulysses data, Hammond et al. (1996)), and between 1 and 6 au (Cassini data, Graham et al. (2017)). We investigate the behaviour of the strahl electrons in the inner heliosphere, using Helios mission data, sampling the distances between 0.3 nad 1 au (Article A, Ch. 2).

Since the strahl electrons are the main carriers of the *heat flux*, the energy stored in the asymmetry of the electron VDF, the strahl scattering mechanisms are important for the heat flux regulation in the solar wind. Besides that, the scattered strahl electrons might become a part of almost isotropic halo population. The study of radial evolution of separate electron VDF components over a radial distance between 0.3 and 3 by Štverák et al. (2009) reveals, that while relative density of the core does not vary with radial distance, the relative densities of the strahl and the halo do. Closer to the Sun the strahl is dominant and the halo barely seen, while at further distances the strahl density decreases and the halo density increases. This implies that the halo is formed from the scattered strahl electrons. Furthermore, Graham et al. (2017) report that the strahl ceases to exist at distances larger than 5.5 au as it is most likely completely scattered into the halo population.

The scattering of the strahl electrons and the origin of the halo electrons remain active topics in the physics of solar wind electrons, as well as in global physics of solar wind expansion. During the course of this thesis project we provided pieces of observational and numerical evidence, which are presented in this manuscript and the attached articles, and will hopefully help develop a more complete understanding of the evolution of the solar wind as it escapes from the Sun.

1.2 KINETIC EXOSPHERIC SOLAR WIND MODELS

At the same time as Eugene Parker was developing a fluid, hydrodynamic model of the solar wind (Parker, 1958), Joseph W. Chamberlain was working on a kinetic description, which was published in 1960 in a form of an exospheric solar wind model (Chamberlain, 1960).

Exospheric models were developed with the aim of more accurately describing the solar wind plasma above a radial distance, where the density and temperature drop and the plasma becomes collisionless, and where the Maxwellian assumption adopted by fluid models is no longer valid. This radial distance is, in the frame of exospheric models, referred to as the *exobase*. Compared to the fluid models, which by construction assume Maxwellian VDFs of all fluids included, exospheric models allow a free evolution of the VDF chosen at the exobase, the shape of which then depends only on the forces included in the model. The collisionality of the plasma can be measured with a *Knudsen number* (K_n), which is the ratio between the mean-free path (λ) and the atmospheric density scale-height (H):

$$K_n = \frac{\lambda}{H}. \tag{5}$$

When $K_n > 1$, the plasma is collisionless, and departures from Maxwellian VDF can be expected. Accordingly to the Parker's fluid solar wind model, the exobase, the radial distance at which $K_n = 1$, is located at 4 R_S (Brasseur and Lemaire, 1977).

The evolution of a particle velocity distribution (VDF, f_α) is described with the *Boltzmann equation*:

$$\frac{\partial f_\alpha}{\partial t} + \mathbf{v} \cdot \frac{\partial f_\alpha}{\partial \mathbf{x}} + \mathbf{a} \cdot \frac{\partial f_\alpha}{\partial \mathbf{v}} = \left(\frac{\delta f_\alpha}{\delta t}\right)_c, \tag{6}$$

where **a** is the acceleration due to static electric and magnetic forces. These forces do not account for Coulomb electric field fluctuations. On the right-hand side the collisional term describes the temporal evolution of f_α as a result of particle collisions. In the exospheric solar wind models the contribution of collisions is neglected ($\delta f_\alpha / \delta t = 0$), and the Boltzmann equation describes the conservation of the phase-space density along trajectories, and is related to *Liouville's theorem*. The exospheric solution is stationary and provides us with the shape of an VDF at any position in the exosphere.

In exospheric models particles are divided into 4 particle classes depending on their velocity and angular momentum.

- *Escaping particles* are particles with velocities high enough to escape the gravity of the Sun.
- *Ballistic particles* are particles with velocities lower than the escape velocity, which eventually ballistically fall back to the solar corona.
- *Trapped particles* are particles with velocities lower than the escape velocity, which are trapped by magnetic mirror force, therefore bouncing between the magnetic mirror point and the gravity turning point.
- *Incoming particles* are particles originating from outside of the solar system. Note that this population has been ignored in the existing exospheric models, which equals to assumption that the pressure of the interstellar medium is negligible.

The exospheric particle classes can be related to the solar wind electron VDF model determined from the observations. Three classes consisting of particles with velocities not large enough to escape the Sun (ballistic, trapped, and incoming electrons) represent the electron core. While the escaping electrons correspond to the electron strahl. Exospheric models do not produce a halo population, which is one more reason to believe that the halo is a result of field-particle interactions during the solar wind expansion.

Due to the difference in the mass of electron and proton, gravitational force tends to polarise the plasma consisting of the two species. Therefore, an electrostatic field directed oppositely to the gravitational force is needed to preserve the plasma, quasi-neutrality. The expression for the electric field, present in a gravitationally bound plasma in hydrostatic equilibrium, consisting of protons and electrons, was derived by Pannekoek (1922) and Rosseland (1924):

$$\mathbf{E}_{PR} = -\nabla\Phi_{PR} = -\frac{(m_p - m_e)\mathbf{g}}{2e}, \tag{7}$$

where $\mathbf{g}$ is the gravitational potential, and e the electron charge.

However, the solar wind is not a plasma in hydrostatic equilibrium, and using E_{PR} in the early exospheric models resulted in the subsonic proton expansion velocities. The kinetic model by Chamberlain (1960) produced a plasma with a velocity of $\sim$ 20 km/s, and a density of 370 cm^{-3} at 1 au, and was thus referred to as the *solar breeze model*. As soon as the first solar wind observations confirmed the supersonic prediction by Parker, the exospheric models were proven wrong and largely abandoned. That is until (Lemaire and Scherer, 1970, 1971) discovered this flaw in the electric field assumption, and presented the exospheric models producing supersonic protons. At the same time as Jockers (1970) found a supersonic solution independently.

Lemaire and Scherer (1971) proved that the evaporation of electrons is faster than that of protons, due to the electron small mass and high thermal velocity. The electrostatic field required to balance the flux of evaporating electrons and protons, now also referred to as the *ambipolar* electric field, was calculated assuring quasi-neutrality and zero current condition at any radial distance. The newly obtained total potential difference ($\Delta\Phi$) between the exobase and infinity, assuring that the Sun remains charge free, was more than two times larger than $\Delta\Phi_{PR}$. Using $\Phi(r)$ resulted in radial density, bulk velocity and total temperature profiles, which compared very well to the observations of the slow solar wind. On the other hand, the temperature anisotropy predicted by the exospheric models at 1 au for both solar wind species ($T_{e,\|}/T_{e,\perp} \sim 3$, $T_{p,\|}/T_{p,\perp} \sim 164$) was much higher than that observed.

As this model did not include the effect of rare Coulomb collisions, nor the effect of wave particle interaction, the high anisotropies were accounted to these two phenomena. Later Chen et al. (1972) and Pierrard et al. (2001) showed that the proton anisotropy is significantly reduced, if Parker spiral magnetic field configuration is used instead of purely radial assumption adopted in the previous models.

Many models developed up to this point, kinetic and fluid, were able to produce solar wind with terminal speeds up to 500 km/s assuming realistic coronal proton and electron temperatures. However, none of them could go beyond this velocity limit. That is until the exospheric models were generalised to the use of Kappa VDFs, as opposed to only Maxwellian VDFs used in the previous works (Pierrard and Lemaire, 1996; Maksimovic et al., 1997a). A Kappa VDF exhibits an increase of supra-thermal electrons compared to a Maxwellian VDF with the same temperature. Therefore, assuming a Kappa VDF at the exobase results in a larger coronal electron evaporation flux, which in turn leads to larger $\Delta\Phi$, and higher terminal solar wind speed. These models were the first ones able to produce the solar wind with velocities reaching up to 800 km/s. Zouganelis et al. (2004) showed, that the enhancement of the electron evaporation flux is not only a property of a Kappa VDF, but can be achieved by increasing the relative amount of supra-thermal electrons in the corona in any way. They obtain high terminal solar wind speeds using an initial exobase VDF consisting of a Maxwellian core and another less dense and hotter Maxwellian population.

The first solar wind model accounting for Coulomb collisions by solving the Boltzman equation with the Fokker-Planck collision term was developed by Lie-Svendsen et al. (1997). A Fokker-Planck treatment of Coulomb collisions was used also in the exospheric model by Pierrard et al. (1999), who use a electron VDF observed at 1 au by WIND spacecraft and advance it all the way back to the solar corona. They conclude that the observed features of the VDF (the core, the halo and the strahl) can not be a result of solely the effects of collisions during the expansion. The observed VDFs at 1 au are either a consequence of field-particle interactions during the expansion or the presence of non-thermal features already in the solar corona.

In this manuscript we present the results of a numerical kinetic model of the solar wind, based on the exospheric kinetic models (Landi and Pantellini, 2001, 2003; Landi et al., 2010, 2012, 2014). This is a simple model, not accounting for any type of wave-particle interactions, but exposing the effects of particle kinetic properties on the solar wind expansion. The benefits of the numerical model in comparison to the existing exospheric models are:

- a statistical treatment of binary Coulomb collisions instead of using an ad-hoc Fokker-Planck collision operator,
- a self-consistent calculation of the ambipolar electric field, and
- a continuous transition between the collisional and collision-less regime (the exobase is not defined as a single radial distance and is not required as an input parameter).

The goal of our project is to analyse and understand the in-situ measurements of solar wind electrons in the inner heliosphere, to then, using a numerical model, try to relate them to the state of the solar corona at their origin. On the way to the spacecraft, electron trajectories get modified as a consequence of expansion and interaction with other particles and EM-fields, and this interaction needs to be well understood, if we wish to back-trace the observe electron VDFs to their origin.

1.3 VELOCITY DISTRIBUTION FUNCTIONS

Throughout the work we use a kinetic plasma physics description, which provides the statistical properties of the plasma, using the *particle velocity distribution functions* $f_\alpha(\mathbf{x}, \mathbf{v}, t)$. f_α is normalised so that its integral over three-dimensional space and three-dimensional velocity space equals to the number of particles (n_α):

$$n_\alpha = \int f_\alpha(\mathbf{x}, \mathbf{v}, t) d^3\mathbf{x} d^3\mathbf{v}. \tag{8}$$

f_α can be reduced to a set of macro-physical parameters only exhibiting three dimensions in space and one in time. Therefore, these parameters are obtained through an integration over a full velocity space of the distribution function, and are referred to as the plasma *bulk parameters*, or *velocity moments*.

The zeroth velocity moment corresponds to the *number density* n_α (Eq. 8), the first plasma moment to the *bulk velocity* $\mathbf{u}_\alpha$:

$$\mathbf{u}_\alpha = \frac{1}{n_\alpha} \int \mathbf{v} f_\alpha d^3\mathbf{v}, \tag{9}$$

and the second plasma moment to the *pressure tensor* P_α:

$$P_\alpha = m_\alpha \int (\mathbf{v} - \mathbf{u}_\alpha)(\mathbf{v} - \mathbf{u}_\alpha) f_\alpha d^3\mathbf{v}. \tag{10}$$

It is often useful to express the pressure tensor in a frame aligned with the background magnetic field (B), to obtain the components parallel ($\|$) and perpendicular ($\perp$) to B. If I_3 is a three-dimensional unit matrix, and $\hat{b} \equiv \mathbf{B}/|\mathbf{B}|$,

$$p_{\perp,\alpha} \equiv \frac{1}{2} P_\alpha \text{ for } (I_3 - \hat{b}\hat{b}) \tag{11}$$

$$p_{\|,\alpha} \equiv P_\alpha \text{ for } (\hat{b}\hat{b}). \tag{12}$$

From here we can obtain plasma temperatures parallel and perpendicular to B:

$$T_{\perp,\|,\alpha} = \frac{p_{\perp,\|,\alpha}}{n_\alpha k_B}. \tag{13}$$

We expressed only the first four plasma moments, but infinite amount of higher moments exist, and can be obtained using the same pattern as above.

The fundamental model velocity distribution function (VDF) frequently used in space physics is a *Maxwellian VDF*, the velocity distribution of a gas in thermodynamic equilibrium:

$$f_M(\mathbf{v}) = \frac{n}{\pi^{3/2} w^3} \exp\Big(-\frac{(\mathbf{v}-\mathbf{u})^2}{w^2}\Big), \tag{14}$$

where

$$w = \sqrt{\frac{2k_B T}{m}}. \tag{15}$$

We assume a cylindrical three- dimensional system, where the asymmetric axis is aligned with the magnetic field B. Eq. 14 representing isotropic distribution function is adapted to account for anisotropies with respect to B, regularly observed in space plasmas. The *bi-Maxwellian VDF* is defined as:

$$f_{bM}(v_\perp, v_\parallel) = \frac{n}{\pi^{3/2} w_\perp^2 w_\parallel} \exp\Big(-\frac{v_\perp^2}{w_\perp^2} - \frac{(v_\parallel - u_\parallel)^2}{w_\parallel^2}\Big), \tag{16}$$

where $w_\perp$ and $w_\parallel$ can be expressed in terms of perpendicular and parallel temperature:

$$w_{\perp,\parallel} = \sqrt{\frac{2k_B T_{\perp,\parallel}}{m}}. \tag{17}$$

Another commonly used model distribution is the *Kappa VDF* (Tsallis, 1988; Maksimovic et al., 1997a; Livadiotis and McComas, 2013; Livadiotis, 2017), exhibiting an excess of high-energy particles in comparison to a Maxwellian VDF.

$$f_\kappa(\mathbf{v}) = \frac{n}{\pi^{3/2} w_\kappa^3 \kappa^{3/2}} \frac{\Gamma(\kappa+1)}{\Gamma(\kappa-1/2)} \cdot \Big(1 + \frac{(\mathbf{v}-\mathbf{u})^2}{\kappa w_\kappa^2}\Big)^{-\kappa-1}, \tag{18}$$

where $\Gamma(x)$ is the Reimann Γ-function (Abramowitz and Stegun, 1972), and

$$w_\kappa = \sqrt{\frac{\kappa - 3/2}{\kappa} \cdot \frac{2k_B T}{m}}. \tag{19}$$

The parameter κ, always greater than $3/2$, determines the amount of suprathermal electrons. In the limit $\kappa \to \infty$, a Kappa VDF tends towards a Maxwellian VDF. A *bi-Kappa VDF* can be defined, accounting for anisotropy along B:

$$f_{b\kappa}(v_\perp, v_\parallel) = \frac{n}{\pi^{3/2} w_{\kappa,\perp}^2 w_{\kappa,\parallel} \kappa^{3/2}} \frac{\Gamma(\kappa+1)}{\Gamma(\kappa-1/2)} \cdot \Big(1 + \frac{v_\perp^2}{\kappa w_{\kappa,\perp}^2} + \frac{(v_\parallel - u_\parallel)^2}{\kappa w_{\kappa,\parallel}^2}\Big)^{-\kappa-1}, \tag{20}$$

where

$$w_{\kappa,\perp,\parallel} = \sqrt{\frac{\kappa - 3/2}{\kappa} \cdot \frac{2k_B T_{\perp,\parallel}}{m}}. \tag{21}$$

1.4 SIMPLE COLLISIONLESS FOCUSING MODEL

Due to the radial gradient in the interplanetary magnetic field (B), solar wind is subject to the focusing mechanism. All particle species are affected by it, however, the effects are much stronger on the subsonic, than on the supersonic VDFs. The comparison between sub- and supersonic focusing is shown in Fig. 2 in Landi et al. (2012). We focus on the behaviour of subsonic, solar wind electrons. Electron core component is dominated by Coulomb collisions, efficiently counteracting the focusing at lower energies. However, at higher, strahl electron energies, the focusing effect can be observed. As the strahl electrons move in the antisunward direction, to the regions with weaker magnetic field, their velocity perpendicular to B gets converted into parallel one, conserving magnetic moment and electron energy:

$$\mu = \frac{m_e v_\perp^2}{2B} = \text{const.} \tag{22}$$

$$\mathcal{E} = \frac{m_e}{2}(v_\perp^2 + v_\parallel^2) - e\phi = \text{const.}, \tag{23}$$

where ϕ is the ambipolar potential. The contribution of gravity on the solar wind electrons was neglected.

We make use of these two simple equations to model the radial, collisionless expansion of the solar wind electrons in a radially decreasing B ($B \propto r^{-2}$). An illustration of the VDF evolution with distance is shown in Fig. 1. The variables in this model are the location of the exobase (r_0), the distance at which collisions are not able to support a Maxwellian VDF and where the focusing starts, the electron VDF at this distance (f_0), the distance of interest (r_1), and the difference of electric potential between r_1 and r_0 ($\Delta\phi$).

This simple model has three main drawbacks. It does not account for non-radial, Parker spiral behaviour of B; it assumes there exists a single exobase, a discrete distance at which focusing begins to have effect; and it does not account for Coulomb collisions. We were able to isolate the importance of the last two phenomena, the multi-exobase and Coulomb collisions, which are accounted for in the kinetic model BiCoP. The comparison between the simple and BiCoP model is shown in Ch. 3.

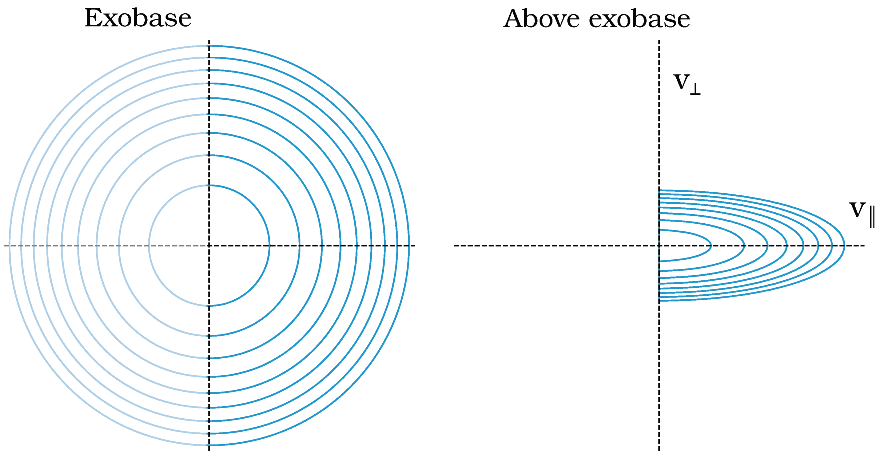

Figure 1: An example of a uniform Maxwellian distribution representing the electron VDF in the solar corona (left), and a part of electron VDF at a farther distance resulting from a collisionless focusing of the anti-sunward portion of the VDF (right). The VDFs are represented with a contour plot, in a frame aligned with the magnetic field direction.

1.4.1 *Characterisation of the focused VDF*

Due to the nature of the focusing phenomena, we characterise the strahl VDF with two parameters, the *pitch-angle width* (PAW) and the *strahl parallel temperature* ($T_{||}$). PAW is defined as a full width half maximum (FWHM) of the pitch-angle distributions separately for each energy bin, allowing for energy dependent focusing and scattering mechanisms.

$$f_i(\alpha) = f_{max,i} \cdot \exp\left(-\frac{\alpha^2}{2\sigma_i^2}\right), \qquad PAW_i = 2\sqrt{2\ln 2} \cdot \sigma_i, \tag{24}$$

where $f_i(\alpha)$ is the pitch-angle distribution of ith energy bin, and α is the pitch angle.

$T_{s,||}$ is obtained by fitting a 1-dimensional Maxwellian to the parallel cut through the strahl VDF ($f_{||}$) in the logarithmic space:

$$\ln f_{||}(v_{||}) = -\frac{m_e}{2k_B \cdot T_{s||}} \cdot v_{||}^2 + \ln\left(n_s\sqrt{\frac{m_e}{2\pi k_B \cdot T_{s||}}}\right). \tag{25}$$

Strahl characterisation with PAW and $T_{s,||}$ is illustrated in Fig. 2, and was done the same way from our observational and modelled VDFs, assuring an easy comparison between different research approaches.

PAW characterisation was previously used by Hammond et al. (1996) and Graham et al. (2017), however, strahl electrons have so far been modelled also by a bi-Maxwellian (**e.g**; Landi et al., 2014), and a bi-Kappa VDF (**e.g.**; Štverák et al., 2009). The relation between the the

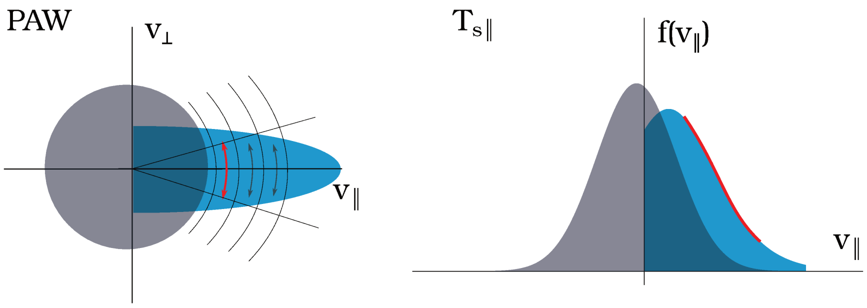

Figure 2: A schematics showing the characterisation of the strahl VDF with parameters PAW (left) and $T_{s,||}$ (right).

different strahl descriptions is not always straight-forward. We therefore show the examples, of how different properties of the observed electron VDF appear in the PAW characterisation.

Any isotropic VDF centred on $v_{||} = 0$ results in PAW tending towards infinity. Fig. 3 shows how the PAW evolves with energy for a uniform VDFs ((a) Maxwellian and (b) Kappa) with the anisotropy ($\perp/||$) of 0.5. Plots (c) to (e) show examples of PAWs for two-component electron VDFs, consisting of the core and the strahl component.

Fig. 3 (c) represent a VDF assuming typical parameters observed at 1 au (Wilson et al., 2019b), where the strahl is modelled with a drifting Kappa VDF. Similar dependence between PAW and electron energy was indeed observed at 1 au and reported by Graham et al. (2017) and in Article A.

Examples (d) and (e) imitate the electron VDFs observed closer to the Sun (example shown in Article B). The strahl in this case is modelled with a Maxwellian or Kappa VDF with a $v_{||} = 0$, present only for $v_{||} > 0$.

1.4.2 *Expectations from the simple collisionless focusing model*

We investigate how changing different model parameters affects the PAW and $T_{s,||}$ obtained at the distance of 35 R_S ($r_1 = 35\ R_S$). Initial VDF at r_0 is set to be an isotropic Maxwellian VDF with the temperature of 86 eV and evolved over radial distance using Eq. 22 and 23. Fig. 4 shows the comparison between model results obtained using the same exobase location r_0, but varying the potential difference $\Delta\phi$. We found that both, PAW and $T_{s,||}$, are independent of $\Delta\phi$ parameter. Climbing out of the potential well the energy of electrons is decreased for $e\Delta\phi$, however, this does not affect the shape of the resulting VDF. In Fig. 5, $\Delta\phi$ is kept constant, while we vary the location of the exobase (r_0). r_0 has a strong effect on the resulting PAW, however, the shape of the parallel slice through the VDF ($f_{||}$) and $T_{s,||}$ remains unchanged for all examples.

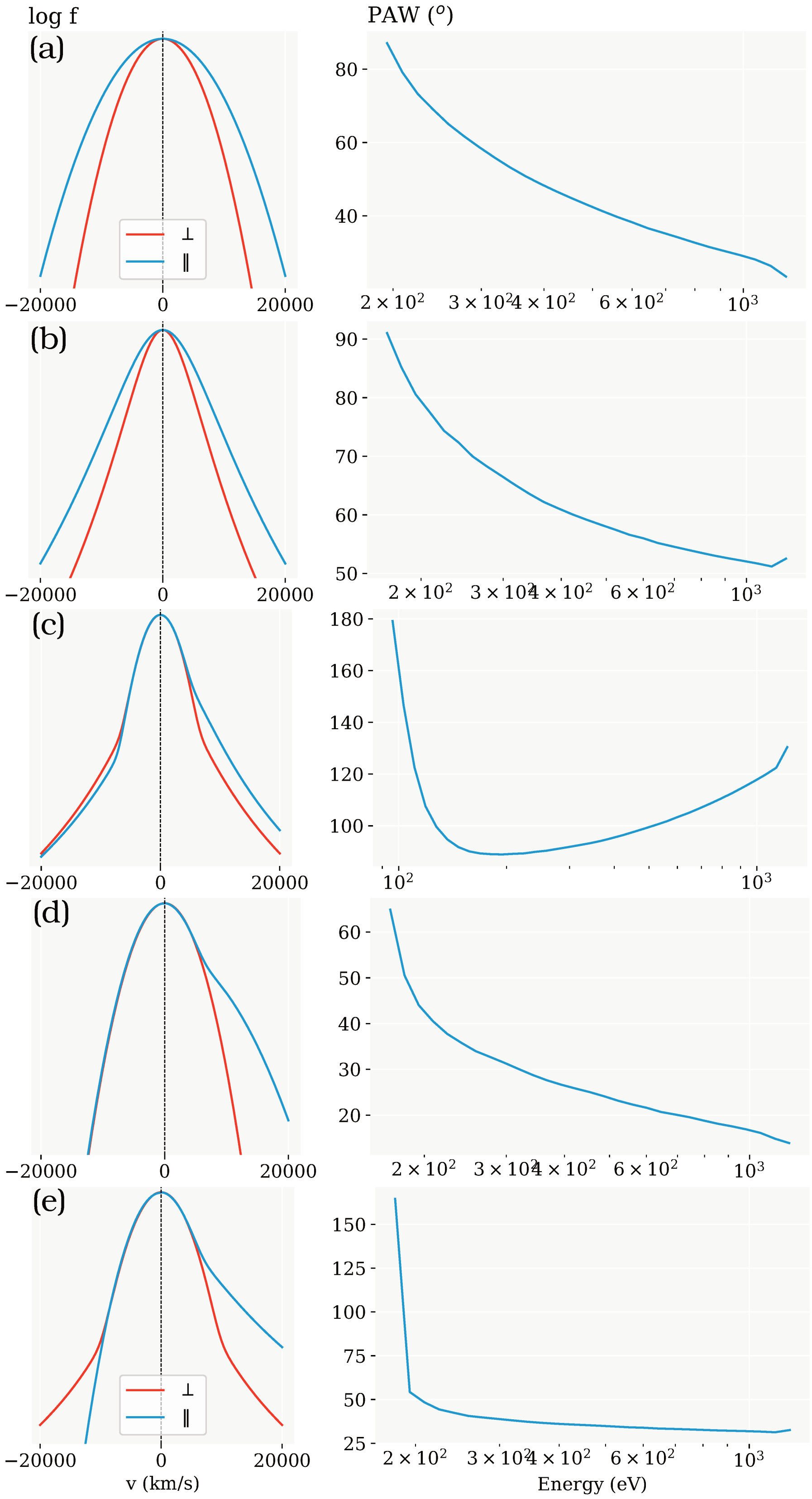

Figure 3: Parallel (‖) and perpendicular (⊥) slice through the example VDF (left plot), and the PAW of the same VDF for the positive $v_{\|}$ values. (a) Maxwellian VDF: $T_{\|}$ = 86 eV, $T_{\perp}$ = 43 eV, $v_{\|}$ = 0; (b) Kappa VDF: $T_{\|}$ = 61 eV, $T_{\perp}$ = 31 eV, $v_{\|}$ = 0, κ = 5; (c) Maxwellian core: $T_{\|}$ = 13 eV, $T_{\perp}$ = 13 eV, $v_{\|}$ = -25 km/s, + Kappa strahl: $T_{\|}$ = 29 eV, $T_{\perp}$ = 26 eV, $v_{\|}$ = 2110 km/s, κ = 4; n_s/n_c = 0.04; (d) Maxwellian core: $T_{\|}$ = 22 eV, $T_{\perp}$ = 22 eV, $v_{\|}$ = -100 km/s, + Maxwellian strahl: $T_{\|}$ = 86 eV, $T_{\perp}$ = 22 eV, $v_{\|}$ = 0 km/s, only present for the positive $v_{\|}$; n_s/n_c = 0.05; (e) Maxwellian core: $T_{\|}$ = 22 eV, $T_{\perp}$ = 22 eV, $v_{\|}$ = -100 km/s, + Kappa strahl: $T_{\|}$ = 86 eV, $T_{\perp}$ = 22 eV, $v_{\|}$ = 0 km/s, κ = 4, only present for the positive $v_{\|}$; n_s/n_c = 0.05.

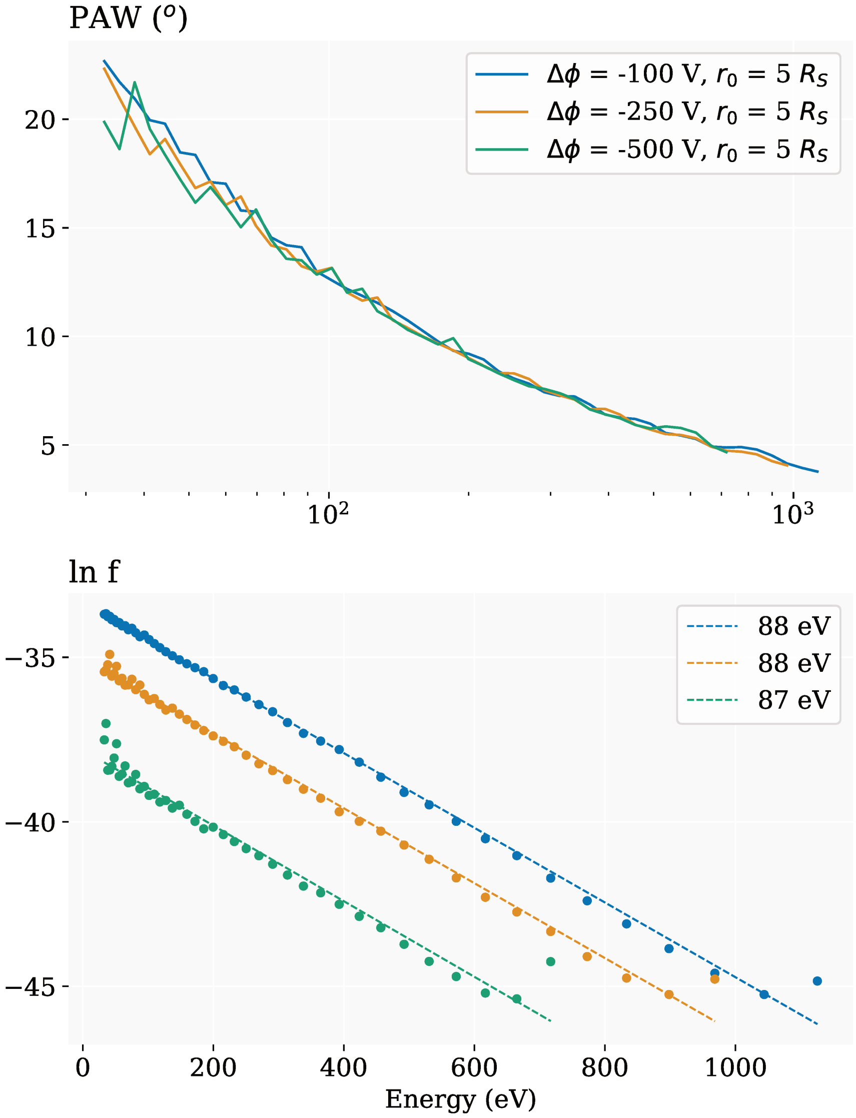

Figure 4: PAW (upper plot), and parallel slice through the VDF ($f_{||}$, lower plot) with respect to electron energy, resulting from the simple collisionless focusing model at the distance of 35 R_S. Different colours correspond to the examples with different $\Delta\phi$. The dashed line in the lower plot represents a 1D Maxwellian fit to $f_{||}$, giving the $T_{s,||}$ marked in the legend.

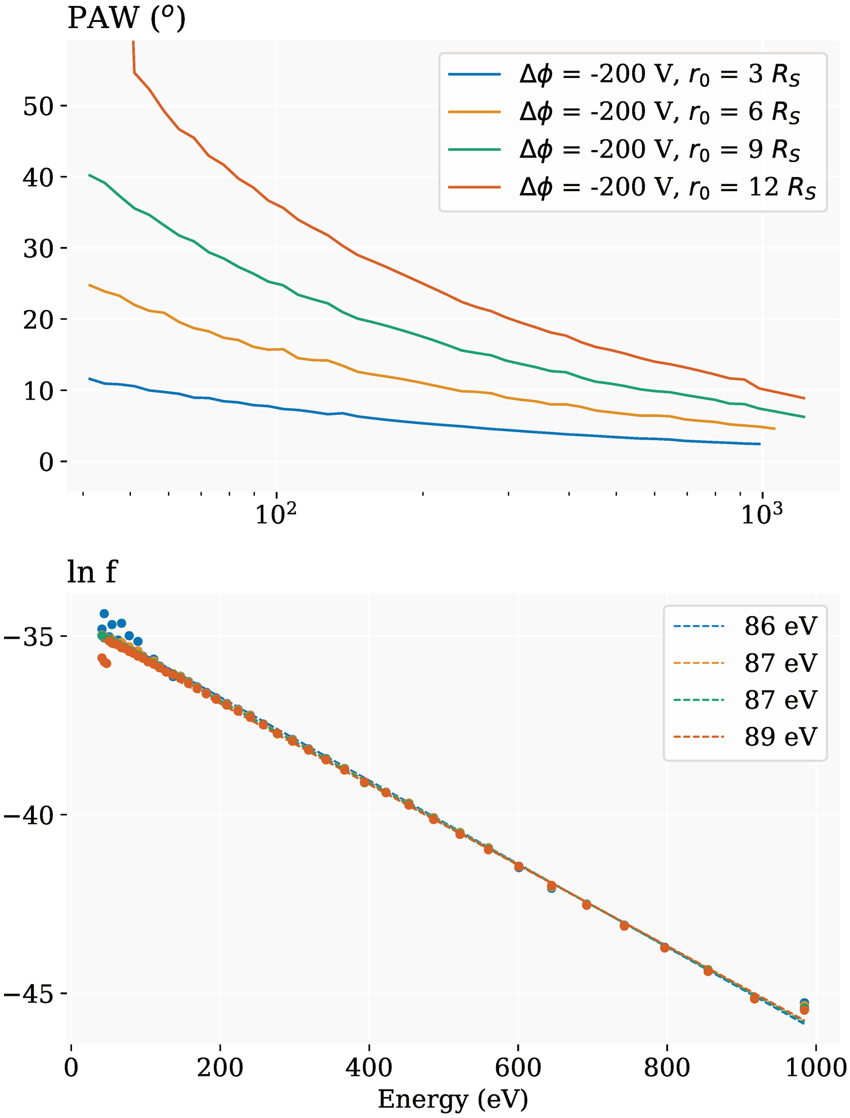

Figure 5: PAW (upper plot), and parallel slice through the VDF ($f_{||}$, lower plot) with respect to electron energy, resulting from the simple collisionless focusing model at the distance of 35 R_S. Different colours correspond to the examples with different r_0. The dashed line in the lower plot represents a 1D Maxwellian fit to $f_{||}$, giving the $T_{s,||}$ marked in the legend.

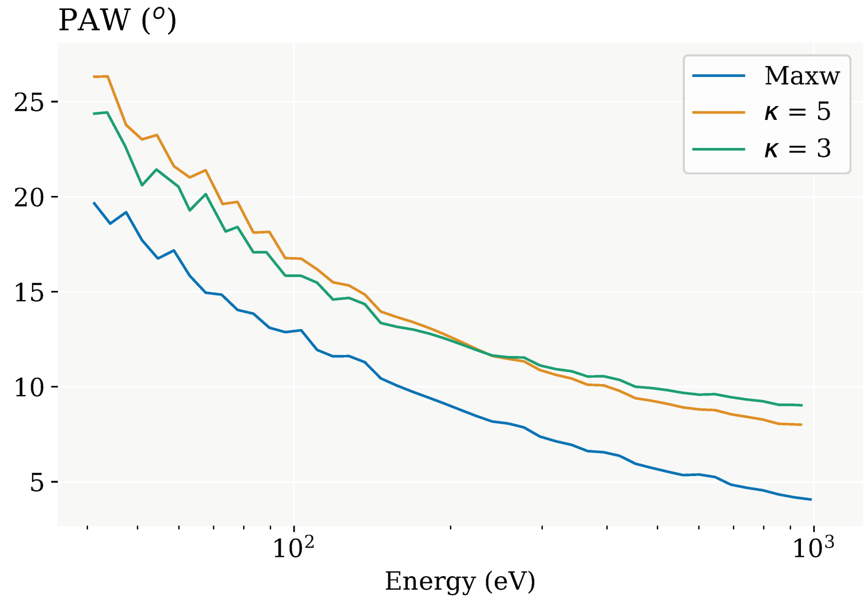

Figure 6: PAW with respect to electron energy, resulting from the simple collisionless focusing model at the distance of 35 R_S. Different colours correspond to the examples with different exobase VDFs (Maxwellian VDF, Kappa VDF with $\kappa = 5$ and Kappa VDF with $\kappa = 3$.)

We demonstrated that $T_{s,||}$ is not affected by a simple collisionless focusing and remains unchanged from the exobase. This conclusion is only valid, if the VDF at the exobase is Maxwellian. For a Kappa VDF at the exobase, we expect a dependence on $\Delta\phi$, because the velocity derivative of a Kappa VDF is not constant over velocity space. Therefore, the shape of a VDF shifted in energy is not the same as the shape of the VDF centred on $v = 0$.

The expected PAWs at $r_1 = 35R_S$ for different shapes of the VDF at the exobase are compared in Fig. 6, with the model parameters $r_0 = 5R_S$, and $\Delta\phi = -200V$. The exobase VDFs – a Maxwellian and two Kappa VDFs with different κ ($\kappa = 5$ and $\kappa = 3$) – were set to all have the same thermal velocity w (see Eq. 15 and Eq. 21). We found that Maxwellian exobase condition results in the lowest PAWs. At lower electron energies, PAWs from all three examples present a similar slope with respect to energy, while at higher energies the κ examples appear flatter. The gradient is the smallest for the VDF with $\kappa = 3$.

We have presented the scientific background regarding the kinetic properties of the solar wind electrons investigated in this work, and shown the expectations about the behaviour of the strahl electrons accordingly to the simple collisionless, waveless assumption. In nature these conditions are not fulfilled, and departures from the simple model are expected. In the following Chapter 2 we present the observational findings obtained from the electron VDFs measured by Helios and PSP spacecrafts. After, in Chapter 3 we present the results of a kinetic model accounting for Coulomb collisions, compared to the simple model and the observational results. Combining the three approaches allows us to isolate the effects of separate physical mechanisms on the electron VDF.

2

OBSERVATIONS

2.1 HELIOS

The Helios mission includes two probes build in Germany, and launched onto an ecliptic orbit around the Sun in years 1974 and 1976. The mission objective was to investigate the solar wind in the inner heliosphere over the radial distance from 0.3 to 1 au (or 64.5 to 215 R_S). Measurements provided by the two Helios spacecrafts led to a better understanding of the solar wind and are, even almost 40 years after the end of the mission operation, still used in new scientific publications (e.g. Articles A and B).

Electron VDFs observed by the Helios mission were presented by Pilipp et al. (1987a) and Pilipp et al. (1987b), and the radial evolution of the core electron temperature was studied by Marsch et al. (1989). They reported that the radial temperature gradient for solar wind electrons is smaller than that of protons. The radial evolution of the suprathermal electron components was presented with a combination of Helios and Ulysses observations by Maksimovic et al. (2005). They report the decrease of the relative strahl electron density with distance. This trend was confirmed by Štverák et al. (2008, 2009, 2015), who provide statistical analysis of electron VDFs measured by Helios, Cluster and Ulysses mission. They show that both, plasma instabilities and collisions play a role in isotropisation of the electron core population. κ-value, a measure of the relative abundance high-energy tails, was found to decrease with the radial distance and the solar wind velocity, showing that high-energy tails are predominant at large heliocentric distances and in the fast solar wind. In contrast to solar wind protons, the observed temperature gradients of the solar wind electrons do not require the existence of important heating mechanisms. The electron heating rates were actually found to be negative for both the slow and fast solar wind.

Macneil et al. (2020) use Helios electron measurements to reveal that the sunward directed strahls, appearing due to local inversions of the magnetic field lines, referred to as the switchbacks, are broader and less intense than their outward directed counterparts. They account this effect to the longer path travelled by these strahl electrons resulting in more scattering along the way.

We used Helios electron VDF to study the radial evolution of the strahl electron component between 0.3 and 1 au (Article A). We found that the strahl properties are different for the solar wind separated by electron core beta parameter $\beta_{e,c}$. The strahl of the low-$\beta_{e,c}$ solar wind, corresponding to faster and more tenuous solar wind, was found to be narrower than in the high-$\beta_{e,c}$ solar wind. In the low-$\beta_{e,c}$ solar wind, the strahl electrons with energies below ~ 250 eV slightly focus over the radial distance within 0.74 au. At higher energies and in the high-$\beta_{e,c}$ solar wind, the strahl broadens with radial distance, as reported previously by Hammond et al. (1996) and Graham et al. (2017) for the distances above 1 au.

More energetic strahl electrons of the low-$\beta_{e,c}$ solar wind show a correlation between the strahl PAW and their energy, for which we developed a simple empirical model. The increase of strahl electron velocity perpendicular to the magnetic field was observed to be exponentially related to the parallel strahl electron velocity and the change in radial distance. Further studies are required to understand which phenomena could scatter strahl electrons in this particular way described with Eq. 18 in Article A.

Strahl electrons in the high-$\beta_{e,c}$ solar wind are effectively scattered over their whole energy range. From an anticorrelation between the PAW and electron energy at 0.34 au, the strahl gets scattered to PAs above 100^{o} at 1 au, many times disappearing completely from the electron VDF. We believe that the stronger scattering observed is related to the $\beta_{e,c}$ parameter itself – high-$\beta_{e,c}$ solar wind is more unstable with respect to the kinetic instabilities.

2.1.1 *Electron core and halo properties*

Besides our novel treatment of the Helios strahl electron observations (described in Sec. 3 of Article A), we present a larger statistics of the electron core, and halo moments, compared to the previous published Helios electron studies.

The electron instruments on-board Helios probes only provided a 2-dimensional VDF measurement, taking advantage of the spin of the spacecraft to sample electrons in the ecliptic plane. Consequently, the fitting of the measured VDFs with a traditional bi-Maxwellian or bi-Kappa electron VDF model, could only be performed during times when the magnetic field was in the ecliptic plane – the plane of measurement. The data sets presented by Štverák et al. (2008, 2009, 2015) and in Article A, are therefore limited to this criteria, as these studies explore the properties of the electrons along the magnetic field direction.

However, the electron properties perpendicular to the magnetic field can be obtained also from the VDFs measured at times when magnetic field is not in the plane of measurement. We preformed a Maxwellian core, and a Kappa halo fit following the method description in Sec. 3

of Article A to all the electron VDFs measured by Helios 1 mission, which resulted in 200159 successful fits. This large statistics of the perpendicular electron VDF properties was used by Maksimovic et al. (2020), presenting the anti-correlation between the total electron temperature and the solar wind velocity in the near-Sun regions. In Figs. 7 and 8 we show the 2-dimensional, column normalised histograms revealing the relation between the perpendicular temperature of the core ($T_{c,\perp}$) and halo ($T_{h,\perp}$) components separately, and the solar wind velocity for different radial distances.

The strongest difference between $T_{c,\perp}$ and $T_{h,\perp}$ in the slow and fast wind can be seen in the upper plots of Figs. 7 and 8, presenting the parameter variation in the radial bin closest to the Sun. In the farthest radial bin (lower plots), the anti-correlation between $T_{c,\perp}$ and $T_{h,\perp}$, and v_p is barely observed, resulting in only the slightest difference in the temperature of the slow and the fast solar wind. This implies that, while the electrons of the slow solar wind cool down significantly between 0.3 and 1 au, the electrons of the fast solar wind barely change their temperature.

Furthermore, two separate populations can be recognised by two separate peaks in the 1D histogram of $T_{c,\perp}$ in the radial bin closest to the Sun (Fig. 7, upper plot). In the middle radial bin the two populations can be barely separated, and in the farthest bin only one peak in $T_{c,\perp}$ is seen. The different solar wind populations observed by Helios mission are presented by Stansby et al. (2020), who relate the populations' properties to their different origins. The higher-$T_{c,\perp}$ population corresponds to a mixture of slow non-Alfvénic, and slow Alfvénic solar wind, while the lower-$T_{c,\perp}$ corresponds to the fast solar wind.

We investigate the relation between $T_{h,\perp}$ and κ value for different radial distance bins (see Fig. 9). Low κ values mark the halo VDFs with strong high-energy tails. As the κ value increases, the halo VDFs tend more towards a Maxwellian distribution, and limits to a Maxwellian for $\kappa \to \infty$.

A positive correlation was found between $T_{h,\perp}$ and κ for all radial distances. The solar wind with higher $T_{h,\perp}$ corresponds to the slow solar wind, which was observed to exhibit higher T_c and higher plasma density. Higher electron temperature and density result in higher plasma β value, placing the electron VDF closer to the kinetic plasma instability thresholds (see Fig. 6 in Article A). VDF relaxation through plasma instabilities could explain the halo population ten towards a Maxwellian VDFs in the slow solar wind. On the other hand, the fast solar wind is characterised by lower $T_{h,\perp}$, T_c, and plasma density and exhibits a relatively higher amount of suprathermal electrons. This lower-β solar wind is far from plasma instability thresholds and is believed to be younger compared to the slow wind

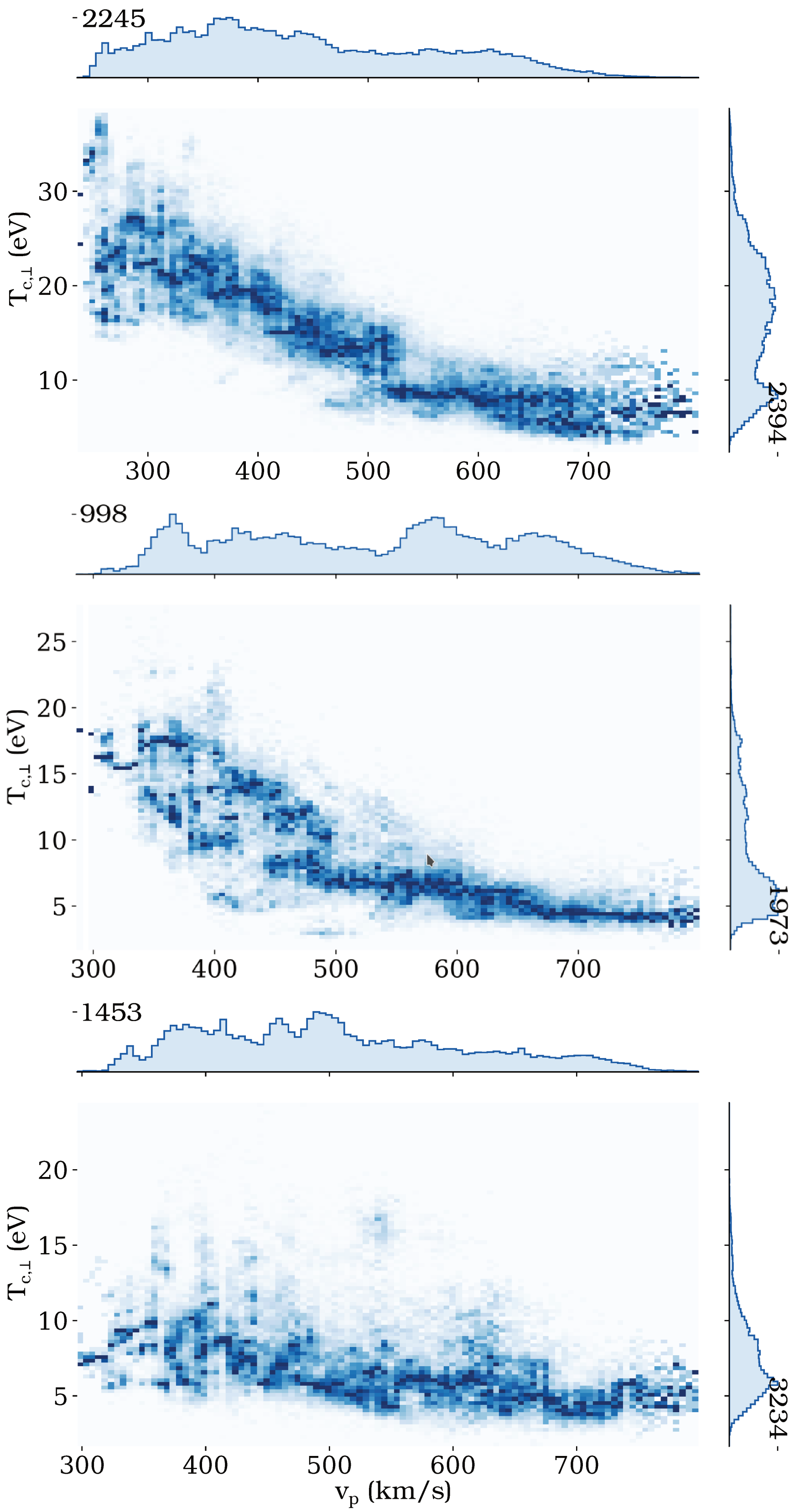

Figure 7: 2D column normalised histograms showing the variation of the core perpendicular temperature ($T_{c,\perp}$) with proton velocity (v_p) for data binned into three radial distances: upper plot – 64 to 144 R_S, middle plot – 144 to 164 R_S, and lower plot 164 - 215 R_S. 1D histograms above and to the right of the 2D histograms reveal the distribution of measurement for each parameter ($T_{c,\perp}$ and v_p) separately.

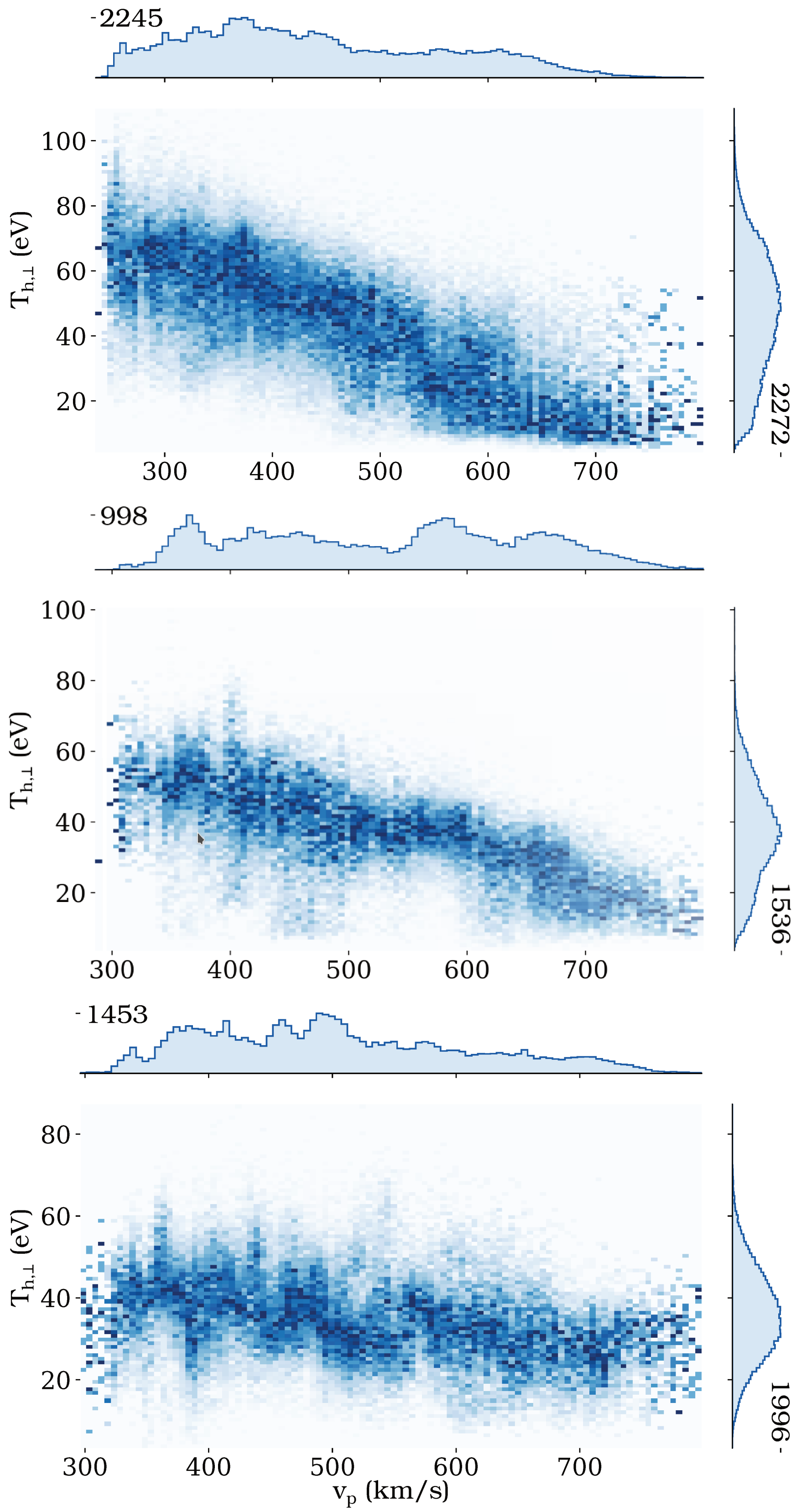

Figure 8: The same representation as described in the caption of Fig. 7, but presenting the variation of the halo perpendicular temperature ($T_{h,\perp}$) with κ value. All the κ values larger than 20 are shown in the highest κ bin.

measured at the same radial distance: its journey from the solar corona was shorter, providing less time for the relaxation of the halo VDF towards a Maxwellian. Presented results agree with the evolution of κ values presented by Štverák et al. (2009).

On the other hand, our conclusions are in contradiction with Sec. 2.2 of Lazar et al. (2017). An anti-correlation between the halo temperature and κ was found in this study, and accounted to the fundamental properties of the Kappa distribution function.

2.1.2 *Noise level*

An artefact was found in the Helios electron VDF measurements. The upper plots in Fig. 10 present the electron VDF measurements in one instrument azimuth bin aligned with the magnetic field, directed anti-sunward (left plot), and sunward (right plot). All the data presented in this section was obtained between Dec 1 1974 and Mar 8 1975, and is filtered only to instances during which the average magnetic field was in the plane of measurement (the exact criteria used is described in Sec. 3 of Article A).

From the VDF slices shown in Fig. 10 (left) one can recognise a steep energy gradient at low electron energies ($<$ 30 eV) corresponding to the electron core population. A second, less steep gradient covers most of the shown energy range and corresponds to the electron strahl. The same can be seen in Fig. 10 (right), however, the high-energy population is not the strahl but the halo, as the slices displayed describe the electrons moving in the sunward direction. For the highest three measured energy bins (at 790, 1119, and 1581 eV), one can observe that some of the VDF measurements end up on exactly the same VDF values, even though these measurements were taken over a time span of three months. We believe that this artefact appears when only a few counts were recorded during the integration time. These one-, two- or three-count measurements then correspond to exactly the same VDF value. Unfortunately the data set used for the analysis, taken from the Helios data archive (http://helios-data.ssl.berkeley.edu) does not include the information on the actual number of counts measured. Neither does the documentation provide the noise levels of the instruments.

Highest-energy measurements are the most relevant for the determination of the strahl and the halo populations, as these are the energies where we expect the high-energy, Kappa distribution tails. We preformed a test to determine how much effect do these last three energy bins have on the halo population moments obtained by fitting a Kappa VDF. The same fitting procedure was applied to the electron VDF measured in all energy bins (upper plot in Fig. **??**), and the electron measurements in all but last three energy bins (lower plot in

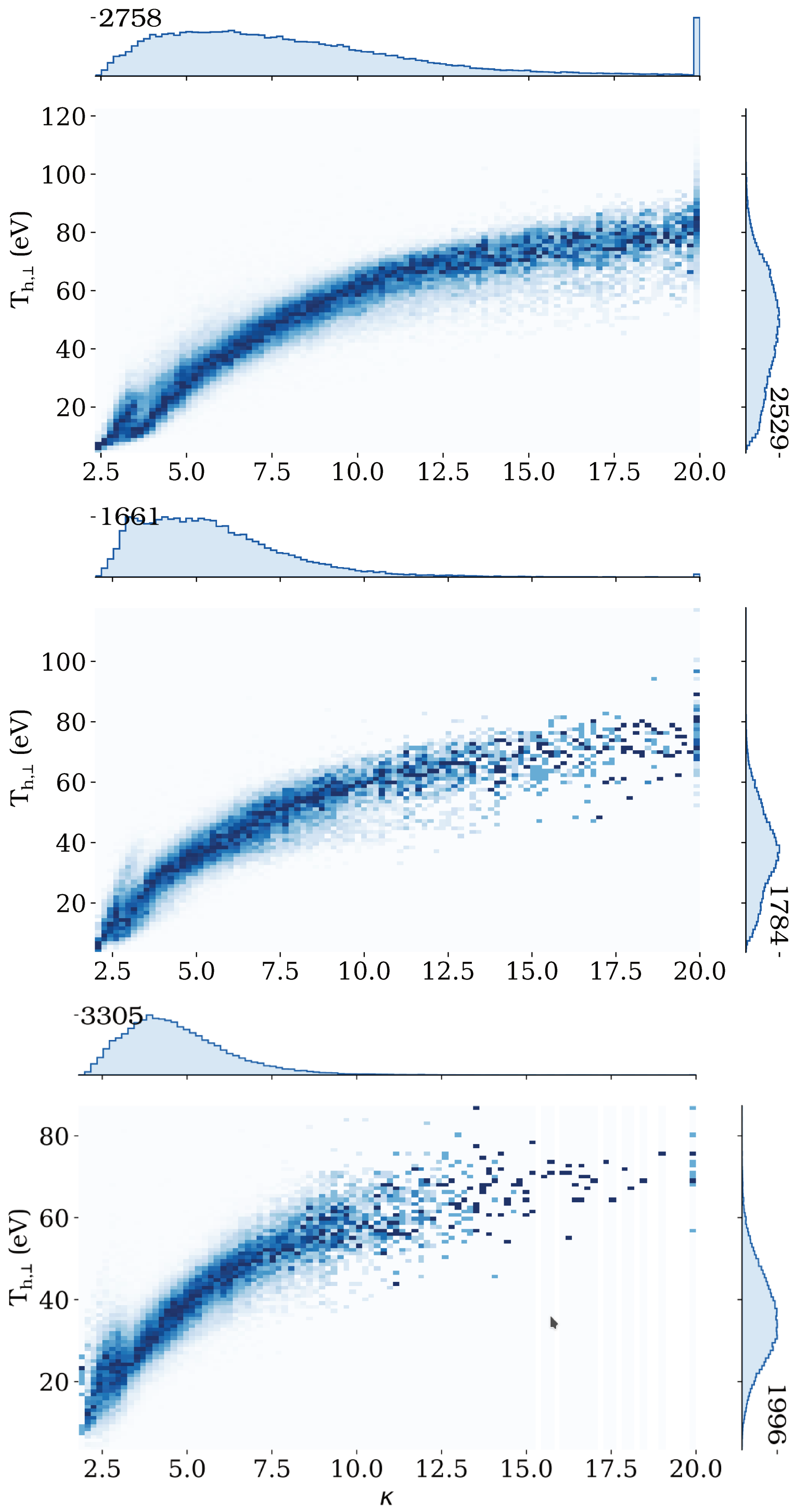

Figure 9: The same representation as described in the caption of Fig. 7, but presenting the variation of the halo perpendicular temperature ($T_{h,\perp}$) with proton velocity (v_p).

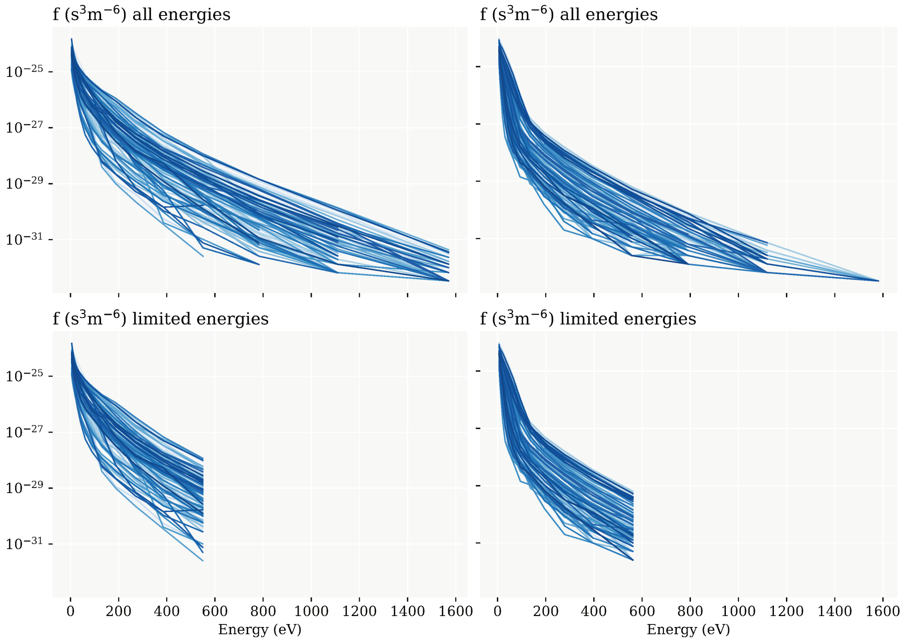

Figure 10: VDF slices measured by Helios 1 at different times (Dec 1 1974 - Mar 8 1975) in the azimuth bin aligned with the magnetic field, and measuring electrons moving away from (left plots), and towards (right plots) the Sun. Each line represents a different electron measurement. In the upper plot all energy bins are shown, while in the lower plot last three energy bins are not displayed.

Fig.**??**). The obtained fitting parameters: κ value, total halo temperature ($T_h = (2 \cdot T_{h,\perp} + T_{h,\|})/3$), and the halo density (n_h) are compared in Fig. 11. In each plot a dashed black line shows the $x = y$ line.

Fitting to the VDF limited in energy results in a higher κ values. From Eq. 20 we see that the κ parameter also effects the obtained $w_{\kappa,\perp,\|}$ and therefore also $T_{\perp,\|,\kappa}$. Higher κ values are expected to result in higher T_h, which was also found in the results of our test (see middle plot in Fig. 11). The trend is not as strong for n_h (lower plot in Fig. 11), however, the majority of values obtained from the fit to the VDF limited in energy are smaller than the ones obtained by the fit to the total VDF.

The performed test reveals that assumed few-count measurements at high electron energies have a strong effect on the parameters obtained from a fit to the electron halo population. This result was expected since high-energy tails, at velocities a few times the distribution's thermal velocity, are crucial for the definition of the κ parameter. At lower energies the differences between a Kappa and a Maxwellian distribution function are much more subtle, often too small to be captured by the instrument resolution.

We conclude that the halo Kappa VDF fit depends strongly on the measured suprathermal tails. The most affected fitting parameter is κ, which was found to vary to ~ 50 % depending on the energy selection of the data before the fit. For the Helios electron measurements the high energy measurement were found to be unreliable and probably affected by the instrument noise. One needs to consider this limitation when interpreting the published observational results.

2.2 PARKER SOLAR PROBE

Parker Solar Probe (PSP) is a recent heliospheric mission launched on Aug 12 2018, with a goal to explore the near-Sun solar wind. Its orbit from the launch to Oct 1 2020 is shown in Fig. 12. Soon after the launch, PSP encountered Venus and with its gravity assist reached the first perihelion at the distance of 35.7 R_S from the Sun. After the third orbit, another gravity assist assured the closest approach at 29.3 R_S. This manuscript, and the associated publication (Article B), only include the data from orbits 1, 2 and 4. The 3rd encounter measurements have not been used in this work because the data of one of the instruments used in the data analysis – the Solar Probe Cup (SPC), providing the proton plasma moments – is not available. The solar wind measurements obtained during the first encounters of PSP already led to new understanding of the solar wind (Bale et al., 2019; Kasper et al., 2019; Howard et al., 2019; McComas et al., 2019).

Electrons on board PSP are measured by two electrostatic analysers (SPAN-E), SPAN-A and SPAN-B. They are located in the opposite

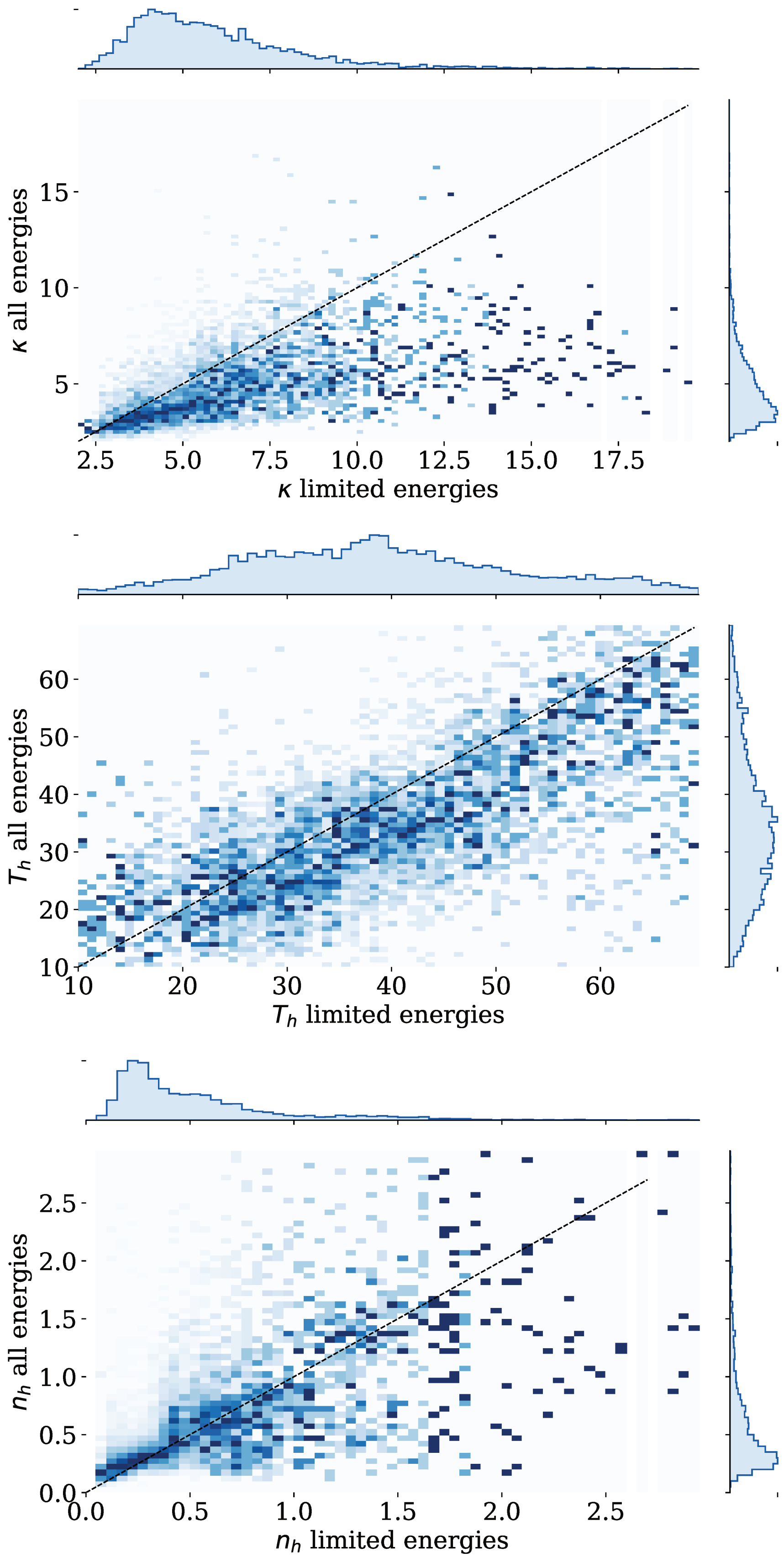

Figure 11: 2D column normalised histograms comparing the halo fit parameters obtained by fitting to VDFs limited in energy, and to VDFs at all energies: (upper plot) κ value, (middle plot) halo temperature (T_h), (lower plot) halo density (n_h). The dashed black line marks the $x = y$ line.

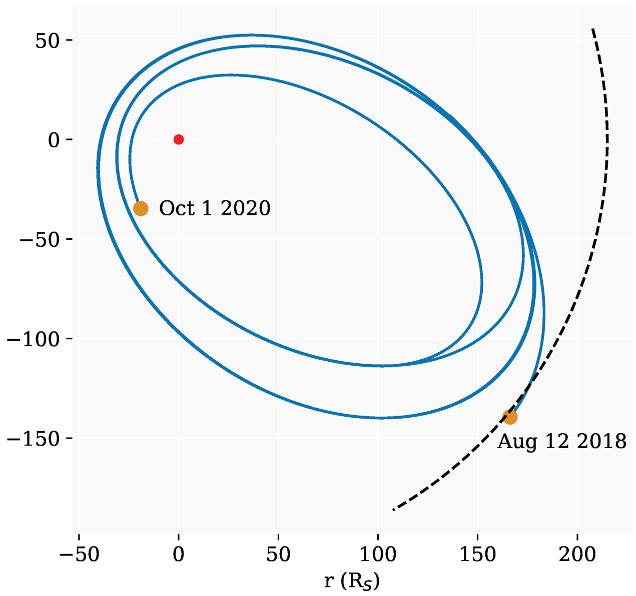

Figure 12: The orbit of PSP between the launch and Oct 1 2020 (blue line). The black dashed line represents the orbit of the Earth.

sides of the spacecraft and together cover almost a full solid angle. A detailed description of SPAN-E instruments is provided by Whittlesey et al. (2020). One of the difficulties encountered with the SPAN-E data analysis is combining the SPAN-A, and SPAN-B field of views (FOVs) and accurately accounting for the FOV limitations. A description of the angular space sampled by SPAN-E is presented in the Appendix A, giving the motivation for a method used in Article B to obtain $T_{s,||}$.

The statistical properties of the solar wind electrons observed during the first two orbits were shown by Halekas et al. (2019). The measured VDFs agree with the core, halo, and strahl model assumed from the electron observations farther from the Sun. As shown by Štverák et al. (2009) using Helios, Cluster and Ulysses data, the strahl appears to dominate the suprathermal electrons close to the Sun, and the halo is barely observed. While SPAN-E instruments have a sufficient energy coverage to measure a large part of the halo and strahl VDF, their sensitivity is not high enough to sample the tenuous halo at very high energies during the first four encounters. As the PSP approaches the Sun and the plasma density increases we might be able to distinguish the suprathermal populations also at very high electron energies. Observations presented by Halekas et al. (2019), thus indicate that the halo does not exist in the solar corona and that it is a product of the strahl scattering. The absence of halo VDF measurements at very high energies for now constrains the modelling of the halo. As mentioned in Sec. 2.1.2, the high-energy tails are the most important to differentiate between a Maxwellian and a Kappa VDF. As for now, the halo was found to be well represented by a Maxwellian VDF (Halekas et al., 2019). However, future closer approaches of the PSP might let us investigate the halo properties in a more affirmative way, and draw conclusions on the existence of the halo population closer to the Sun.

An anti-correlation between electron total temperature and the solar wind speed was found for the first time in the near-Sun regions, which implies that the temperature of electrons carries the information about the state of the corona at the origin (Halekas et al., 2019; Maksimovic et al., 2020). In our work (Article B) we go even a step farther. Assuming collisionless focusing of the strahl electrons in the absence of any wave-particle interactions, the shape of the strahl parallel slice through the VDF ($f_{s,||}$) does not evolve with radial distance. Therefore the shape of the coronal electron VDF should be preserved in the parallel component of the strahl electron population.

We performed the analysis of strahl *pitch-angle width* (PAW) to estimate the importance of strahl scattering mechanisms from the Sun to the distances between 35 - 60 R_S. The PAW was found to be relatively narrow and decreasing with electron energy for the lower-$\beta_{e,c}$ solar wind ($\beta_{e,c} < 0.7$), representing the majority of measurements. Large increase in PAW was found for the energies below 200 eV, which we believe to be a consequence of the Coulomb collisions of the strahl with the core electrons. In agreement with the findings of Article A, strahl electrons in the high-$\beta_{e,c}$ solar wind appear broader. Even though we believe that the observed strahl electrons have already been slightly scattered before intercepted by PSP, we investigated whether the $f_{s,||}$ can be related to the coronal origins. Because the observed $f_{s,||}$ is well represented by a one-dimensional Maxwellian, we characterise its shape with a *strahl parallel temperature* ($T_{s,||}$). $T_{s,||}$ obtained from PSP as well as Helios observations, does not vary with radial distance, but it shows an anti-correlation with the solar wind velocity. This implies that the strahl in fact carries the information about the state of the VDF in the solar corona.

$T_{s,||}$ appear to be slightly larger than the expected coronal electron temperature, which leads to the conclusion that $T_{s,||}$ has been somewhat affected by the scattering mechanisms taking place within 35 R_S. The effect of scattering by Coulomb collisions was investigated using the kinetic model accounting BiCoP, and the results are presented in the following Chapter 3.

EM fields measurements on board PSP reveal the presence of waves at frequencies that could affect the solar wind electrons. Malaspina et al. (2020), for the first time, report an observation of *electrostatic whistler waves* with a frequency of 0.7 of the electron gyro-frequency (f_{ce}). They are present in the steady solar wind periods with magnetic field close to the radial direction, and are accompanied with the large electron core drift. Their wave-frequency makes is a good candidate to have an effect on electron VDFs locally, however the nature of this possible interaction is yet to be investigated. The existence of *EM whistler waves* in the solar wind is well known (see Ch. 1), and was confirmed also by the PSP. Interestingly, however, the EM whistlers observed by PSP appear to be propagating sunward (Agapitov et al., 2020), as opposed to anti-sunward whistler observed at larger distances (Stansby et al., 2016). The local interaction between this type of waves and solar wind electrons has not yet been investigated.

2.3 RADIAL EVOLUTION OF CORE ELECTRON MOMENTS OBTAINED BY HELIOS & PSP

Merging the data sets from the PSP encounter periods 1, 2, and 4 and Helios 1, we present the radial evolution of core electron parameters. Total of 162606 VDF samples were used from PSP, and 39180 from Helios. The data has been separated according to the solar wind velocity into slow ($v_p < 500$ km/s) and fast ($v_p > 500$ km/s) solar wind. Slow solar wind represents 98.5 % of PSP measurements and 48.5 % of Helios measurements.

This could be a consequence of the *limited statistics* of PSP: even though the number of measurements is high, PSP has not spend a long period of time in the solar wind. There is a possibility that PSP has not yet been lucky enough to observe a pure fast solar wind stream. Another explanation is that at the radial distances probed by PSP, the solar wind in ecliptic plane mostly originates from the *streamer belt*. However, due to the super-expansion of the pure fast solar wind originating from the polar coronal holes, the observed solar wind in the ecliptic plane farther from the Sun, has a higher probability to originate from the coronal holes and reach high wind speeds. This could explain the different proportions of the fast wind found in PSP and Helios data. A third explanation is that the PSP has reached the solar wind *acceleration* region, measuring the solar wind which has not yet reached its terminal velocity. In fact, for now unpublished results reveal that the same solar wind stream observed at the distance of PSP crossed the Earth's orbit, preserving the variations in B and v_{SW}, however, with a higher solar wind speed. Another proof of solar wind acceleration was found in Helios data by Maksimovic et al. (2020), who from the statistical analysis of the solar wind between 0.3 and 1 au found an acceleration reaching up to 90 km/s/au.

The radial evolution of core electron density (n_c) is shown in Fig. 13. Two dashed lines, representing the expected radial density gradient for a spherical expansion with constant velocity ($\sim r^{-2}$), are added to the plots for comparison. While the density of the fast wind (upper plot) appears to follow well the r^{-2} lines, the density of the slow wind (lower plot) decreases faster than that. Gradient, faster than r^{-2}, would take place in the solar wind acceleration region: the slow solar wind close to the Sun has not yet reached its terminal velocity and is accelerating slightly over radial distances up to 100 R_S, from where on the density appears to follow the expected radial evolution.

Fig. 14 shows the radial evolution of core electron temperature (T_c). T_c is smaller in the fast solar wind (upper plot), where a clear radial decrease is only observed close to the Sun. Above the distance of $\sim$ 100 R_S, T_c remains almost constant. The data was fitted with a power law distribution shown with red dashed line. For comparison, a result from the work by Moncuquet et al. (2020), who obtain the power law index only from quasi-thermal noise electron temperature measurements on-board PSP, is added to the plots with black dashed line. As Moncuquet et al. (2020) do not separate for different solar wind populations, the obtained relation $r^{-0.74}$ comes from a fit to all the measurements done during the first two PSP encounters.

A stronger radial gradient can be seen for T_c in the slow solar wind (lower plot) for the Helios data set ($r > 60 R_S$, see dashed green fit), which corresponds to the results of Maksimovic et al. (2020). However, PSP T_c measurements appear to be lower than expected from the fit to the Helios data. This could be a hint that solar wind separation solely according to velocity is not enough to classify solar wind into different types. As already proposed above, an explanation could lie in the solar wind acceleration. A portion of the solar wind classified as slow, which peaks at temperature 25 eV ($= 10^{1.4}$ eV, see right 1D histogram in the lower plot of Fig. 14), could still be accelerating, and could be at larger distances classified as fast. In fact this peak would match well with the upper plot where a peak in T_c below 65 R_S can be found at the same value.

A fit to the combination of PSP and Helios data sets therefore gives a power law index -0.71, smaller than the index obtained solely from Helios data set.

Core temperature anisotropy ($\perp$ / $\|$) shown in Fig. 15, was observed to be farther from unity in the fast than in the slow solar wind, with a predominant parallel direction. Taking into account only

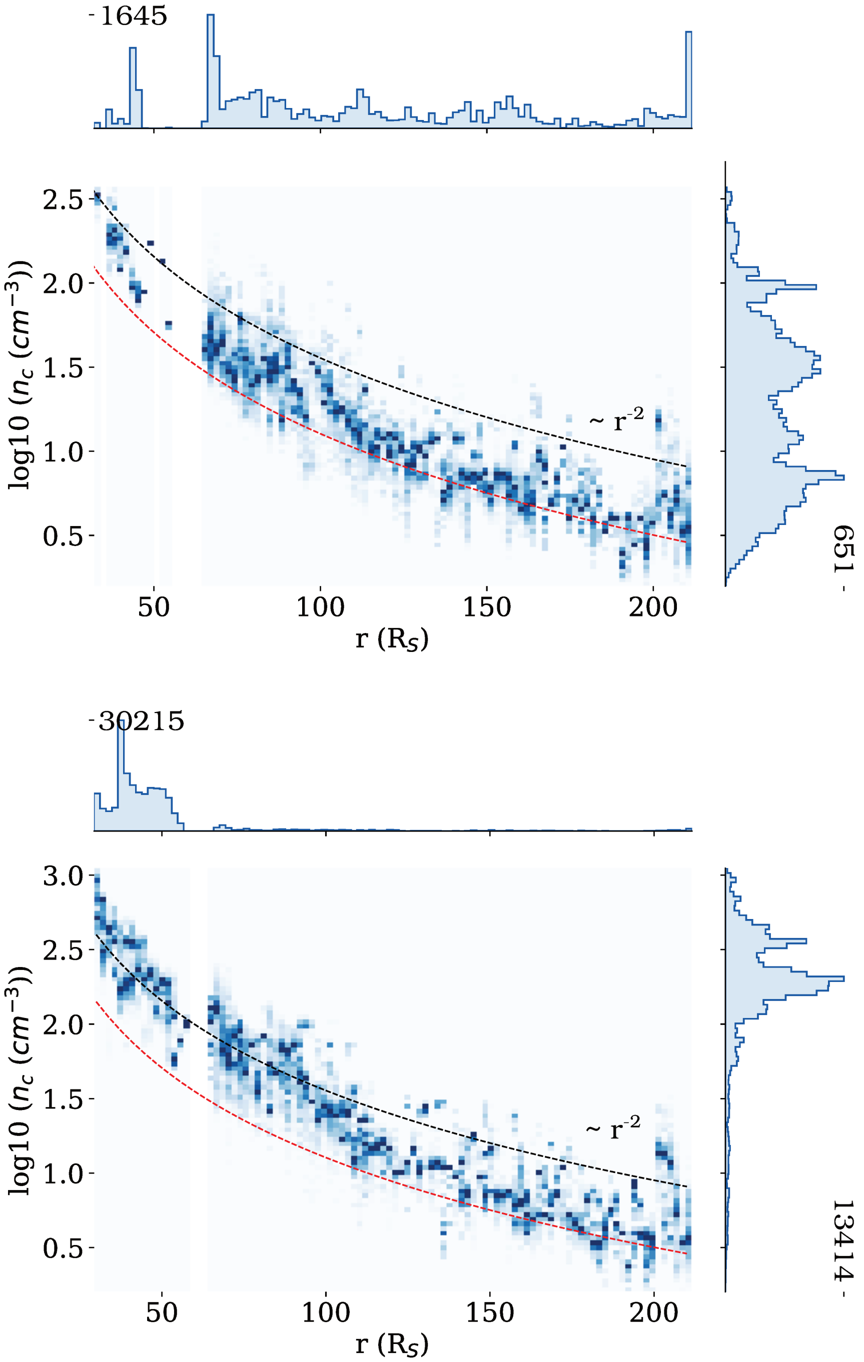

Figure 13: 2D column normalised histograms showing the variation of the core electron density (n_c) with radial distance (r) for data binned into two bins according to the solar wind velocity: upper plot – fast solar wind, $v_p > 500$km/s, and lower plot – slow solar wind $v_p < 500$km/s. 1D histograms above and to the right of the 2D histograms reveal the distribution of measurement for each parameter (n_c and r) separately. The number of instances in the most populated bin is marked on the plot for each of the two 1D histograms. For comparison, black and red dashed lines represent curves decreasing with r^{-2}.

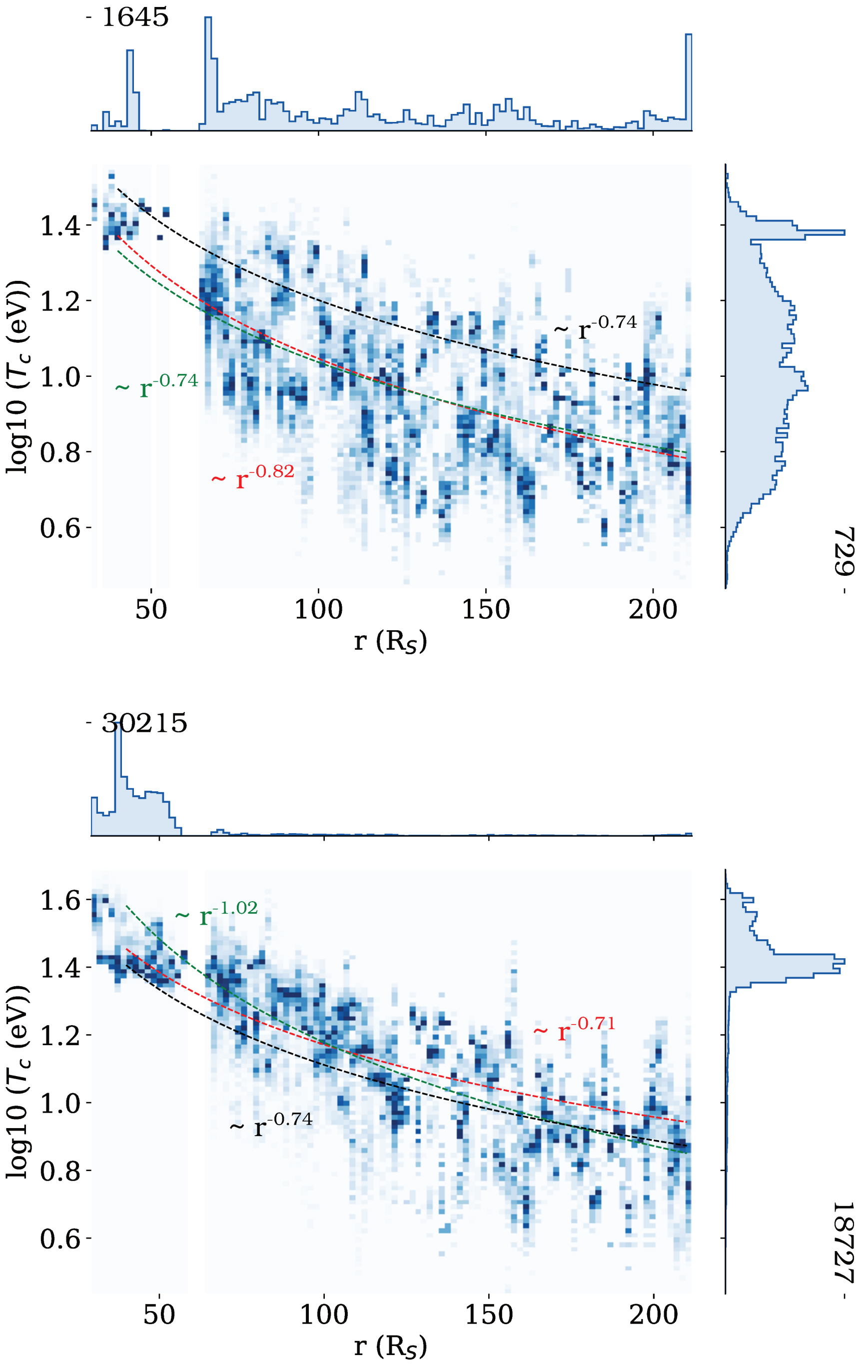

Figure 14: The same representation as described in the caption of Fig. 13, but presenting the variation of the total core temperature (T_c) with radial distance (r). The black dashed line represents a curve decreasing with $\sim r^{-0.74}$, a power law index obtained by Moncuquet et al. (2020). The red dashed line represents a fit to all the presented data, from which $r^{-0.82}$ relation was obtained for the fast, and $\sim r^{-0.71}$ for the slow solar wind. The green dashed line represents fits only to the Helios data set ($r > 60 R_S$), resulting in relations $\sim r^{-0.74}$, and $\sim r^{-1.02}$, for the fast and the slow wind respectively.

the solar wind expansion, electrons are expected to become more anisotropic with radial distance. However, as shown by (Štverák et al., 2008), Coulomb collisions and EM wave instabilities are efficient in isotropising the electron core. Accordingly no clear radial trend was found from our data analysis.

Fig. 16 shows the evolution of the absolute value of the parallel core drift velocity in the solar wind proton rest frame ($v_{||}$). The core electrons are most of the time drifting sunward with respect to the protons, to balance the antisunward flux of the fast, anti-sunward streaming, strahl electrons. Štverák et al. (2009) used Helios, Cluster and Ulysses data, and Halekas et al. (2019) PSP data, to verify whether the oppositely directed fluxes cancel each other out and fulfil the zero-current condition predicted in the solar wind. In both studies small departures from zero-current values were found, but were attributed to a measuring or data analysis uncertainties.

Strahl electrons in the fast solar wind appear more focused (Article A), and relatively denser than in the slow solar wind (Štverák et al., 2009). Accordingly higher $v_{||}$ were found in the fast wind. However, strahl electrons were found to scatter with radial distance and decrease in their relative density (Hammond et al., 1996; Graham et al., 2017; Štverák et al., 2009), therefore we would expect to see a decrease in $v_{||}$ with radial distance. Yet, no strong radial trends were observed between 30 to 215 R_S.

We have shown that the electron VDF measurements in the solar wind are crucial to develop our understanding of the physical mechanisms modifying trajectories of the solar wind electrons. While great amount of data already exists and provides reliable statistics including several years of observations, new missions with state-of-the-art technology let us dig deeper, conduct the measurements in a faster and more precise way, in the yet unexplored areas of our solar system.

Modelling the observed VDFs with separate components, the core, the strahl and the halo, we try to separate and isolate the physical phenomena affecting each of them. This allows us to connect the observations with various theoretical models, analytical and numerical solutions capturing one or a few phenomena at the time. In the following Chapter 3 the observations are compared to the numerical results the kinetic simulation of the solar wind accounting for Coulomb collisions between particles.

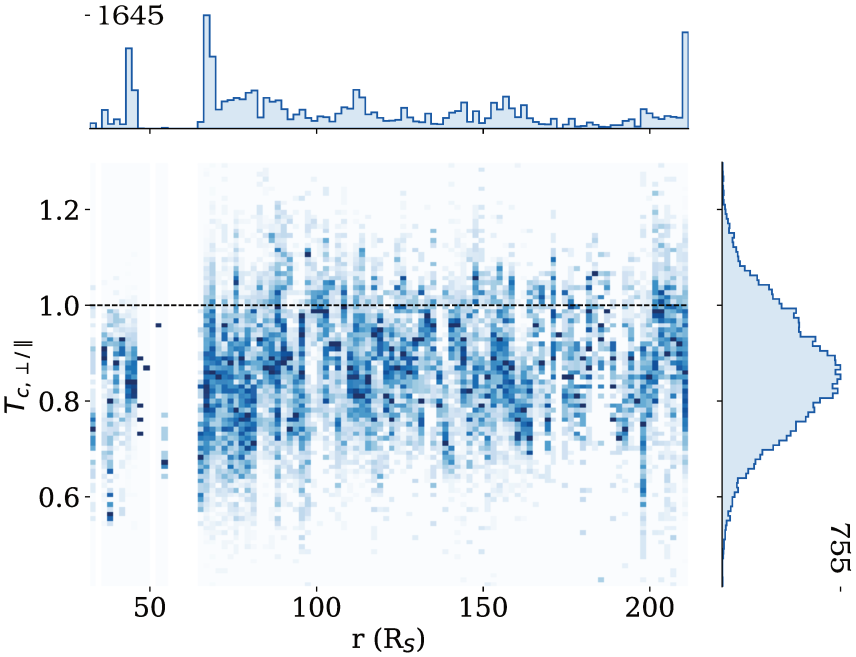

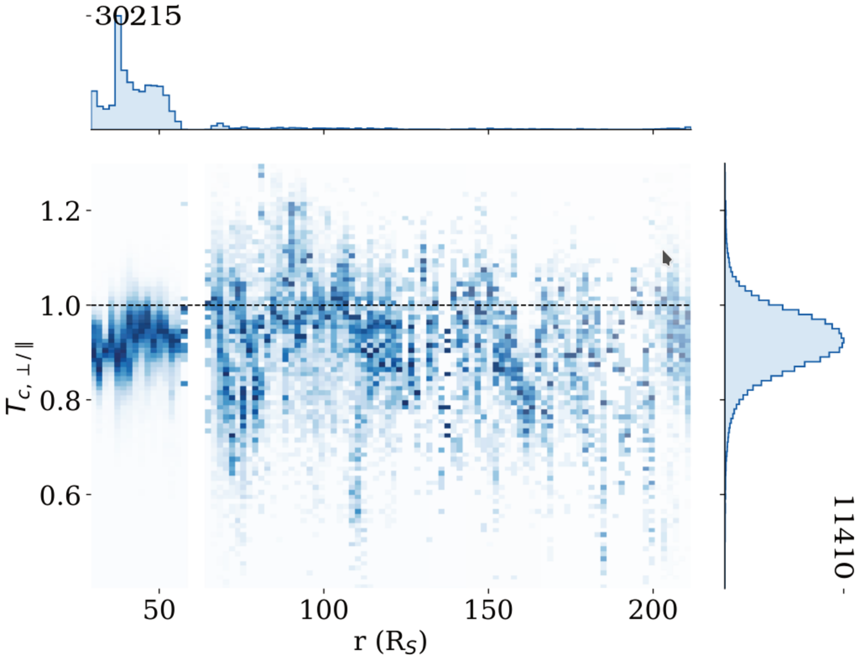

Figure 15: The same representation as described in the caption of Fig. 13, but presenting the variation of the core temperature anisotropy ($T_{c,\perp/\parallel}$) with radial distance (r).

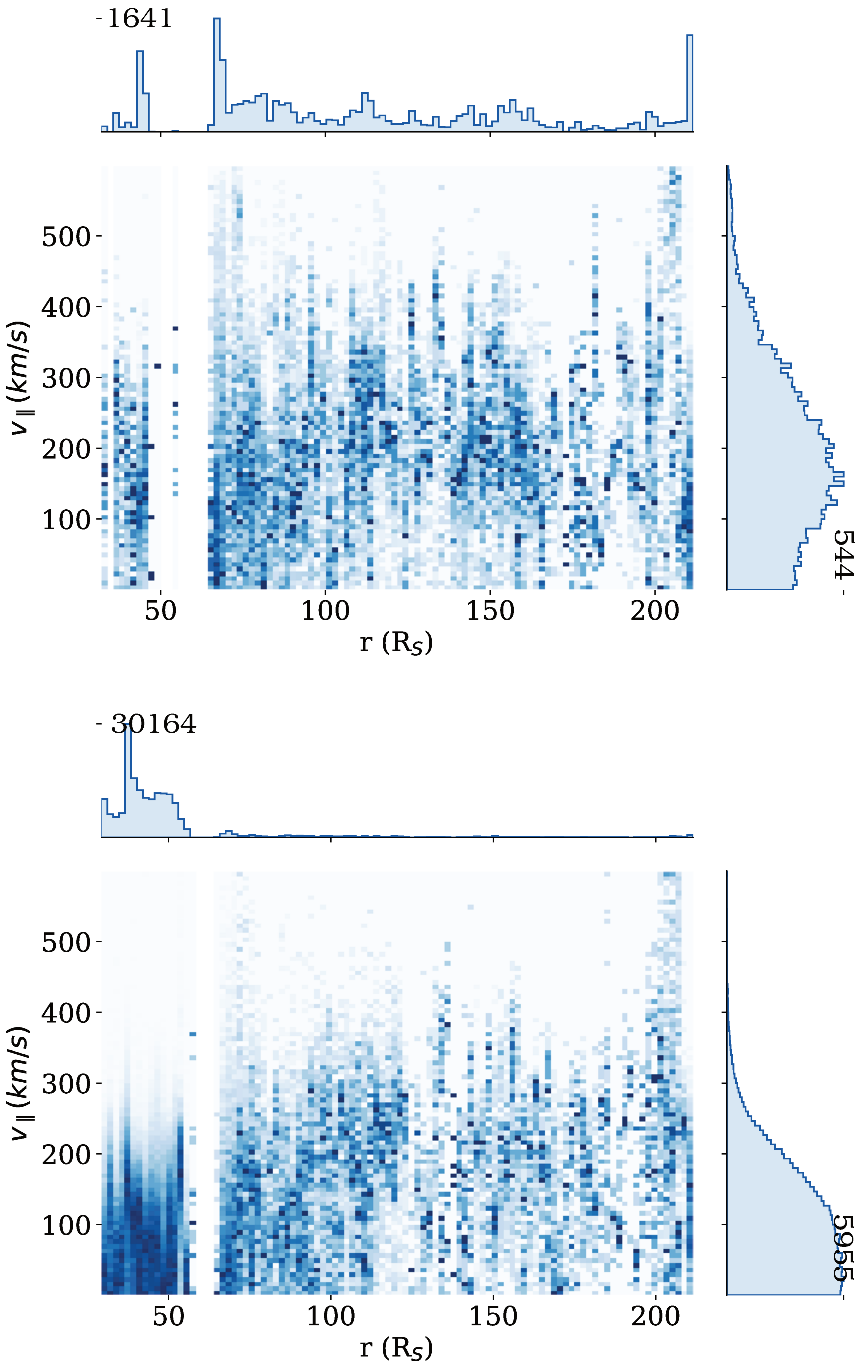

Figure 16: The same representation as described in the caption of Fig. 13, but presenting the variation of the parallel core drift ($v_\parallel$) with radial distance (r).

3

KINETIC SIMULATIONS BICOP

We use a kinetic solar wind model named BiCoP (Binary Collisions in Plasmas), developed by Landi and Pantellini (2001, 2003). The model is 1-dimensional in space and 3-dimensional in velocity space, and allows us to study the radial evolution of solar wind under the effect of gravity and binary Coulomb collisions. It does not account for the non-radial magnetic field (Parker spiral) or the EM wave interactions. BiCoP has been used to study the evolution of electron heat flux over a 0.2 R_S wide slab above the solar surface assuming a non-thermal VDFs in the solar corona (Landi and Pantellini, 2001). The next study, also focused on electron heat flux, includes simulations over a radial distance of 50 R_S from the Sun (Landi and Pantellini, 2003). Despite the reduced proton-to-electron mass ratio in the first two works, the model proved to describe well the solar wind kinetic dynamics. The following works used realistic plasma input parameters, investing the evolution of electron VDF from 0.3 to 3 au, where effects of gravity can be neglected (Landi et al., 2010, 2012, 2014). The obtained plasma parameters match well with the observed parameters measured at 1 au.

A short description of the model in given in Article C. Here we provide a more detailed model description and the unpublished results.

3.1 MODEL DESCRIPTION

3.1.1 *Equation of motion*

In the model, electrons and protons are free to move along the one spatial dimension which is aligned with the radial direction (see Fig. 17). The two particle species can be separated only by mass, and the oppositely signed electric charge. They are subject to a gravitational and an electric force, and their motion is determined by the equations:

$$\frac{d^2r}{dt^2} = -\frac{GM_S}{r^2} + \frac{\mathbf{L}^2}{m^2r^3} + \frac{q}{m}E(r), \tag{26}$$

$$\mathbf{L} = m\mathbf{r} \times \mathbf{v}, \tag{27}$$

where r denotes the radial distance from the Sun, G the gravitational constant, M_S the mass of the Sun, $\mathbf{L}$ the angular momentum,

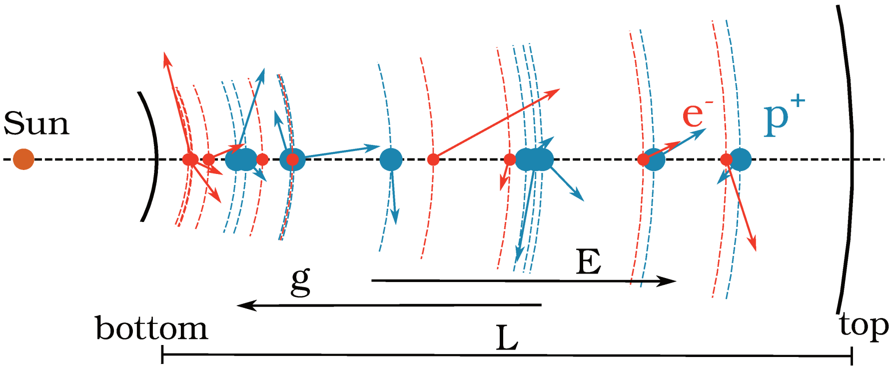

Figure 17: A schematics of the kinetic model. Electrons (red) and protons (blue) are able to move along a radial direction between the bottom and top boundary. Particles can be thought of as thin spherical shells, as one spatial dimension is used to describe a spherically symmetric solar wind expansion. Particle velocities are defined in a 3-dimensions.

and E the charge-neutralising electric field. The charge q is oppositely signed for the two particle species, and m denotes the particle mass. The real electron to proton mass ratio was used in the model ($m_p = 1836\ m_e$). Besides the gravitational and electric potential, the particles experience binary Coulomb collisions. The one dimensional spatial domain is limited by the bottom and top boundary, which are described with the simulation input parameters.

3.1.2 *Coulomb collisions*

The algorithm works in the following way. First it uses particles' position and velocity to calculate which two particles will be the first to find themselves in the same position. Then all the particles are advanced for this Δt required for the first pair of particles to meet. Whether these two particle will collide or not is decided accordingly to the Coulomb collision cross-section. Collision probability decreases with $v_{i,j}^4$, where $v_{i,j}$ represents the relative velocity between the colliding particles i and j. If the two particles do collide, their velocities are recalculated accordingly with the conservation of momentum and energy, as expected for an elastic collision. However, we still need to determine the direction of the velocity vector of the two particles after a collision. Direction in 3-dimensional velocity space is defined with two spherical angles, ϕ denoting angles perpendicular to, and θ denoting the angle from the radial direction. Since the simulation is symmetrical about the radial direction, angle ϕ is chosen randomly on an interval $[0, 2\pi)$. Angle θ is obtained in a way that $\cos^2\theta$ equals to a random number on an interval [-1,1], to account for the asymmetry along the radial direction (Pantellini, 2000). If the particle pair does not collide they continue with unchanged velocities. Using this particle advancing technique and discretization of the simulation spatial domain is avoided.

To decrease the computational time the collision probability can be varied in the model. For collision pairs with relative velocity below v_C, defined on the input, a collision is conducted every time. For $v_{i,j} > v_C$, the probability remains unchanged, decreasing with $v_{i,j}^4$. It was shown by Pantellini and Landi (2001), that as long as v_C is smaller than the most probable relative velocity, the results of the used kinetic model compare well the Fokker-Planck description of a collisional plasma.

3.1.3 *Electric field*

The electric field in the simulation is composed of two contributions. First is a global electric field, radially decreasing with r^2, keeping the balance between electron and proton fluxes. This electric field is obtained in the first simulation phase lasting until $n_{coll,el0}$ are conducted. At the beginning of the first phase the electric field is set by an input parameter el_0, which prescribes a radially decreasing electric field in the simulation domain: $E = el_0/r^2$, following the Pannekoek-Rosseland electric field (E_{PR}, Eq. 7). E_{PR} is an electric field that arises due to the difference in mass between electrons and protons in all gravitational bound plasmas in hydrostatic isothermal equilibrium. It is known that E in the solar wind is larger than E_{PR}, including positive terms due to the acceleration, the pressure gradient and Coulomb collisions. At the end of the first phase we obtain a corrected el_0, aligning better with the simulated system.

Second part is the charge-neutralising electric field, a local polarisation field resulting from local charge imbalances. This field is obtained by considering each particle as a thin spherical conducting shell centred in the Sun, and calculating the local field of a system of conducting spherical plates. Second phase lasts until n_{coll} are conducted in total, or $n_{coll,el0}$ after the end of first phase. The local polarisation field is then added to the global electric field, together forming the total ambipolar electric field, responsible for the acceleration of the simulated solar wind.

3.1.4 *Simulation boundaries*

The simulation is bounded on two ends, with the bottom boundary lying closer to the Sun and the top boundary farther from it. Besides the general simulation inputs listed in the upper part of the Tab. 1 in Appendix B, we need to define the simulation boundary conditions (lower part in Tab. 1). The model tends toward a stationary solution for an expanding solar wind, therefore the parameters set at the two boundaries need to align with this solution. If boundary conditions are not suitably chosen, the model does not converge, or quasi-neutrality is not fulfilled.

At the bottom boundary we have to define the shape of the electron and proton VDF. The chosen shape was either Maxwellian, or a non-thermal Kappa function defined as:

$$f_M = n_M \cdot \left(\frac{m_\alpha}{2\pi k_B T_{\alpha,loc}}\right)^{3/2} \exp\left(-\frac{v^2}{v_{\alpha,l}^2}\right), \tag{28}$$

$$f_K = A_k \cdot \left(1 + \frac{v^2}{(\kappa - 3/2) v_{\alpha,l}^2}\right)^{-\kappa-1}, \qquad v_{\alpha,l} = \sqrt{\frac{2k_B T_{\alpha,l}}{m_\alpha}}, \tag{29}$$

where either $v_{\alpha,l}$, or $T_{\alpha,l}$, and κ in case of the Kappa-like boundary, are defined on the input. At the bottom boundary $v_{e,bot}$ for electrons is defined with $ve_{th,bot}$, and $v_{p,bot}$ for protons through the temperature ratio, rT_{bot}. For simplicity, the temperature of the protons and electrons at the bottom boundary was set to be the same ($rT_{bot} = 1$) for all the simulation runs. As the protons are accelerated to supersonic velocities in the simulation domain, they all escape at the top boundary and are not injected back from the top, so a prescription for a proton VDF there is not necessary. However, electrons remain subsonic, and a definition of the electron VDF shape at the top boundary is required, representing electrons coming into the simulation domain from farther distances. $v_{e,top}$ is set with a parameter $ve_{th,top}$. It has a great influence on the final result of the simulation and is highly dependant on $v_{e,bot}$. For all the successful runs shown below, many tests were required to iterate towards a good setting of $ve_{th,top}$.

Anther important boundary parameters are the velocities of both species at the bottom and top, v_{bot} and v_{top}, defining the total particle flux at the boundaries.

3.1.5 *Velocity Distribution Functions*

VDFs are sampled at each radial bin by making a statistics of the passing particles over time, starting with the second simulation phase. Simulation runs with larger $n_{coll,loc}$ therefore provide statistically better VDFs. Kinetic properties of the protons are not addressed is this work, as their near-Sun dynamics is strongly affected by EM instabilities, not accounted for in BiCoP. From proton plasma moments one can see that the proton VDFs are very anisotropic, but nevertheless supersonic.

Electron VDFs are sampled on a $n_v \times n_v$ grid spanning speeds up to $v_{max,e}$. A 3-dimensional velocity space is described with a 2-dimensional cylindrical coordinates ($f(v_{\|}, v_{\perp})$) assuming gyrotropy along the radial direction, which is also aligned with the magnetic field. The velocities parallel to the radial direction ($v_{\|}$) are sampled on an interval [-$v_{max,e}$, $v_{max,e}$], while the perpendicular velocities ($v_{\perp}$) are sampled on [0, $v_{max,e}$], doubling the velocity resolution. The measured quantity in the simulation is not the electron VDF $f(v_{\|}, v_{\perp})$, but:

$$g(v_{\|}, v_{\perp}) = f(v_{\|}, v_{\perp}) \cdot v_{\|}. \tag{30}$$

3.1.6 *From simulation to physical units*

The physical parameters in BiCoP are, like in most of numerical models, normalised in a convenient way. The normalisations of all parameters, except for the plasma density, can be derived from the length of the simulation domain, L, and a normalisation used for the velocity:

$$v_0 = \sqrt{\frac{2k_B T_{e,bot}}{m_e}}. \tag{31}$$

This velocity represents the thermal velocity of the electrons at the bottom boundary, and only depends on the choice of the temperature of the electrons at the bottom boundary ($T_{e,bot}$ in Kelvins). Since all the other quantities in equation of motion (Eq. 26) are constants provided that we are simulating a plasma of electrons and protons in the gravitational field of the Sun, $T_{e,bot}$ and L, are the only variables affecting the dynamics of the system. The dynamics is determined by the ratio between gravitational and the electron thermal energy at r_0:

$$\gamma = \frac{GM_S}{r_0} \cdot \frac{m_e}{2k_B T_{e,bot}}. \tag{32}$$

Gravity is thus expressed as

$$g_0 = \gamma \frac{L}{r_0}, \tag{33}$$

where L is the length of the simulation domain and r_0 the location of the bottom boundary. The ratio between the two, $h_{top} = L/r_0$, is an important dimensionless parameter. The spatial simulation dimension z is defined on the interval [0,1], where 0 is the bottom and 1 the to boundary. The radial distance in physical units can therefore be written as:

$$r = r_0 \cdot (1 + h_{top} \cdot z). \tag{34}$$

The physical units of an electric field E and potential ϕ are obtained from Newton's equation:

$$m_e \frac{dv}{dt} = -eE, \tag{35}$$

where the physical quantities can be expressed with the normalised simulation quantities: $v = \widetilde{v} v_0$, $t = \widetilde{t} L / v_0$, and $E = \widetilde{E} E_0$. We obtain:

$$\frac{m_e v_0^2}{Le} \frac{d\widetilde{v}}{d\widetilde{t}} = -\widetilde{E} E_0, \tag{36}$$

and

$$E_0 = \frac{m_e v_0^2}{Le}. \tag{37}$$

Accordingly, electric potential is normalised to $\phi_0 = E_0 r_0$.

The relation between the number of particles N in the simulation and the physical plasma density n, has to be found otherwise as n does not take place in the Eq. 26. We find it through the physics of Coulomb collisions. The Fokker-Planck electron-proton collision frequency can be written as:

$$\nu_{e,p}^{FP} = \frac{n e^4}{3 \epsilon_0^2 m_e^{1/2} (2\pi k_B T_e)^{3/2}} \ln\Lambda, \tag{38}$$

where

$$\ln\Lambda = \ln\left(\frac{12\pi (\epsilon_0 k_B T)^{3/2}}{n^{1/2} e^3} \right), \tag{39}$$

is the Coulomb logarithm. We compare the predicted collision frequency $\nu_{e,p}^{FP}$ with the measured collision frequency in the simulation $\nu_{e,p}$. The comparison is made in the densest radial bin, close to the Sun where collisions are very frequent.

Since n is the unknown, but also required for the calculation of $\ln\Lambda$, we first obtain predicted density n' assuming $\ln\Lambda = 24$. This value is obtained from Eq. 39, assuming typical expected plasma parameters: $\ln\Lambda(T = 172 eV, n = 10^6 cm^{-3}) = 24.3$.

$$n' = \frac{\nu_{e,p} v_{th,0}}{l} \cdot \frac{3 \epsilon_0^2 m_e^{1/2} (k_B T)^{3/2}}{4 (2\pi)^{1/2} e^4} \frac{1}{24}. \tag{40}$$

The final density n_0 is then obtained by:

$$n_0 = n' \frac{24}{\ln\Lambda(n')}, \tag{41}$$

The density in the rest of the radial bins (n_i) is determined by comparing the number of particles in this bin (N_i) to the first bin with the known density n_0 ($n_i = N_i / N_0 \cdot n_0$).

3.2 BICOP RESULTS

3.2.1 *Solar wind acceleration and terminal velocity*

We use BiCoP to study the radial evolution of electron VDF from the solar corona to a few tens of R_S, to be able to relate the observed VDFs at the location of PSP and Helios missions to plasma properties in the solar corona at the solar wind origin. The region just above the solar corona is referred to as the acceleration region, and is marked by strong gravitational field and frequent Coulomb collisions. In Article C we show that the solar wind protons originating from a Maxwellian-like, T_e = 2MK, corona get accelerated to supersonic velocity only by force exerted on them by the solar wind electrons. As described already in Chapter 1, the faster and lighter electrons have velocities high enough to escape the Sun, however, they are decelerated by the ambipolar electric field E, which ensures the quasi-neutrality and zero current condition in the solar wind, and accelerates the protons. The terminal speed reached this way equals 206 km/s, which is still much less than the values reported from the solar wind observations. Thus we conclude, that electrons are partially responsible for the acceleration of the solar wind, however, they alone are not able to provide acceleration to velocities observed even in the slow solar wind.

In the Article C we only include the simulation runs starting from a Maxwellian-like corona, because, as mentioned in the previous chapter, the strahl VDFs observed by PSP appear to be well represented by a Maxwellian. However, Kappa-like electron corona has often been considered in the frame of exospheric solar wind models and is known to produce a faster solar wind. Here we extend the results of the Article C to the Kappa-like bottom boundary condition. While the bottom temperature (T_e) is the same for all, the VDFs shapes are different, including a Maxwellian VDF, and Kappa VDFs with κ values from 6 to 3. The input parameters are listed in Appendix B in Table 2. The simulation run $Maxw$ is the same as the run A from Article C. All the runs span the radial distance between 1 and 46 R_S, and start, at the solar surface with a zero bulk velocity.

Fig. 18 compares radial evolution of plasma moments for different simulation runs. The density (n) exhibits very high gradients within 5 R_S, corresponding to the fast increase in velocity (v). At farther radial distances velocity remains almost constant and the density approaches r^{-2} radial trend. Densities in all simulation runs have approximately the same value, because the amount of particles (N), T_e and v_C, parameters important for the calculation of density, remained unchenged. As shown for the exospheric solar wind models (Pierrard and Lemaire, 1996; Maksimovic et al., 1997a; Zouganelis et al., 2004), the terminal velocity of the solar wind depends on the amount of suprathermal

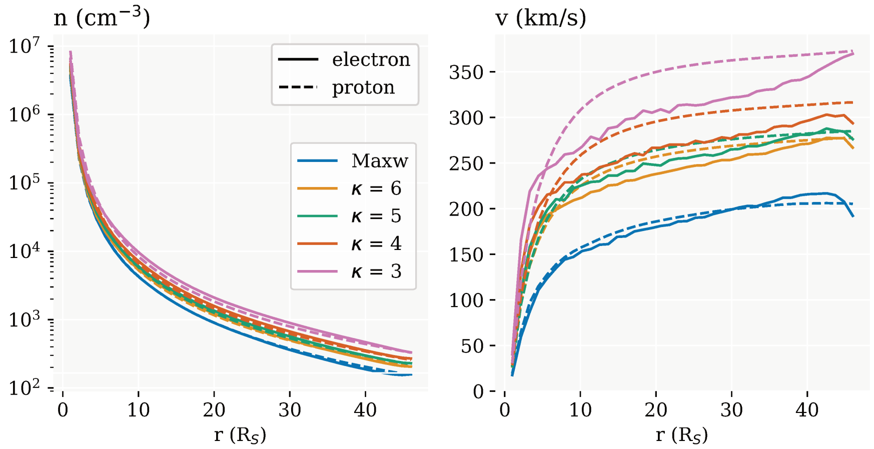

Figure 18: The evolution of electron and proton density (n) and velocity (v) for all the presented simulations runs specified in Tab. 2.

electrons in the solar corona, and is the largest for simulation run κ = 3. However, the velocities obtained with BiCoP model are still small compared to the results of a transonic collisionless model by Zouganelis et al. (2004), who find a terminal velocity of 520 km/s for a 1 MK corona modelled with a Kappa VDF with κ = 3. We believe that this difference is due to Coulomb collisions, effectively slowing down the solar wind in our kinetic model.

3.2.2 *The effects ob ambipolar electric field*

The ambipolar electric field (E) obtained in all the simulation runs was found to be on the order of *Dreicer electric field* (Dreicer, 1959), a measure of electric field strength in comparison to the collisionality of the system. E_D is defined as:

$$E_D = \frac{k_B T_{e,core}}{e\lambda_{mfp}}. \tag{42}$$

Fields of that strength are expected to deform electron Maxwellian VDF in the form of *runaway* electrons (Scudder, 2019). A separation velocity v_D, depending on the ratio E/E_D, exists and divides the velocity space into two regions: an overdamped region, where collisions are frequent enough to overdamp the electric force and preserve a Maxwellian VDF, and an underdamped region, where electrons can be accelerated by E and departures from a Maxwellian VDF can be found.

$$v_D = \sqrt{\frac{3k_B T_e}{m_e} \cdot \frac{2E_D}{E}}. \tag{43}$$

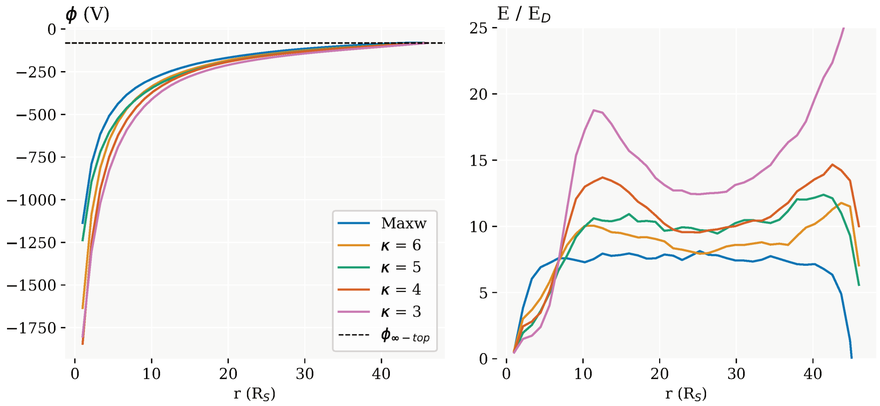

Figure 19: (left) Electric potential (ϕ) measured in the simulations and shifted for the estimated potential above the top simulation boundary ($\phi_{\infty-\mathrm{top}}$), (right) The ratio between ambipolar and Dreicer electric field.

Accordingly to exospheric solar wind models, the total electric potential at any radial distance also plays a role in shaping the electron VDF. The separation velocity v_ϕ is believed to mark the fastest sunward directed electrons, or the so called electron cutoff.

$$v_\phi(r) = \sqrt{\frac{2e\phi(r)}{m_e}}. \tag{44}$$

The radial evolution of electrostatic potential and the ambipolar electric field for all the simulation runs is shown in Fig. 19. One can see that the potential difference ($\Delta\phi$) is the highest for the $\kappa = 3$ simulation run, corresponding to the highest E/E_D, and the highest terminal velocity shown in Fig. 18. The peak in E/E_D can be found just above 10 R_S for all the κ runs but not for the $Maxw$ case. It corresponds to a peak in plasma temperature at the same radial distance, a know property of a solar wind originating from a Kappa-like corona (see e.g. Zouganelis et al. (2004)). As $T_{e,\mathrm{core}}$ is included in Eq. 42, the two quantities are closely related.

We investigated the radial evolution of electron VDF in different simulation runs. Obtained VDFs appear to be well represented by two separate populations: the core at lower energies, and the strahl at higher energies and in the antisunward direction. Example VDF slices from $\kappa = 4$ and $Maxw$ run for two different radial distances are shown in Fig. 20. The peak in the sunward portion of VDF (negative velocities) is a consequence of top boundary condition not perfectly matching the antisunward portion of the VDF. The feature is injected at the top and then propagated through the simulation domain to the solar surface.

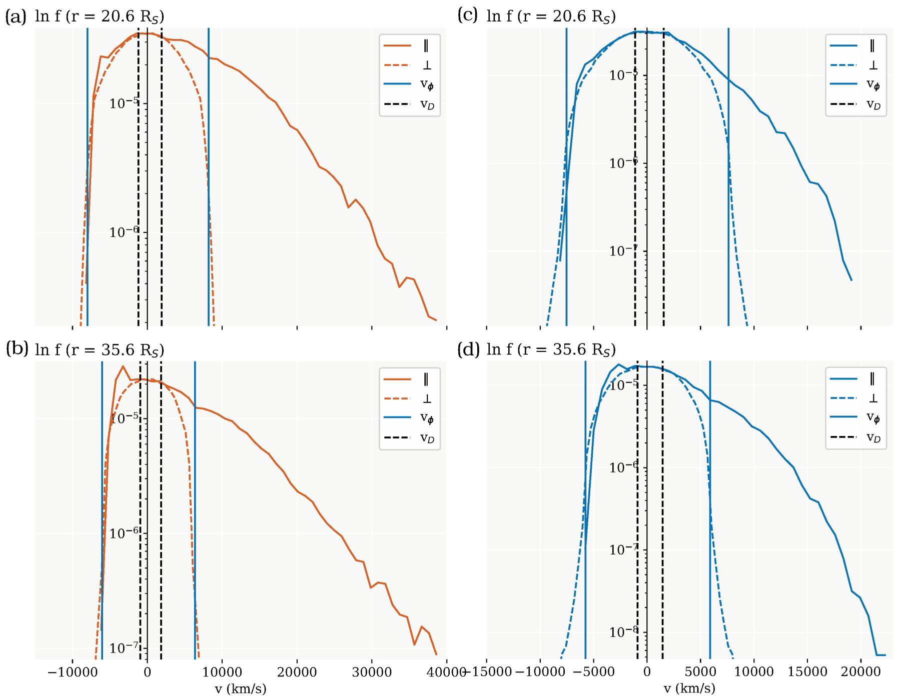

Figure 20: Parallel and perpendicular cuts through an electron VDF at the distance of 20.6 R_S (a, c) and 35.6 R_S (b, d) for the simulation run $\kappa = 4$ (a, b) and $Maxw$ (c, d). The cuts are plotted in core electron resting frame. v_ϕ and v_D are indicated with blue and black lines.

We believe it does not have a strong effect on the evolution of the rest of electron VDF.

Visually comparing the VDFs from the two different runs, one can see that the core components look alike, while the strahl extends to much higher velocities in the $\kappa = 4$ run. Also the shape of the strahl is different: the parallel cut through the strahl VDF appears to decrease slower for the $\kappa = 4$ than for the $Maxw$ case.

The predicted separation velocities, v_ϕ and v_D, are overplotted in Fig. 20, and appear to correspond well to some features of the electron VDF. In the sunward direction v_ϕ describes the electron cutoff velocity, while in the antisunward direction v_D marks the lowest velocity of the strahl electrons, or the strahl break point velocity. The same result was found in Article C. Additionally, v_ϕ in the antisunward direction corresponds to a small dip in the parallel cut through electron VDF ($f_{||}$), clearly seen in Fig. 20. Below v_ϕ, $f_{||}$ consists of both, core and the strahl VDF, however, above this value cor VDF steeply decreases and only strahl remains.

A new representation method introduced by Behar et al. (2020), and also used in Article C, is used to highlight higher order VDF features and their departures from isotropy. Left plot in Fig. 21 displays an orig-

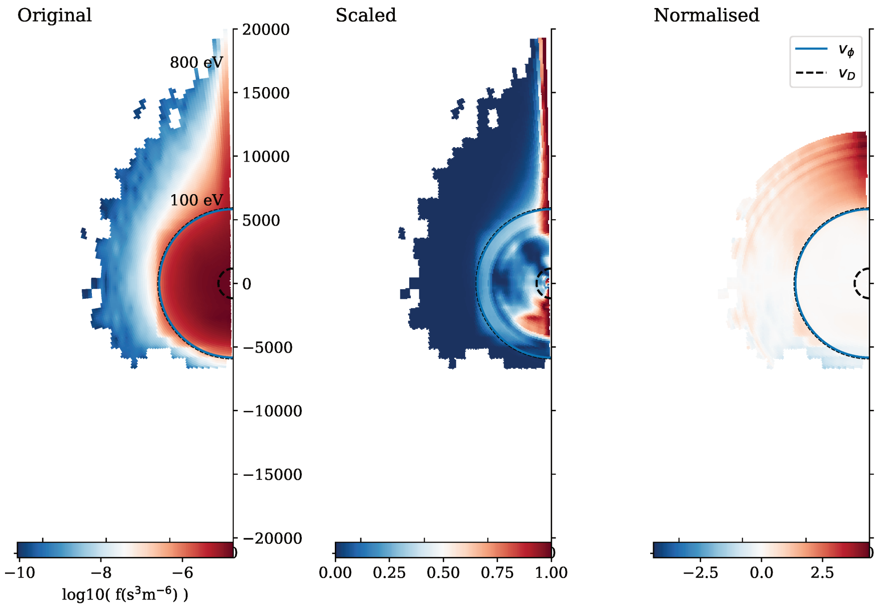

Figure 21: Two-dimensional representation of a gyrotropic electron VDF at 35.6 R_S for the *Maxw* run. The original electron VDF is shown on the left, a scaled VDF in the middle, and a normalised VDF on the right. We use the core electron resting frame where magnetic field is aligned with the y-axis. The electric potential velocity (v_ϕ) and the Dreicer velocity (v_D) are marked with blue and black lines.

inal gyrotropic VDF from the simulation run $Maxw$. A 2-dimensional linear interpolation between the sampled points was used, resulting in a smoother and more continuous plot. Logarithmic colour scale allows a recognition of the typical electron VDF features: a dense and isotropic core component and a beam-like strahl at positive velocity values.

The middle plot shows the same VDF in the *scaled* representation, where each energy bin – each circular belt in the $(v_{||}, v_{\perp})$ parameter space is scaled to the values between 0 and 1. With this representation we lose the information about the absolute value of f and its strong gradient along the energy dimension, but we expose the smaller anisotropic features at all energies. In cases where two features arise in the same energy bin, the scaled VDFs can be misleading, only highlighting the bigger feature. This can be seen already in Fig. 21 (middle plot), at energies dominated by the overdensity in the sunward direction (red feature at negative velocity values). As the overdensity is larger than the strahl feature at the same energy, strahl is not visible, until the energy where the sunward density disappears.

The right plot shows the *normalised* representation, where the values are normalised to the perpendicular cut through electron VDF ($f_{\perp} = f(v_{||} = 0)$). Regions of VDF where the density flux is lower than along the perpendicular direction appear in blue and regions with higher density in red. With this representation the small VDF features are less pronounced than in the scaled VDF, however, a relation with the original VDF is preserved through a norm, in this case chosen to be $f_{\perp}$. VDFs are shown in electron core resting frame, as this is the frame in which isotropy is expected.

The scaled distribution reveals two features aligned with magnetic field: the strahl present at positive velocities, and another overdensity at small negative velocities. The second feature is very small and does not appear in the normalised representation. It results from a slight mismatch between the anti-sunward portion of electron VDF leaving the simulation at the top boundary and the sunward portion defined with input parameters.

v_D and v_ϕ are overplotted as half circles with dashed black, and full blue line, respectively. Negative signed v_D corresponds to the velocity where the overdensity in the sunward direction starts to form (see the scaled representation), while negative signed v_ϕ coincides with the cutoff, clearly seen in blue in the normalised representation. In fact positive signed v_D corresponds to the strahl break point velocity, which is clearly seen in the VDF slice representation shown in Fig. 20, however it can be not well seen in the scaled representation due to the second feature at the same electron energy - the sunward directed overdensity.

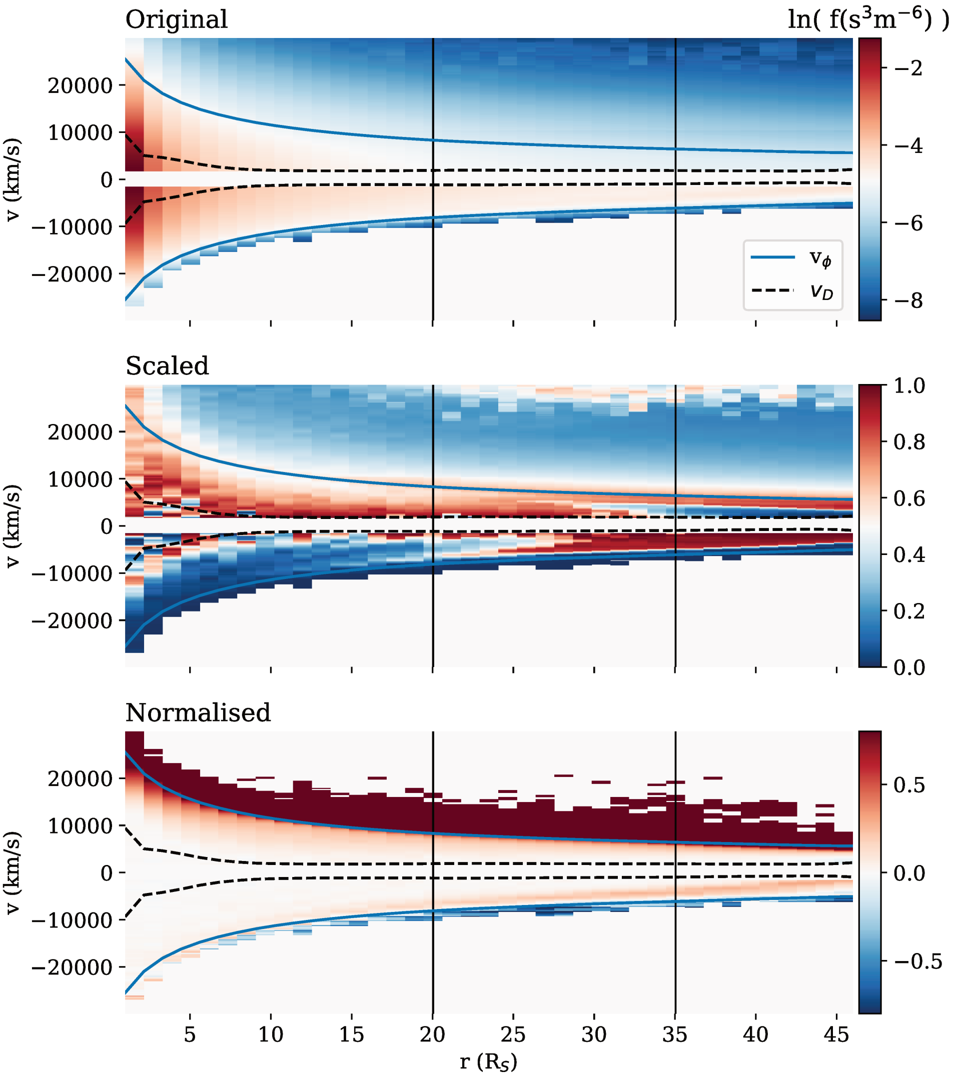

Figure 22: Parallel cuts through electron VDF plotted with respect to the radial distance in original (top), scaled (middle), and normalised (bottom) representation for the simulation run $\kappa = 4$. v_ϕ and v_D are marked with blue and black lines. Black vertical lines denote the radial distance of the VDFs shown in Fig. 20 (a, b).

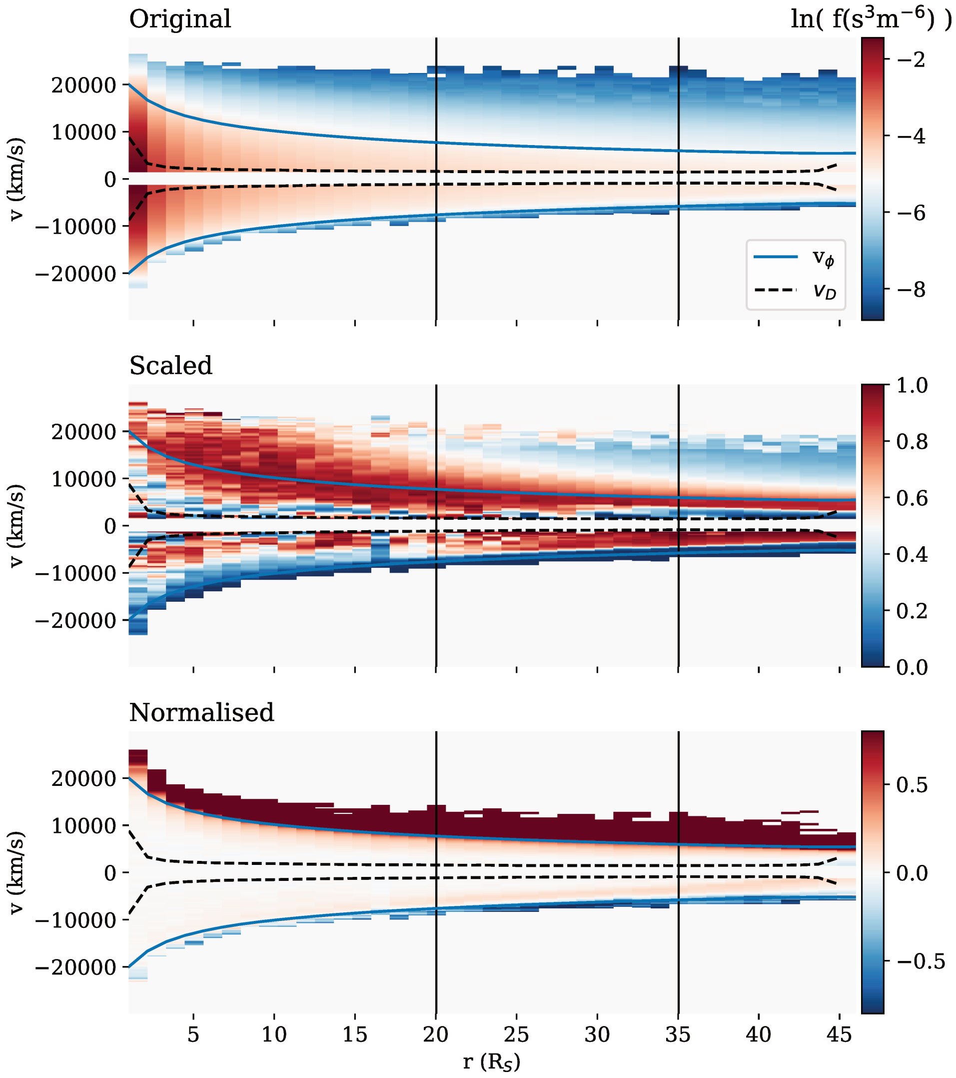

Figure 23: Parallel cuts through electron VDF plotted with respect to the radial distance in original (top), scaled (middle), and normalised (bottom) representation for the simulation run *Maxw*. v_ϕ and v_D are marked with blue and black lines. Black vertical lines denote the radial distance of the VDFs shown in Fig. 20 (c, d).

We are mainly interested in the behaviour of electron VDF parallel to the magnetic field, thus we average the values within a pitch-angle 10° to create parallel cuts through the VDF in original, scaled and normalised representation. These cuts are then plotted with respect to the radial distance to form a spectrogram in Fig. 22 for $\kappa = 4$, and in Fig. 23 for $Mawx$ simulation run. This plotting technique allows us to observe the radial evolution of the core and the strahl component.

The same properties as found in a single VDF representation in Fig. 21 appear to work well for the parallel VDF cuts at all radial distances. Blue line marking v_{Φ} for both of the runs nicely follows the colour transitions in the normalised VDF representation. All through out the simulation domain it denotes the start of the deficit in blue (for negative v values), and the start of the overdensity in red (for the positive v values). The transition in the scaled representation is below 30 R_S well described with the black dashed line, noting v_D. At larger radial distances the electron strahl is a weaker feature than the sunward directed peak, as discussed above, making the strahl break point velocity not showing up on this type of representation. Similar trends were found for the rest of the simulation runs listed in Table 2 for which plots are not shown.

BiCoP modelled electron VDFs appear to be well described by the velocities v_{Φ} and v_D, derived from exospheric model and Dreicer electric field theory, respectively. Exospheric theory describes the global effects of the electric potential, with v_{Φ} marking the electron cutoff velocity in the sunward direction, and the velocity at which the strahl becomes dominant over the core population in the antisunward direction. The velocity derived from Dreicer electric field (E_D), used also in the SERM model (Scudder, 2019), was found to describe well the effects of the ambipolar electric field (E) locally. v_D in the antisunward direction indicates the velocity at which the collisions are weak enough to allow the formation of the strahl component through the focusing mechanism.

According to the collisionless exospheric description electrons belong to a Maxwellian core if their energy is smaller than the local electric potential energy, and to the escaping strahl if their energy is bigger than that. By contrast, our model results show that *the strahl electrons can exist below the energy needed to escape the potential well*. The smallest strahl velocity is determined only by the collisionality of the system.

3.2.3 *Strahl pitch-angle width (PAW) and parallel temperature* ($T_{s,||}$)

In Article C, we present the effect of collisions on the strahl PAW and $T_{s,||}$, by comparison of simulation runs with different collisionalities.

We found that at the distance of 35 R_S, energies above 250 eV are not affected by Coulomb collisions. For energies below 250 eV Coulomb collisions are able to scatter the strahl electrons and change the dependence of PAW on electron energy. The shape of the PAW in the most collisional run was found to match the shape observed in the low-β solar wind by PSP (shown in Article B).

Analogously with Sec. 1.4, we computed the pitch-angle widths (PAWs) of obtained VDFs for the simulation runs presented in this chapter at the distance of 35.6 R_S (Fig. 24). Strahl from $Maxw$ run appears broader and reaches lower energies than the strahl in the rest of the runs. The PAWs for all the κ runs are smaller and almost identical. We compare the results with the PAWs obtained from a simple collisionless model starting from a Kappa-like corona with $\kappa = 4$, with different exobases ($r_0 = 1$ or $2R_s$). While the highest strahl energies correspond well to the PAWs from a simple model with $r_0 = 1R_S$, the lower agree better with the model starting at $r_0 = 2R_S$. This comparison results in the same conclusion as in Article C: the multi-exobase phenomena has a strong effect on the strahl PAW. Electrons with very high energies start focusing at the bottom boundary, where lower energy electrons are still dominated by collisions and form the electron core. These lower energy electrons only start focusing $1R_S$ above the bottom boundary, and thus correspond better to the simple model with $r_0 = 2R_S$.

Following the exospheric prediction, the parallel cut through the strahl VDF ($f_{||}$) should preserve the shape of the electron VDF in the solar corona. In Article C we verified that the $f_{||}$ resulting from a Maxwellian-like bottom boundary remains Maxwellian, however, the strahl parallel temperature $T_{s,||}$ increases slightly with radial distance. The same was found the the $Mawx$ run shown in this chapter.

The radial increase in $T_{s,||}$ is graphically demonstrated with Fig. 25 for simulation run $Maxw$. Both plots include electron VDFs integrated along the perpendicular direction for different distances ($f_{||,i}$), which are then normalised with a known VDF. The normalisation function used in the upper plot is the VDF at the bottom boundary integrated along the perpendicular direction, so the lines represent:

$$l = \frac{\int f_i(v_{||}, v_\perp) dv_\perp}{\int f_{Maxw(T=T_0}(v_{||}, v_\perp) dv_\perp}, \tag{45}$$

where index i describes the radial bin, and $f_{Mawx(T=T_0)}$ a Maxwellian VDF with a temperature of the bottom boundary ($T_{e,bot}$). The bottom plot is obtained analogically, but instead of $f_{Mawx(T=T_0)}$, we use a Maxwellian VDF with a temperature slightly larger than than set at the bottom boundary ($f_{Mawx(T=1.05 \cdot T_0)}$).

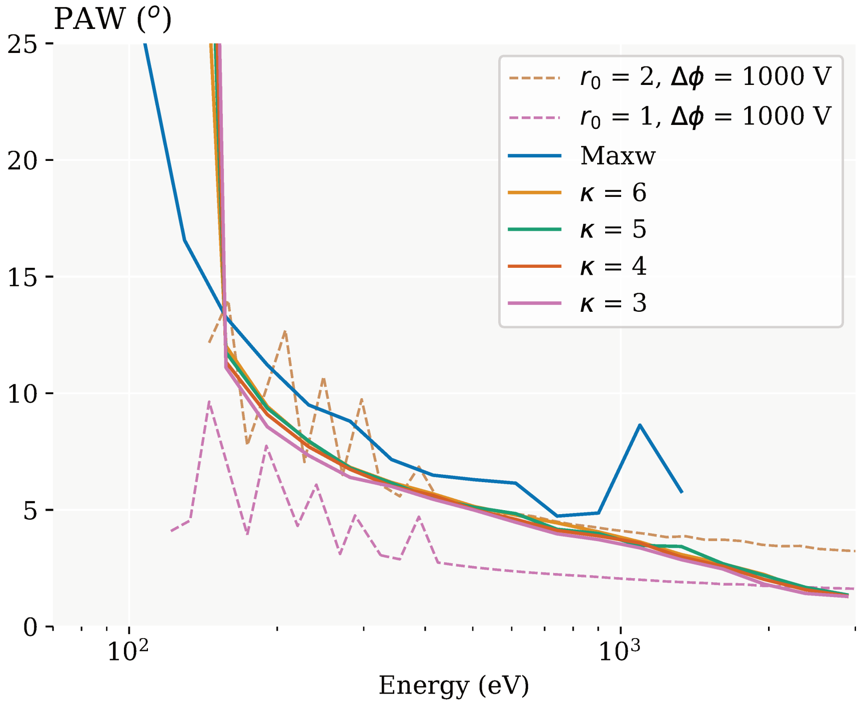

Figure 24: Strahl PAWs shown for electron VDFs at the radial distance of 35 R_S for the simulation runs from Table 2. The coloured dashed lines show PAWs obtained from collisionless single-exobase focusing model for different choices of the exobase (r_0).

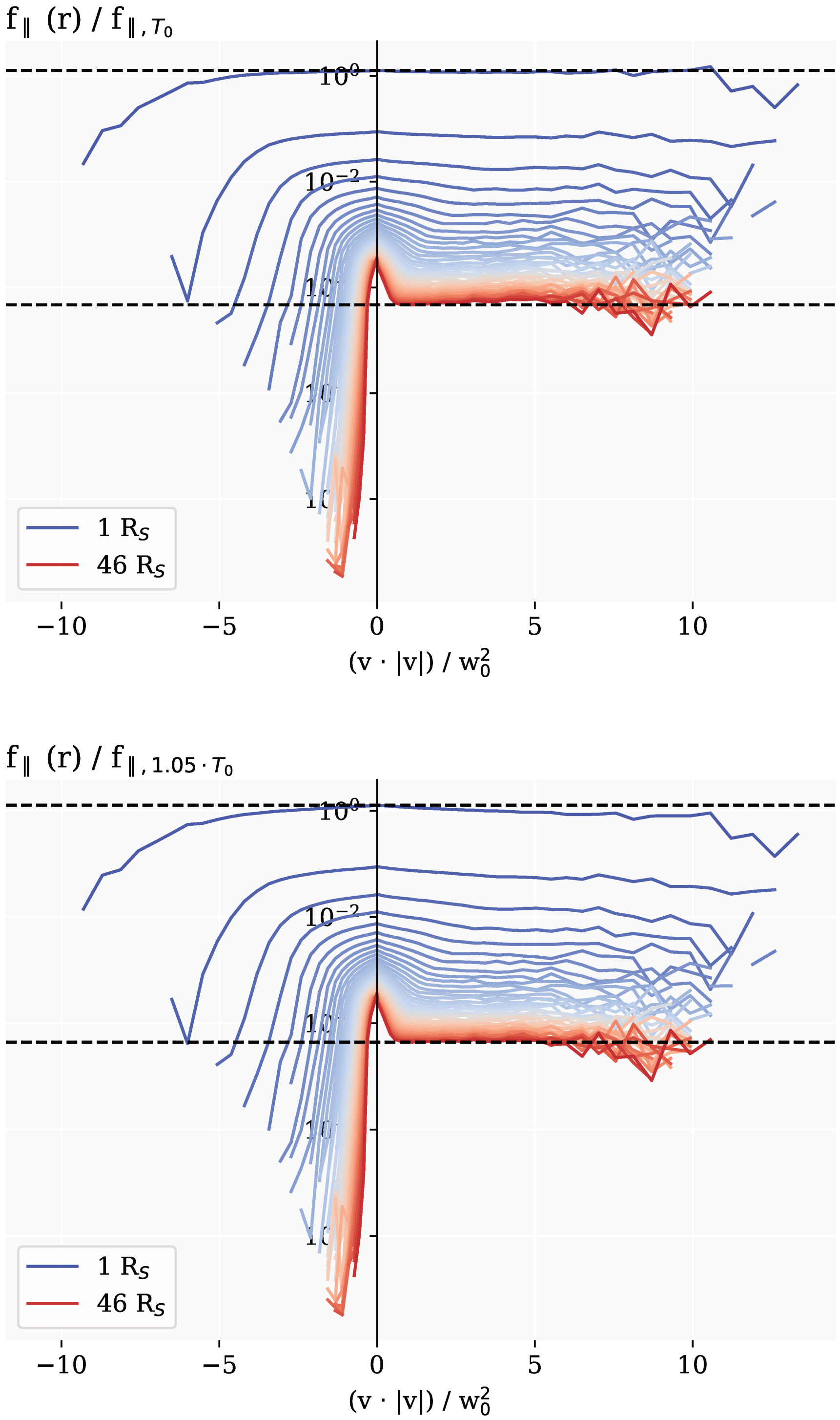

Figure 25: Electron VDFs, integrated along the ⊥ direction, for different radial bins, normalised with a Kappa VDF with the temperature $T_{e,bot}$ (upper plot), and $1.05 \cdot T_{e,bot}$ (lower plot). X-axis represents velocity (v) multiplied with its absolute value in the units of square of thermal velocity of the electron VDF at the bottom boundary (w_0^2). Radial distance is presented in colour spanning from blue closer to the Sun to red at the top boundary. Presented data is from *Maxw* run.

With this type of representation we can see whether the $f_{s,\|}$ varies with radial distance. Close to the Sun (blue lines) the strahl portion of the integrated VDF above $\sim 1w_{k,0}$ appears flat, which means that its shape is close to the initial VDF. Far from the Sun (red lines), however, we observe a slight positive slope in the integrated VDF indicating the increase of the flux at higher electron energies. When the VDF are normalised with a Maxwellian with a higher temperature (bottom plot) a decrease is observed for the blue lines, while the red lines appear to flatten out. From here we conclude, that $T_{s,\|}$ has increased with radial distance for the $Maxw$ simulation run. In Article C we even show that this increase is related to the collisionality of the system, and therefore conclude that it is a consequence of Coulomb collisions. We also propose a mechanism that could expain this effect of Coulomb collisions on $T_{s,\|}$.

Contrary to the Maxwellian VDF, an increase in temperature with radial distance is expected for the Kappa VDF. This phenomena is referred to as the velocity filtration (Scudder, 1992a,b), and is a result of the radially decreasing electric potential. Further investigation is required to properly account for the velocity filtration of the Kappa VDF, and separate its contribution from the increase of the $T_{s,\|}$, found to exist for the Maxwellian case as a consequence of Coulomb collisions.

Modelled solar winds originating from a Kappa-like solar corona possess the global, plasma moment features predicted by the exospheric solar wind models (Pierrard and Lemaire, 1996; Maksimovic et al., 1997a; Zouganelis et al., 2004). The obtained electron VDFs showed similar core electron properties for the Maxwellian and Kappa runs, however, differences were found in strahl electron population. The conclusions presented in Article C, were all met also by the κ runs. Furthermore, the result of the increasing $T_{s,\|}$ with radial distance was strengthened, as the strahls are more pronounced and have a more peculiar shape in the κ simulation runs.

Even though some evidences of a Kappa-like electron VDF in the solar corona exist, we, based on the shape and behaviour of the modelled and observed electron VDF in the solar wind close to the Sun, conclude that the coronal electron VDF is not a Kappa VDF. Our simulation results starting from a Maxwellian corona compare far better to the VDFs measured by PSP (see Ch. 2, Article B).

4

CONCLUSIONS

We present a study of the solar wind electrons the in the inner heliosphere. Due to their low mass and high velocities, electrons are responsible for a significant part of the solar wind acceleration. As a consequence of their lightness, the electron time scales are short, much shorter than the time scales related to the solar wind protons. To understand their behaviour we thus need space instrumentation with a sampling cadence high enough to capture the electron physics, and sufficient sensitivity to detect the low electron fluxes entering the instruments during these short integration times. This used to be one of the reasons why, observational studies of solar wind electrons used to be difficult. However, with the evolution of technology and the state-of-the-art scientific instruments, in-situ electron measurements now provided us with detail and fast electron VDF measurements. We believe that a combination of the novel PSP observations, combined with numerical and analytical modelling, will help resolve long-standing open questions related to the evolution of the electron VDF and its importance for solar wind acceleration.

We analysed electron VDFs measured in the inner heliosphere by Helios and PSP missions. We found that solar wind separated with respect to the solar wind velocity, and the core electron beta ($\beta_{ec,\|}$), exhibits different properties, which can be related to the different conditions at the solar wind origin, in the solar corona.

An anti-correlation between the temperature and the solar wind velocity was found separately for each of the electron populations: the core, the halo and the strahl. We found that the difference between core and halo electron temperature ($T_{c,h}$) in the slow and the fast wind was the largest close to the Sun, and then slowly decreased with radial distance, to almost completely disappear at 1 au. This result points toward different cooling ratios in the fast, and slow solar wind (Halekas et al., 2019; Maksimovic et al., 2020).

The variation with radial distance was not found for the strahl parallel temperature ($T_{s,\|}$) obtained from a 1D non-drifting Maxwellian fit to a parallel cut through strahl electron VDF. This observation agrees with the exospheric solar wind model prediction, that in the absence of collisions and wave-particle interactions, the fast streaming strahl electrons preserve the information about the shape of the electron VDF in the corona.

However, strahl pitch-angle widths (PAWs) obtained by a simple collisionless (single-exobase) focusing model, assumed also in the exospheric models, were found to be much lower than the ones observed in-situ. Wider PAWs can be a consequence of a multi-exobase phenomena, or scattering mechanisms like Coulomb collisions and field-particle interactions, not accounted for by the simple collisionless model. Using the kinetic model BiCoP we were able to investigate the effect of the first two. Three simulation runs with different collisionalities reveal that the high energy strahl electrons are collisionless, exhibiting the same PAWs at the radial distance of 35 R_S. These PAWs are still larger than the ones obtained by the simple collisionless model with the same exobase (bottom boundary in the simulation runs). The difference between the two is accounted to the the fact that all electrons do not have the same exobase location. While the highest energy electrons start focusing at the simulation bottom boundary, some electrons are still dominated by collisions and only start focusing at larger radial distances. In the frame of exospheric models these electrons are believed to have different exobase locations.

Coulomb collisions were found to scatter the strahl electrons with energies below 250 eV at the radial distance of 35 R_S. The shape of PAW with respect to electron energy for our most collisional run appears to agree well with the shape of PAW observed in the low-β solar wind during the first two perihelia by PSP. However, the observed strahl electrons still appear $\sim 15^\circ$ broader. We believe that this difference could result from either a global effect of a Parker spiral magnetic field configuration not included in BiCoP model, or magnetic field fluctuations during the integration time of the VDF measurement. In fact, in-situ measured PAWs for energies above 300 eV were found to be between 10 and 15° larger for the instances during which the standard deviation of B was above 10 nT, than when it was below that value.

The scattering of the strahl, not captured in BiCoP model, could also result from wave-particle interactions. In particular, *fast magnetosonic* modes, also called *whistler* modes are frequently observed in the solar wind with frequencies comparable to electron gyro-frequency (Lacombe et al., 2014; Stansby et al., 2016; Tong et al., 2019; Agapitov et al., 2020; Jagarlamudi et al., 2020). A local correlation between a narrow-band whistler wave activity and the broadening of the strahl electrons at a specific energy range was found by Kajdič et al. (2016). This observation supports the scenario of strahl scattering through through the cyclotron resonance of a whistler wave propagating parallel to the magnetic field. The cyclotron resonance velocity corresponds to the anti-sunward strahl electrons when the wave is propagating in the sunward direction. However, at 1 au, where the correlation was observed, majority of whistlers were found to propagate in the anti-sunward direction (Stansby et al., 2016). Interestingly, the whistler waves observed during the first encounter of *Parker Solar Probe* (PSP) at ~ 35 R_S were found to propagate in sunward direction (Agapitov et al., 2020).

The effects of different types of waves have on electron VDF were studied with the particle-in-cell simulations by Saito and Gary (2007), and a kinetic model in a framework of quasi-liner theory by Vocks et al. (2005). The quasi-parallel narrow-band whistler waves were related to an anti-correlation between PAW and electron energy, while the quasi-parallel broad-band whistler waves, generated by the magnetic field power spectrum in the whistler range, were found to result in an increase of PAW with electron energy. However, the assumption that broad-band whistler waves exist as part of the magnetic field power spectrum in the solar wind is in contradiction with the observations reported by Chen et al. (2010), who observe most of the spectral power is in the perpendicular component. Nevertheless, no matter how small the parallel spectral power contribution is, it could still resonate with the solar wind electrons.

Generally, there are two ways to exchange energy between particles and waves. Energy can be deposed to a particle VDF through a resonant interaction with a wave, as described above, or can be taken from a non-equilibrium particle VDF and transferred to a wave. Mechanisms transferring energy from free-energy sources, like non-equilibrium VDFs, are called *plasma instabilities* (Rosenbluth, 1965). Scattering of the strahl electrons through an instability was investigated by Verscharen et al. (2019a). They analytically and numerically showed that the strahl-driven oblique whistler instability creates whistler waves in the low-β solar wind, when the velocity of the strahl electrons reaches above 3 times the thermal velocity of the total electron VDF. The resulting oblique waves propagate with an angle of ~ 60^o with respect to the magnetic field and with a parallel velocity smaller than that of the strahl electrons. The described strahl-driven instability could explain the observations of increasing PAW with electron energy shown in Article A.

High energy strahl electrons could also be scattered through a non-resonant energy diffusion process called *stochastic heating*. If the magnetic field spatial fluctuations are on the order of a gyro-orbit scale of electrons, and if the fluctuation frequency is small compared to the electron gyro-frequency, the electrons can diffuse in the perpendicular direction (Verscharen et al., 2019b). The perpendicular heating appears to be important for the solar wind protons (Chandran et al., 2013; Martinović et al., 2019), however, to our knowledge no similar studies exist for the solar wind electrons.

The increasing signatures were found for PAWs observed in the low-β solar wind by Helios mission at farther distances from the Sun (above ~ 100 R_S). A slight increase of PAW with energy was also found for the high-β solar wind observed by PSP (35 - 60 R_S). We conclude that these PAWs shapes, observed at distances above ~ 100 R_S, and in high-β solar wind already at 35 R_S, require the existence of wave-particle scattering mechanisms. However, PAWs in low-β solar wind close to the Sun, can be explained by Coulomb collisions scattering.

At the time of writing PSP is exploring the yet unknown regions in vicinity of the Sun, and the Solar Orbiter is sampling the regions visited by the Helios mission. The large quantities of the high-quality EM field measurements, combined with the fast cadence electron VDFs, will allow a new perspective on the field-particle interactions and the consequences they have on a global scale evolution of the solar wind.

The scattering of the low-energy strahl electrons by Coulomb collisions in the BiCoP model was found to have an effect on the parallel cut through the strahl VDF, modifying the information carried by the strahl about the state of coronal electron VDF. $T_{s,||}$ was found to increase with radial distance, mostly close to the Sun, in the solar wind acceleration region. In the simulation runs with Maxwellian-like coronal electron VDFs, $T_{s,||}$ increased for up to 15 % sampled at the radial distance of 35 R_S.

The PSP observations of PAW in the low-β solar wind coincide best with the PAWs found in a Maxwellian coronal electron VDF run, where the $T_{s,||}$ increases by 15 %. Therefore, we conclude that the measured $T_{s,||}$ presented in Article B overestimates the temperature of the electron in the solar corona. Instead of the average reported value of 96 eV, we believe the average coronal temperature over the measured period equals to 83 eV.

The given numbers are just first order approximations for the average solar wind observed by the PSP so far. With a growing observational data base we will be able to study separate solar wind types at different distances from the Sun, and with a use of BiCoP model relate these observations to the different plasma conditions in the solar corona.

The ambipolar electric field (E), accelerating the solar wind in the BiCoP model, was found to be on the order of Dreicer electric field (E_D). This means that the collisions are not strong enough to damp the effects of E, and departures from the Maxwellian VDF are expected. In fact, the separation velocity v_D (Scudder, 1996) was found to correspond to the strahl break-point velocity, the velocity at which departure from Maxwellian shape appears in the anti-sunward direction. Separation velocity v_Φ, a consequence of the electron potential predicted by the exospheric models, was found to limit the core population in both, sunward and anti-sunward direction. In cases where

$v_D < v_\phi$, we found that non-Maxwellian features do exist even for electrons trapped by the electric potential. This is a new finding, as until now it was believed that electrons with velocities below v_ϕ strictly belong to the collision-dominated core population.

A Kappa-like electron VDF, or any VDF with a sufficient excess of high-energy electrons, existing in the solar corona is known to produce the fast solar wind in the exospheric solar wind models. Coulomb collisions were found to weaken the solar wind acceleration, as the simulation runs with Kappa-like boundary condition, even though producing a faster wind compared to the Maxwellian runs, reached only velocities up to 350 km/s.

Although some spectroscopic, observational evidence of the presence of high-energy tails in coronal electron VDFs exist (Dzifčáková et al., 2018; Saqri et al., 2020), the Maxwellian shape of the strahl electron VDF observed close to the Sun by PSP proves otherwise. Furthermore, the observed strahl VDFs relate much better to the strahl VDFs obtained from BiCoP runs with Maxwellian-like, than Kappa-like bottom boundary conditions. The observed strahl VDF, thus leads to the conclusion that the electron VDF in the solar corona is Maxwellian.

We emphasise that this conclusion was drawn on the basis of near-Sun PSP measurements providing an accurate information about electron VDF up to the energy of ~ 800 eV. At the radial distance ~ 35 R_S the electron flux above that energy is too low to be captured by the instrument. However, as PSP approaches the Sun, and the plasma densities increase, we might be able to measure electrons at higher energies and more precisely model the strahl VDF. The Solar Orbiter mission, currently sampling the distances a bit farther from the Sun might also reveal new features of the electron VDF, that may not have been caught by the older technology used on the Helios spacecrafts. The Solar Orbiter will in the future be the only spacecraft measuring the fast solar wind originating from the polar regions, which might exhibit high-energy tails in electron VDFs.

Kappa-like VDFs have not been observed in the near-Sun solar wind observed by PSP, however, they describe well the strahl, and especially the halo VDFs at distances above ~ 100 R_S. We believe that the high-energy tails, non-Maxwellian VDFs, cloud be produced during the solar wind expansion by wave-particle interaction or exchange of energy with turbulence.

During the course of this thesis project we advanced the data analysis techniques used for investigating the observed and modelled solar wind electron VDFs. Techniques were implemented to the PSP electron data and will be useful for representing the electron VDFs also during the future solar encounters. Our future goal is to implement our analysis also to the Solar Orbiter data, which will make it easy to compare measurements between the two concurrently operating heliospheric missions. Furthermore, using the shown VDF representations we can easily relate the observations to results of the various numerical models, which often provide a phase space distribution function, which includes the evolution of VDF in space.

VDF space is 4-dimensional (three dimensions in the velocity space and one energy dimension), thus using the right data analysis and representation approach is crucial to find the information they posses. If we are able to recognise the higher order VDF features, they can give us a new insight on the electron dynamics and physical mechanisms taking place in the solar wind.

The studies of the Sun and the solar wind surrounding our magnetosphere are not only important for the space weather applications, which have a direct effect on the Earth. Majority of stars are believed to produce stellar winds. For the less massive stars, like our Sun, the high temperature just above the solar surface causes a small part of solar mass to escape and form the stellar wind, similar to one we know here. For more massive stars the large amounts of radiation pressure blow away significant parts of the stellar mass in a form of much denser stellar wind. The proximity of the Sun gives us a unique opportunity for observation and exploration, impossible in the context of any other star. That is why deep understanding of the mechanisms driving the Sun and the solar wind, might be an important key to learn more about the dynamics of other stellar winds.

Part I

APPENDIX

A

DESCRIPTION OF THE SPAN-E FIELD OF VIEW (FOV)

Each of the SPAN-E instruments provides a three-dimensional information describing solar wind electron VDF: 32 energy bins, and 16 azimuth anodes × 8 elevation bins describing the angular distribution. The combined field of view (FOV) of the two instruments together covers almost a full solid angle. SPAN-A and B configuration is shown in the upper plots of Fig. 26 for the first two encounters and in Fig. 27 for the third and the fourth encounter. Lower plots of the same figures show example measurements of the electron VDF at times when the magnetic field is almost aligned with the radial direction, providing the strahl electrons to be partly blocked by the heat shield.

The azimuth angle in both instruments is sampled with anodes of different sizes: 8 anodes with the width of 6°, and 8 with the width of 24°, which can be recognised in Figs. 26 and 27. This configuration allows a finer sampling of the strahl electrons. The strahl, following the magnetic field lines, which close to the Sun become more and more aligned with the radial direction, is expected to enter the instruments just on the edges of the heat shield. Therefore, the small anodes are set to sample the directions close to the heat shield.

The effect of the heat shied on the strahl electron measurements during the first two encounters is presented in the Appendix A of Article B.

We present how the different elevation settings affect the FOV of SPAN-E. Initially, during encounters 1 and 2, the deflecting voltages have been overestimated, which resulted in extreme elevation bins sampling angles corresponding to the heat shield or the spacecraft payload. Therefore the two extreme elevation bins have not been used in the data analysis, and are shown in Fig. 26 as empty grids. With the third orbit the voltage settings have been corrected which resulted in a better FOV coverage shown in Fig. 27.

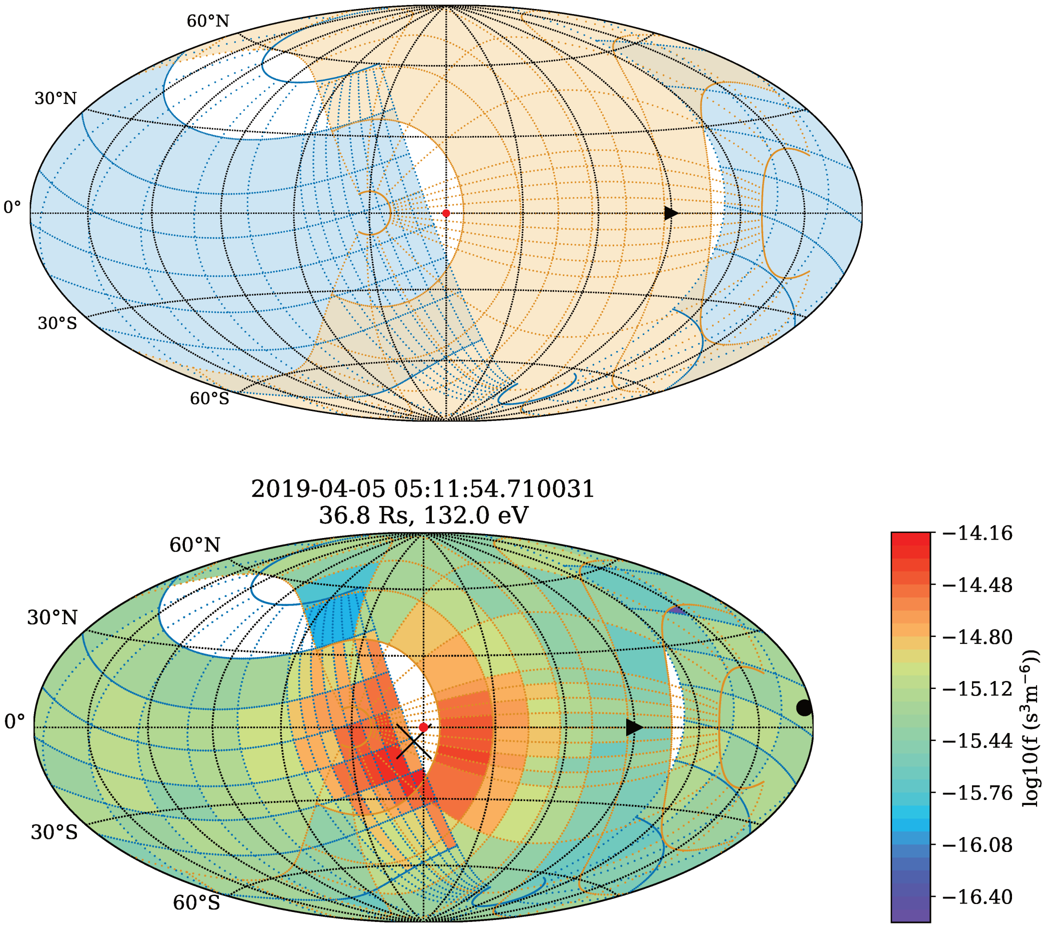

Figure 26: (upper) The combined FOV of SPAN-A in blue, and SPAN-B in yellow, resulting from the instrument configuration during the first two encounters. The grid represents the pixels of each instrument. The presented orientation corresponds to the position of the spacecraft during the encounter periods, when the heat shield points towards the Sun. The Sun is marked with a red dot in the centre of the figure, and the spacecraft RAM direction with a black triangle. The horizontal axis is aligned with the ecliptic plane. (lower) An example of an electron VDF two-dimensional measurement from the second encounter (Apr 5 2019) in the energy bin centred on 132.0 eV. The black dot and cross represent the positive and negative direction of the magnetic field vector, averaged over the integration time of the VDF measurement.

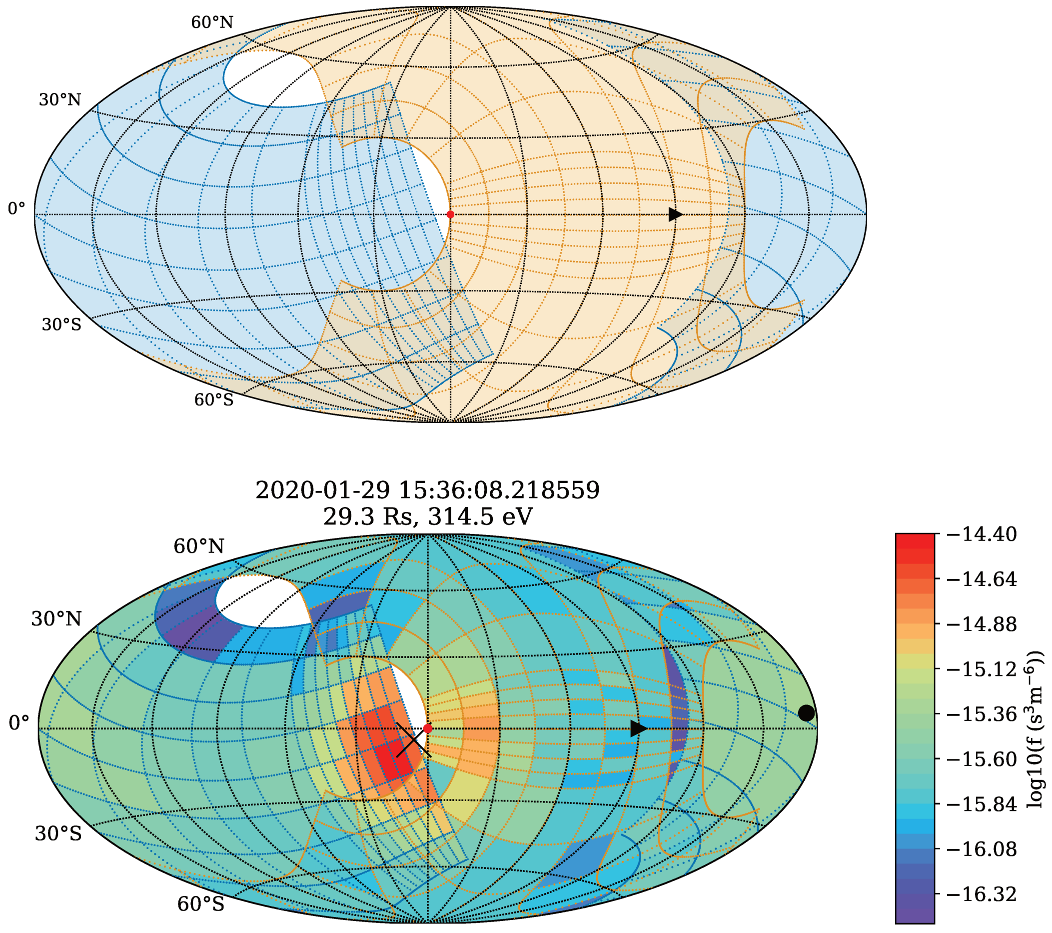

Figure 27: (upper) The combined FOV of SPAN-A in blue, and SPAN-B in yellow, resulting from the instrument configuration during the third and fourth encounter. See Fig. 26 for further description. (lower) An example of an electron VDF two-dimensional measurement from the fourth encounter (Jan 29 2020) in the energy bin centred on 314.5 eV. The black dot and cross represent the positive and negative direction of the magnetic field vector, averaged over the integration time of the VDF measurement.

B

TABLES OF PARAMETERS USED IN BICOP SIMULATIONS

Table 1: Simulation input parameters

Notation	Parameter	Units
T_e	Temperature of electrons at the bottom boundary	K
v_C	Velocity below which collisions is conducted every time	v_0
n_{coll}	Total number of collisions	
N	Number of each of the species in the simulation domain	
g_0	Ratio between gravitational and thermal force (Eq. 32)	
h_{top}	Ratio between length and the position of bottom boundary (L/r_0)	
el_0	Initial guess of the charge-neutralising electric field	V/m
$n_{coll,el0}$	Number of collisions conducted before setting a first order E	
$n_{coll,loc}$	Number of collisions conducted after $n_{coll,el0}$, during which the plasma moments are sampled and the second order E is determined	
n_z	Number of bins along the radial direction	
n_v	Number of bins separating electron velocity space	
$v_{max,e}$	Maximal velocity value in electron velocity space	v_0
v_{bot}	Velocity of both species at the bottom boundary	v_0
v_{top}	Velocity of both species at the top boundary	v_0
$ve_{th,bot}$	Thermal velocity of electrons at the bottom boundary	v_0
$ve_{th,top}$	Thermal velocity of electrons at the top boundary	v_0
ke_{bot}	Kappa parameter of the Kappa electron VDF at the bottom boundary	

Table 2: Simulation input parameters

Notation	Maxw	$\kappa = 6$	$\kappa = 5$	$\kappa = 4$	$\kappa = 3$	Units
T_e	2	2	2	2	2	MK
v_C	0.4	0.4	0.4	0.4	0.4	v_0
n_{coll}	3	3	2	3	3	10^{11}
N	22500	22500	22500	22500	22500	
g_0	0.14162	0.14162	0.14162	0.14162	0.14162	
h_{top}	45	45	45	45	45	
el_0	150	150	150	150	150	V/m
$n_{coll,el0}$	2	2	2	2	2	10^{10}
$n_{coll,loc}$	4	4	4	4	4	10^{10}
n_z	40	40	40	40	40	
n_v	80	80	80	80	80	
$v_{max,e}$	5	5	5	5	5	v_0
v_{bot}	0	0	0	0	0	
v_{top}	0.028	0.033	0.036	0.038	0.046	v_0
$ve_{th,bot}$	1	1	1	1	1	v_0
$ve_{th,top}$	0.41	0.37	0.39	0.395	0.4	v_0
ke_{bot}		6	5	4	3	

Part II

PUBLICATIONS

A

SCATTERING OF STRAHL ELECTRONS IN THE SOLAR WIND BETWEEN 0.3 AND 1 AU: HELIOS OBSERVATIONS

Monthly Notices
of the
ROYAL ASTRONOMICAL SOCIETY

MNRAS **486,** 3404–3414 (2019)
Advance Access publication 2019 April 17

doi:10.1093/mnras/stz1007

Scattering of strahl electrons in the solar wind between 0.3 and 1 au: Helios observations

L. Berčič,[1,2]★ M. Maksimović,[1]★ S. Landi[2,3]★ and L. Matteini[1]

[1] *LESIA, Observatoire de Paris, PSL Research University, CNRS, UPMC Université Paris 6, Université Paris-Diderot, 5 Place Jules Janssen, F-92190 Meudon, France*
[2] *Physics and Astronomy Department, University of Florence, Via Giovanni Sansone 1, I-50019 Sesto Fiorentino, Italy*
[3] *INAF - Osservatorio Astrofisico di Arcetri, Largo Enrico Fermi 5, I-50125 Firenze, Italy*

Accepted 2019 April 4. Received 2019 April 1; in original form 2018 November 17

ABSTRACT

Electron velocity distribution functions in the solar wind according to standard models consist of four components, of which three are symmetric – the core, the halo, and the superhalo, and one is magnetic field-aligned, beam-like population, referred to as the strahl. We analysed *in situ* measurements provided by the two Helios spacecrafts to study the behaviour of the last, the strahl electron population, in the inner Solar system between 0.3 and 1 au. The strahl is characterized with a pitch-angle width (PAW) depending on electron energy and evolving with radial distance. We find different behaviour of the strahl electrons for solar wind separated into types by the core electron beta parallel value ($\beta_{ec\parallel}$). For the low-$\beta_{ec\parallel}$ solar wind the strahl component is more pronounced, and the variation of PAW is electron energy dependent. At low energies a slight focusing over distance is observed, and the strahl PAW measured at 0.34 au agrees with the width predicted by a collisionless focusing model. The broadening observed for higher energy strahl electrons during expansion can be described by an exponential relation, which points towards an energy-dependent scattering mechanism. In the high-$\beta_{ec\parallel}$ solar wind the strahl appears broader in consistence with the high-$\beta_{ec\parallel}$ plasma being more unstable with respect to kinetic instabilities. Finally we extrapolate our observations to the distance of 0.16 au, predicting the strahl PAWs in the low-$\beta_{ec\parallel}$ solar wind to be ∼29° for all energies, and in the high-$\beta_{ec\parallel}$ solar wind a bit broader, ranging between 37° and 65°.

Key words: plasmas – scattering – methods: observational – space vehicles: instruments – Sun: heliosphere – solar wind.

1 INTRODUCTION

Electrons as the lighter constituents of the solar wind are the carriers of the heat flux and therefore play an important role in the energy balance during the solar wind expansion. Electron velocity distribution functions (VDFs) are highly non-thermal and can be divided into four components: a core, a thermal and dense population well represented by a Maxwellian function, a halo with a higher temperature and exhibiting strong high-energy tails, an even hotter superhalo spanning from a few to a few hundred keV, and a magnetic field aligned component, called a strahl (Feldman et al. 1975; Hammond et al. 1996; Maksimovic, Pierrard & Riley 1997a; Lin 1998; Maksimovic et al. 2005; Wang et al. 2012; Graham et al. 2017).

Strahl electrons can propagate in a positive or negative magnetic field direction, but generally away from the Sun (Feldman et al. 1978; Pilipp et al. 1987a). Bidirectional strahls have also been observed and serve as indicators of certain magnetic field structures, like magnetic field loops and magnetic clouds (Gosling et al. 1987).

It is commonly believed that these antisunward field-aligned electrons originate from the hot solar corona, escaping from a thermal VDF and focusing around the magnetic field as they conserve their magnetic moments (Feldman et al. 1975; Pierrard, Maksimovic & Lemaire 1999; Salem, Bale & Maksimovic 2007). The formation of the strahl from a thermal population during the spherical expansion was simulated by Landi, Matteini & Pantellini (2012) using a fully kinetic model including Coulomb collisions. However, it was shown with particle-in-cell simulations that strahl could also be created by a resonant interaction of halo electrons with whistler-mode waves generated by electron core anisotropy (Seough et al. 2015). The question of the origin of strahl electrons as well as other non-thermal components of electron VDF awaits

---

★ E-mail: laura.bercic@obspm.fr (LB); milan.maksimovic@obspm.fr (MM); slandi@arcetri.astro.it (SL)

Published by Oxford University Press on behalf of the Royal Astronomical Society

for new theoretical and observational studies, soon fortified by the two upcoming solar missions: Parker Solar Probe and Solar Orbiter.

The properties of strahl population, and its evolution during the expansion have been shown on the basis of various near-Earth, and interplanetary *in situ* observations. The theoretically predicted focusing effect during the radial expansion was not observed. On the opposite, widening of strahl VDF with distance from the Sun has been reported by Hammond et al. (1996) using Ulysses data (1–3.5 au), and Graham et al. (2017) using Cassini data (1–6 au). The authors of the later state that the strahl ceases to exist at distances larger than 5.5 au as it is most likely completely scattered into the halo population. This hypothesis agrees with the study of Maksimovic et al. (2005) and Štverák et al. (2009), showing a decrease in relative density of strahl component with radial distance, but an increase of the halo density. Štverák et al. (2009) find the same tendency in both the slow and the fast solar wind between 0.3 and 4 au using data from Helios, Cluster, and Ulysses missions.

The strahl is more pronounced and narrower in the fast wind as opposed to the slow wind, where it appears less dense, broader, and sometimes even not present at 1 au (Fitzenreiter et al. 1998; Gurgiolo & Goldstein 2017).

Studying the variation of the strahl pitch-angle width (PAW) with electron energy might reveal which scattering mechanisms are at work at different radial distances, and for different solar wind types. Both increasing and decreasing trends were observed so far. Kajdič et al. (2016) find anticorrelation between PAW and electron energy, which gets broken for a certain energy range at times of observed whistler-mode wave activity. Their analysis includes mostly the slow solar wind at 1 au (Cluster observations). Particle-in-cell simulations provided by Saito & Gary (2007) confirm that strahl scattered by whistlers which were generated by whistler anisotropy instability would in fact exhibit decreasing trend between the width and electron energy. The same behaviour was observed by Feldman et al. (1978), Pilipp et al. (1987a), and Fitzenreiter et al. (1998). Positive correlation between strahl width and electron energy was reported by Pagel et al. (2007) in the study of cases with especially broad strahl observed at 1 au by ACE spacecraft. This trend can result from scattering by whistler waves generated by k^{-3} power spectrum (Saito & Gary 2007). We mention two examples of the strahl scattering mechanisms that can be related to the variation of the strahl PAW with electron energy, but more mechanisms have been proposed so far. These include firehose instability generated fluctuations (Hellinger et al. 2014), Langmuir waves (Pavan et al. 2013), lower hybrid waves (Shevchenko & Galinsky 2010), oblique kinetic Alfv´en waves (Gurgiolo et al. 2012; Chen et al. 2013), and Coulomb collisions (Horaites, Boldyrev & Medvedev 2018), and are discussed latter in the article.

With an exception of analysis by Štverák et al. (2009), none of the observational studies present the radial evolution of strahl electrons within 1 au, separated by the solar wind type. As discussed above, the strahl population is more pronounced in the fast solar wind and close to the Sun, thus it is important to study strahl properties exploring the data set from Helios missions still providing the closest *in situ* measurements from the Sun.

The two almost identical Helios spacecrafts were launched in the 70’s with a mission to explore the innermost parts of interplanetary space (Porsche 1981). During 10 yr of active mission for the first spacecraft, and three years for the second one an intriguing and currently still unique data set was produced, sampling the solar wind in the ecliptic plane with the closest perihelion of 0.29 au (Helios 2).

In this work we provide a statistical analysis of these data with a focus on strahl electrons behaviour within 1 au. Our results in general agree with previously published works, but give us an additional insight into regions closer to the Sun, from where we were able to estimate strahl properties that will be observed during the first perihelion of the Parker Solar Probe, 0.16 au from the Sun.

2 INSTRUMENT DESCRIPTION

To study kinetic properties of solar wind electrons we analysed the data from the electron particle instrument I2, part of E1 Plasma Experiment onboard Helios 1 and 2 missions (Rosenbauer et al. 1981; Pilipp et al. 1987b).

I2 is designed to measure a 2D distribution function of solar wind electrons within 1 au from the Sun. The instrument aperture pointing perpendicular to the spin axis of the spacecraft is followed by deflection plates, preventing sunlight-beam electrons to enter the analyser part. Electron energy is measured by a hemispherical electrostatic analyser in 16 exponentially spaced energy steps. Two different operation modes allow the measurement of either low- (0.5 to 13.3 eV) or high- (9 to 1445 eV) energy electrons. A channeltron sits at the end point of the electrostatic analyser and provides the electron count rate.

The narrow instrument field of view covers $19^\circ \times 2^\circ$ (elevation x azimuth) and is centred on the ecliptic plane. Both spacecrafts spin around the axis perpendicular to that plane with a spin period of 1 s allowing the instrument to sample a full 360° azimuthal angle. This is done in eight steps (eight azimuth sectors), each lasting for 78.06 ms for Helios 1 and 31.1 ms for Helios 2, corresponding to angular sector width of 28.1° and 11.2°, respectively. Thus one scan over 16 energy steps and eight azimuthal directions is normally obtained in 16 s and repeated every 40 s.

3 METHOD

3.1 Data set

This study is based on the data provided by plasma experiments onboard Helios missions: the electron VDFs – instrument I2 (described in Section 2), proton plasma moments – instruments I1a and I1b, and magnetic field vectors – instruments E2 and E3.

The core of this analysis are electron VDFs described in Section 3.2.

The proton onboard integrated densities and velocity vectors were taken from the original Helios files in Helios data archive.[1] The measured proton densities are likely to be underestimated, therefore the measurement with the higher value between the two – I1a and I1b – with 10 per cent uncertainty was considered.

The proton core temperatures we use are taken from a new Helios proton data set provided with descriptions by Stansby et al. (2018).

Instruments E2 and E3 are the two fluxgate magnetometers onboard Helios missions. E2 samples data with a frequency of 4 Hz which is saturated at 50 nT, and E3 gives a 6s-averaged measurements. The E2 data are used if available, and if the absolute magnetic field value is smaller than 50 nT. In other cases the E3 data are used. A mean value of magnetic field vector is obtained for each 16-s electron VDF. We note that magnetic field vectors obtained this way differ from the ones used in all previous Helios data electrons studies, e.g. (Štverák et al. 2009).

---

[1] Link to the data archive: http://helios-data.ssl.berkeley.edu.

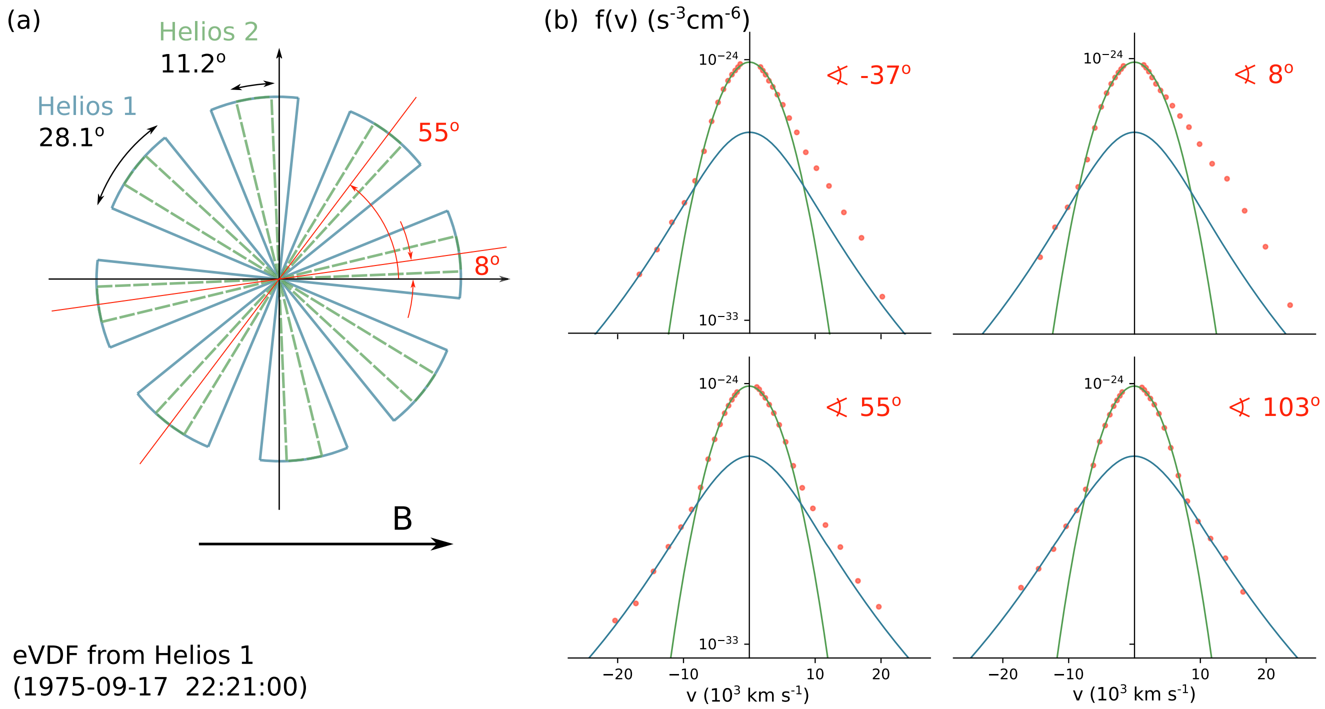

Figure 1. (a) A schematics of I2 instrument azimuth sectors in the magnetic field frame corresponding to the example electron VDF shown in panel (b). The difference in sector size between Helios 1 and 2 is marked with colour. Note, however, that the example measurement was taken by Helios 1 spacecraft, and Helios 2 azimuth sectors are added to the schematics only to highlight the differences between the two. (b) An example electron VDF measured at the distance of 0.32 au from the Sun. Each of the four plots shows a pair of oppositely directed azimuth sectors: the red dots are measurements corrected for spacecraft potential, and green and blue line represent the fit to core and halo population, respectively. For each sector pair the angle indicates the position with respect to the magnetic field direction.

The data set has many limitations, but we have the benefit of using measurements collected over several years by two almost identical spacecrafts. Moreover, this is the only data set providing insight on the solar wind plasma parameters in the near-Sun regions. The analysed period spans between 1974 and 1982 for Helios 1 and between 1976 and 1979 for Helios 2. We only use scans when all the above parameters are available and when the measured magnetic field vector lies within 5° from the I2 measuring plane (the ecliptic plane).

3.2 Electron VDF

The measurements of the solar wind electrons are strongly polluted by two phenomena: photoelectrons emitted from the spacecraft body, and spacecraft charging. A method for correcting these effects making use of other *in situ* plasma measurements is well described by Salem et al. (2001).

Photoelectrons appear as a sharp peak at low energies and have already been removed in the provided Helios data set.

A charged spacecraft deforms electron VDF depending on the shape and magnitude of the spacecraft potential which varies as a function of the surrounding plasma (Pedersen et al. 2008). In the solar wind at 1 au the typical values of spacecraft potential are between 1 and 10 V (Salem et al. 2001), and decreasing with distance from the Sun. A positive charge accelerates electrons towards the instrument making their energies seemingly larger. The density obtained by integration of this deformed VDF would therefore be overestimated.

Salem et al. (2001) suggest the use of electron density obtained by a thermal noise receiver measuring the plasma peak to scale the VDF preforming a linear shift in electron energy. We apply the same method to determine the spacecraft potential, however, since there were no thermal noise receiver measurements made by the two Helios missions, we use a less reliable proton density measurement from I1a and I1b instruments instead. We assume quasi-neutrality ($n_{\mathrm{e}} = n_{\mathrm{p}} + 2n_{\alpha}$), and a typical alpha particle to proton number ratio of 0.05.

The corrected VDF is then shifted to the plasma zero velocity frame using the proton velocity measurement, and rotated to the magnetic-field-aligned frame defined by the magnetic field measurement during each scan. In this frame the 0 deg angle is aligned with the direction of either positive or negative magnetic field vector and always pointing antisunward. An example of a VDF at this point is shown in Fig. 1(b), where each of the four plots consists of two oppositely located azimuth sectors. The angles indicate how far each sector pair lays from the magnetic field direction. The sign of the angle [within the interval (−180°, 180°)] is kept for easier understanding of the schematics in Fig. 1(a), but it is not relevant for our further analysis.

A non-linear least squares method is used to fit two solar wind electron components: a core and a halo (see Fig. 1b). We do not fit strahl component because our aim is to study the energy-dependent radial evolution of it, neither the superhalo component as it is out of the measuring energy range of the instrument. To model the core we use a 2D bi-Maxwellian function $f_c(v_\perp, v_\parallel)$ (see equation 1), and for the halo a 2D bi-Kappa function $f_h(v_\perp, v_\parallel)$ (see equation 2), the same model as used by Maksimovic et al. (2005):

$$A_c = n_c\left(\frac{m_e}{2\pi k_B}\right)^{3/2}\frac{1}{T_{c\perp}\sqrt{T_{c\parallel}}}$$
$$f_c(v_\perp, v_\parallel) = A_c \exp\left(-\frac{m_e}{2k_B}\left(\frac{(v_\perp-\Delta v_{c\perp})^2}{T_{c\perp}}+\frac{(v_\parallel-\Delta v_{c\parallel})^2}{T_{c\parallel}}\right)\right) \quad (1)$$

$$A_h = n_h\left(\frac{m_e}{\pi k_B(2\kappa-3)}\right)^{3/2}\frac{1}{T_{h\perp}\sqrt{T_{h\parallel}}}\frac{\Gamma(\kappa+1)}{\Gamma(\kappa-\frac{1}{2})}$$
$$f_h(v_\perp, v_\parallel) = A_h\left(1+\frac{m_e}{k_B(2\kappa-3)}\left(\frac{(v_\perp-\Delta v_{c\perp})^2}{T_{h\perp}}+\frac{(v_\parallel-\Delta v_{c\parallel})^2}{T_{h\parallel}}\right)\right)^{-\kappa-1} \quad (2)$$

In the above equations $v_\perp$ and $v_\parallel$ are the independent variables of functions f_c and f_h. With m_e we mark the mass of an electron, and with k_B the Boltzman constant. Quantities n, v, and T with indices c – core and h – halo, stand for the density, the velocity, and the temperature of the respective electron components. The drift velocity between the core and the halo is assumed to be 0, thus the values $\Delta v_{c\perp}$ and $\Delta v_{c\parallel}$ in equation (2) are the values obtained from the fit to the core population. We are left with nine fitting parameters: n_c, $\Delta v_{c\perp}$, $\Delta v_{c\parallel}$, $T_{c\perp}$, $T_{c\parallel}$, n_h, $T_{h\perp}$, $T_{h\parallel}$, and κ.

To isolate the strahl population the fit ($f_c + f_h$) is subtracted from the measured values. If the residual is a positive value higher than $0.9 \times (f_c + f_h)$ it is kept as a strahl VDF. The ratio 0.9 was chosen because it appears to correctly separate the core electron fit errors from the lowest strahl electron energies. We believe that a strahl component was detected, if the strahl VDF consists of at least five data points. In the opposite case we mark that the strahl was not observed.

We assume that the strahl is symmetric with respect to the magnetic field vector. As already said, these electrons are aligned with the magnetic field in the antisunward direction, so they can be detected by maximum four azimuth sectors, but commonly by only two of them. We enhance the angular resolution by averaging over consecutive scans, assuming that during the averaging time solar wind conditions do not change significantly. To make sure of that we only group up to 15 scans which belong to the same solar wind type (see Section 3.3) and satisfy the following arbitrary conditions: $\Delta v_p < 40\ \mathrm{km\,s^{-1}}$, $\Delta n_p < 15\ \mathrm{cm^{-3}}$, $\Delta B < 10$ nT, and $\Delta\Psi_B < 30^\circ$, where Δ stands for the difference between two consecutive scans following the equation: $\Delta X = |X_i - X_{i+1}|$. Index p stands for proton, ΔB is the variation of magnetic field amplitude, and $\Delta\Psi_B$ the variation of the magnetic field angle in the ecliptic plane. Fig. 2 shows an example result of this kind of averaging in velocity space.

In the example strahl VDF from the Helios 1 spacecraft (Fig. 2) we can still recognize the instrumental properties: the size of the azimuth sectors (28.1°) and energy bins. Even though the resolution is improved by averaging consecutive scans (with slightly different magnetic field vector direction), the smallest measurable angle stays fundamentally limited by the angular breadth of the azimuth sectors of I2 instruments (Helios 1: 28.1°, and Helios 2: 11.2°).

We study the width of strahl VDF, and a way to define it is using the full width at half-maximum parameter (FWHM), also used by e.g. Hammond et al. (1996) and Graham et al. (2017). We measure FWHM for each energy bin, by fitting the values of this bin with a normal distribution function, centred at angle 0° – the magnetic field direction:

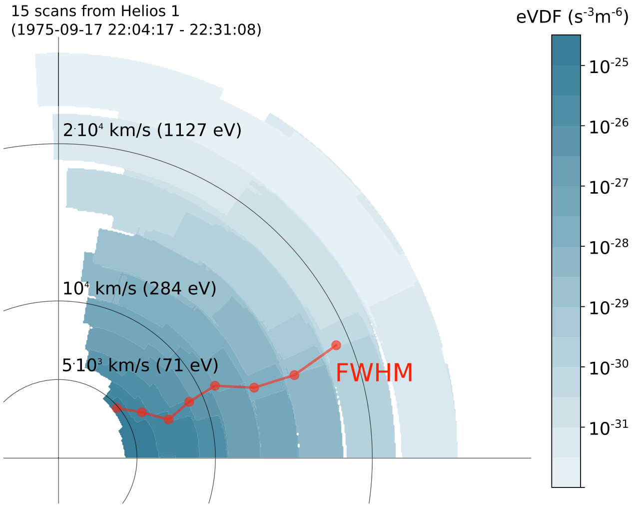

Figure 2. Strahl VDF in velocity space where *x*-axis presents velocity parallel to the magnetic field, and *y*-axis the perpendicular one. The instrumental properties like azimuth sector width and energy bin size are still distinguishable.

$$f(\mathrm{PA}) = a\exp\left(-\frac{1}{2}\left(\frac{\mathrm{PA}^2}{\sigma^2}\right)\right), \quad (3)$$

where a and σ are the fitting parameters and PA stands for pitch-angle, the angle from the magnetic field direction (see Fig. 2). This angle is defined in terms of parallel and perpendicular velocity as:

$$\mathrm{PA} = \tan^{-1}(v_\perp/v_\parallel). \quad (4)$$

FWHM is calculated from σ parameter using $\mathrm{FWHM} = 2\sqrt{2\ln 2}\times\sigma$, and is referred to as strahl PAW.

3.3 Binning

The solar wind is usually separated into fast, and slow wind according to its proton velocity. Another interesting separation was proposed in a recent work of Stansby et al. (2018), where the solar wind is separated into three types: slow Alfv´enic, slow non-Alfv´enic, and fast Alfv´enic wind, by its measured proton anisotropy and cross helicity. Even though both of the mentioned separation techniques give the same main observational results of this article for the fast, and the slow solar wind, we find that it is better to separate the solar wind into types according to a parameter more closely related to the kinetic properties of the solar wind electrons. In the following sections the solar wind is separated according to core electron parallel beta value ($\beta_{ec\parallel}$), the ratio of plasma parallel pressure to magnetic pressure, defined as:

$$\beta_{ec\parallel} = \frac{2\mu_0 n_c k_B T_{c\parallel}}{B^2}, \quad (5)$$

where μ_0 is the permeability of free space, and B the magnitude of the measured magnetic field. We chose $\beta_{ec\parallel}$ as a separation parameter because it spans over a large range of more than two magnitudes, but does not exhibit a radial dependency. This is not true for the halo electron parallel beta ($\beta_{eh\parallel}$), which is observed to increase with the radial distance (see Fig. 6b). We define three solar wind types: low-$\beta_{ec\parallel}$ wind ($\beta_{ec\parallel} < 0.2$), intermediate-$\beta_{ec\parallel}$ wind ($0.2 < \beta_{ec\parallel} < 0.4$), and high-$\beta_{ec\parallel}$ wind ($\beta_{ec\parallel} > 0.4$). The arbitrary chosen separation values are marked in an electron anisotropy-$\beta_{ec\parallel}$ parameter space in Fig. 6(a) with red dashed lines.

How our solar wind separation compares to the solar wind proton velocity and anisotropy (Matteini et al. 2007) is shown with histograms in Fig. 3. The low-$\beta_{\mathrm{ec}\parallel}$ wind corresponds to the faster solar wind with higher proton anisotropy averaging to $a_{\mathrm{p}} = 2.4$, while the high-$\beta_{\mathrm{ec}\parallel}$ wind represents the slow almost isotropic solar wind.

The data set is naturally binned in energy by instrumental energy bins, and additionally according to the distance from the Sun into seven equally spaced bins. A mean value of the strahl pitch angle width with its standard error is assigned to each bin.

Starting from 231 778 scans with the magnetic field vector close to the ecliptic plane, 51 570 were successfully fitted with models for core and halo components and matched with the solar wind proton data. Of these 14 052 (27 per cent) were identified as the low, 15 060 (29 per cent) as the intermediate, and 22 263 (44 per cent) as the high-$\beta_{\mathrm{ec}\parallel}$ solar wind. The mean velocity of the low-$\beta_{\mathrm{ec}\parallel}$ wind is 528 $\mathrm{km\,s^{-1}}$, the intermediate 459 $\mathrm{km\,s^{-1}}$, and the high-$\beta_{\mathrm{ec}\parallel}$ wind 377 $\mathrm{km\,s^{-1}}$. Strahl was not observed in 4359 examples. This means that strahl was absent in 8.5 per cent of our observations with a mean velocity, and a standard deviation of 441 and 105 $\mathrm{km\,s^{-1}}$. This is much less than ~20 per cent observed by Gurgiolo & Goldstein (2017) or 25 per cent by Anderson et al. (2012). This difference might be due to the fact that most of our measurements were taken within 1 au, while both of the mentioned studies are based on the analysis of the data from 1 au, which is consistent with the gradual disappearance of strahl with radial distance (Maksimovic et al. 2005; Štverák et al. 2009; Graham et al. 2017).

It is important to note that the number of the fast solar wind samples is decreasing with radial distance. This is because our data set, and analysis are limited for low plasma densities. The proton measurement is less accurate for low proton densities, therefore making our estimation of the spacecraft potential more inaccurate, which deforms the electron VDF and results in an unsuccessful fit.

Another instrumental limitation could be the time needed to obtain one 2D VDF scan. We checked how much the magnetic field angle varies during the sampling time (16 s), and found no correlation between broader strahls and the variation of magnetic field angle. The standard deviation varies between 1.5° and 5.5°, where larger values were found in the low-$\beta_{\mathrm{ec}\parallel}$ solar wind.

4 OBSERVATIONS

Different properties of strahl electrons were found for the low-, intermediate-, and the high-$\beta_{\mathrm{ec}\parallel}$ wind. For each of them, Fig. 4 shows how strahl PAW varies with electron energy. The differently coloured lines represent different distances from the Sun. We focus on the low-, and the high-$\beta_{\mathrm{ec}\parallel}$ type, as the intermediate possesses the properties of both of them.

The strahl component in the low-$\beta_{\mathrm{ec}\parallel}$ wind, which can be related to the fast solar wind, appears narrower than in the high-$\beta_{\mathrm{ec}\parallel}$ case. The PAW properties depend on the electron energy. For the lower energies, up to 343 eV the PAW is decreasing with electron energy. The PAWs vary very little between 0.34 and 0.74 au, however, a slight decrease with radial distance is observed in this low electron energy range. The PAW seems to saturate just below 40°, which is an effect of a limited angular resolution of the electron instrument I2.

Interestingly, for the electron energies above the 499 eV bin strahl PAW increases with electron energy and the distance from the Sun.

Strahl electrons in the high-$\beta_{\mathrm{ec}\parallel}$ wind appear more than 20° wider than in the low-$\beta_{\mathrm{ec}\parallel}$ wind already at 0.34 au. An anticorrelation between PAW and electron energy can be observed. Moving away from the Sun, the strahl is becoming broader and less correlated with electron energy. At the distance of 0.94 au from the Sun PAW is no longer correlated with the energy and reaches values above 100°.

5 DISCUSSION

5.1 Low-$\beta_{\mathrm{ec}\parallel}$ solar wind

We observe that the strahl electrons in the low-$\beta_{\mathrm{ec}\parallel}$ solar wind exhibit different trends depending on their energy. In the low-energy part observations of strahl electrons for the first time show a slight decrease in the strahl PAW with the radial distance. All the existing observational studies of the evolution of strahl PAW with distance (Hammond et al. 1996; Graham et al. 2017, 2018) show a broadening of the strahl during expansion, however, none of them samples the radial distances below 0.8 au, where the focusing was found in this work. Thus, the decrease of PAW with distance is particular for the low-$\beta_{\mathrm{ec}\parallel}$ solar wind, and for the regions closer to the Sun (down to 0.3 au).

As mentioned in the introduction, the strahl electrons are the electrons which at some distance close to the Sun escape the dense corona dominated by collisions, and during their escape undergo the focusing effect induced by the radially decreasing magnetic field. We present a simple collisionless focusing model, often used in the exospheric models (e.g. Maksimovic, Pierrard & Lemaire 1997b), to understand what would be the shape of the electron strahl originating from an isotropic function close to the Sun at the point of our first observations, at 0.34 au. We assume that at a given point an isotropic distribution function starts to focus conserving the electron energy and the magnetic moment:

$$\frac{m_{\mathrm{e}}}{2}(v_{\perp}^{2} + v_{\parallel}^{2}) - e\Phi = \mathrm{const.} \qquad \text{and} \qquad \frac{m_{\mathrm{e}} v_{\perp}^{2}}{2B} = \mathrm{const.} \tag{6}$$

In equations e stands for elementary charge, and Φ for the electrostatic ambipolar potential in the solar wind, with $\Phi = 0$ at infinity. We now write these equations indexing quantities at the focusing starting point with 0, and at the distance of our first observation (0.34 au) with 1. The strahl PAW of the isotropic distribution function at the focusing starting point is described with the PAW of 180°, thus the parallel velocity ($v_{\parallel 0}$) equal to 0.

$$\frac{m_{\mathrm{e}}}{2} v_{\perp 0}^{2} - e\Phi_{0} = \frac{m_{\mathrm{e}}}{2} v_{\parallel 1}^{2} + \frac{m_{\mathrm{e}}}{2} v_{\perp 1}^{2} - e\Phi_{1}, \tag{7}$$

$$\frac{m_{\mathrm{e}} v_{\perp 0}^{2}}{2B_{0}} = \frac{m_{\mathrm{e}} v_{\perp 1}^{2}}{2B_{1}}. \tag{8}$$

From equations 7 and 8 we obtain expressions for parallel and perpendicular velocities at the observation point,

$$v_{\parallel 1}^{2} = v_{\perp 0}^{2}\left(1 - \frac{B_{1}}{B_{0}}\right) + \frac{2e}{m_{\mathrm{e}}}\Delta\Phi \tag{9}$$

$$v_{\perp 1}^{2} = v_{\perp 0}^{2}\frac{B_{1}}{B_{0}}, \tag{10}$$

where $\Delta\Phi = \Phi_{1} - \Phi_{0}$ is the difference in electrical potential between the observation and the starting point. To compare the model directly to our observations in Fig. 4 we would like to express the model PAW in terms of electron energy (E):

$$E = \frac{m_{\mathrm{e}}}{2} v_{\perp 0}^{2} + e\Delta\Phi. \tag{11}$$

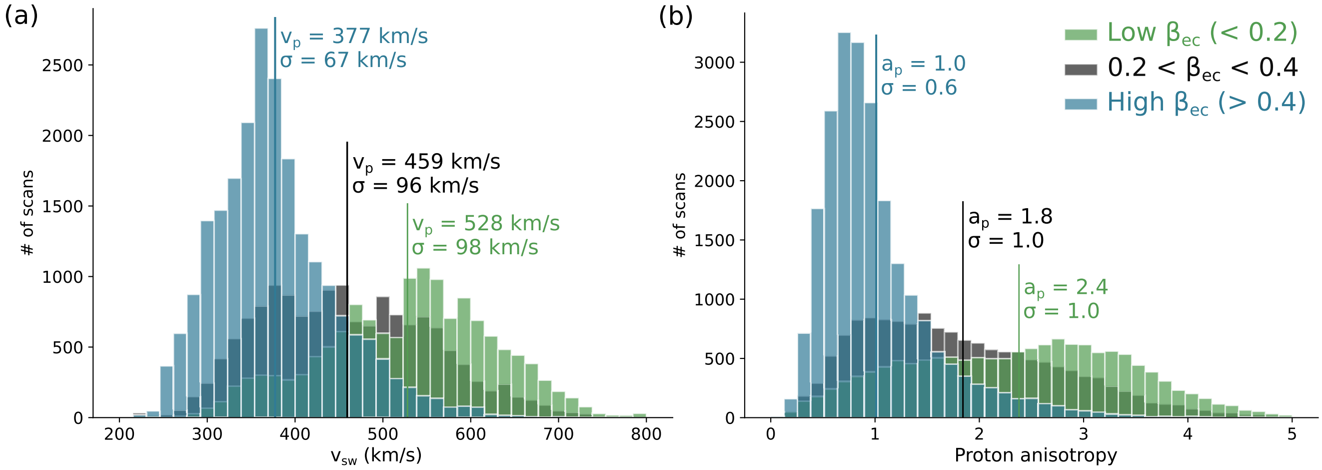

Figure 3. Histograms showing how the three solar wind types according to $\beta_{ec\parallel}$ relate to the solar wind velocity – (a), and proton core anisotropy – (b). The mean values with the standard deviations for each type are marked in both plots.

Using equation (11) we can rewrite the expressions for the parallel and the perpendicular velocity (equations 9 and 10) as:

$$\frac{m_e}{2}v_{\parallel 1}^2 = E - \frac{B_1}{B_0}\Big(E - e\Delta\Phi\Big) \qquad (12)$$

$$\frac{m_e}{2}v_{\perp 1}^2 = \frac{B_1}{B_0}\Big(E - e\Delta\Phi\Big). \qquad (13)$$

Combining equations (12) and (13), we obtain an expression for the strahl PAW of the model distribution at r_1, which we denote as PAW$_{cf}(E)$:

$$\mathrm{PAW}_{cf}(E) = 2\,\tan^{-1}\left(\frac{v_{\perp 1}}{v_{\parallel 1}}\right) = 2\,\tan^{-1}\left(\sqrt{\frac{E - e\Delta\Phi}{\frac{B_0}{B_1}E - E + e\Delta\Phi}}\right). \qquad (14)$$

We find that PAW$_{cf}$ is a decreasing function of energy if the magnetic field strength, and the electric potential are decreasing with the distance from the Sun. This is normally true in the solar wind. We calculate the PAW$_{cf}$ for a simplified case where we assume that magnetic field strength changes with r^2 and use the electric potential values from a transonic collisionless model of the solar wind by Zouganelis et al. (2004).[2] The value r_0, the focusing starting point, is set to 4 solar radii, following Maksimovic et al. (1997a), who find that in their kinetic model of the solar wind with Kappa distribution functions the exobase is located between 2.8 and 10.2 solar radii, where the distance 4 solar radii corresponds to typical equatorial region solar wind conditions. This solution shown with a black line in Fig. 4(a) gives a strahl component which is about half the width of the strahl observed for low energies at 0.34 au.

Still assuming that the magnetic field strength decreases with r^2, we fit the model to the PAWs observed for the lowest two energies at 0.34 au (the dashed red line in Fig. 4a). To recover the observed strahl width the focusing of the solar wind electrons needs to start further away from the Sun, at the distance of $r_0 = 8.4\,R_S$, which is still in the range discussed by Maksimovic et al. (1997a). The potential difference obtained from the fit ($\Delta\Phi = -1171$ V) is very close to the one taken for the same r_0 from the model of Zouganelis et al. (2004).[3] For comparison the strahl PAW solution according to the model of Zouganelis et al. (2004) for $r_0 = 8.4$ is plotted in Fig. 4(a) with a red solid line.

We conclude that the strahl PAWs observed for the low electron energies close to the Sun could be a result of collisionless focusing of the solar wind electrons during expansion. The shape of the observed strahl distribution function at 0.34 au corresponds well to the shape predicted by a collisionless focusing model with parameters in the range of the ones reported for the solar wind.

Even though a slight focusing over radial distance is observed for the low energies of the low-$\beta_{ec\parallel}$, the PAW decrease is not strong enough to follow collisionless focusing described by equation (6). We consider collisions as a possible strahl scattering mechanism in this low strahl electron energy range. In the future we plan to use a fully kinetic solar wind simulation (Landi et al. 2012; Landi, Matteini & Pantellini 2014) to explore the limiting energy at which the Coulomb collisions are still able to effect the electron VDF. However, the lowest strahl energy presented in this article, 68 eV, already equals to more than three times the typical core electron thermal energy, so collisions are expected to be very rare.

The positive correlation between strahl PAW and electron energy, observed for the more energetic strahl electrons in the low-$\beta_{ec\parallel}$ solar wind, was already reported in the study of Pagel et al. (2007). The authors analyse 29 events during times when extremely broad strahl was observed at 1 au. The mean solar wind velocity of these 29 events, 501 km s^{-1}, is comparable to the mean velocity of our low-$\beta_{ec\parallel}$ population, 528 km s^{-1}. From the relation between PAW and electron energy they conclude that the source of the scattering of the strahl electrons are most likely the quasi-parallel broadband whistler-mode waves generated by the magnetic field power spectrum in the whistler range. The cyclotron resonance of the faster electrons corresponds to smaller k-vectors, for which the magnetic field fluctuations are larger in the solar wind, providing stronger scattering of the higher energy electrons.

Supporting this hypothesis are the particle-in-cell simulations provided by Saito & Gary (2007), and a kinetic model in a framework of quasi-linear theory by Vocks et al. (2005). However, sunward-directed wave k-vectors parallel to the background

---

[2] The electrostatic potential values are taken from Fig. 1 for $\kappa = 2.5$, $r_0 = 4\,R_S$: $\Delta\Phi = -2165$V.

[3] For $\kappa = 2.5$, $r_0 = 8.4\,R_S$: $\Delta\Phi = -1008$V.

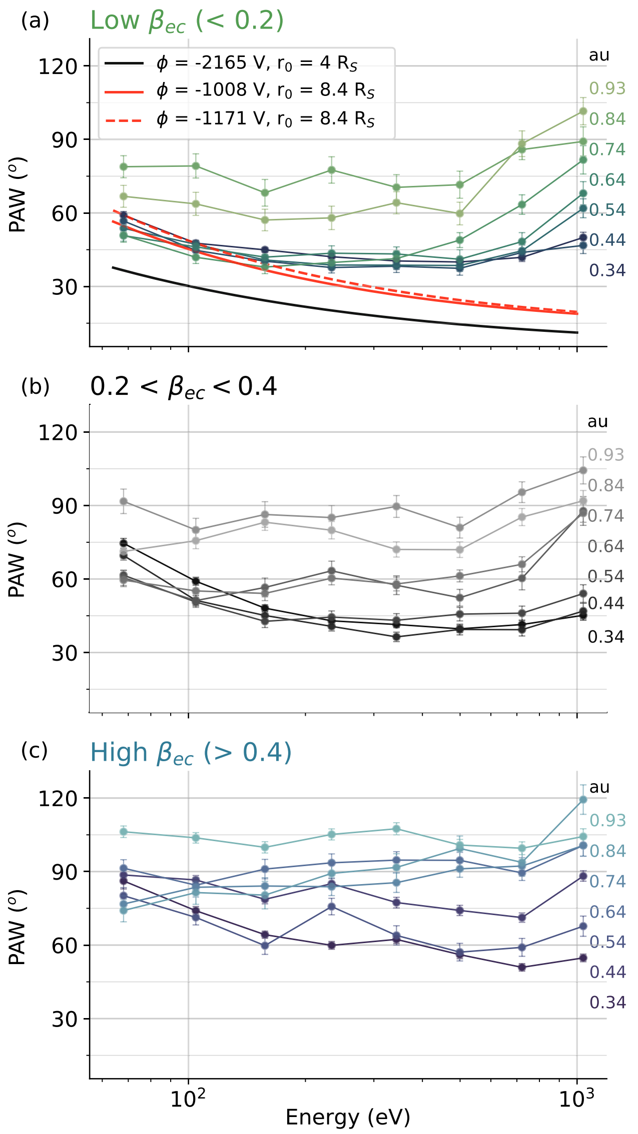

Figure 4. Strahl PAW versus electron energy shown separately for the low – (a), intermediate – (b), and high – (c) $\beta_{ec_{\parallel}}$ solar wind. The darker coloured lines denote distances closer, and lighter coloured lines distances farther from the Sun. In the upper plot a dashed red, a solid red, and a solid black line denote a curve resulting from a simple collisionless focusing model for three different parameter pairs (see Section 5.1).

magnetic field needed for whistlers to be able to resonate with antisunward moving electrons (Gary 1993) were observed to be rare at sub-ion scales. Moreover, Chen et al. (2010) observe the power in the parallel spectral component ($\delta B(k_{\shortparallel})^2$) to be only 5 per cent of the power in perpendicular one ($\delta B(k_{\perp})^2$). Another possibility is that the correlation between the strongly scattered faster strahl electrons and the magnetic field power spectrum results from a mechanism related to the perpendicular magnetic field fluctuations. An example of this kind of mechanism is stochastic heating studied for the case of solar wind protons by Chandran et al. (2013). To our knowledge no similar theory has been developed for electrons so far.

Variations in the magnetic field could affect the trajectories of the gyrating electrons if their gyroradius would be of the same scale as the changes in the magnetic field. Typically the gyroradius of the strahl electrons, directly proportional to their perpendicular velocity, spans between a few tenths and 30 km, larger radii corresponding to more energetic electrons. We can now again draw the correlation with the magnetic field power spectra: k-vectors are inversely proportional to the gyroradii, and the amplitude of the fluctuations in the solar wind, thus more energetic electrons are diffused by the stronger fluctuating magnetic field. It should be noted that this diffusion process has not yet been studied in detail, and is for now just a candidate to explain our observations.

To better quantify the observations presented in this article, a simple empirical model of the scattering of the strahl components is proposed. The mechanism at work has to first overcome the theoretically predicted focusing effect, and then further scatter strahl electrons. We estimate how strong the focusing is for each radial distance starting from the observed strahl at 0.34 au and applying the electron energy and magnetic moment conservation (see equation 6). As above, the electric potential values are taken from the work of Zouganelis et al. (2004). By adding to the observed strahl PAW the angle for which the strahl has been focused over a given radial distance we obtain the total-required-scattering PAW, used in Fig. 5. We only consider distances from 0.34 to 0.64 au from the Sun, as at larger distances the strahl PAWs do not appear to follow a continuous function anymore (see for example most right plot in Fig. 7a) and the measurements become less reliable due to the higher relative error on the measurement of the solar wind density. We can describe these PAWs with a perpendicular scattering process, in which electrons are scattered across the magnetic field as a function of their parallel velocity ($v_{\shortparallel}$) with an empirical exponential form:

$$v_\perp(v_\parallel) = c_1 \cdot \exp\left[C \cdot v_\parallel\right], \tag{15}$$

where c_1 and C are the fitting parameters. This can be easily seen in Fig. 5(a), as the higher energy part of strahl PAWs observed at different radial distances form almost straight lines in linear-logarithmic scale space. We find that the first parameter, c_1, does not vary significantly with the radial distance and can be fixed to a value 1309.3 km s^{-1}. The latter parameter, C, depends on the distance from the Sun as shown in Fig. 5(b). We can write C, and consequentially $v_\perp$ as

$$C(\Delta r) = c_2 + c_3 \cdot \Delta r \quad \text{and} \quad \Delta r = r - 0.34\text{au}, \tag{16}$$

$$v_\perp(v_\parallel, \Delta r) = c_1 \cdot \exp\left[(c_2 + c_3 \cdot \Delta r) \cdot v_\parallel\right]. \tag{17}$$

r stands for the distance from the Sun for each of the observations. Note that this type of scattering does not necessarily conserve the particle total energy. As electrons are scattered in perpendicular direction they can take the energy from the scattering source (i.e. ambient electromagnetic waves, or background turbulence), and if that is the case, their parallel velocity can remain unchanged.

The values of fitting parameters are noted in Table 1.

An exponential relation between $v_\perp$ and $v_{\shortparallel}$ is in a case when $v_{\shortparallel}$ does not vary with distance (the total particle energy is not conserved) a solution of the differential equation which can be written as:

$$\frac{1}{v_\perp}\frac{\mathrm{d}v_\perp}{\mathrm{d}r} = c_3 \cdot v_\parallel, \tag{18}$$

where the constant c_3 describes the scattering strength. We would like to emphasize that this model is solely empirical and is developed with the purpose to better understand the observations. Further studies of the scattering mechanisms are required to understand

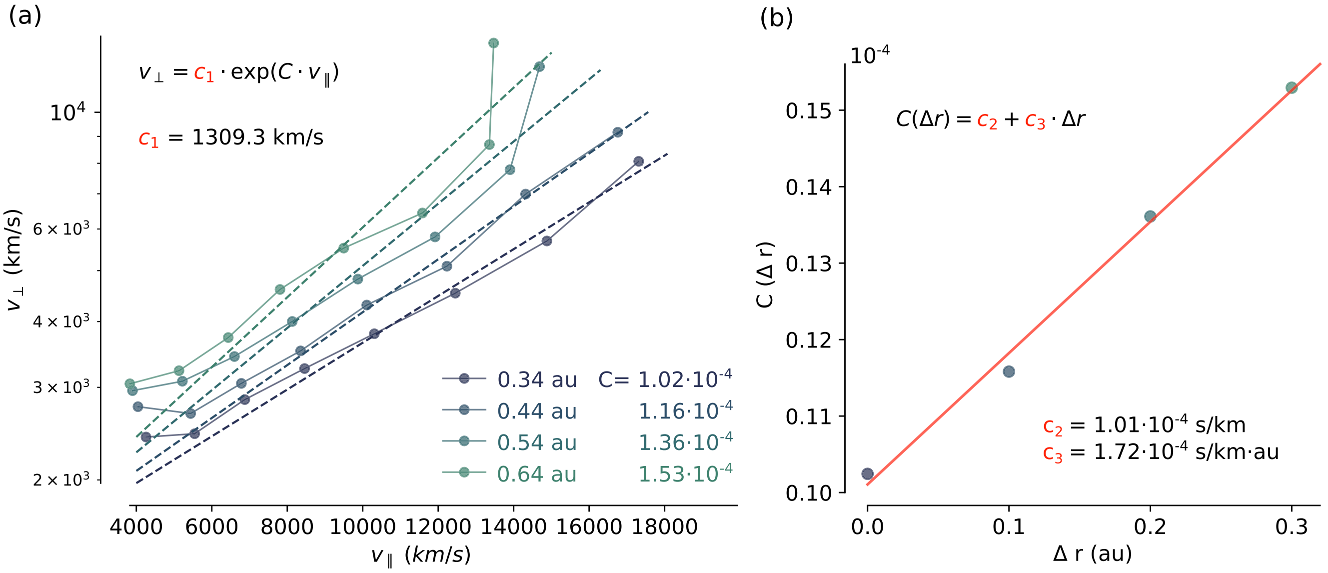

Figure 5. Comparison between the empirical model (dashed line), and observations for four closest distances from the Sun of low-$\beta_{ec_{\parallel}}$ solar wind (dots).

Table 1. Fitting parameters.

c_1	c_2	c_3
1309.3 km s^{-1}	1.01×10^{-4} s km^{-1}	1.72×10^{-4} s/(km au)

whether a physical phenomena (or a combination of them) can result in above described velocity-dependent scattering.

5.2 High-$\beta_{ec_{\parallel}}$ solar wind

For the high-$\beta_{ec_{\parallel}}$ solar wind with the mean velocity of 377 km s^{-1}, scattering of the strahl electrons appears to be extremely efficient over the whole electron energy range. In the work of Gurgiolo & Goldstein (2017) the authors show that 20 per cent of the observed solar wind at 1 au with velocities below 425 km s^{-1} appears without the strahl electron component, and pose the question whether this is a consequence of the strahl origin, or of some transit mechanisms acting upon it during its expansion. Our radial-dependent observations confirm the latter: during the radial evolution, the strahl broadens until the point when it is completely scattered into the halo component. Electron VDFs without the strahl were mainly observed in the high-$\beta_{ec_{\parallel}}$ solar wind at larger distances from the Sun.

A reason for this efficient scattering might lay in the $\beta_{ec_{\parallel}}$ parameter itself. This dense population of the solar wind electrons takes up a region of the $\beta_{ec_{\parallel}}$-anisotropy parameter space constrained by instabilities, e.g. whistler, or firehose instability (given in Fig. 6).

A direct correlation between narrow-band whistler activity and the broadening of the strahl was presented by Kajdič et al. (2016). On the basis of statistical study of the slow solar wind (the velocity is below 400 km s^{-1} for most of the samples) at 1 au they conclude that anticorrelation between the PAW and electron energy is broken in the presence of narrow-band whistler-mode waves which scatter a portion of strahl VDF. Note that in this work the direction of the detected whistler waves could not be inferred. The broadening is energy dependent, spanning from 5° to 28° [4] influencing electrons with energies between 250 and 600 eV. In our data set decrease of the PAW with energy was not observed close to 1 au, but very similar tendencies were found in the slow solar wind closer to the Sun: PAW decrease with electron energy, and broader strahl for energies between 200 and 500 eV. The source of these whistles, however, is not discussed in the above cited work.

Properties of whistler-mode waves observed in near-Earth regions were studied by Lacombe et al. (2014). Authors believe that whistlers are most likely generated by the whistler heat flux instability, as they were found at times when electron distributions were close to this instability threshold. Their observations show that electron temperature anisotropy ($T_\perp/T_\parallel$, taken as moments of a total VDF) is most of the time below unity, therefore excluding a possibility that whistlers are created by the whistler anisotropy instability.

However, our obtained anisotropies separately for core and halo components, plotted against the whistler and firehose instability conditions, which were calculated for an electron VDF consisting of maxwellian core and a kappa halo (Lazar et al. 2018) give the impression that both instabilities, limiting high $\beta_{ec_{\parallel}}$ values could play a role in the generation of whistler-mode waves (see Figs 6 a – core, and b – halo).

Whistler-mode waves generated by the heat-flux instability have a preferred propagation direction in the direction of the positive heat flux (Gary et al. 1975). Thus, this kind of waves will propagate away from the Sun, and will not be able to interact with strahl electrons. An observational study by Stansby et al. (2016) indeed shows that 98 per cent of the measured whistlers propagate in the antisunward direction. Anyhow, the generation of whistlers itself could change the shape of the strahl VDF. With a tendency towards a more stable, isotropic state, the strahl electrons' parallel velocities will decrease while their perpendicular velocities will increase.

---

[4] These values were converted to FWHM for consistency. Strahl PAW in the analysis by Kajdič et al. (2016) is defined as standard deviation, σ, and FWHM $= 2\sqrt{2\ln 2} \times \sigma$.

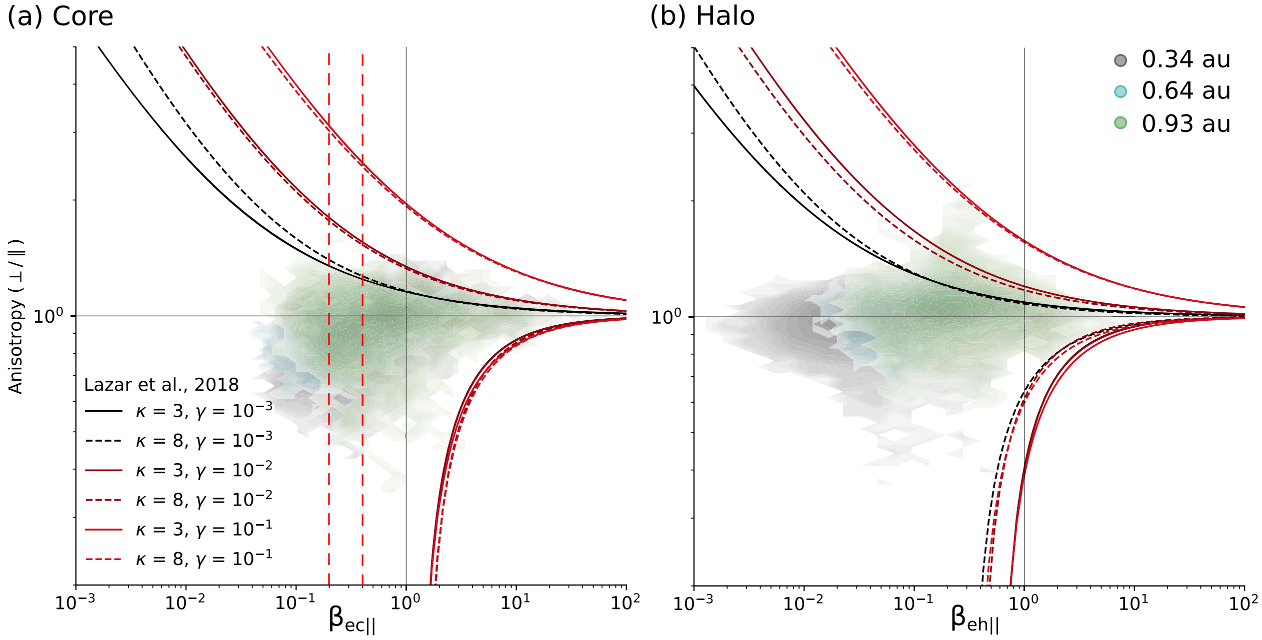

Figure 6. A contour plot showing radial evolution of core – (a) and halo – (b) electrons in anisotropy-beta parameter space. The three colours denote measurements taken within three different 0.1 au wide radial bins centred on the values given in the plot. The blue lines present the whistler instability ($a_e > 1$), and firehose instability ($a_e < 1$) maximum growth rate curves obtained by Lazar et al. (2018). The two red dashed lines show the arbitrary chosen $\beta_{\mathrm{ec}\parallel}$ values separating solar wind into three types.

Symmetric whistlers, parallel and antiparallel to the magnetic field direction, can theoretically develop from the whistler anisotropy instability (e.g. of a symmetric halo component), and sunward-directed portion of them could resonate with strahl electrons, enhancing their perpendicular velocities. A numerical simulation of this mechanism (Saito & Gary 2007) predicts a scattered strahl with a negative correlation between PAW and electron energy, as observed closer to the Sun in this work, and at 1 au by Kajdič et al. (2016). However, as mentioned in the previous paragraph, this is in contradiction with the observations showing that sunward-directed whistlers are extremely rare at 1 au (Stansby et al. 2016).

An alternative scattering source to whistler waves are self-generated Langmuir waves discussed by Pavan et al. (2013). Using numerical simulations the authors show that Langmuir waves can contribute to the widening of the strahl component resulting in an anticorrelation between PAW and energy, however, the velocities at which the diffusion is effective only reach up to two times the thermal speed of electrons. The directly observed scattering of the strahl electrons into the halo reported by Gurgiolo et al. (2012) appears at similar energy scales. In this last work the proposed source of scattering are the highly oblique kinetic Alfv´en fluctuations, which can widen the strahl through Landau damping. These two scattering mechanisms both take place at lower energies and could be effective up to ~100 eV.

5.3 Estimations of strahl pitch-angle width closer to the Sun

The radial evolution of the strahl is shown in Fig. 7 in velocity space, separately for each solar wind type. The green and blue colours present observations at different distances from the Sun (marked at the bottom), however the leftmost plots marked with a radial distance of 0.16 au are estimated from the observations. For the low-$\beta_{\mathrm{ec}\parallel}$ solar wind an empirical relation between parallel and perpendicular strahl electron velocity (developed in the Section 5.1) was used to estimate the strahl PAW closer to the Sun, while for the high-$\beta_{\mathrm{ec}\parallel}$ solar wind the PAW values are linearly extrapolated from the observations. Linear, the simplest, extrapolation technique is used because no model has been developed for the high-$\beta_{\mathrm{ec}\parallel}$ solar wind.

With red colour we present how efficient is the collisionless focusing effect starting from the observation at 0.34 au. This is the same focusing model as used in Section 5.1 and Fig. 5 taking the electrostatic potential values from the work by Zouganelis et al. (2004).

We choose to extrapolate our observations to the distance of 0.16 au as this will be the first perihelion of the Parker Solar Probe (Fox et al. 2016). We believe that the strahl electrons will be observed narrower than at 0.34 au in the high-$\beta_{\mathrm{ec}\parallel}$, as well as for the energies above ~200 eV in the low-$\beta_{\mathrm{ec}\parallel}$ solar wind. Using the empirical model for the low-$\beta_{\mathrm{ec}\parallel}$ solar wind we predict that the positive correlation between the strahl PAW and electron energy will no longer be present at 0.16 au, in fact, the strahl PAW will become almost independent on the electron energy with a mean value of ~29° (leftmost plot of Fig. 7a). Considering the limitation of the I2 instrument in measuring small PAs (minimal angular width ~28°), we believe this will be the upper limit for the strahl PAW observed at 0.16 au. We expect the high-$\beta_{\mathrm{ec}\parallel}$ solar wind strahl to be broader, between 37° and 65° (see leftmost plot of Fig. 7b).

The low-energy strahl electrons (bellow ~200 eV) in the low-$\beta_{\mathrm{ec}\parallel}$ solar wind are observed to focus slightly during expansion already between 0.34 and 0.74 au, and we believe that the focusing effect will be observed, and even stronger at 0.16 au. The shape of the strahl component will coincide with the collisionless focusing model shown in Fig. 4(a). Closer to the Sun, during the upcoming perihelions, we should be able to observe the shifting point between

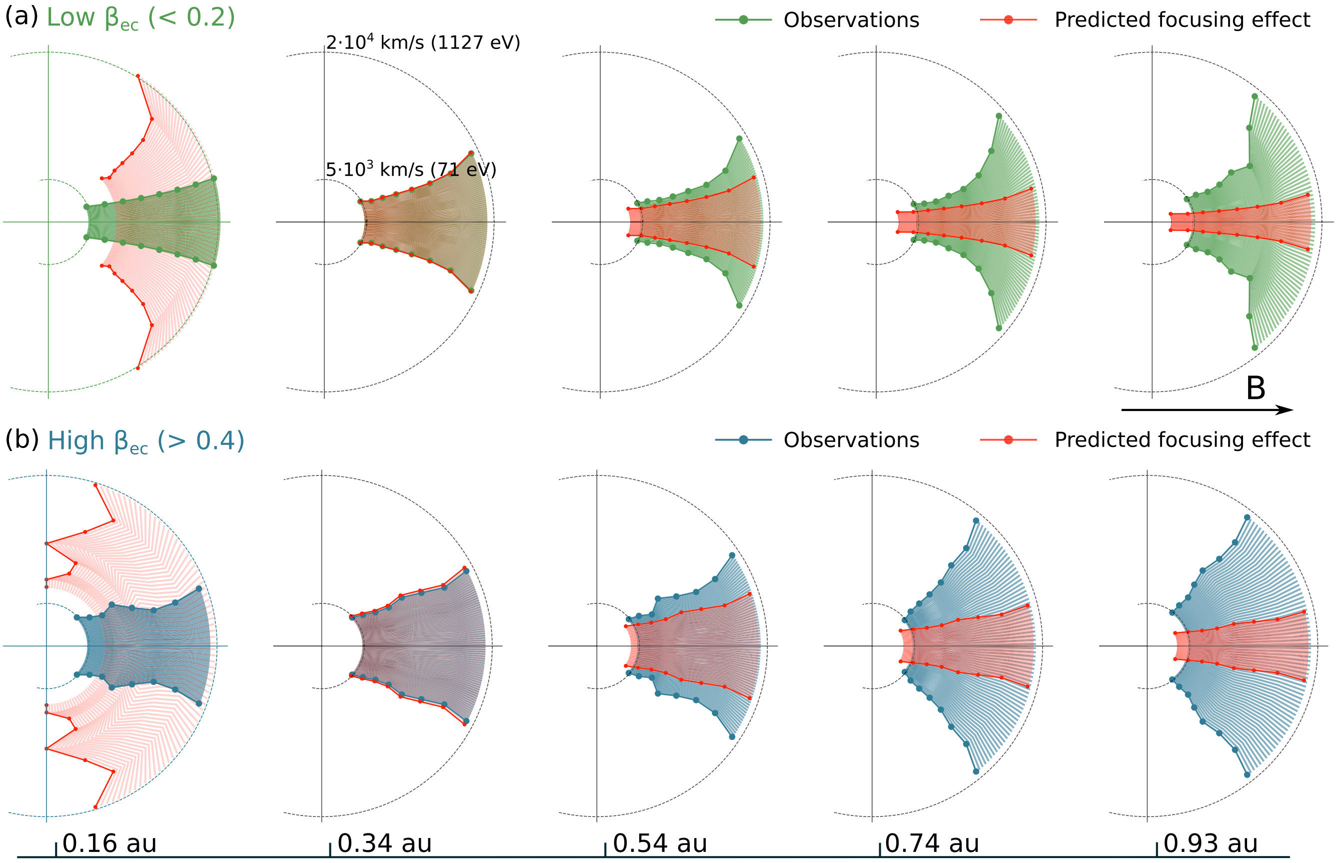

Figure 7. Radial evolution of the electron strahl component in velocity space for the low – (a), and the high – (b) -$\beta_{ec\parallel}$ solar wind. The radial position of each plot is marked on the bottom of the figure. The leftmost plot, marked with a distance of 0.16 au is an estimation, in (a) obtained from the empirical model developed above, and in (b) a linear extrapolation of the observations. In red we show the shape of the strahl component resulting only from collisionless focusing.

focusing and scattering with radial distance for the higher electron energies as well.

6 CONCLUSIONS

An observational study of the electron strahl width in the inner Solar system reveals different behaviour of the strahl depending on the value of the electron core beta ($\beta_{ec\parallel}$) in the solar wind.

Strahl electrons appear narrower in the low-$\beta_{ec\parallel}$ – faster, and more tenuous – solar wind, and their behaviour is closely related to their energy. The slower strahl electrons experience anticorrelation between PAW and their energy, and a slight focusing over radial distance for distances up to 0.74 au. Comparing the observations to a simple collisionless focusing model, we find that the strahl observed at 0.34 au for the lower energies could result from the collisionless focusing. Model parameters, r_0 and $\Delta\Phi$, found from fitting the data are very close to the ones reported for the solar wind.

More energetic strahl electrons show a correlation between the strahl PAW and their energy, for which we develop a simple empirical model. We observe that the increase of the electron $v_\perp$ is exponentially related to the electron $v_\parallel$ and the change in radial distance Δr. Further studies are required to understand which phenomena could scatter strahl electrons in this particular way described with equation (18).

Strahl electrons in the high-$\beta_{ec\parallel}$ solar wind are effectively scattered over their whole energy range. From an anticorrelation between the PAW and electron energy at 0.34 au, the strahl gets scattered to PAs above 100° close to the orbit of the Earth, many times disappearing completely from the electron VDF. We believe that this efficient scattering is a consequence of high-$\beta_{ec\parallel}$ solar wind being more unstable with respect to the kinetic instabilities. We show that the core and the halo components for the high-$\beta_{ec\parallel}$ solar wind sometimes appear close to the whistler anisotropy instability, giving way to the generation of sunward-propagating whistlers, which can resonate and scatter the strahl electrons.

For now the available *in situ* observations only reach down to 0.3 au, but to globally understand the interplay between collisions close to the Sun, and then focusing and scattering of the strahl electrons along their expansion, we need to probe the regions even below the mentioned distance from the Sun. Therefore, a combination of numerical solar wind simulations and the soon available Parker Solar Probe data might be the key to a better understanding of the kinetic properties of the solar wind electrons. In the scope of this article we used the available observations to estimate the strahl PAW at 0.16 au, a distance of the first Parker Solar Probe perihelion. Obtained results point to the fading of the correlation between the strahl PAW and electron energy, with the PAWs in the low-$\beta_{ec\parallel}$ solar wind of ~29°, and in the high-$\beta_{ec\parallel}$ solar wind ranging between 37° and 65°.

ACKNOWLEDGEMENTS

We acknowledge all members of the Helios data archive team (http://helios-data.ssl.berkeley.edu/team-members/) to make the Helios data publicly available to the space physics community. We thank D. Stansby for making available the new Helios proton core data set (https://doi.org/10.5281/zenodo.891405). This work was supported by the Programme Nationale Soleil Terre of Centre National de la Recherche Scientifique (CNRS/INSU).

All the analysis was done, and the plots produced using open source PYTHON libraries NUMPY, MATPLOTLIB, PANDAS, and SCIPY.

We are grateful for the reviewers comments which were constructive and helped to improve the quality of this work.

REFERENCES

Anderson B. R., Skoug R. M., Steinberg J. T., McComas D. J., 2012, J. Geophys. Res., 117, A04107

Chandran B. D. G., Verscharen D., Quataert E., Kasper J. C., Isenberg P. A., Bourouaine S., 2013, ApJ, 776, 45

Chen C. H. K., Horbury T. S., Schekochihin A. A., Wicks R. T., Alexandrova O., Mitchell J., 2010, Phys. Rev. Lett., 104, 255002

Chen C. H. K., Boldyrev S., Xia Q., Perez J. C., 2013, ApJ, 1, 110

Feldman W. C., Asbridge J. R., Bame S. J., Montgomery M. D., Gary S. P., 1975, J. Geophys. Res., 80, 4181

Feldman W. C., Asbridge J. R., Bame S. J., Gosling J. T., Lemons D. S., 1978, J. Geophys. Res., 83, 5285

Fitzenreiter R. J., Ogilvie K. W., Chornay D. J., Keller J., 1998, Geophys. Res. Lett., 25, 249

Fox N. J. et al., 2016, Space Sci. Rev., 204, 7

Gary S. P., 1993, Theory of Space Plasma Microinstabilities. Cambridge Atmospheric and Space Science Series. Cambridge Univ. Press, Cambridge

Gary S. P., Feldman W. C., Forslund D. W., Montgomery M. D., 1975, Geophys. Res. Lett., 2, 79

Gosling J. T., Baker D. N., Bame S. J., Feldman W. C., Zwickl R. D., Smith E. J., 1987, J. Geophys. Res., 92, 8519

Graham G. A. et al., 2017, J. Geophys. Res., 122, 3858

Graham G. A., Rae I. J., Owen C. J., Walsh A. P., 2018, ApJ, 855, 40

Gurgiolo C., Goldstein M. L., 2017, Ann. Geophys., 35, 71

Gurgiolo C., Goldstein M. L., Vi nas A. F., Fazakerley A. N., 2012, Ann. Geophys., 30, 163

Hammond C. M., Feldman W. C., McComas D. J., Phillips J. L., Forsyth R. J., 1996, A&A, 316, 350

Hellinger P., Trávníček P. M., Decyk V. K., Schriver D., 2014, J. Geophys. Res., 119, 59

Horaites K., Boldyrev S., Medvedev M. V., 2019, MNRAS, 484, 2474

Kajdič P., Alexandrova O., Maksimovic M., Lacombe C., Fazakerley A. N., 2016, ApJ, 833, 172

Lacombe C., Alexandrova O., Matteini L., Santolík O., Cornilleau-Wehrlin N., Mangeney A., de Conchy Y., Maksimovic M., 2014, ApJ, 796, 5

Landi S., Matteini L., Pantellini F., 2012, ApJ, 760, 143

Landi S., Matteini L., Pantellini F., 2014, ApJ, 790, L12

Lazar M., Shaaban S. M., Fichtner H., Poedts S., 2018, Phys. Plasmas, 25, 22902

Lin R. P., 1998, Space Sci. Rev., 86, 61

Maksimovic M., Pierrard V., Riley P., 1997a, Geophys. Res. Lett., 24, 1151

Maksimovic M., Pierrard V., Lemaire J. F., 1997b, A&A, 324, 725

Maksimovic M. et al., 2005, J. Geophys. Res., 110, A09104

Matteini L., Landi S., Hellinger P., Pantellini F., Maksimovic M., Velli M., Goldstein B. E., Marsch E., 2007, Geophys. Res. Lett., 34, L20105

Pagel C., Gary S. P., de Koning C. A., Skoug R. M., Steinberg J. T., 2007, J. Geophys. Res., 112, A04103

Pavan J., Viñas A. F., Yoon P. H., Ziebell L. F., Gaelzer R., 2013, ApJ, 769, L30

Pedersen A. et al., 2008, J. Geophys. Res., 113, 1

Pierrard V., Maksimovic M., Lemaire J., 1999, J. Geophys. Res., 104, 17021

Pilipp W. G., Miggenrieder H., Montgomery M. D., Mühlhäuser K. H., Rosenbauer H., Schwenn R., 1987a, J. Geophys. Res., 92, 1075

Pilipp W. G., Miggenrieder H., Montgomery M. D., Mühlhäuser K. H., Rosenbauer H., Schwenn R., 1987b, J. Geophys. Res., 92, 1075

Porsche H., 1981, in Burke W. R., ed., HELIOS mission: Mission objectives, mission verification, selected results, vol. 164. Solar System and its Exploration

Rosenbauer H., Schwenn R., Miggenrieder H., Meyer B., Grünwaldt H., Mühlhäuser K. H., Pellkofer H., Wlofe J., 1981, Research report W 81-015: Luft - and space Weltraumforschung / Weltraumtechnologie

Saito S., Gary P. S., 2007, Geophys. Res. Lett., 34, 1

Salem C., Bosqued J.-M., Larson D., Mangeney A., Maksimovic M., Perche C., Lin R., Bougeret J.-L., 2001, jgr, 106, 21701

Salem C., Bale S. D., Maksimovic M., 2007, in Second Solar Orbiter Workshop. Solar Wind Electrons And Associated Heat Conduction In The Inner Heliosphere, 641, p. 9

Seough J., Nariyuki Y., Yoon P. H., Saito S., 2015, ApJ, 811, L7

Shevchenko V. I., Galinsky V. L., 2010, Nonlinear Process. Geophys., 17, 593

Stansby D., Horbury T. S., Chen C. H. K., Matteini L., 2016, ApJ, 829, L16

Stansby D., Salem C., Matteini L., Horbury T., 2018, Sol. Phys., 293, 155

Štverák Š., Maksimovic M., Trávníček P. M., Marsch E., Fazakerley A. N., Scime E. E., 2009, J. Geophys. Res., 114, 1

Vocks C., Salem C., Lin R. P., Mann G., 2005, ApJ, 627, 540

Wang L., Lin R. P., Salem C., Pulupa M., Larson D. E., Yoon P. H., Luhmann J. G., 2012, ApJ, 753, L23

Zouganelis I., Maksimovic M., Meyer-Vernet N., Lamy H., Issautier K., 2004, ApJ, 606, 542

This paper has been typeset from a TEX/LATEX file prepared by the author.

B

CORONAL ELECTRON TEMPERATURE INFERRED FROM THE STRAHL ELECTRONS IN THE INNER HELIOSPHERE: PARKER SOLAR PROBE AND HELIOS OBSERVATIONS

The Astrophysical Journal, 892:88 (14pp), 2020 April 1 https://doi.org/10.3847/1538-4357/ab7b7a

Coronal Electron Temperature Inferred from the Strahl Electrons in the Inner Heliosphere: *Parker Solar Probe* and *Helios* Observations

Laura Berčič[1,2], Davin Larson[3], Phyllis Whittlesey[3], Milan Maksimović[1], Samuel T. Badman[3], Simone Landi[2,4], Lorenzo Matteini[1], Stuart. D. Bale[3,5,6,7], John W. Bonnell[5], Anthony W. Case[8], Thierry Dudok de Wit[9], Keith Goetz[10], Peter R. Harvey[5], Justin C. Kasper[8,11], Kelly E. Korreck[8], Roberto Livi[3], Robert J. MacDowall[12], David M. Malaspina[13], Marc Pulupa[5], and Michael L. Stevens[8]

[1] LESIA, Observatoire de Paris, PSL Research University, CNRS, UPMC Université Paris 6, Université Paris-Diderot, Meudon, France; laura.bercic@obspm.fr
[2] Physics and Astronomy Department, University of Florence, Sesto Fiorentino, Italy
[3] Physics Department, University of California, Berkeley, CA, USA
[4] INAF—Osservatorio Astrofisico di Arcetri, Firenze, Italy
[5] Space Sciences Laboratory, University of California, Berkeley, CA 94720-7450, USA
[6] The Blackett Laboratory, Imperial College London, London, SW7 2AZ, UK
[7] School of Physics and Astronomy, Queen Mary University of London, London E1 4NS, UK
[8] Smithsonian Astrophysical Observatory, Cambridge, MA, USA
[9] LPC2E, CNRS and University of Orléans, Orléans, France
[10] School of Physics and Astronomy, University of Minnesota, Minneapolis, MN 55455, USA
[11] University of Michigan, Ann Arbor, MI, USA
[12] Solar System Exploration Division, NASA/Goddard Space Flight Center, Greenbelt, MD, 20771, USA
[13] Laboratory for Atmospheric and Space Physics, University of Colorado, Boulder, CO 80303, USA

Received 2020 January 27; revised 2020 February 24; accepted 2020 February 28; published 2020 April 1

Abstract

The shape of the electron velocity distribution function plays an important role in the dynamics of the solar wind acceleration. Electrons are normally modeled with three components, the core, the halo, and the strahl. We investigate how well the fast strahl electrons in the inner heliosphere preserve the information about the coronal electron temperature at their origin. We analyzed the data obtained by two missions, *Helios*, spanning the distances between 65 and 215 R_S, and *Parker Solar Probe* (*PSP*), reaching down to 35 R_S during its first two orbits around the Sun. The electron strahl was characterized with two parameters: pitch-angle width (PAW) and the strahl parallel temperature ($T_{s||}$). *PSP* observations confirm the already reported dependence of strahl PAW on core parallel plasma beta ($\beta_{ec||}$). Most of the strahl measured by *PSP* appear narrow with PAW reaching down to 30°. The portion of the strahl velocity distribution function aligned with the magnetic field is for the measured energy range well described by a Maxwellian distribution function. $T_{s||}$ was found to be anticorrelated with the solar wind velocity and independent of radial distance. These observations imply that $T_{s||}$ carries the information about the coronal electron temperature. The obtained values are in agreement with coronal temperatures measured using spectroscopy, and the inferred solar wind source regions during the first orbit of *PSP* agree with the predictions using a PFSS model.

Unified Astronomy Thesaurus concepts: Solar wind (1534); Solar physics (1476); Space plasmas (1544); Space vehicle instruments (1548); Astronomy data analysis (1858); Solar corona (1483); Solar atmosphere (1477)

1. Introduction

The solar wind is the constant flux of plasma that leaves the solar corona and expands in our solar system (Parker 1958). It consists of mostly electrons and protons, both exhibiting nonthermal velocity distribution function (VDF) features. Electrons are usually modeled by three components. The lower electron energies are dominated by the core, Maxwellian-like population taking up most of the total electron density. Electrons with higher energies are either part of the magnetic field–aligned strahl population or of the halo population present at all pitch angles (Feldman et al. 1975; Pilipp et al. 1987; Maksimovic et al. 2005; ŠtveráK et al. 2008; Štverák et al. 2009; Tao et al. 2016; Wilson et al. 2019a, 2019b; MacNeil et al. 2020). These models were based on the observations of the solar wind far from the Sun (the closest at 0.3 au), where the solar wind already propagates with a supersonic velocity and where most properties of the pristine coronal plasma have been changed. But how does the electron VDF look like in the solar corona? Does it exhibit high energy tails, or is the excess of the high-energy electrons observed in the interplanetary solar wind created during the expansion from purely Maxwellian coronal electrons?

Multicomponent distribution functions are used in the kinetic exospheric models of the solar wind initially assuming collisionless evaporation of the solar corona into interplanetary space (Jockers 1970; Lemaire & Scherer 1971). The acceleration of the solar wind in these models is provided by solar wind electrons. As their velocities are much higher than the velocities of protons with the same temperature in the solar corona, a portion of electrons manage to escape the Sun and create charge imbalance in the plasma. The imbalance gives rise to an anti-sunward-directed electric field, accelerating the heavier solar wind protons. This dynamics produces two main populations in electron VDF. Electrons with energies smaller than the electric potential energy needed to sustain the anti-sunward electric field are bounded to the Sun and present the dense thermal core population. The faster anti-sunward-directed electrons, which are able to overcome the potential, escape and form the strahl. The escaping strahl electrons are governed by the magnetic momentum ($\frac{m_e v_\perp^2}{2B} = \text{const.}$) and energy ($E_{\mathrm{kin}} + E_{\mathrm{pot}} = \mathrm{const.}$) conservation. As they expand into regions with a weaker magnetic field, they experience focusing (Schwartz & Marsch 1983).

Similarly, a two-component VDF was obtained by the exospheric models accounting for collisions with the Fokker–Planck equation solver using a test particle approach (Lie-Svendsen et al. 1997; Pierrard et al. 2001; Smith et al. 2012) and by the kinetic simulation of the solar wind accounting for Coulomb collisions statistically (Landi et al. 2012, 2014).

These models describe well the formation of the core and the strahl, but they do not explain the formation of the halo. It is possible that the halo is already present in the solar corona, consisting of hot electrons leaking from the dense coronal regions with closed magnetic field loops. Exospheric models assuming an excess of high-energy electrons in the corona were the first models able to self consistently produce fast solar wind reaching velocities above ∼700 km s^{-1} (Maksimovic et al. 1997a; Dorelli & Scudder 1999; Lamy et al. 2003; Zouganelis et al. 2004).

On the other hand, observations have shown that the relative density of the two high-energy electron populations exchanges as a function of radial distance. The strahl is more pronounced close to the Sun while the halo density increases over the radial distance (Štverák et al. 2009). This suggests that the halo is not present in the solar corona and is formed during the solar wind expansion from the strahl component.

The strahl and the halo populations, not sensitive to collisions, were early assumed to be the remnants of the hot coronal electrons in the solar wind (Feldman et al. 1975). The focusing mechanism experienced by the strahl during the expansion does not affect the shape of the magnetic field–aligned cut through the strahl VDF ($f_{s\|}$) nor the strahl parallel temperature ($T_{s\|}$). Therefore, the strahl, in the absence of collisions any other interactions, preserves the temperature and the shape of the VDF of the coronal electrons at its origin.

This is only valid in the kinetic models not including collisions or wave–particle interactions. The strahl electrons have been observed to not focus but scatter with radial distance (Hammond et al. 1996; Graham et al. 2017; Berčič et al. 2019) accounting this phenomena to some extent to Coulomb collisions (Horaites et al. 2018, 2019), but also to wave–particle interactions (Vocks et al. 2005; Kajdič et al. 2016) and scattering by the background turbulence (Pagel et al. 2007; Saito & Gary 2007). Graham et al. (2017) report that the strahl was rarely observed at distances higher than 5 au. The strahl and the halo electrons do interact with the surrounding plasma and electric and magnetic fields but on much larger spatial scales than the thermal, core electron component.

The core electron temperature was recently found to be correlated to the solar wind origin in the inner heliosphere; however, the correlation is almost completely lost by the time the solar wind reaches the distance of 1 au (Maksimovic et al. 2020).

Whether the high-energy electron components preserve information about the solar wind origin at the radial distance of 1 au has been tested through comparison to the oxygen charge-state ratio ($\mathrm{O}^{7+}/\mathrm{O}^{6+}$), an established proxy for measuring the coronal electron temperature. While Hefti et al. (1999) find a correlation between the $T_{s\|}$ and the oxygen charge-state ratio, MacNeil et al. (2017) find that the correlation is not very strong, and it varies depending on the choice of interval.

We aim to investigate whether the information about the solar wind origin is present at the closest distances sampled by in situ instruments so far: 35 R_S for the *Parker Solar Probe* (*PSP*) and 65 R_S for the *Helios* mission. As the oxygen charge-state ratio is not measured by these two space crafts, we use the solar wind velocity as an indicator of the solar wind origin.

2. Data Sets

2.1. Parker Solar Probe

Launched in 2018 August, *PSP* (Fox et al. 2016) is a mission designed to study the solar wind in the vicinity of the Sun, eventually reaching as close as 8.8 R_S from its surface. We analyze the data gathered during the first two orbits of *PSP* with the perihelion of 34.7 R_S and the aphelion between the orbits of Venus and Earth.

Electrons on board *PSP* are measured with two SPAN Electron (SPAN-E) electrostatic analyzers: SPAN-A and SPAN-B (Whittlesey et al. 2020), part of the SWEAP instrument suite (Kasper et al. 2016). Positioned on the ram and on the anti-ram side of the spacecraft with their 120° × 240° field of views (FOVs) 90° tilted with respect to each other, they cover almost a full 4π solid angle. The azimuth angle (ϕ) on each of the SPAN-Es is measured by eight small (6°) and eight large (24°) anodes, while the elevation (θ) angles are sampled by the electrostatic deflectors. During the first two encounters, deflectors separated the elevation measurements in eight angular bins with a resolution of 20°, of which the two extreme elevation bins have not been used in our analysis. The combined FOV of the two instruments is represented in Figure 1, where the gray surfaces represent solid angles that are not sampled by the instruments. To be able to withstand high levels of solar radiation, *PSP* is equipped with a heat shield. When the spacecraft is within 0.7 au from the Sun, the shield points straight to it and blocks approximately an angle of 10° from the Sun-spacecraft line (the center of the FOVs in Figure 1). Electron energy is measured by toroidal electrostatic analyzers, which are adapted to the high variation of electron fluxes with a mechanical attenuator controlling the size of the entrance to the aperture. Energies between 2 eV and 2 keV are sampled in 32 exponentially spaced bins with the energy resolution ($\Delta E/E$) of 0.07.

The duration of one sweep over all the energy and deflection bins is 0.218 s. The data product used for the presented data analysis are full 3D spectra (32 energies, 8 elevations, 16 azimuths) integrated over a period of 27.9 s during Encounter 1 (2018 October 29–November 14) and over a period of 14.0 s during Encounter 2 (2019 March 29–April 10). When the spacecraft is farther from the Sun (>60 R_S), the instruments are operating in cruise mode with the cadence of 895 s and integration period of 27.9 s.

Detailed descriptions of the SPAN-E instruments and their operating modes are provided by Whittlesey et al. (2020).

In addition to the electron measurements, we use the solar wind proton velocity and density moments calculated from the SPC instrument (Case et al. 2020) and a vector magnetic field measured by a triaxial fluxgate magnetometer MAG part of the FIELDS investigation (Bale et al. 2016). SPC is a Faraday cup instrument sticking out of the heat shield and measuring the plasma flowing directly from the Sun, also part of the SWEAP investigation (Kasper et al. 2016). The cadence of both, SPC and MAG, is higher than that of SPAN-E; thus, the averages

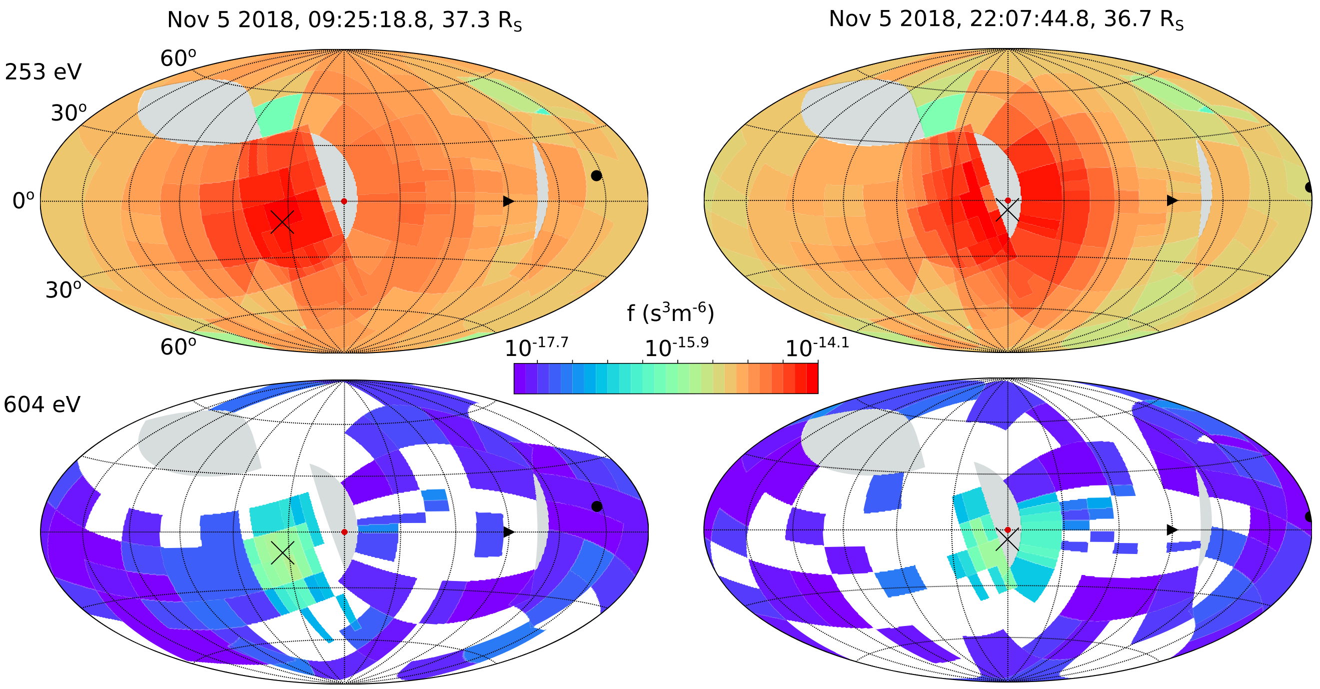

Figure 1. Combined SPAN-E FOVs showing two examples (columns) of a full angular scan for two energy bins (rows). The examples (left—November 5 2018, 9:25:18, right—22:07:44) were selected due to their different orientations of the magnetic field in the FOV. A color denotes the value of the VDF in each angular bin. The horizontal axis of FOVs is aligned with the spacecraft orbital plane. The Sun-spacecraft line is marked with the red dot and is in the middle of each plot. The vertical dimension thus shows angles out of orbital plane. The spacecraft is moving toward the black triangle, and the black dot and the black cross denote magnetic field positive and negative directions. The light gray areas represent the solid angles not sampled by the two instruments.

over the duration of each full SPAN spectra are used in further analysis.

2.2. Helios 1

The predecessors of the *PSP* are the two *Helios* missions launched in the 70 s (Porsche 1981). For more than 6 years, these two spacecraft were exploring the inner heliosphere down to 0.3 au (64 R_S) and providing us with a big data set of various solar wind parameters, among others revealing radial and solar cycle related trends (Feldman et al. 1975; Pilipp et al. 1987; Maksimovic et al. 2005; Marsch 2006; Štverák et al. 2009). These data were of great importance during the preparation for the *PSP* mission and stay important due to the large statistics and radial and time coverage. In this work, we use the data from *Helios 1* gathered between 1974 and 1980.

Electron VDFs on board the *Helios 1* mission are sampled by a single narrow 2° × 19° FOV aperture, which uses spacecraft spin to obtain a 2D measurement in the plane perpendicular to the spin axis. The sampled plane is aligned with the ecliptic plane. The 360° azimuth angle measurement is completed in 8 steps resulting in 28°.1 wide azimuth bins with gaps in between them (see schematics in Figure 4(a)). Energies between 9 eV and 1.5 keV are sampled in 16 exponentially spaced energy steps. The full 2D measurement (16 energies, 8 azimuths) is completed in 16 s with a cadence of 40 s.

The proton onboard integrated densities and velocity vectors were taken from the original *Helios* files in *Helios* data archive.[14]

The magnetic field vector is a composite measurement of two fluxgate magnetometers: E2 for all instances where measured magnetic field was less than 50 nT, and E3 for the rest. More details about the *Helios* data set and instrumentation can be found in our previous work with *Helios* observations (Berčič et al. 2019).

3. Method

3.1. Parker Solar Probe

The measured electron distribution functions are subject to instrumental as well as environmental effects. An important issue on the instrumental side is the determination of the sensitivities of each of the azimuth anodes. The sensitivity coefficients used for our analysis were obtained through in-flight calibration described in the work of Halekas et al. (2020). The effects of the spacecraft own magnetic field and electric charge on the particle trajectories were studied by McGinnis et al. (2019). They show that, even though the spacecraft magnetic field is relatively large (it was predicted to reach the strength of 500 nT), the effect on some of the plasma moments is small (see Table 2 in McGinnis et al. 2019). The biggest errors were found for the bulk velocity calculation, as it strongly depends on low-energy measurements. The smallest errors, on the other hand, arise for the temperature calculation, as it is more dependent on higher-energy measurements. The spacecraft potential was estimated to be low, on the order of a few Volts negative during the first two encounters. As our main focus in this article is the high-energy (strahl) electrons, we believe that our results are not affected significantly by these effects, which are more relevant for the low-energy electrons (Salem et al. 2001).

The instruments' lower-energy bins are contaminated by secondary electrons emitted from the spacecraft. Halekas et al. (2020) choose to include them in their fitting model as a Maxwellian distribution with a temperature of 3.5 eV. For the

---

[14] Link to the data archive: http://helios-data.ssl.berkeley.edu.

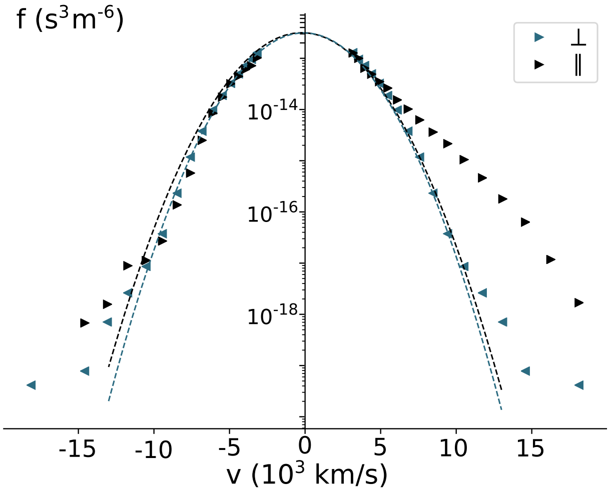

Figure 2. Parallel (∥) and perpendicular (⊥) cuts through an electron VDF measured by SPAN-E instruments on November 5 at 9:25:18 (the same example as on the left side of Figure 1). The positive velocity values for the parallel cut represent the part of the distribution aligned with the magnetic field and directed in the anti-sunward direction. The perpendicular values are the same on both sides of the plot, as there is no preferred direction perpendicular to magnetic field. The data points presented with rightward pointing triangles (>) were provided by SPAN-A, while the leftward pointing triangles (<) represent the points from SPAN-B instrument. The strahl electrons in this scan are detected by SPAN-A agreeing with the FOV representation in Figure 1.

purpose of our work, we find that it is sufficient to simply neglect the contaminated lower-energy measurements.

We start our analysis with a rotation of the SPAN-A and -B velocity vectors from their initial instrument frame to the common RTN (Radial-Tangential-Normal) coordinate frame. In this frame, the R-axis is aligned with the Sun-spacecraft line and pointing away from the Sun, the T-axis is perpendicular to the R-axis and pointing in the spacecraft ram direction, and the N-axis completes the right-handed frame. The spacecraft velocity and the solar wind proton velocity as measured by SPC are then subtracted to shift the VDFs in the plasma rest frame. After that, the magnetic field measurement averaged to the SPAN full scan duration is used to rotate the VDFs to the magnetic field–aligned frame.

Following the works of Maksimovic et al. (1997b), Štverák et al. (2009), and Berčič et al. (2019) the core electrons are modeled with a bi-Maxwellian distribution function

$$f_c(v_{\perp 1}, v_{\perp 2}, v_\parallel) = A_c \exp\left(\frac{(v_{\perp 1} - \Delta v_{\perp 1})^2}{w_\perp^2} + \frac{(v_{\perp 2} - \Delta v_{\perp 2})^2}{w_\perp^2} + \frac{(v_\parallel - \Delta v_\parallel)^2}{w_\parallel^2}\right) \quad (1)$$

where $\Delta v_{\perp 1,\perp 2,\parallel}$ are the drift velocities corresponding to three axes of the magnetic field–aligned frame. The fits were preformed on the full three-dimensional VDFs using a least-square minimization algorithm[15] provided by Scipy Optimization package for Python programming language (Virtanen et al. 2019). Because the VDF values span over several orders of magnitude (see Figure 2), the fitting was carried out in logarithmic space ($\ln(f_c)$). This technique decreases the large difference in the weight of fitted data points, giving more importance to the low VDF values. From our six fitting parameters—A_c, $w_\perp$, $w_\parallel$, and $\Delta v_{\perp 1,\perp 2,\parallel}$—we can obtain the core density n_c from:

$$n_c = A_c \cdot \pi^{3/2} w_\perp^2 w_\parallel. \quad (2)$$

The thermal speeds parallel ($w_\parallel$) and perpendicular ($w_\perp$) to the magnetic field can be expressed in terms of core temperature $T_{c\perp,\parallel}$:

$$T_{c\perp,\parallel} = \frac{m_e w_{\perp,\parallel}^2}{2k_B}, \quad (3)$$

where k_B is the Boltzman constant and m_e is the mass of an electron. The core density and parallel temperature are then used to calculate the electron parallel plasma beta parameter:

$$\beta_{ec\parallel} = \frac{2\mu_0 n_c k_B T_{c\parallel}}{B^2}, \quad (4)$$

with μ_0 standing for vacuum permeability and B for magnetic field.

An example of electron VDF measured on the November 5 is presented with the cuts through the parallel (∥) and the perpendicular (⊥) direction with respect to the magnetic field in Figure 2. We recognize the expected electron VDF features: a core fitted with a bi-Maxwellian distribution (dashed line in the Figure 2), a field–aligned strahl component only seen parallel to the magnetic field direction, and a weak halo departing from a Maxwellian fit at higher electron energies. Another feature we do not plan to discuss in the present work, already observed by Halekas et al. (2020), can be recognized in Figure 2. Directed toward the Sun (on the left side) and aligned with the magnetic field (dark blue), there appears to be a deficit in the core electron distribution—a part of phase space where the measured VDF appears to be smaller than the best-fitting Maxwellian distribution function.

Even though the two SPAN-E instruments cover almost a full solid angle, there exist cases when the electron VDFs are not fully characterized by the measurement. As introduced in Section 1, we investigate the behavior of the strahl electrons, a population aligned with the magnetic field and directed away from the Sun. The magnetic field closer to the Sun fluctuates around a vector more and is more aligned with the radial direction following the Parker spiral model (Parker 1958). This means that, often, the magnetic field measurement over one full SPAN-E scan duration will lie in the portion of the FOV where the solar wind electrons are blocked by the spacecraft heat shield (marked with gray in the center of the FOVs in Figure 1). A case when this happens is shown on the right side of Figure 1. At lower energies where the width of the strahl electron beam is larger (upper FOV: 253 eV), the effect of the FOV obstruction does not play a big role, while at high electron energies (lower FOV: 604 eV) where the strahl electron population often appears very narrow, we might be missing a big part of the strahl VDF. An opposite case, when the strahl is detected as accurately as possible, is presented on the left side of Figure 1. When the magnetic field direction lies within the area of the FOV covered by the small anodes of the SPAN-A, the strahl electrons are measured with the angular resolution of 6 × 20° (azimuth × elevation) (Whittlesey et al. 2020). We do not wish to limit our data set with respect to the magnetic field

---

[15] scipy.optimize.leastsq (https://docs.scipy.org/doc/scipy/reference/generated/scipy.optimize.leastsq.html).

direction because we expect that the physical mechanisms shaping the electron VDFs will also depend on the magnetic field vector. Instead, we use a fitting method described below that accounts for the field-of-view limitation. The differences resulting from the FOV obstruction are further analyzed and presented in Appendix A.

We characterize the strahl electrons with two parameters: strahl pitch-angle width (PAW) and strahl parallel temperature ($T_{s||}$).

We expect to observe the strahl component aligned with the magnetic field and moving away from the Sun. This means that if the magnetic field radial component is negative, the strahl electrons will be antiparallel to the magnetic field vector. However, this is not always the case. Bi-directional strahls have been observed and related to magnetic field structures like closed magnetic loops and magnetic clouds (Gosling et al. 1987). Sunward-directed strahls have also been observed and serve as the indicators of magnetic field structures sometimes referred to as the switchbacks (Pilipp et al. 1987; Balogh et al. 1999; Yamauchi et al. 2004; MacNeil et al. 2020), which are frequently observed also during the first perihelion of the *PSP* (Bale et al. 2019; Kasper et al. 2019). In this study, we do not consider special cases and focus on the anti-sunward moving strahl electrons in the nominal solar wind.

To obtain the strahl PAW, we first calculate pitch angles (α) for each measured energy bin of the electron VDF put in the plasma rest (defined by the solar wind protons) and magnetic field–aligned frame using the following criteria:

if $B_r > 0$:

$$\alpha(v_{\perp 1}, v_{\perp 2}, v_{||}) = \arccos\left(\frac{v_{||}}{\sqrt{v_{\perp 1}^2 + v_{\perp 2}^2}}\right), \tag{5}$$

if $B_r < 0$:

$$\alpha(v_{\perp 1}, v_{\perp 2}, v_{||}) = \arccos\left(\frac{-v_{||}}{\sqrt{v_{\perp 1}^2 + v_{\perp 2}^2}}\right). \tag{6}$$

The obtained pitch angles (α_i) thus lay on the interval [0°, 180°], where 0° denotes the direction along the magnetic field and pointing away from the Sun, 90° direction perpendicular to the magnetic field, and 180° the direction along the magnetic field and pointing toward the Sun.

These pitch-angle distributions are then fitted for each energy bin separately with a Gaussian distribution function:

$$f_i(\alpha) = f_{\max,i} \cdot \exp\left(\frac{\alpha^2}{2\sigma_i^2}\right), \tag{7}$$

where subscript i denotes iteration over all of the energy bins. Two fits are preformed for each energy bin. A first fit to all of the available points in an energy bin to separate the strahl from the background, and a second fit only to the points aligning with the first fit selected by the following criteria:

$$|(f_{\rm data} - f_{\rm fit,1})|/f_{\rm data} < 0.99, \tag{8}$$

where $f_{\rm data}$ are the data points and $f_{\rm fit,1}$ are the values predicted by the first fit. The second fit was performed when at least four data points conform to the criteria above (Equation (8)). Two examples of the second fit are shown in Figure 3(a) (dashed lines). The selected points representing the strahl part of the distribution are marked with red or blue color. We use the parameters from the second fit to then calculate the FWHM, which we refer to as the PAW:

$$\mathrm{PAW}_i = 2\sqrt{2\ln 2} \cdot \sigma_i. \tag{9}$$

The instances when PAW exceeds the value of 180° are excluded from further analysis, as they indicate almost

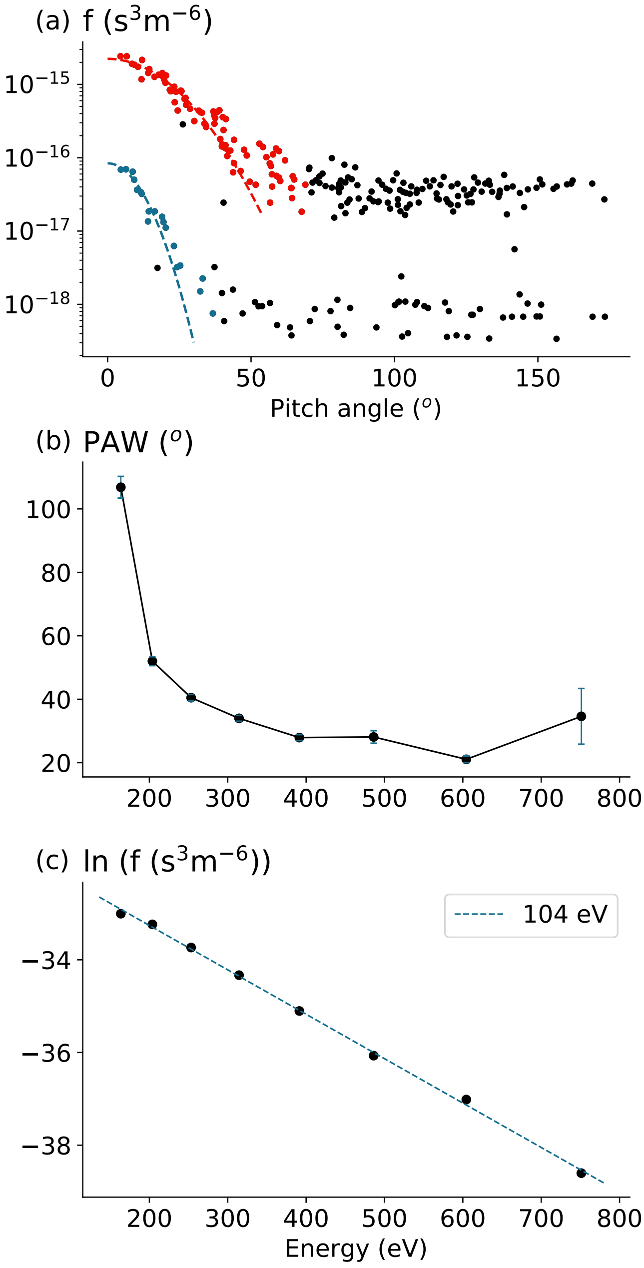

Figure 3. An example illustrating the strahl characterization method. All three plots come from one SPAN-E full spectra measurement, the same as shown in Figure 2 and the left panel of Figure 1. Panel (a): pitch-angle distributions shown for two different energy bins (253 eV in red and 604 eV in blue) with fitted normal functions (Equation (7)) marked with dashed lines. The points used calculation of PAW and $f_{\max}$ are marked with red and blue, and the background is marked in black. The obtained PAWs for these two energy bins were 40° and 22°. Panel (b): strahl PAW (Equation (9)) calculated for each of the energy bins. The error bars denote an interval of one standard deviation. Panel (c): natural logarithm of the $f_{\max,i}$ plotted against the electron energy and the linear fit preformed in this parameter space (dashed line) to obtain the strahl parallel temperature ($T_{s||}$) in this example resulting to 104 eV (see Equation (10)).

isotropic pitch-angle distributions and could be dominated by one of the more isotropic solar wind electron components, the core or the halo. In this work, we choose to perform the PAW analysis on the full electron VDF and not only on the strahl VDF, which can be obtained by subtraction of the modeled core and halo components from the total measured VDF (as done by Berčič et al. 2019, Section 3.2). Using the full VDF, we avoid the errors resulting from the core and the halo modeling. The core population taking up the lower electron energy is more sensitive to the effects of spacecraft's magnetic and electric fields and exhibits the yet unstudied deficit in the sunward, magnetic field–aligned portion of the VDF. The halo component is difficult to model because it was observed to be very tenuous and, during the encounter periods when the instrumental mechanic attenuator was closed, represented only by a few data points (Halekas et al. 2020). The strahl component, on the other hand, takes up higher energies and appears relatively dense, especially during the encounter periods. For these reasons, we fit Equation (7), the full measured VDF, and rely on the assumption that the energy bins resulting in PAW $< 180°$ are dominated by the strahl electron component. The same approach was used by Hammond et al. (1996) and Graham et al. (2017). An example of the PAWs calculated for each energy bin of one measured scan is shown in Figure 3(b).

In the inner heliosphere and for the energy ranges sampled by the SPAN-E instruments, the strahl VDFs along the parallel direction to the magnetic field are well represented by a Maxwellian distribution function. For the scope of this work, we are only interested in the temperature of this Maxwellian—the slope of the parallel strahl VDF. However, the peak of the pitch-angle distributions aligned with magnetic field is sometimes not sampled due to the heat shield FOV obstruction. Thus, instead of using the measured VDF closest to the parallel direction, we use the maximum VDF values ($f_{\max,i}$) from the fit to the pitch-angle distributions at each energy bin (see Equation (7)).

We perform a fit in the parameter space where a Maxwellian distribution forms a straight line with a slope depending only on its temperature:

$$\ln f_{\max,i}(v_\parallel) = -\frac{m_e}{2k_B \cdot T_{s\parallel}} \cdot v_\parallel^2 + \ln\left(n_s \sqrt{\frac{m_e}{2\pi k_B \cdot T_{s\parallel}}}\right), \quad (10)$$

where ln denotes the natural logarithm. An example of the strahl distribution in this representation is shown in Figure 3(c). Fitting a straight line in this parameter space, we assume that the drift velocity of the Maxwellian is zero or very small in comparison to the electron velocity (v). This agrees with the exospheric models predicting that the VDF stays the same as in the corona, where the bulk velocity of electrons is zero.

3.2. Helios 1

The same two parameters to characterize the strahl electrons, PAW and $T_{s\parallel}$, were obtained from the *Helios 1* observations. The PAWs as well as some other parameters like the core electron density (n_c) and temperature ($T_{c\parallel,\perp}$), velocity of the protons (v_p), and magnetic field (B), have already been used and are described in our previous work (Berčič et al. 2019).

The strahl temperature is determined in a similar way as described for the *PSP*; however, the *Helios 1* mission did not have a heat shield, and the 2D electron instrument was able to point straight at the Sun. Thus, using the $f_{\max,i}$ parameter from the PAW fits is not necessary. Instead, we limit the data set to instances when magnetic field lies within one of the eight azimuth bins and fit the Equation (10) to the data points from this azimuth bin (marked in blue in Figure 4(a)). We use a full measured distribution function in this bin and not the strahl distribution presented in Berčič et al. (2019), which was obtained by subtraction of the core and the halo from the measured VDF ($f_{\rm strahl} = f_{\rm measured} - f_{\rm core} - f_{\rm halo}$). The full distribution was used to unify the methods of $T_{s\parallel}$ calculation between *PSP* and *Helios* data set.

This process is illustrated in Figure 4(b). From the *Helios* data set, it is not as obvious that the strahl parallel VDF can be modeled by a Maxwellian. The VDFs appear noisier, and especially farther from the Sun (lighter blue values Figure 4(b)), they may exhibit traces of high energy tails, previously modeled by Kappa-like distribution functions (Maksimovic et al. 1997a; Štverák et al. 2009). However, for a certain energy range (between ~200 and 800 eV), strahl VDFs still present a straight line in the $\ln f(v^2)$ parameter space and give us the information about the strahl parallel temperatures. Fitting only the selected energy range, we avoid the inclusion of the electron core component.

4. Observations

Strahl PAWs with respect to electron energy for the different plasma $\beta_{ec\parallel}$ values are shown in Figure 5. Only data gathered during the first two encounter periods (35–60 R_S) was used and plotted separately ((a)—encounter 1, (b)—encounter 2). We separated the data because of the different integration time of the instruments for each encounter (see Section 2.1) and because of an unresolved issue with the instruments' response during the encounter 2. This artifact can be seen in Figures 5(b), A1(b), and B1(b) as a zig-zag pattern of PAW along the energy dimension for higher energies. It appears as if the PAW is slightly broader for every second energy bin. A possible reason for this kind of measurement response could lie in the hysteresis of the instrument deflection plates. A predicted correction for this effect has been applied on the whole data set; however, the hysteresis could be time dependent with a stronger effect on the measurements made during encounter 2. Nevertheless, the irregularities do not exceed the statistical error and, thus, do not change any conclusions of the present work.

Both plots in Figure 5 show the increase of PAW with $\beta_{ec\parallel}$. For the lower two $\beta_{ec\parallel}$ cases, the PAW decreases with electron energy reaching down to 30°, while for the highest $\beta_{ec\parallel}$ case the PAW stays more or less constant with a value ~55° for the energies above ~200 eV. This high-$\beta_{ec\parallel}$ regime where the strahl appears to be more affected by the scattering mechanisms was found for 26% of electron spectra during the encounter 1 and for 13% during encounter 2. For all cases, a fast increase of PAW is observed for the low electron energies, denoting the presence of the electron core population below the energy of ~200 eV .

No radial dependence was found during the encounter periods (from 35 to 60 R_S), most likely as a consequence of the presently limited *PSP* data set. It appears that the type of the

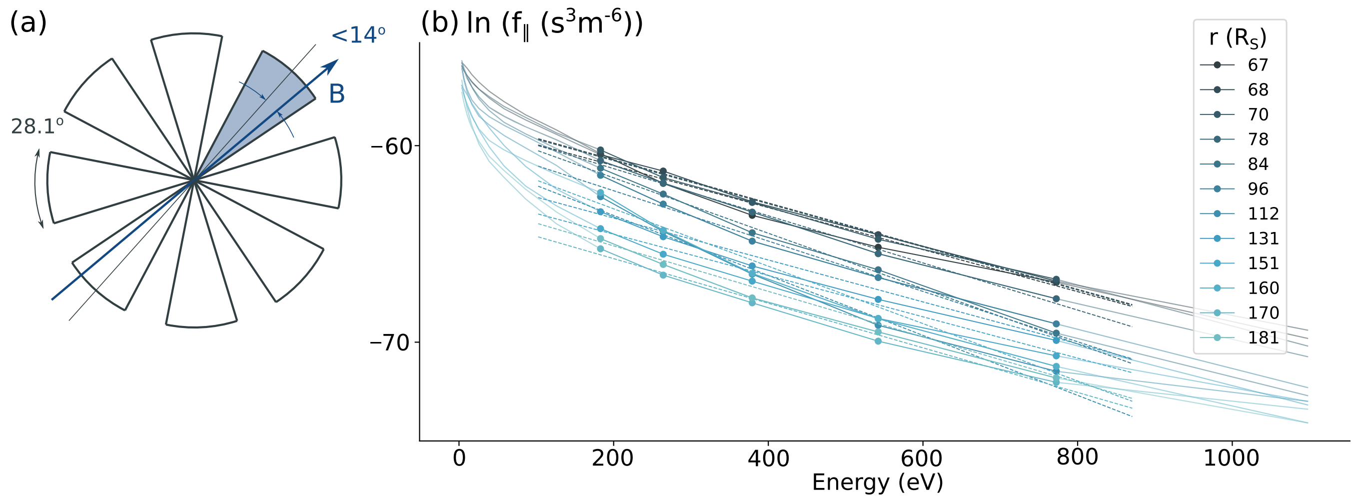

Figure 4. (a) Schematics of the electron instrument on board *Helios 1* mission. The instrument has eight azimuth bins that are 28°1 wide and separated with gaps. With “B”, we mark the magnetic field direction. (b) Each line represents an electron VDF detected by the azimuth bin aligned with the magnetic field direction (marked with blue in the schematics) and averaged over 10 consecutive measurements. We compare VDF examples from a half of *Helios 1* orbit between 1975 September 21 and December 8 spanning distances from 67 to 181 R_S (see the legend). The dots mark the measurements used for the $T_{s\|}$ fits, which are shown with the dotted lines.

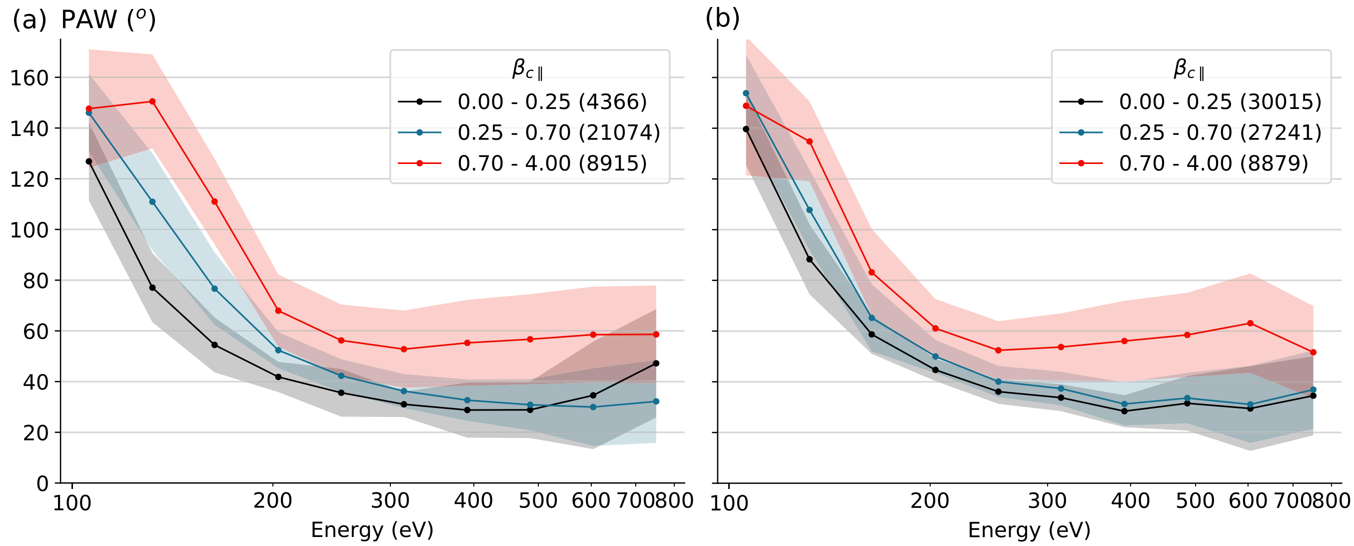

Figure 5. Strahl PAW with respect to electron energy, separated into three bins according to the local $\beta_{ec\|}$ value marked in the legend. The number in parenthesis denotes a number of VDFs in each $\beta_{ec\|}$ bin. The shaded region for each line gives the span of one standard deviation. (a) Encounter 1, (b) Encounter 2.

solar wind we observe has more of an effect on PAW than the radial distance.

Strahl temperatures obtained from *Helios* and *PSP* data sets are presented separately in Figures 6 and 7. The results from *Helios* data set are the outcome of binning several years' of solar wind measurements, while for the *PSP*, we use the data obtained over less than 6 months. Nonetheless, during the *PSP* encounter periods, the data rate is very high, and we were lucky to have already sampled different types of solar wind providing us with a satisfactory statistics. For the *Helios* data set, sampled distances range from 65 to 215 R_S, while for that of the *PSP*, the radial coverage is much smaller, from 35 and 58 R_S (first two encounters). Similarly, measured proton velocities in the *PSP* data set have a smaller span than in the *Helios* data set. The 2D histograms in both cases show the same result, no strong trends in variation of the $T_{s\|}$ with radial distance (r) and an anticorrelation with the solar wind proton velocity (v_p). The overall mean value of $T_{s\|}$ measured by *PSP* is 93 eV with a standard deviation of 13 eV, and by *Helios* 105 eV with a standard deviation of 23 eV.

Figure 8 presents the evolution of $T_{s\|}$ with part of the *PSP* orbit 1 trajectory ballistically projected down to the corona (2 R_S) to produce sub-spacecraft points (marked with colored dots). SWEAP in situ proton velocity measurements are used to perform this projection. The colored lines show the magnetic field lines mapped from each of the sub-spacecraft points down to the solar surface as predicted by the PFSS model (see Bale et al. 2019; Badman et al. 2020 for more details about the PFSS modeling). The polarity inversion line is shown in white.

This interval was chosen because it exhibits distinctive coronal features: a small coronal hole occurring during the first encounter period (region marked with a box in upper plot in Figure 8, enlarged in the lower plot), and a big coronal hole occurring after the encounter period (the center of the upper

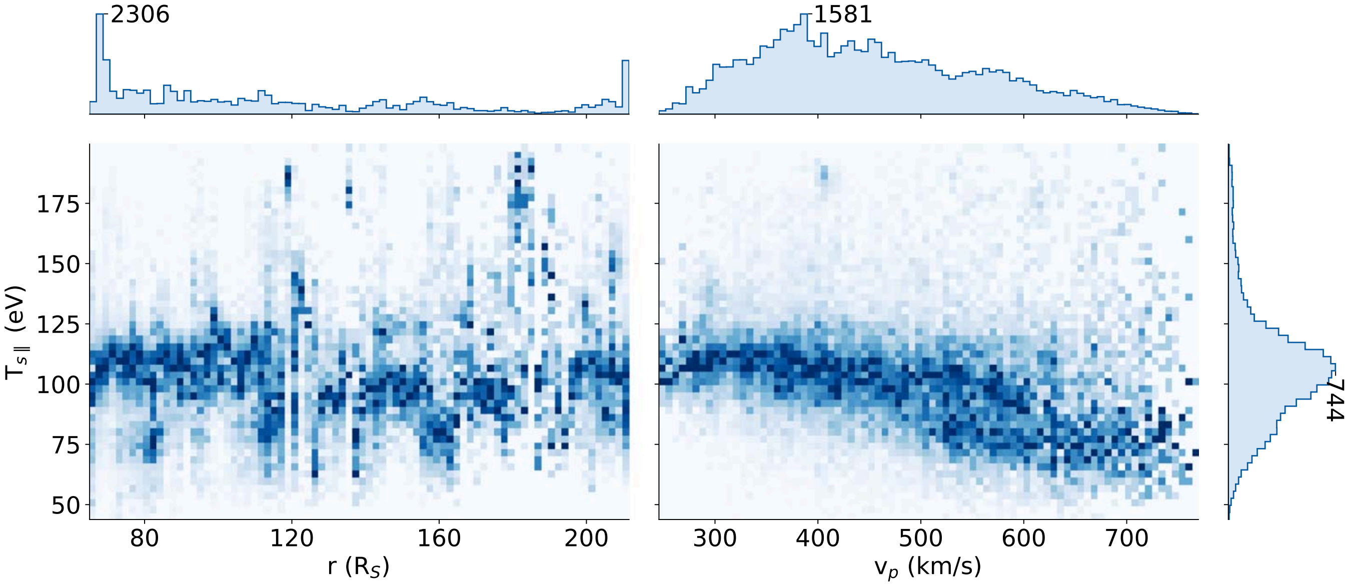

Figure 6. Histograms showing the variation of $T_{s\|}$ with radial distance (r) (left panel), and solar wind proton velocity (v_p) (right panel) for the *Helios* data set. The histograms are normalized to the maximum value in each vertical column. Above each of the 2D histograms and on the right side, 1D histograms present the probability distribution of the corresponding parameters (r, v_p, and $T_{s\|}$).

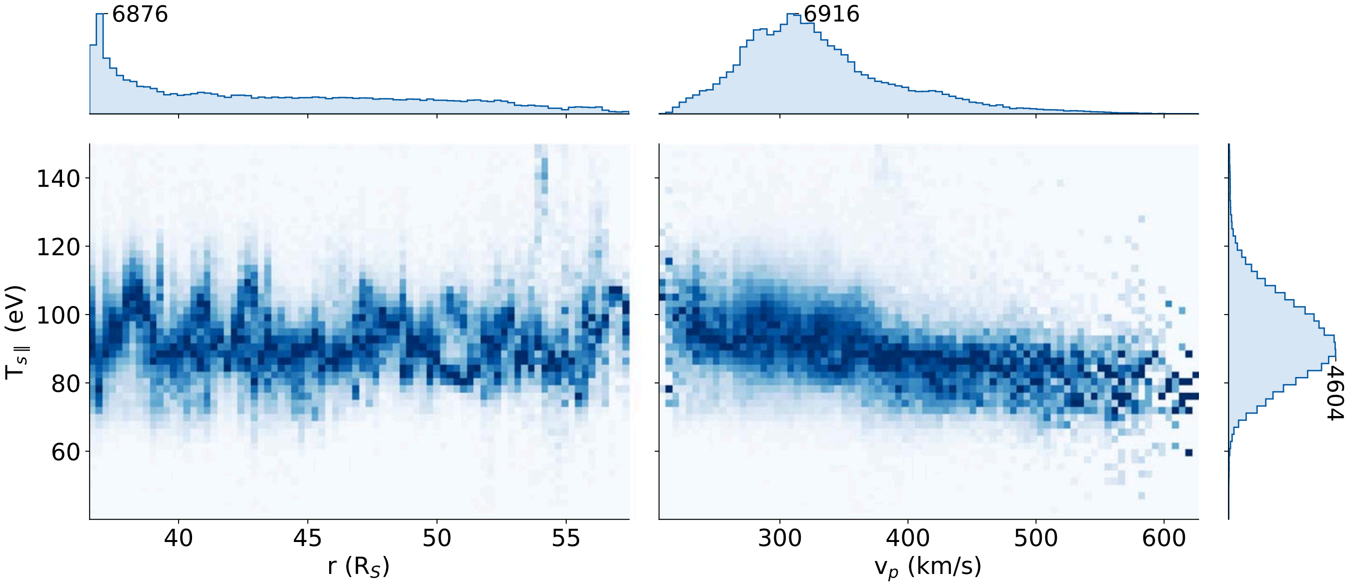

Figure 7. Histograms showing the variation of $T_{s\|}$ with radial distance (r) (left panel), and solar wind proton velocity (v_p) (right panel) for the *PSP* data set. The histograms are normalized to the maximum value in each vertical column.

plot in Figure 8). Coronal holes appear as the darker parts in the images produced from the 193 Å emission line, as these are the regions marked by low plasma density and open magnetic field lines. Oppositely, the bright regions in the image correspond to higher plasma densities, normally related to closed magnetic field loops. A similar plot has been shown in the work of Badman et al. (2020), who use a PFSS model to map the magnetic field lines measured by the spacecraft back to the solar surface (see Figures 5 and 8 in the referred article).

Our crude separation of $T_{s\|}$ appears to discern distinct coronal features as identified in the PFSS model: Very low $T_{s\|}$ (marked in black in Figure 8) is measured as *PSP* traces over the larger, positive polarity coronal hole after the first encounter and measured a fast wind stream, while a mix of intermediate $T_{s\|}$ (blue) and high $T_{s\|}$ (red) occurs in association with the smaller coronal hole *PSP* looped over at perihelion. The high strahl temperatures are associated with mapping to the edges of the coronal hole and the proximity to the current sheet (white contour in Figure 8), while the intermediate temperature occurs at a time when the solar wind bulk speed increased and *PSP* was directly over the center of the coronal hole.

In lower plot in Figure 8, presenting a zoom-in of the first encounter, the intermediate $T_{s\|}$ do not correspond directly to the darker regions on the image. Coronal holes are dynamic features, and this small coronal hole has been observed to drift over the limb of the Sun on November 2 (a date marked in

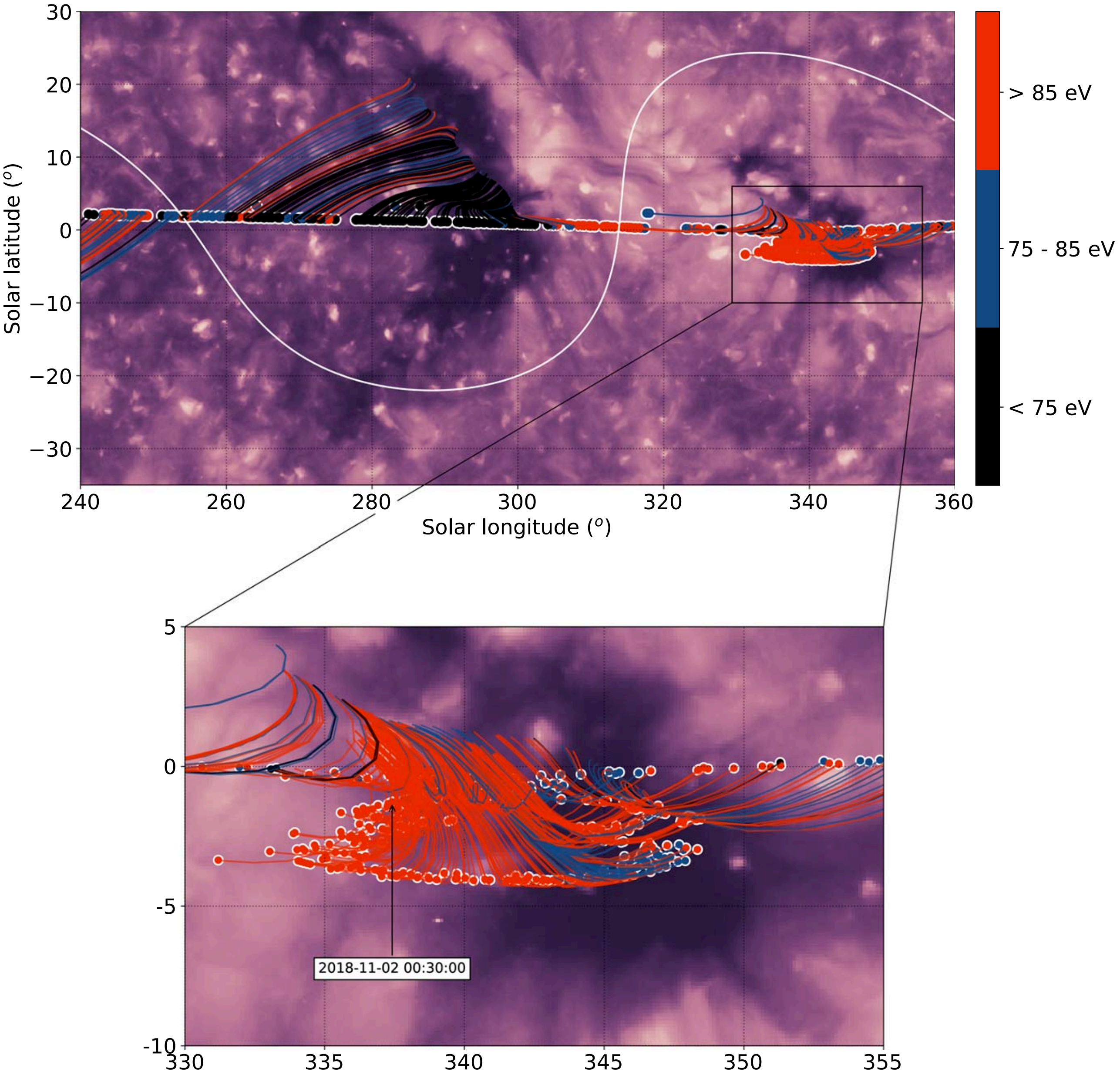

Figure 8. The evolution of $T_{s\|}$ with part of the *PSP* orbit 1. The *PSP* trajectory is ballistically projected down to the corona (2 R_S) to produce sub-spacecraft points. The colored lines denote the magnetic field lines mapped from the sub-spacecraft points to the solar surface as predicted by the PFSS model with source surface height 2 R_S, the same as used in Bale et al. (2019) and Badman et al. (2020). The white line shows the PFSS neutral line. The points and magnetic field lines are colored with respect to hour-long averages of $T_{s\|}$ (see the color bar in (a)). The corresponding image of the Sun is a synoptic map of the 193 Å emission synthesized from STEREO/EUVI and *SDO*/AIA for Carrington Rotation 2210, identical to the one used by Badman et al. (2020) in their Figures 5 and 9. The upper plot presents a larger time interval (2018 October 30, 00:30–2018 November 23, 17:30), and the lower presents a zoom of the encounter period (2018 October 30, 15:30–2018 November 14, 8:30).

Figure 8(b)). Therefore, we cannot be sure of the position of the small coronal hole at the time of the *PSP* crossing, and a slight disagreement between the image and $T_{s\|}$ is expected.

5. Discussion

PAWs observed by the *PSP* agree very well with the reported observations from the *Helios* mission (Figure 4 in Berčič et al. 2019). The most obvious change in the radial evolution from the closest regions to the Sun probed by *Helios* spacecraft (65 R_S) to the first two perihelia of the *PSP* reaching down to 35 R_S is the fast increase in PAW at low electron energies (see Figure 5). We attribute this increase to the presence of the core electron component reaching the temperatures above 30 eV (Halekas et al. 2020).

The observed anticorrelation between PAW and electron energy for the lower two $\beta_{ec\|}$ bins (Figure 5) might be a consequence of a collisionless focusing mechanism. Focusing of the solar wind electrons starts taking place at a distance above the solar surface where collisions cannot dominate the electron VDF anymore, a distance in the frame of exospheric solar wind models referred to as the exobase (Jockers 1970; Lemaire & Scherer 1971). The location of the exobase can be between 2 and 10 R_S (Maksimovic et al. 1997a) and depends

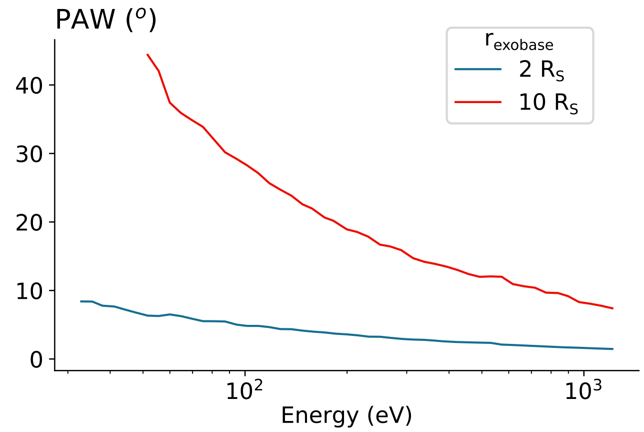

Figure 9. Relation between PAW and electron energy at the distance of 35 R_S resulting from a simple focusing model. The difference between the two curves is the selection of the exobase marked in the legend. The electric potential used for both examples was the same, equal to −500 V.

on the type of the solar wind. The expected relation between PAW and electron energy at the distance of 35 R_S accounting only for the focusing mechanism is shown in Figure 9 for the low and the high exobase limit. The model assumes an isotropic Maxwellian VDF at the exobase expanding along a radially decreasing magnetic field ($B \propto 1/r^2$). Following energy and momentum conservation (Equation (6) in Berčič et al. 2019), we obtain a VDF at 35 R_S and calculate the PAW as described in Section 3. In comparison to the majority of observations, the modeled PAWs still appear at least two times narrower.

In reality, the transition between collision-dominated and collisionless regimes does not happen at one distance but is a continuous process. This could be one of the reasons why our single exobase focusing model predicts lower PAWs than observed. Another possibility is that the strahl has already been affected by scattering mechanisms also resulting in an anticorrelation between PAW and electron energy. A good candidate is Coulomb collisions. A study using kinetic theory is presented in works by Horaites et al. (2018, 2019), providing a theoretical prediction of the strahl PAW, accounting for collisions between particles. PAW seems, to some extent and for some energy range, to agree with the results from Horaites et al. (2018), predicting relations in the form PAW $\propto \sqrt{n}$, and PAW $\propto E^{-1}$, where n strands for density and E for electron energy. However, Equation (15) from Horaites et al. (2019) does not predict our observations.

The focusing experienced by the strahl electron component during the solar wind expansion does not affect $T_{s\|}$. If the scattering mechanisms do not strongly modify the electron VDF, the temperature of the VDF at the exobase stays imprinted in the strahl population. The density of the VDFs and the core T decrease with radial distance, but the slope—the temperature—of the parallel cut through the strahl part of the VDF remains unchanged (see schematics in Figure 10). Even though the strahl PAW are observed to be somewhat broader than that predicted by the exospheric models, no radial trends were found in the $T_{s\|}$ observed by *Helios* and *PSP* missions (see Figures 6 and 7). This raises the question of the efficiency of the scattering mechanisms in modifying $T_{s\|}$. The answer requires further observational and numerical studies, which are beyond the scope of this work.

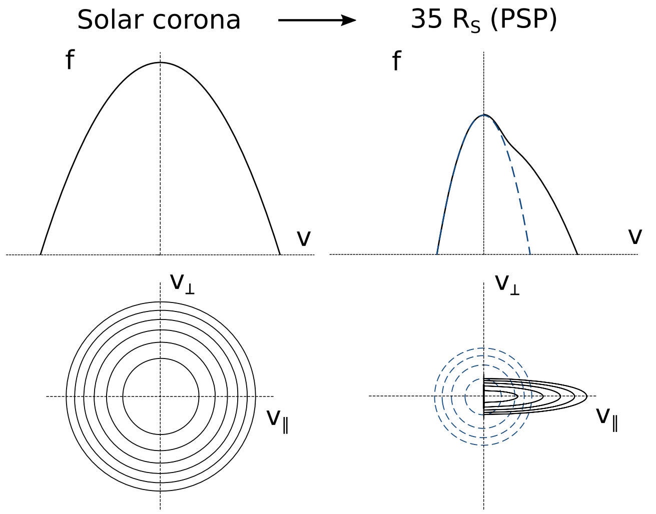

Figure 10. A schematic diagram demonstrating how the information about the temperature of coronal electrons is preserved in the $T_{s\|}$. The upper row shows a cut through a distribution function with respect to electron velocity, while the lower row shows the same two distributions in velocity space where $v_\|$ is aligned with magnetic field direction.

The constant behavior of $T_{s\|}$ over radial distance is a new observation, which is in contradiction with the current beliefs about its radial evolution. Recent near-Earth observational studies, from either Wind or Cluster spacecraft (Viñas et al. 2010; Tao et al. 2016; MacNeil et al. 2017; Wilson et al. 2019b), report significantly lower strahl T than the ones reported in this work. As a consequence, it was accepted that the strahl temperature must decrease over the distance from Sun to Earth. But the reason for different observational results lies mostly in the different data analysis approach. We follow the exospheric theory and, therefore, fit the strahl field–aligned VDF cut with a Maxwellian centered on $v_\| = 0$. Viñas et al. (2010) isolate the strahl component and obtain the plasma moments by integration. The obtained strahl T are on the order of 10 eV with $T_\perp \sim 2$ times bigger than $T_\|$, and the obtained drift velocities are relatively high. With this approach, they measure the width of the strahl distribution, while we are interested in the slope. Wilson et al. (2019b) model the strahl with a Kappa distribution with a drift and report the mean $T_{s\|,\kappa}$ of 44.2 eV. Tao et al. (2016) and MacNeil et al. (2017) also use Kappa distribution function but centered on $v_\| = 0$, and they find means $T_{s\|,\kappa}$ of 51.1 eV and ∼50 eV, respectively. We performed a test to quantify the effect of the different model choice on the obtained $T_\|$. Figure 11 shows the same example as Figure 3(c) but fitted with a Kappa distribution function for $\kappa = 10$ and $\kappa = 5$. The fit was made in the logarithmic space with the one-dimensional Kappa distribution function:

$$f_\kappa(v_\|) = \frac{n_\kappa}{\kappa^{3/2}\sqrt{\pi}\, w_\kappa} \frac{\Gamma(\kappa+1)}{\Gamma(\kappa-1/2)} \cdot \left(1 + \frac{v_\|^2}{w_\kappa^2 \kappa}\right)^{-\kappa-1}, \quad (11)$$

where the κ parameter is given, and the density (n_κ) and the thermal velocity (w_κ) are the fitting parameters. The strahl parallel Kappa temperature ($T_{s\|,\kappa}$) can be calculated from w_κ:

$$w_\kappa = \sqrt{\frac{2\kappa - 3}{\kappa k_B T_{s\|,\kappa}}}. \quad (12)$$

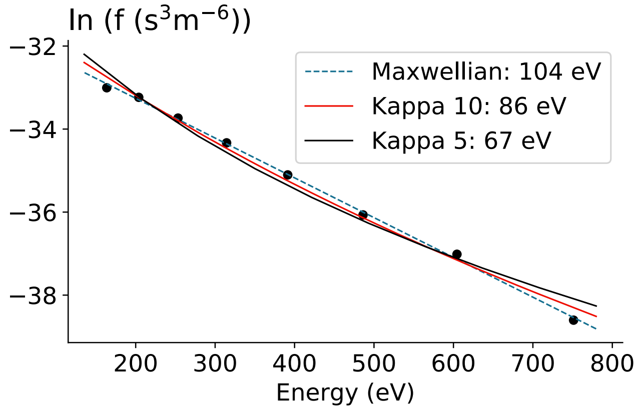

Figure 11. The same example as shown in Figure 3(c). Additionally to the Maxwellian fit (dashed blue line), two Kappa fits are shown: $\kappa = 10$ (red line) and $\kappa = 5$ (black line).

In fact, the temperature obtained with the Kappa fit ($T_{s\|,\kappa}$) is much lower than the temperature obtained with a Maxwellian fit. The $T_{s\|,\kappa}$ for the $\kappa = 5$ case falls within the range of observations shown by Tao et al. (2016) and MacNeil et al. (2017).

A Maxwellian model was chosen because it most accurately represents new observations of the strahl provided by *PSP*. For the measured energy range, up to 800 eV, the strahl VDF cutting through the parallel direction shows no signs of high energy tails. This is not strictly true for the strahl measured by *Helios*, especially at larger distances, neither for the strahl observed at 1 au (Tao et al. 2016; MacNeil et al. 2017; Wilson et al. 2019b). The radial evolution of the strahl modeled by a Kappa function is presented by Štverák et al. (2009). They report the increase of κ values at smaller distances from the Sun, reaching ~14 at 0.3 au (64.5 R_S). For large κ values, a Kappa distribution tends toward a Maxwellian; therefore, the *PSP* observations of a Maxwellian-like strahl VDF below 60 R_S were not unexpected.

On the other hand, the increase of κ for small distances (Štverák et al. 2009), and the measured Maxwellian-like strahls by the *PSP*, could be an instrumental artifact. Closer to the Sun, the total electron temperature is larger; therefore, the unaltered instrument energy span becomes relatively smaller than farther from the Sun. We are only able to measure a smaller portion of the strahl VDF, which could be missing the high energy tails—the most important part for distinction between a Kappa and a Maxwellian VDF.

The idea that the strahl electrons carry the information about the temperature of the electrons at the exobase is a part of exospheric solar wind models, as they initially do not take into account collisions or wave–particle interactions (Jockers 1970; Lemaire & Scherer 1971).

Two studies investigated the relation between the temperature of the supra-thermal electron population observed at 1 au, and the coronal temperature so far. Both of them make use of the oxygen charge-state ratio (O^{7+}/O^{6+}) measurements as an estimate for the coronal electron temperature. In the study by Hefti et al. (1999), a clear correlation between the strahl parallel temperature and the oxygen charge ratio was observed, while MacNeil et al. (2017) present a data interval where the correlation is present and a data interval where it is not. Unfortunately, neither of the two spacecraft presented in this work provide us with a measurement of oxygen state ratios. But this measurement will be provided by the Solar Orbiter, the new probe exploring the inner heliosphere launched on 2020 February 10 (Müller et al. 2013).

Another parameter strongly correlated with the temperature of the solar corona, which is often used as an indicator of the solar wind origin, is the solar wind velocity (Lopez & Freeman 1986). The solar wind originating from the center of the coronal holes, where the proton plasma temperature is higher than that of electrons, has a higher terminal velocity than the wind coming from the edges of the coronal holes. Figures 6 and 7 agree with this global picture as they display a clear anticorrelation between $T_{s\|}$ and the solar wind proton velocity.

Using the sub-spacecraft points in combination with the synoptic map of the Sun allows us to follow the time evolution of the $T_{s\|}$ and compare it with the current state of the solar corona (Figure 8). Through comparison with the PFSS modeling of the magnetic field line topology during the first orbit of *PSP* presented in the study by Badman et al. (2020), we crudely separated the strahl temperature data into three bins. The coldest $T_{s\|}$ ($T_{s\|} < 75$ eV) were observed at times when measured magnetic field lines appear to connect to a bigger equatorial coronal hole encountered just after the first *PSP* perihelion. During the first encounter, when a period of high-speed solar wind implies connectivity to the smaller coronal hole (Figure 8(b)), the strahl temperatures appear a bit higher temperature, $75\,\text{eV} < T_{s\|} < 85\,\text{eV}$. These values are in agreement with the coronal electron temperatures obtained via the spectroscopy technique presented by David et al. (1998) and Cranmer (2002). They report the coronal hole electron temperature just above the solar surface to be 0.79 MK (=68 eV), reach its maximum temperature at 1.15 R_S, stay below 1 MK (=86 eV), and decrease after (Figure 2 in the referred article). For the quiet equatorial corona, the temperatures appear to be higher, starting at 1 MK and increasing until they reach 3.16 MK (=272 eV) at 1.3 R_S.

This evidence lead us to believe that $T_{s\|}$ indeed retains the information about the temperature of electrons at their origin. However, to be convinced that $T_{s\|}$ is not just correlated with but equals to the coronal electron temperature, further analysis is required. As mentioned above, the exobase is not a discrete point above the solar surface but a continuous region over which the collisions become less and less important. Another thing one needs to account for is the energy-dependent scattering of the strahl electrons. The strahl was, for most of the measurements, observed to be narrow but still broader than what is expected from the simple collisionless model. For example, scattering by Coulomb collisions at only lower energies would result in a higher $T_{s\|}$. The study of the effect of continuous exobase and Coulomb collisions making use of kinetic simulations BiCop (Landi & Pantellini 2001, 2003) is a current work in progress.

6. Conclusions

The PAW data obtained during the first two orbits of *PSP* agrees well with the results obtained from the *Helios* data set presented by Berčič et al. (2019). We find the same PAW dependence on $\beta_{ec\|}$: in high-$\beta_{ec\|}$ solar wind, the strahl appears broader than in the low-$\beta_{ec\|}$ solar wind. For the measured energy range, the PAW was found to decrease with electron energy reaching down to 30° for the lower two $\beta_{ec\|}$ bins, representing the majority of measurements.

We present, for the first time, observations of $T_{s\|}$ from both the *PSP* and *Helios* missions. An anticorrelation was found between $T_{s\|}$ and the solar wind velocity (v_p), while $T_{s\|}$ was observed to be constant over radial distance (r). These findings lead us to conclude that the strahl carries information about the coronal electron temperature at the point of its origin and can be used as a good proxy for connectivity studies involving remote sensing and in situ data. In fact, the origins of the solar wind measured by *PSP* anticipated from the strahl temperature measurements compare very well to the ones obtained using a PFSS model presented by Bale et al. (2019) and Badman et al. (2020). Even though the measured values of $T_{s\|}$ agree very well with the coronal electron temperatures measured with the spectroscopes on board the *SOHO* spacecraft (David et al. 1998; Cranmer 2002), we believe further analysis is required to confirm that $T_{s\|}$ is a direct measure of the electron temperature in the corona.

We are grateful for the reviewer's comments, which were constructive and helped to improve the quality of the present work. This work was supported by the Programme National PNST of CNRS/INSU co-funded by CNES. All analysis was done and the plots were produced using open-source Python libraries NumPy, Matplotlib, Pandas, and SciPy. We also acknowledge all members of the *Helios* data archive team (http://helios-data.ssl.berkeley.edu/team-members/) to make the *Helios* data publicly available to the space physics community.

Appendix A
PAW—FOV Effects

The combined FOV of SPAN-E instruments is not uniform (Kasper et al. 2016; Whittlesey et al. 2020). Electrons are detected by two instruments, and the azimuth anodes of each of them have two possible angular widths: 6° and 24°. Part of the full solid angle is not sampled and is part blocked by the heat shield (see Figure 1). We investigated how much the nonuniform FOV affects our data analysis.

We identified two extreme configurations of the magnetic field vector in the FOV. The measurement is the most precise when the magnetic field vector lies within part of the FOV covered by the small azimuth anodes of SPAN-A. The most problematic measurement of the strahl electrons happens when the magnetic field is aligned with the radial direction, because in this case, the strahl electrons get blocked by the heat shield, which is during the encounter time directed directly toward the Sun.

The results are presented in Figure A1. PAWs measured at low electron energies are independent of the configuration of the magnetic field in the FOV. However, the strahl electrons with higher energies during the first encounter appear ∼10° broader when the magnetic field lies outside of the FOV covered by the small anodes of SPAN-A. The variation is less pronounced during the second encounter.

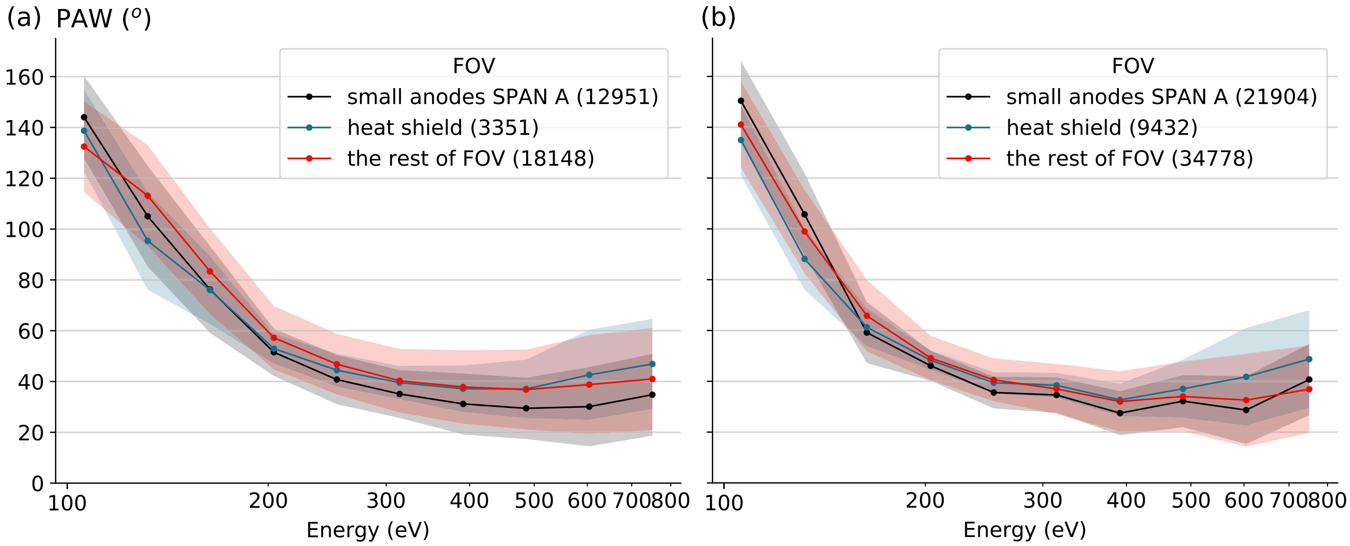

Figure A1. Strahl PAW with respect to electron energy, separated into three bins according to location of the magnetic field vector in the FOV of the instruments. Bin edges are noted in the legend followed by a number of instances belonging to each bin. (a) Encounter 1, (b) Encounter 2.

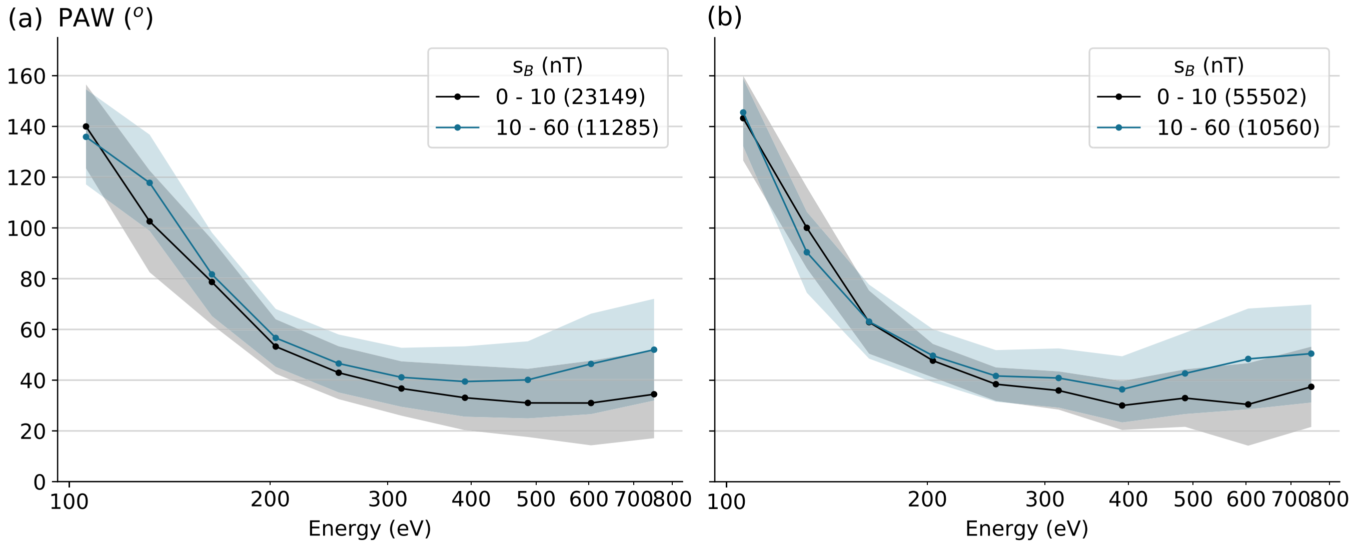

Figure B1. Strahl PAW with respect to electron energy, separated into two bins according to the standard deviation of the magnetic field measurement during the duration of one scan. (a) Encounter 1, (b) Encounter 2.

Appendix B
PAW—Standard Deviation *B*

Another test was conducted to determine how much the variation of the magnetic field during the integration time of SPAN-E instruments affects our strahl PAW measurements. We calculated the standard deviation of a 294 Hz magnetic field measurement during each SPAN-E scan lasting 27.96 s for the first encounter. For the second encounter, the magnetic field was sampled with a cadence of 147 Hz, and the duration of one scan was set to 13.98 s.

Figure B1 shows PAWs separated into two groups according to the standard deviation of B. The effect of the strong variation of the magnetic field during the SPAN-E measurement is increasing with increasing electron energy and can make the strahl appear up to 20° broader than during times of small magnetic field variation.

ORCID iDs

Laura Berčič https://orcid.org/0000-0002-6075-1813
Davin Larson https://orcid.org/0000-0001-5030-6030
Phyllis Whittlesey https://orcid.org/0000-0002-7287-5098
Milan Maksimović https://orcid.org/0000-0001-6172-5062
Samuel T. Badman https://orcid.org/0000-0002-6145-436X
Simone Landi https://orcid.org/0000-0002-1322-8712
Lorenzo Matteini https://orcid.org/0000-0002-6276-7771
Stuart. D. Bale https://orcid.org/0000-0002-1989-3596
John W. Bonnell https://orcid.org/0000-0002-0675-7907
Anthony W. Case https://orcid.org/0000-0002-3520-4041
Thierry Dudok de Wit https://orcid.org/0000-0002-4401-0943
Keith Goetz https://orcid.org/0000-0003-0420-3633
Peter R. Harvey https://orcid.org/0000-0002-6938-0166
Justin C. Kasper https://orcid.org/0000-0002-7077-930X
Kelly E. Korreck https://orcid.org/0000-0001-6095-2490
Roberto Livi https://orcid.org/0000-0002-0396-0547
Robert J. MacDowall https://orcid.org/0000-0003-3112-4201
David M. Malaspina https://orcid.org/0000-0003-1191-1558
Marc Pulupa https://orcid.org/0000-0002-1573-7457
Michael L. Stevens https://orcid.org/0000-0002-7728-0085

References

Badman, S. T., Bale, S. D., Oliveros, J. C. M., et al. 2020, ApJS, 246, 23
Bale, S. D., Badman, S. T., Bonnell, J. W., et al. 2019, Natur, 576, 237
Bale, S. D., Goetz, K., Harvey, P. R., et al. 2016, SSRv, 204, 49
Balogh, A., Forsyth, R. J., Lucek, E. A., Horbury, T. S., & Smith, E. J. 1999, GeoRL, 26, 631
Berčič, L., Maksimović, M., Landi, S., & Matteini, L. 2019, MNRAS, 486, 3404
Case, A. W., Kasper, J. C., Stevens, M. L., et al. 2020, ApJS, 246, 43
Cranmer, S. 2002, in COSPAR Coll. Ser. 13, ed. P. C. H. Martens & D. P. Cauffman (Amsterdam: Elsevier), 3
David, C., Gabriel, A. H., Bely-Dubau, F., et al. 1998, A&A, 336, 90
Dorelli, J. C., & Scudder, J. D. 1999, GeoRL, 26, 3537
Feldman, W. C., Asbridge, J. R., Bame, S. J., Montgomery, M. D., & Gary, S. P. 1975, JGR, 80, 4181
Fox, N. J., Velli, M. C., Bale, S. D., et al. 2016, SSRv, 204, 7
Gosling, J. T., Baker, D. N., Bame, S. J., et al. 1987, JGRA, 92, 8519
Graham, G. A., Rae, I. J., Owen, C. J., et al. 2017, JGRA, 122, 3858
Halekas, J. S., Whittlesey, P., Larson, D. E., et al. 2020, ApJS, 246, 22
Hammond, C. M., Feldman, W. C., McComas, D. J., Phillips, J. L., & Forsyth, R. J. 1996, A&A, 316, 350
Hefti, S., Zurbuchen, T. H., Fisk, L. A., et al. 1999, in AIP Conf. Proc. 471, SOLAR WIND 9, ed. S. R. Habbal (Melville, NY: AIP), 495
Horaites, K., Boldyrev, S., & Medvedev, M. V. 2019, MNRAS, 484 2474
Horaites, K., Boldyrev, S., Wilson, L. B., Viñas, A. F., & Merka, J. 2018, MNRAS, 474, 115
Jockers, K. 1970, A&A, 6, 219
Kajdič, P., Alexandrova, O., Maksimovic, M., Lacombe, C., & Fazakerley, A. N. 2016, ApJ, 833, 172
Kasper, J. C., Abiad, R., Austin, G., et al. 2016, SSRv, 204, 131
Kasper, J. C., Bale, S. D., Belcher, J. W., et al. 2019, Natur, 576, 228
Lamy, H., Pierrard, V., Maksimovic, M., & Lemaire, J. F. 2003, JGRA, 108, 1047
Landi, S., Matteini, L., & Pantellini, F. 2012, ApJ, 760, 143
Landi, S., Matteini, L., & Pantellini, F. 2014, ApJL, 790, L1
Landi, S., & Pantellini, F. 2001, A&A, 372, 686
Landi, S., & Pantellini, F. 2003, A&A, 400, 769
Lemaire, J., & Scherer, M. 1971, JGR, 76, 7479
Lie-Svendsen, y., Hansteen, V. H., & Leer, E. 1997, JGRA, 102, 4701
Lopez, R. E., & Freeman, J. W. 1986, JGRA, 91, 1701
MacNeil, A. R., Owen, C. J., & Wicks, R. T. 2017, AnGeo, 35, 1275
MacNeil, A. R., Owens, M. J., Lockwood, M., Štverák, Š, & Owen, C. J. 2020, SoPh, 295, 16

Maksimovic, M., Bale, S. D., Berčič, L., et al. 2020, ApJS, 246, 62
Maksimovic, M., Pierrard, V., & Lemaire, J. F. 1997a, A&A, 324, 725
Maksimovic, M., Pierrard, V., & Riley, P. 1997b, GeoRL, 24, 1151
Maksimovic, M., Zouganelis, I., Chaufray, J. Y., et al. 2005, JGRA, 110, 1
Marsch, E. 2006, LRSP, 3, 1
McGinnis, D., Halekas, J., Whittlesey, P., Larson, D., & Kasper, J. 2019, JGRA, 124, 7369
Müller, D., Marsden, R. G., St., Cyr, O. C., Gilbert, H. R. & The Solar Orbiter Team 2013, SoPh, 285, 25
Pagel, C., Gary, S. P., de Koning, C. A., Skoug, R. M., & Steinberg, J. T. 2007, JGR, 112, 1
Parker, E. N. 1958, ApJ, 128, 664
Pierrard, V., Maksimovic, M., & Lemaire, J. 2001, JGRA, 106, 29305
Pilipp, W. G., Miggenrieder, H., Montgomery, M. D., et al. 1987, JGR, 92, 1075
Porsche, H. 1981, ESA Spec. Publ., 164, 43
Saito, S., & Gary, P. S. 2007, GeoRL, 34, L01102
Salem, C., Bosqued, J.-M., Larson, D., et al. 2001, JGR, 106, 21701
Schwartz, S. J., & Marsch, E. 1983, JGR, 88, 9919
Smith, H. M., Marsch, E., & Helander, P. 2012, ApJ, 753, 31
Štverák, Š, Maksimovic, M., Trávníček, P. M., et al. 2009, JGRA, 114, 1
ŠtveráK, Š, Trávníček, P., Maksimovic, M., et al. 2008, JGRA, 113, A03103
Tao, J., Wang, L., Zong, Q., et al. 2016, ApJ, 820, 22
Viñas, A., Gurgiolo, C., Nieves-Chinchilla, T., Gary, S. P., & Goldstein, M. L. 2010, in AIP Conf. Proc. 1216, Twelfth Solar Wind Conf., ed. M. Maksimovic et al. (Melville, NY: AIP), 265
Virtanen, P., Gommers, R., Oliphant, T. E., et al. 2019, arXiv:1907.10121
Vocks, C., Salem, C., Lin, R. P., & Mann, G. 2005, ApJ, 627, 540
Whittlesey, P. L., Larson, D. E., Kasper, J. C., et al. 2020, arXiv:2002.04080
Wilson, L. B. I., Chen, L.-J., Wang, S., et al. 2019a, ApJS, 243, 8
Wilson, L. B. I., Chen, L.-J., Wang, S., et al. 2019b, ApJS, 245, 24
Yamauchi, Y., Suess, S. T., Steinberg, J. T., & Sakurai, T. 2004, JGRA, 109, A03104
Zouganelis, I., Maksimovic, M., Meyer-Vernet, N., Lamy, H., & Issautier, K. 2004, ApJ, 606, 542

C

THE INTERPLAY BETWEEN AMBIPOLAR ELECTRIC FIELD AND COULOMB COLLISIONS IN THE SOLAR WIND ACCELERATION REGION

The interplay between ambipolar electric field and Coulomb collisions in the solar wind acceleration region

L. Berčič [1,2], S. Landi [1,3], M. Maksimović [2]

[1]Physics and Astronomy Department, University of Florence, Firenze, Italy
[2]LESIA, Observatoire de Paris, PSL Research University, CNRS, UPMC Université Paris 6, Université Paris-Diderot, Meudon, France
[3]INAF - Osservatorio Astrofisico di Arcetri, Firenze, Italy

Key Points:

- We use a kinetic model of expanding solar wind accounting for Coulomb collisions. This model produces a slow, supersonic solar wind proton population accelerated only through the ambipolar electric field, which arises due to the difference of mass between electron and proton.
- The self-consistently calculated ambipolar electric field in the model is on the order of Dreicer electric field.
- We present the radial evolution of the strahl electron component under the influence of Coulomb collisions.

Corresponding author: Laura Berčič, `laura.bercic@obspm.fr`

Abstract

The solar wind protons are accelerated to supersonic velocities within the distance of 10 solar radii from the Sun, as a consequence of a complex physical mechanism including particle kinetic effects as well as the field-particle energy and momentum exchange. We use a numerical kinetic model of the solar wind, accounting for Coulomb collisions (BiCoP), and model a solar wind accelerated only by the *ambipolar* electrostatic filed (E) arising due to the difference in mass between electron and proton, and assuring quasi-neutrality and zero current. We study the effect E, which was found to be on the order of Dreicer electric field (E_D) (Dreicer, 1959), has on the resulting electron velocity distribution functions (VDF). The strahl electron radial evolution is represented by means of its *pitch-angle width* (PAW), and the *strahl parallel temperature* ($T_{s,\|}$). A continuous transition between collisional and weakly collisional regime results in broader PAW, compared to the single-exobase prediction imposed by the exospheric models. Collisions were found to scatter strahl electrons below 250 eV, which in turn has an effect on the measured $T_{s,\|}$. A slight increase was found in $T_{s,\|}$ with radial distance, and was stronger for the more collisional run. We estimate that the coronal electron temperature inferred from the observations of $T_{s,\|}$ in the solar wind, would be overestimated for between 8 and 15%.

1 Introduction

The solar wind is a continuous flux of magnetised plasma which originates in the solar corona and permeates the interplanetary space. The first physical model explaining its existence was proposed by Parker (1958) in a form of a fluid hydrodynamic flow. The mass conservation of solar wind expansion results in a strong radial gradient in plasma density, decreasing with radial distance as r^{-2}, and even faster in the solar wind acceleration region. The plasma that escapes the hot and dense, collision dominated solar corona, therefore significantly decreases in density and becomes almost collisionless, over a few solar radii (R_S). Frequently used measure of collisionality is the ratio between the mean-free path of the particles (λ) and the atmospheric density scale-height (H), called the *Knudsen number* (K_n). Values $K_n \ll 1$ are typical for the solar corona, while $K_n > 1$ marks the weakly collisional and collisionless regimes, where departures from a thermal equilibrium, Maxwellian particle velocity distribution function (VDF), are expected. Accordingly with the Parker (1958) model, the transition between the two regimes (defined with $K_n = 1$) lies at the radial distance of about 4 R_S (Brasseur & Lemaire, 1977).

Kinetic *exospheric* solar wind models were developed, with a goal to provide a more detailed description of the solar wind expansion physics above the transition point ($K_n = 1$), referred to as the *exobase*. A common element of all the exospheric solar wind models is an explicit existence of the global electrostatic field, resulting from the difference in mass between electron and proton. The first proposed kinetic model by Chamberlain (1960) assumed that this electrostatic field is the Pannekoek-Rosseland electric field, arising in any gravitationally bound plasma in hydrostatic equilibrium (Pannekoek, 1922; Rosseland, 1924). As the solar wind is not in such equilibrium, the electric field was underestimated, resulting in a subsonic solar wind solution, called *the solar breeze.*

Due to their smaller mass and consequently larger thermal velocity, the electrons evaporate from the solar corona faster than the heavier protons. The arising global electric field, also referred to as the *ambipolar* electrostatic field (E), must thus assure the equality of electron and proton fluxes at all radial distances, allowing the Sun to remain charge-free. The ambipolar electric field was used in succeeding exospheric models (Lemaire & Scherer, 1970, 1971; Jockers, 1970; Maksimovic et al., 1997; Pierrard et al., 1999; Zouganelis et al., 2004), producing supersonic wind that agrees well with the measured solar wind plasma moments.

Scudder (1996) showed that the value of E in the solar wind critical point, the radial distance at which the solar wind protons become supersonic, should be on the order of *Dreicer electric field* (E_D) (Dreicer, 1959). The electric fields of that size were found to cause the electron *runaway* in the context of fusion laboratory experiments, resulting in large currents (Dreicer, 1960). A theory describing the effect of E on the solar wind electron VDF was developed by Scudder (2019b), who proposes that the supra-thermal electrons result from the runaway mechanism. No observational evidence of E interacting with electron VDF were reported so far.

The benefit of a kinetic description of the solar wind is that it allows the existence of non-thermal VDFs, commonly observed in the solar wind for both protons and electrons. Observed solar wind electron VDFs are normally modelled with three components: the dense electron *core* takes up the low electron energies, while the high energies are represented by field-aligned beam-like electron *strahl* and the electron *halo* present in all directions (Feldman et al., 1975; Pilipp et al., 1987; Maksimovic et al., 2005; Štverák et al., 2008; Štverák et al., 2009; Tao et al., 2016; Wilson et al., 2019b, 2019a; Macneil et al., 2020). In exospheric models the velocity space at any radial distance is separated by the velocity required for an electron to escape from the potential well of the ambipolar electric field. Electrons with velocities smaller than the escape velocity can belong to either trapped, ballistic or incoming exospheric particle class, and are equivalent to the core component. Electrons with velocity high enough to escape, belong to the escaping class, and correspond to the strahl component (Lemaire & Scherer, 1971). The halo component is not present in the exospheric models, and is thus believed to be created through the electromagnetic (EM) field-particle interaction during the solar wind expansion, or exist already deep in the solar corona (Pierrard et al., 1999).

In the collisionless approximation the anti-sunward moving strahl electrons focus around the radially decreasing magnetic field, following the magnetic moment and energy conservation. However, the strahl observed in the solar wind was reported to broaden with radial distance (Hammond et al., 1996; Graham et al., 2017; Berčič et al., 2019), requiring the existence of strahl scattering mechanisms. Coulomb collisions were found to be efficient in isotropising the electron core (Salem et al., 2003; Štverák et al., 2008), but have a much smaller effect on the higher energy electrons. A study of the Coulomb scattering of the strahl electrons using kinetic theory is presented in works by Horaites et al. (2018, 2019), who provide an analytical expression relating the *strahl pitch-angle width* (PAW) to the energy and density of solar wind electrons. PAW was found to decrease with electron energy, at 1 au affecting electrons below $\sim$ 300 eV. Proposed scattering mechanisms, effective at higher electron energies, include wave-particle interactions (Vocks et al., 2005; Kajdič et al., 2016; Verscharen et al., 2019; Krishna Jagarlamudi, 2020) and scattering by the background turbulence (Pagel et al., 2007; Saito & Gary, 2007).

Collisionless focusing in the absence of any field-particle interactions, does not affect the shape of the parallel profile of the strahl VDF ($f_{s,\parallel}$). This argument was used in the works by Hefti et al. (1999); MacNeil et al. (2017); Berčič et al. (2020), trying to relate the temperature of the supra-thermal electron components to the coronal electron temperature at their origin. The study by Berčič et al. (2020), including the analysis of data from Parker Solar Probe (PSP) and Helios missions, reveals that the *strahl parallel temperature* ($T_{s\parallel}$), defined with a Maxwellian fit to the $f_{s,\parallel}$, does not vary with radial distance. Together with the found anti-correlation between $T_{s\parallel}$ and the solar wind speed, the authors conclude that the strahl does carry the information about the state of the electron VDF in the solar corona.

The results presented in this work were obtained using a numerical kinetic model of the solar wind expansion accounting for Coulomb collisions (Landi & Pantellini, 2001, 2003; Landi et al., 2010, 2012, 2014). The model does not capture all of the solar wind physics, but instead allows a detailed view into a kinetic behaviour of the colliding solar wind electrons in the near-Sun regions. In comparison to the existing exospheric models, the benefits of the numerical model are:

- a statistical treatment of binary Coulomb collisions instead of using a Fokker-Planck collision operator,
- a self-consistent calculation of the ambipolar electric field, and
- a continuous transition between the collisional and collision-less regime (the exobase is not defined as a single radial distance and is not required as an input parameter).

The modelled solar wind and its evolution through the acceleration region is described with plasma moments in Sec. 3. The analysis of the obtained electron VDFs permits an investigation of the effects of the ambipolar electric field on the VDFs (Sec. 4), and of the radial evolution of the strahl electron component (Sec. 5).

2 Numerical model

We use the fully kinetic model BiCoP (Binary Collisions in Plasmas) to simulate the radial expansion of the solar wind. Details of the model are described by Landi and Pantellini (2001, 2003), who in the first work present the evolution of solar wind moments over the first 0.2 R$_S$ above the solar surface. In the second work they extend their simulation domain to reach up to 50 R$_S$, however, with decreased proton to electron mass ratio. Later works with BiCoP use realistic solar wind characteristics, like proton-electron mass ratio and the input plasma moments, and present the radial evolution of electron VDF between 0.3 and 3 R$_S$, where the solar wind has already reached its terminal velocity and the effect of gravity can be neglected (Landi et al., 2012, 2014). They show that the model produces a two-component electron VDF function - consisting of the core and the strahl, and the global solar wind moments which compare well with the observed values. With the evolution of the code as well as computer technology we are now able to conduct the simulations of the solar wind acceleration region where the effect of gravity is of great importance (1 R$_S$ - 49 R$_S$) using real proton to mass ratio and reproducing the plasma moments measured by the Parker Solar Probe (Fox et al., 2016).

A schematics of the simulation setup is shown in Fig. 1. The model is 1-dimensional in space and 3-dimensional in velocity space. N macroparticles are included in the simulations representing two species – electrons and protons, defined by their opposite signed charge and realistic mass ratio ($\frac{m_p}{m_e} = 1837$). The particles are accelerated by the Sun's gravitational force and the ambipolar electric field force:

$$\frac{d^2r}{dt^2} = -\frac{GM_S}{r^2} + \frac{\vec{L}^2}{m_i^2 r^3} + \frac{q}{m_i}E(r), \tag{1}$$

where r is the radial distance from the Sun, G the gravitational constant, M_S the mass of the Sun, m_i the mass of a particle and $E(r)$ the ambipolar electric field. $\vec{L}$ is the angular momentum that can be expressed in terms of perpendicular particle velocity: $\vec{L} = m_i\vec{r} \times \vec{v}$. In the model we assume a radial magnetic field so that angular magnetic conservation is equivalent to the magnetic moment conservation (Landi et al., 2012).

The main parameter defining the behaviour of the system is the ratio between the gravitational potential and the electron thermal energy at r_0, the distance from

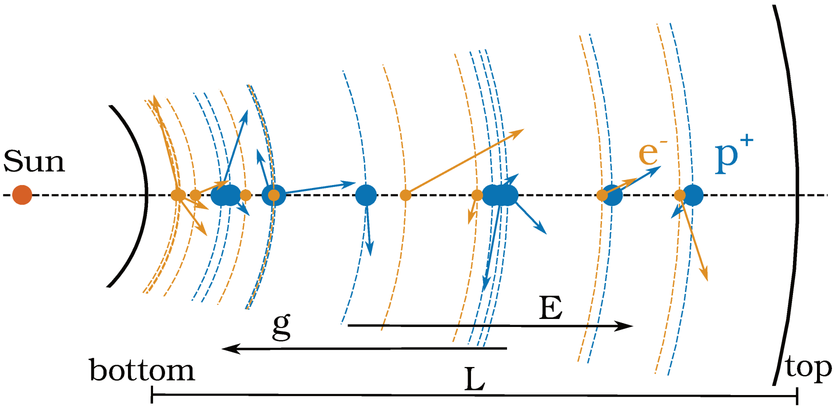

Figure 1. A schematics of the BiCoP model. The same amount of electrons (yellow) and protons (blue) moves in one dimension, which is aligned with the radial direction. The particles' velocities are defined in 3-dimensional space and represented by arrows in the schematics. We marked the two simulation boundaries and the directions of two fields acting upon the particles: the gravitational and the electric field.

the Sun's centre and the simulation bottom boundary:

$$\gamma = \frac{GM_S}{r_0} \cdot \frac{m_e}{2k_B T_{e,bot}}, \tag{2}$$

where $T_{e,bot}$ is the temperature of electrons at the bottom simulation boundary. Gravity is thus expressed as

$$g_0 = \gamma \frac{l}{r_0}, \tag{3}$$

with l the length of the simulation domain.

A benefit of the described kinetic model is a self-consistent calculation of the ambipolar electric field. The electric field in the simulation is composed of two contributions. First is a global electric field, radially decreasing with r^2, keeping the balance between electron and proton fluxes. Second is the charge-neutralising electric field, a local polarisation field resulting from local charge imbalances (Landi & Pantellini, 2001). This field is obtained by considering each particle as a thin spherical conducting shell centred in the Sun, and calculating the local field of a system of conducting spherical plates (Landi & Pantellini, 2003).

Another BiCoP strength is the statistical treatment of binary Coulomb collisions. When two particles find themselves on the same position along the dimension of the simulation, they can either suffer an elastic collision or pass each other undisturbed. The collision probability decreases with v^4, as predicted by Coulomb cross-section. To save the computational time particles with relative velocity lower than a defined velocity limit (v_C) will collide every time. Landi and Pantellini (2001) show that this computational simplification does not change the Coulomb collisions properties and have the same effect on the electron VDF as long as v_C is smaller than the thermal velocity of the electrons at any radial distance ($v_C < v_{th}$). Even more, we make use of this parameter to vary the collisionality of the system.

The one-dimensional simulation domain is limited by the bottom and the top boundary, of which the bottom boundary is located closer to the Sun. The shape of the proton and electron VDFs in these two points is defined with the input parameters $T_{e,p,bot}$, $T_{e,top}$. In the present study all the boundary VDFs are isotropic

Table 1. Presented simulation runs and their crucial input parameters.

Parameters	Unit	A	LC	MC	HC
N		22500	22500	22500	22500
v_C	$v_{th,0}$	0.4	**0.4**	**0.3**	**0.2**
$T_{e,p,bot}$	10^6 K	2	1.4	1.4	1.4
$T_{e,top}$	10^6 K	0.82	0.77	0.77	0.77
g_0		0.1416	0.0225	0.0225	0.0225
r	R_S	**1 - 46**	3 - 49	3 - 49	3 - 49
v_{bot}	km/s	0	104	104	104
v_{top}	km/s	218	228	228	228

and Maxwellian-like, which leaves us with the temperature and the bulk velocity as the only free parameters. The bottom and top velocities are the same for both species (v_{bot}, v_{top}). We define the temperature of the both species at the bottom ($T_{e,bot}, T_{p,bot}$), and the temperature of electrons on the top ($T_{e,top}$), as the protons at the top have a supersonic velocity, thus all leaving the simulation domain and being re-injected at the bottom. On the contrary, electrons are subsonic, thus a portion of them has to be injected back from the top boundary with a probability and velocity which are given by the distribution function assumed at the top. The equal flux between the two species is assured everywhere in the system only by the self-consistent electric field. The kinetic model tends toward a stationary, quasi-neutral solar wind solution only if the boundary conditions are also a part of this solution. Therefore the choice of $T_{e,top}$ and v_{top} is not really free, and depends on the $T_{e,bot}$ and $T_{p,bot}$, as well as on the collisionality of the system. For each of the presented simulation runs, test runs were preformed iterating towards good values for the top boundary parameters.

The particle's velocity distribution functions are built by binning the spatial domain in 40 bins and the velocity space in 80 × 80 bins in the radial and perpendicular direction. Once the stationary state has been reached the position and velocity of the particles are regularly sampled to build the velocity distribution function as function of the distance. Moments of the distribution function are also directly computed in the simulation.

The presented simulation runs with their key parameters are listed in Tab. 1.

3 Density, velocity & temperature

3.1 Method

3.1.1 Physical unit density

Fig. 2 shows the radial evolution of density (n), velocity (v), and core electron temperature ($T_{e,core}$) over the simulation domain for the four presented simulation runs. The physical units of the parameters in the equation of motion (Eq. 1: r, v, T, E) are all determined through the mass, gravity and temperature of the corona. Particle density, however, does not affect gravitational and electric fields, but it plays an important role for the properties of Coulomb collisions. The physical units for density are thus determined using the electron-proton collision frequency ($\nu_{e,p}(r)$) measured in the simulation and comparing it to the Fokker-Planck electron-proton transport collision frequency for a plasma with known density (n) and temperature (T):

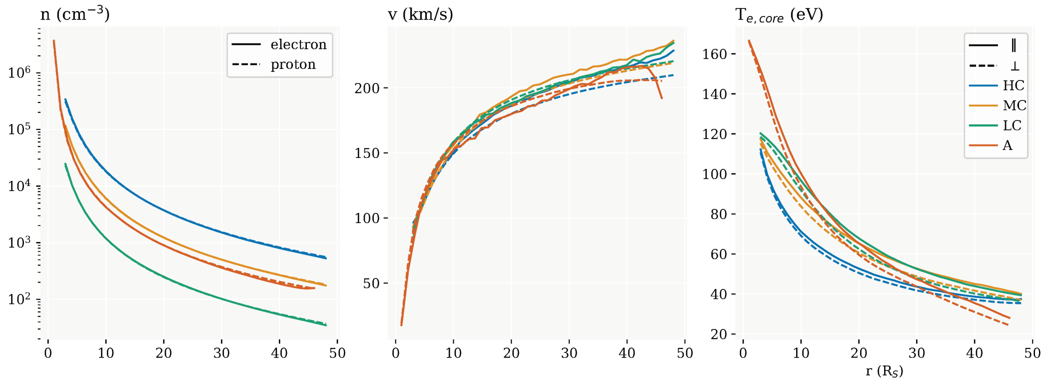

Figure 2. The evolution of electron and proton density (left), velocity (middle), and electron core parallel and perpendicular temperature (right) for all the presented simulations runs specified in Tab. 1.

$$n = \frac{\nu_{e,p} v_{th,0}}{l} \cdot \frac{3\epsilon_0^2 m_e^{1/2} (k_B T)^{3/2}}{4(2\pi)^{1/2} e^4} \frac{1}{ln\Lambda}, \tag{4}$$

where $v_{th,0}$ is the electron thermal velocity in the first radial bin and $ln\Lambda$ is the Coulomb logarithm:

$$ln\Lambda = ln(\frac{12\pi(\epsilon_0 k_B T)^{3/2}}{n^{1/2} e^3}). \tag{5}$$

Since the unknown density n is required for the calculation of $ln\Lambda$, we first obtain n' assuming $ln\Lambda = 24$ in Eq. 4, which is close to expected value for resulting plasma parameters: $ln\Lambda(T = 172eV, n = 10^6 cm^{-3}) = 24.3$, $ln\Lambda(T = 120eV, n = 10^4 cm^{-3}) = 26.1$. The final density n_0 is ten obtained by:

$$n_0 = n' \frac{24}{ln\Lambda(n')}, \tag{6}$$

The first radial bin is the densest and most collisional, thus n_0 is calculated there, and used to normalise the other radial bins accordingly with the number of particles they contain.

Simulation run A, the only presented run starting from $r_0 = 1R_S$, exhibits very strong gradients in density, velocity and temperature for its first three radial bins ($< 3R_S$, see Fig. 2). The Knudsen number, rises from $\sim 10^{-2}$ (1st bin) to ~ 0.5 (3rd bin), remaining in the collisional regime. Because the collisionality continues to stay high in the 3rd radial bin, the density there can be determined through the comparison with the Fokker-Planck collision frequency as well. However, the value obtained this way turns out to be an order of magnitude lower than the value calculated through normalisation to the first radial bin. This gives us a high uncertainty on the calculated physical unit density. The accuracy could be improved by increasing the amount of particles used in the simulation, which would substantially increase the computation time. Instead, we decided to exclude the high-gradient region just above the solar surface and conducted our other presented simulation runs staring from $r_0 = 3R_S$. This way, the used amount of particles is sufficient to provide a good estimate of the physical unit density.

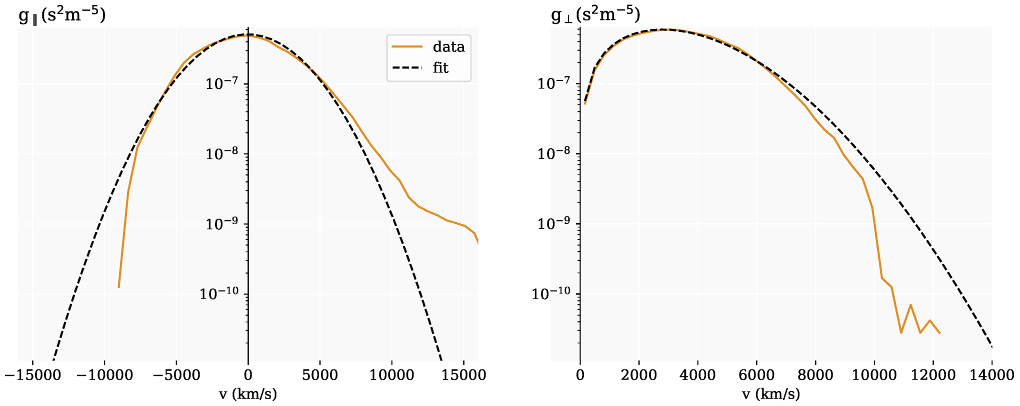

Figure 3. An example of a core fit to $g(v_{\|}, v_{\perp})$, shown with the parallel (left), and the perpendicular (right) cut through electron VDF multiplied by $v_{\perp}$. An example is taken from simulation run MC at the radial distance of 35 R_S.

3.1.2 Core electron fit

Electron VDFs in the simulation are produced for each of the 40 radial bins, on a 2-dimensional cartesian grid (80,80) with a maximum velocity of $4v_{th,0}$. The output function $g(v_{\|}, v_{\perp})$ is given in a form:

$$g(v_{\|}, v_{\perp}) = f(v_{\|}, v_{\perp}) \cdot v_{\perp}, \tag{7}$$

where $f(v_{\|}, v_{\perp})$ is the velocity distribution function, and $v_{\|}$ and $v_{\perp}$ are the velocities parallel and perpendicular to the magnetic field (which is in the simulations purely radial). The lower energy part of $g(v_{\|}, v_{\perp})$ is fitted with a bi-Maxwellian distribution function multiplied by $v_{\perp}$ (see Fig. 10):

$$g_c(v_{\perp}, v_{\|}) = A_c \exp\left(\frac{v_{\perp}^2}{w_{\perp}^2} + \frac{(v_{\|} - \Delta v_{\|})^2}{w_{\|}^2}\right) \cdot v_{\perp}, \tag{8}$$

where $\Delta v_{\|}$ is the drift velocity along the magnetic field, and the core density (n_c), and the core parallel and perpendicular temperatures can be obtained by:

$$n_c = A_c \cdot \pi^{3/2} w_{\perp}^2 w_{\|}, \tag{9}$$

$$T_{c\perp,\|} = \frac{m_e w_{\perp,\|}^2}{2k_B}. \tag{10}$$

3.2 Results

Simulation run A starts at the solar surface where we set the input proton and electron VDFs to be isotropic Maxwellians with a temperature of 2 MK (172 eV) and zero bulk velocity (see Tab. 1). The density in the first radial bin reaches $4 \cdot 10^6 cm^{-3}$ (see Fig. 2). The density and velocity of both species are aligned verifying charge neutrality and mass flux conservation. Solar wind protons become supersonic at the distance of 4 R_S and reach their highest velocity of 206 km/s at 42 R_S. As mentioned in the previous section, due to high gradients in the first few radial bins we have a large uncertainty on the calculated density for the simulation run A. We show this run to prove that BiCoP can produce a supersonic wind from a static hot solar

Table 2. Electron moments for simulations HC, MC, and LC at 35 R_S.

Moments	HC	MC	LC
n (cm^{-3})	1129	376	76
v (km/s)	211	217	212
$\mathrm{T}_{e,core,\parallel}$ (eV)	40.7	48.4	47.6
$\mathrm{T}_{e,core,\perp}$ (eV)	39.0	44.6	43.3

corona, and use the obtained temperature and velocity as a guidance for the input parameters for the runs HC (high collisionality), MC (medium collisionality) and LC (low collisionality) starting from 3 R_S. As mentioned above, $T_{e\&p,bot}$ and v_{bot} are not independent parameters, and a simulation starting with $T_{e\&p,bot} = 150$ eV, and $v_{bot} = 90$ km/s at 3 R_S, as follows from the simulation run A, does not result in a stationary solution. That is because the bottom boundary proton and electron VDFs (at 3 R_S) are set to be isotropic Maxwellians, however, in the simulation run A at this distance the VDFs are already deformed: protons appear anisotropic and electrons start to form a tenuous strahl population. Instead of changing the shape of the VDFs at the bottom boundary of the simulations starting at 3 R_S we decrease $T_{e\&p,bot}$ (to 120 eV). This way the radial evolution of v is similar for all runs, while there are some differences in the radial evolution of T.

Because the highest gradients are avoided for the runs HC, MC, and HC, the used amount of particles (22500 electrons and 22500 protons) provides us with much better statistics. We study the effect of Coulomb collisions by varying the system collisionality using the input variable v_C. Run HC is the most collisional ($v_C = 0.4$), which is reflected in higher density and steeper decrease in core electron temperature with radial distance (see Fig. 2). The core stays close to isotropic all through the simulation domain, while in less collisional runs MC ($v_C = 0.3$) and LC ($v_C = 0.2$), the parallel core electron temperature is notably larger than the perpendicular one. The collisionality does not appear to have an effect on the final solar wind velocity, which is similar for all three runs, ~ 220 km/s. This result is in contradiction with the simulation results shown by Landi and Pantellini (2003), who found that denser solar wind is accelerated to higher velocities. The discrepancy between the two results could be a consequence of the reduced proton to electron mass ratio, or much smaller amount of particles used in the simulation runs from Landi and Pantellini (2003).

For a quantitative comparison of the obtained electron moments with the Parker Solar Probe data we list the simulation values at 35 R_S in Tab. 2.

4 Electric field & electric potential

4.1 Method

Another simulation output is the ambipolar electric field (E) at the position of every simulation particle. These values are then binned accordingly with the 40 radial bins and integrated over radial distance to obtain the electric potential (ϕ).

In the exospheric solar wind models, the total electric potential difference between any given distance and infinity has an important effect on the electron VDF. At any radial distance (r) the antisunward moving electrons with the energy higher than the electric potential energy ($\mathcal{E}_\phi(r)$) are able to escape and form the strahl population, while electrons with energy below $\mathcal{E}_\phi(r)$ can not escape and form a ballistic, core population. The antisunward core electrons are trapped in a potential well: they

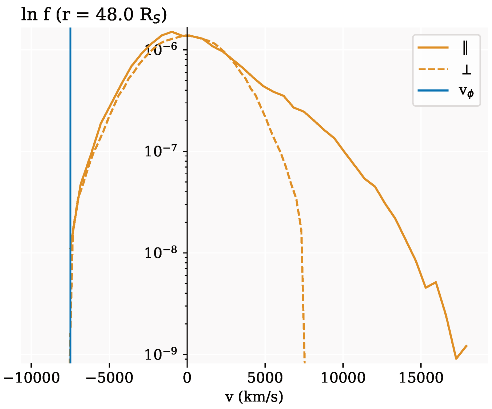

Figure 4. Parallel and perpendicular cuts through electron VDF, in the last radial bin of the simulation run MC, at a distance of 48 R_S, plotted in the *Sun's rest frame.* The negative cutoff velocity is marked with a blue line.

advance up to a distance where their radial velocity becomes zero, and then start falling back towards the Sun, at every distance reaching the same absolute velocity as on the way up, only in the opposite direction. The velocity of electrons with the energy $e\phi$:

$$v_\phi(r) = \sqrt{\frac{2e\phi(r)}{m_e}}, \tag{11}$$

thus represents a boundary in the sunward direction, the cutoff velocity below which no electrons are found. v_ϕ is defined in the Sun's rest frame.

The electric potential difference obtained in the simulation is not the total electric potential supposed to be present in the solar wind, but the potential difference between a given radial distance and the top simulation boundary ($\Delta\phi(r) = \phi_{top} - \phi(r)$). To obtain the total electric potential, and not only the potential over the simulation length, we estimated the potential difference between the top boundary and infinity, or interstellar medium ($\phi_{\infty-top}$). The ambipolar electric field is the strongest close to the Sun where the solar wind acceleration is the fastest, and decreases with radial distance with a power law between 1 and 2. Therefore $\phi(r)$ asymptotically approaches zero for large radial distances and $\phi_{\infty-top}$ is relatively small.

Fist we estimated $\phi_{\infty-top}$ from the electron VDF in the last radial bin. We use the exospheric model prediction and look for the cutoff electron velocity in the sunward direction (see Fig. 4). Technically this cutoff velocity is determined by the electron VDF prescribed at the upper boundary ($T_{e,top}$). Even though $T_{e,top}$ is an input parameter, it is dependant on the conditions set at the bottom boundary, and was found trough iteration towards a stationary solution conserving fluxes of both species. As $T_{e,top}$ is the same for runs HC, MC and LC, so is the cutoff velocity in the last radial bin: $v_{\phi,top} = -7490$ km/s. This velocity corresponds to electric potential $\phi_{\infty-top} = 159$ V.

The estimation of $\phi_{\infty-top}$ can also be found from the radial extrapolation of E measured in the simulation runs. To predict the behaviour of E for the distances above the top boundary, existing values were fitted with a power law function:

$$f_E(r) = a \cdot r^b, \tag{12}$$

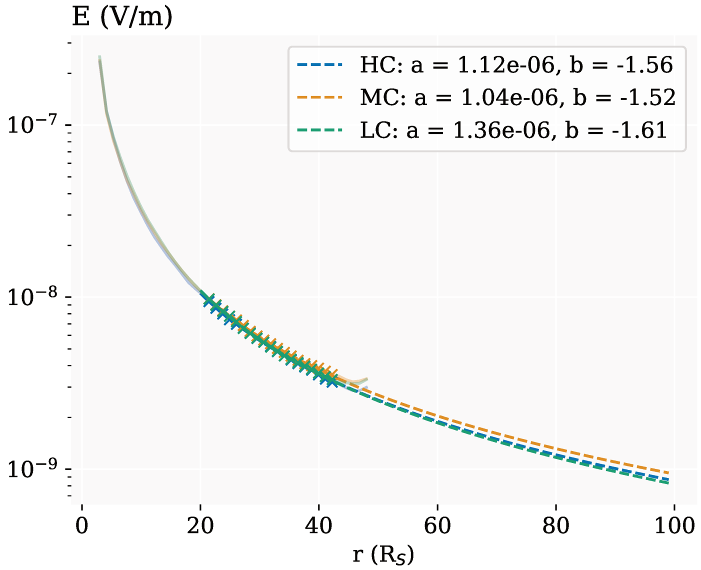

Figure 5. The extrapolation of E above the top simulation boundary. E measured in the simulation runs HC, MC and LC is shown with a pale full line, crosses denote the points used for the fitting with Eq. 12, and the dashed lines the fitted curves. The obtained fitting parameters are shown in the legend.

where a and b are the fitting parameters. The fit was preformed only to the points above the distance of 21 R_S to avoid regions of strong solar wind acceleration. Acceleration contributes to the total value of E, and only above the acceleration region we expect for E to evolve as a power law with the radial distance. An upper radial distance limit was set to 44 R_S, to avoid the effects of the simulation upper boundary. The results of the fitting procedure are shown in Fig. 5, where the fitted values are marked by crosses and the dashed line represents the obtained fit for each of the three simulation runs. The obtained fitting parameters (a and b) are marked in the legend. $\phi_{top,\infty}$ is then obtained by integration of Eq. 12 on the interval between 49 R_S and ∞. The resulting $\phi_{top,\infty}$ are very close to the one estimated from electron VDF, amounting to 159, 181, and 144 V, for simulation runs HC, MC, and LC, respectively.

Even though $\phi_{top,\infty}$ is not a direct output of the simulation, we are confident in the obtained values, as the two different estimation approaches give very similar results. For simplicity, the value $\phi_{\infty-top} = 159$ V obtained from electron VDFs, is used in further analysis.

The absolute value of ambipolar electric field obtained by the simulation is compared to the Dreicer electric field (E_D) (Dreicer, 1959), a measure of electric field strength required for an electron with a kinetic energy of $\frac{3}{2}k_BT_e$ to gain the energy of k_BT_e in one mean-free-collision time. E_D is defined as:

$$E_D = \frac{k_BT_{e,core}}{e\lambda_{mfp}}, \tag{13}$$

where λ_{mfp} stands for the mean-free path, which is calculated as the ratio of electron thermal velocity ($v_{e,th}$) and electron - proton collision frequency ($\nu_{e,p}$) measured in the simulation.

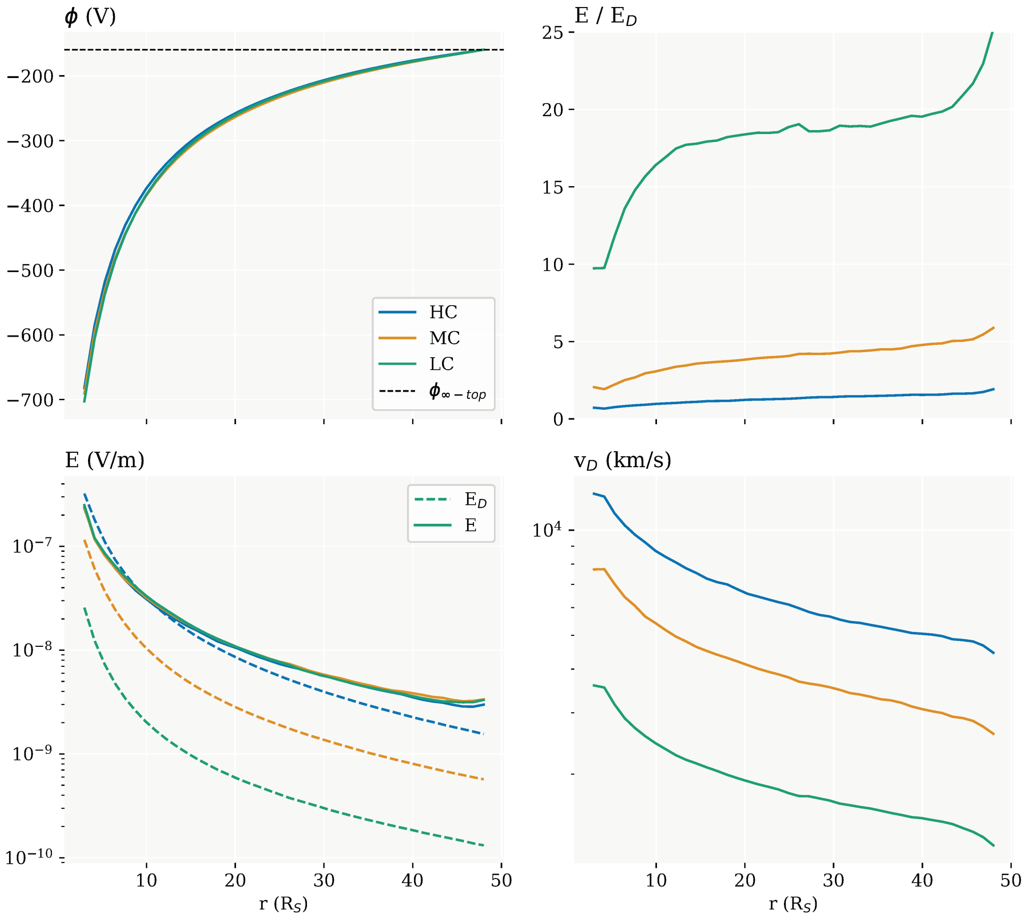

Figure 6. (a) Electric potential measured in the simulations and shifted for the estimated potential above the top simulation boundary ($\phi_{\infty-top}$), (b) Ambipolar electric field (E) (full line) and Dreicer electric field (dashed line), (c) The ratio between ambipolar and Dreicer electric field, (d) separation velocity (v_D).

Following the works of Fuchs et al. (1986); Scudder (1996), the electron velocity space can be separated into two regions by a boundary velocity defined as:

$$v_D = \sqrt{\frac{3k_BT_e}{m_e} \cdot \frac{2E_D}{E}}, \tag{14}$$

where E is the total, ambipolar electric field. Electrons with velocity lower than v_D defined in the ion rest frame, collide frequently enough for the electric force to be overdamped with Coulomb collisions, preserving a Maxwellian shaped VDF. Electrons with velocity higher than the defined boundary are underdamped by collisions and experience an acceleration by the electric force, becoming the so called, runaway electrons.

4.2 Results

The radial evolution of electric potential (ϕ) and electric field (E) is shown in Fig. 6 (a, b). While both of these quantities remain very similar for the three simulations,

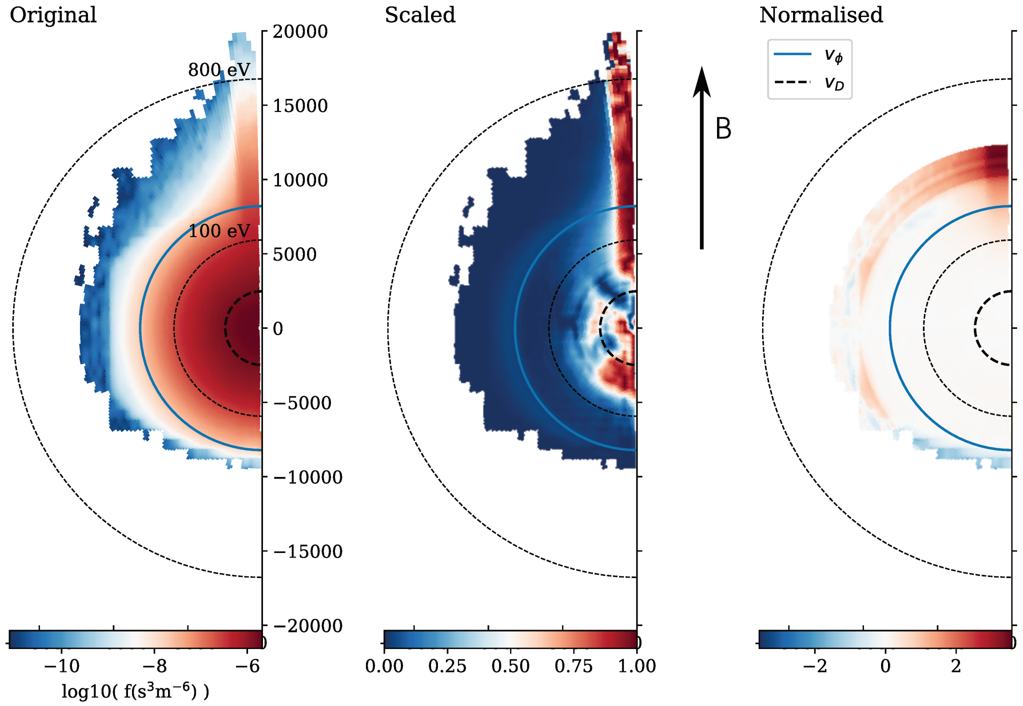

Figure 7. Two-dimensional representation of a gyrotropic electron VDF in the 28th radial bin (35 R_S) of the simulation run MC. The original electron VDF is shown on the left, a scaled VDF in the middle, and a normalised VDF on the right. We use the core electron resting frame where magnetic field is aligned with the y-axis. The electric potential velocity (v_ϕ) and the Dreicer velocity (v_D) are marked with blue and black lines.

a strong variation is seen for the Dreicer electric filed (E_D), a parameter comparing electric field with the collisionality of the system. Accordingly, the ratio E/E_D reaches the highest values for the least collisional case ($\sim$ 20 in run LC), and stays on the order of 1 for the most collisional case (run HC, Fig. 6 (c)). Fig. 6 (d) shows the velocity v_D defined in the previous section, separating the over- and underdamped regions of the VDF.

We compare the calculated separation velocities v_ϕ and v_D with the measured electron VDFs. A new representation method introduced by Behar et al. (2020) is used to highlight higher order VDF features and their departures from isotropy. Left plot in Fig. 7 displays an original gyrotropic VDF from the simulation run MC. A 2-dimensional linear interpolation between the sampled points was used, resulting in a smoother and more continuous plot. Logarithmic colour scale allows a recognition of the typical electron VDF features: a dense and isotropic core component and a beam-like strahl at positive velocity values. The middle plot shows the same VDF in the *scaled* representation, where each energy bin – each circular belt in the $(v_\parallel, v_\perp)$ parameter space – is scaled to the values between 0 and 1. With this representation we lose the information about the absolute value of f and its strong gradient along the energy dimension, but we expose the smaller anisotropic features at all energies. In cases where two features arise in the same energy bin, the scaled VDFs can be misleading, only highlighting the bigger feature. The right plot shows the *normalised* representation, where the values are normalised to the perpendicular cut through electron VDF ($f_\perp = f(v_\parallel = 0)$). Regions of VDF where the density flux is lower than

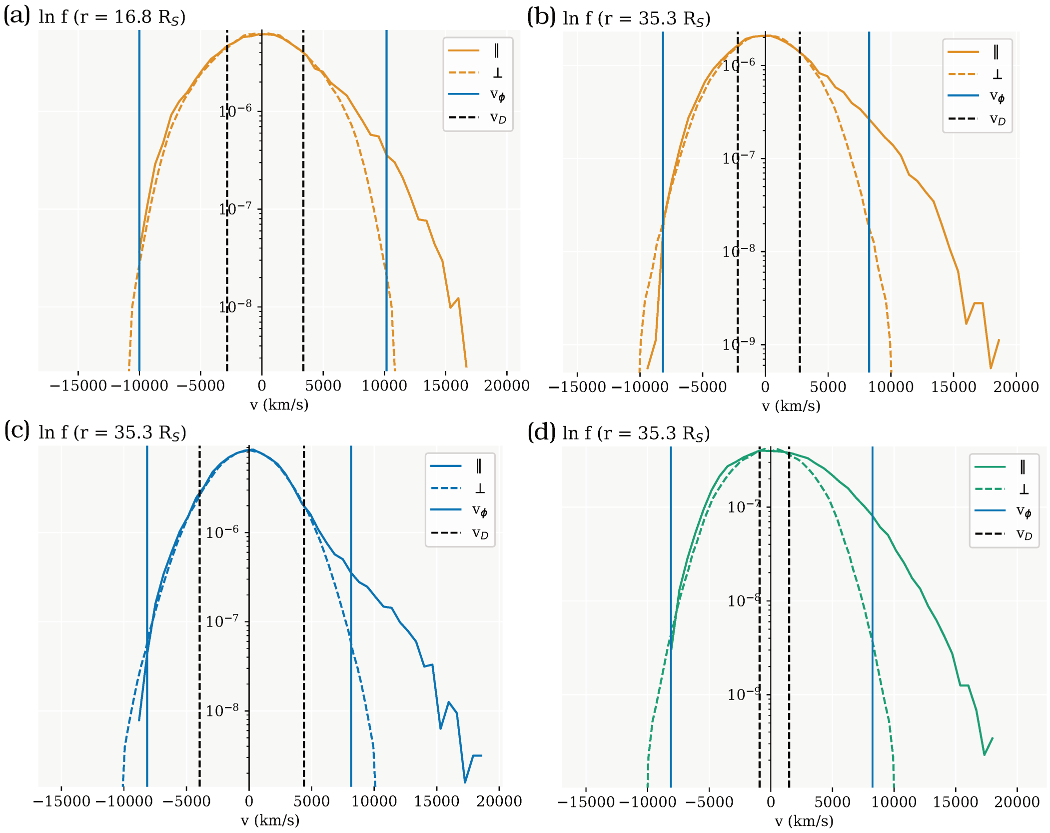

Figure 8. Parallel and perpendicular cuts through an electron VDF at the distance of 17 R_S (a) for the simulation run MC, and at 35 R_S (right) for the simulation runs HC (c), MC (b), and LC (d). The cuts are plotted in core electron resting frame. v_ϕ and v_D are indicated with blue and black lines.

along the perpendicular direction appear in blue and regions with higher density in red. With this representation the small VDF features are less pronounced than in the scaled VDF, however a relation with the original VDF is preserved through a norm, in this case chosen to be $f_\perp$. VDFs are shown in electron core resting frame, as this is the frame in which isotropy is expected.

The scaled distribution reveals two features aligned with magnetic field: the strahl present at positive velocities, and another overdensity at small negative velocities. The second feature is very small and does not appear in the normalised representation. It results from a slight mismatch between the anti-sunward portion of electron VDF leaving the simulation at the top boundary and the sunward portion defined with input parameters.

v_D and v_ϕ are overplotted as half circles with dashed black, and full blue line, respectively. Positive signed v_D corresponds to the velocity where first strahl electrons are found (see the scaled representation), while negative signed v_ϕ coincides with the cutoff, clearly seen in blue in the normalised representation. Since electron core is close to isotropic and drifting with a relatively low speed, positive signed v_ϕ also corresponds to the upper velocity limit of the core population. The same conclusions follow from the electron VDF slices at two different radial distances shown in Fig. 8 (a, b).

We are interested in the behaviour of electron VDF parallel to the magnetic field, thus we average the values within a pitch-angle 10^o to create parallel cuts through the VDF in original, scaled and normalised representation. These values are then plotted with respect to the radial distance in Fig. 9, for the simulation run MC. This plotting technique allows us to observe the radial evolution of the core and the strahl component. Over all radial distances positive v_D follows the transition between the core and the strahl component (see scaled representation), while negative v_ϕ follows the exospheric cutoff (see normalised representation). The same type figures for simulation runs HC and LC are added in Appendix A.

We compare the cuts through electron VDF at the same radial distance, in three different simulations in Fig. 8 (b, c, d). The first notable difference is the break-point velocity between the core and the strahl electrons. In the more collisional run HC the collisions are able to maintain a Maxwellian VDF up to higher velocity compared to the less collisional runs MC and LC. While v_ϕ is almost the same for all the runs, v_D reflecting the collisionality of the system varies between the runs.

Both, positive and negative signed velocities v_ϕ and v_D, are marked on all plots because they are expected to describe the VDF in both senses. In the antisunward direction $v_\phi > v_D$ means that the electrons with energies smaller than the local potential energy, which will eventually be slowed down and start falling back towards the Sun, already exhibit non-Maxwellian features. Whether this results in a non-Maxwellian sunward directed portion of electron VDF can not be determined with the results obtained from our model. The sunward portion of the VDF is defined at the top boundary and is assumed to be Maxwellian.

5 Pitch-angle width (PAW) & strahl parallel temperature ($T_{s,\|}$)

5.1 Method

We define the strahl as the residual anti-sunward component of the electron velocity distribution function and we characterise it with two parameters, the *pitch-angle width* (PAW) and the *strahl parallel temperature* ($T_\|$), in the same way as in the observational studies by Berčič et al. (2019); Berčič et al. (2020). PAW width is obtained as a full width half maximum (FWHM) of the pitch-angle distributions in an

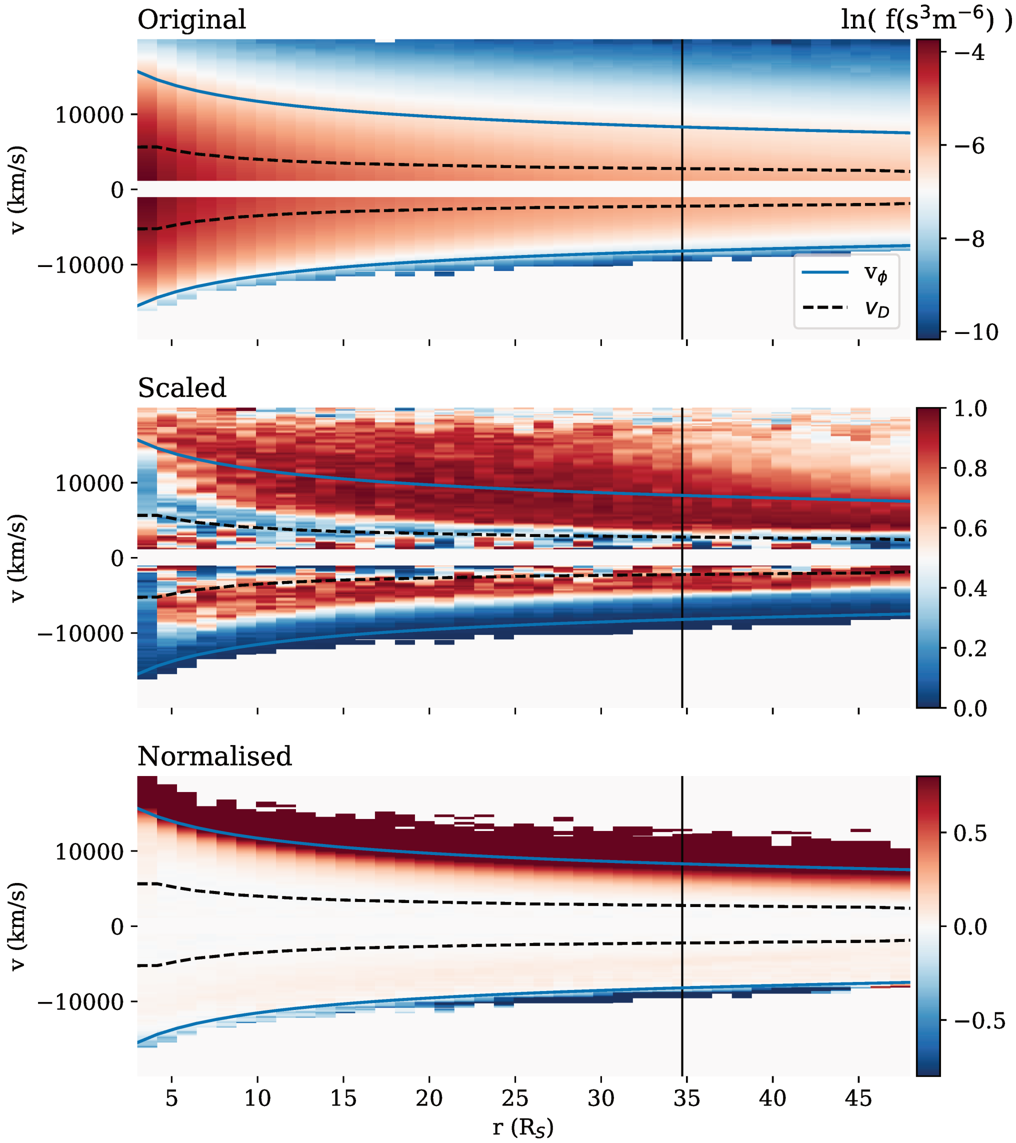

Figure 9. Parallel cuts through electron VDF plotted with respect to the radial distance in original (top), scaled (middle), and normalised (bottom) representation for the simulation run MC. v_ϕ and v_D are marked with blue and black lines. A black vertical line denotes the radial distance of the VDFs shown in Figs. 7 and 8 (right).

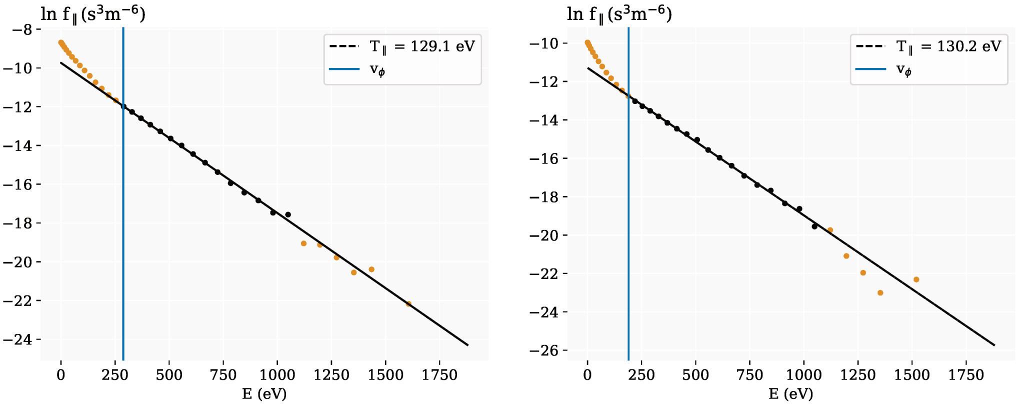

Figure 10. An example of the Maxwellian fit to the parallel strahl VDF ($f_{\|}$) to obtain $T_{s,\|}$, shown for simulation run MC at radial distances 17 R_S (left), and 35 R_S (right). The data points not included in the fit are marked with yellow and the data points included in the fit with black. The black dashed line shows the fit with the resulting $T_{s,\|}$ marked in the legend, and the blue line denotes the assumed separation velocity between the core and the strahl component.

energy bin:

$$f_i(\alpha) = f_{max,i} \cdot \exp\big(\frac{\alpha^2}{2\sigma_i^2}\big), \qquad PAW_i = 2\sqrt{2\ln 2}\cdot \sigma_i, \tag{15}$$

where α is the pitch angle and index i denotes different energy bins. We arbitrarily define 20 logarithmically spaced energy bins between energies 79 and 3162 eV. Logarithmic spacing was used to provide a better comparison between the simulation and observational data, as electrostatic analysers normally sample electron energies in this way.

$T_{s,\|}$ is obtained by fitting a 1-dimensional Maxwellian to the VDF integrated along the perpendicular direction ($f_{\|} = \int f(v_{\|}, v_{\perp}) dv_{\perp}$) in the logarithmic space:

$$\ln f_{\|}(v_{\|}) = -\frac{m_e}{2k_B \cdot T_{s\|}} \cdot v_{\|}^2 + ln\big(n_s\sqrt{\frac{m_e}{2\pi k_B \cdot T_{s\|}}}\big). \tag{16}$$

The fit is preformed only to the antisunward portion of electron velocity space dominated by the strahl electron population. We found that v_ϕ in the sunward and anti-sunward direction describes well the properties of the electron core. Therefore we use it as the separation velocity between the core dominated and strahl dominated portions of electron VDF. An upper energy limit for the energies included in the $T_{s,\|}$ fit was arbitrarily set to 1274 eV to avoid inclusion of the noise.

5.2 Results

The comparison of PAWs at the radial distance of 35 R_S for the three simulation runs shown in Fig. 11 reveals that Coulomb collisions only affect the lower energy strahl electrons. The first plotted PAW value denotes the energy at which the PAW of the electron VDF drops below 180^o, marking the boundary between the core and the strahl electrons. The strahl break point energies are different for the three runs, as already observed from VDF slices (Fig. 8). The PAWs also exhibit different shapes with respect to the electron energy: the transition between broad strahl at lower electron energies, and narrow strahl at high energies is smoother for the more collisional case

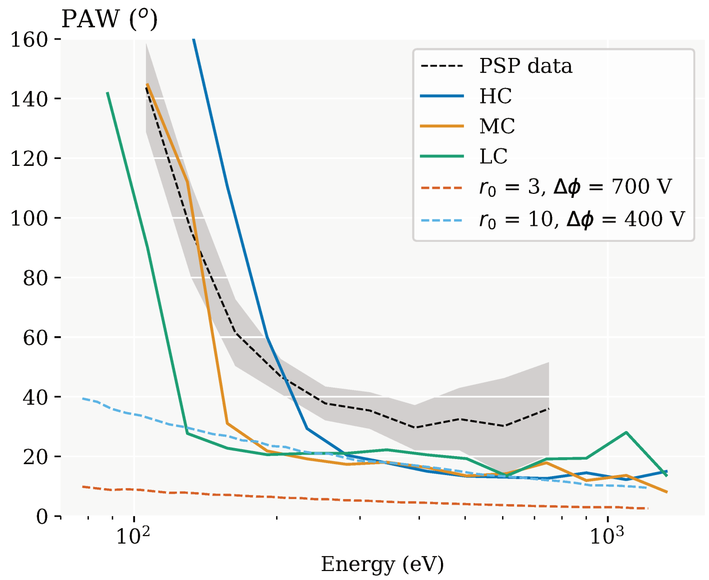

Figure 11. Strahl PAWs shown for electron VDFs at the radial distance of 35 R_S for the simulation runs HC, MC and LC. The coloured dashed lines show PAWs obtained from collisionless single-exobase focusing model for different choices of the exobase (r_0). Averaged PAW observed during the first two encounters of PSP in the low electron beta solar wind is shown with a black dashed line and a grey belt denoting the measurement error. The observational data was taken from Berčič et al. (2020).

HC, and more abrupt for the less collisional cases MC, and LC. Above $\sim$ 250 eV three PAW curves reach the same value, showing that collisionality of the system does not affect the high energy electrons.

Results of the collisionless single-exobase focusing model (see Eq. 6 in Berčič et al. (2019)) are also shown in Fig. 11 for two different sets of input parameters. The red dashed line shows the PAW obtained at 35 R_S if the exobase (r_0) is set to 3 R_S and the potential difference $\Delta\phi = 700V$ (like in BiCoP runs). As it results on still much narrower strahl, we increased the exobase and decreased the potential difference accordingly. The result of a simple model that matches well PAWs obtained from all three simulation runs above $\sim$ 250 eV, and the least collisional run LC down to the energy $\sim$ 130 eV, was found for $r_0 = 10R_S$, and $\Delta\phi = 400V$.

The black dashed line shows PAW values measured in the low electron beta solar wind (< 0.7) during the second encounter of PSP, shown in Berčič et al. (2020) - Fig. 5 (b). The observed strahls appear 10 - 20^o wider for the high electron energy part, but show a smooth transition between broad and narrow strahl, similar to the one found in the simulation run HC. The strahl break point found from PSP data appears at lower energy compared to the run HC, but correlates well to the break point found for run MC.

An increase of $T_{s,||}$ with radial distance was found in all three simulation runs. Fig. 12 shows electron VDFs integrated along the perpendicular direction ($f_{||}$) at different radial distances normalised with a integrated Maxwellian VDF defined at the

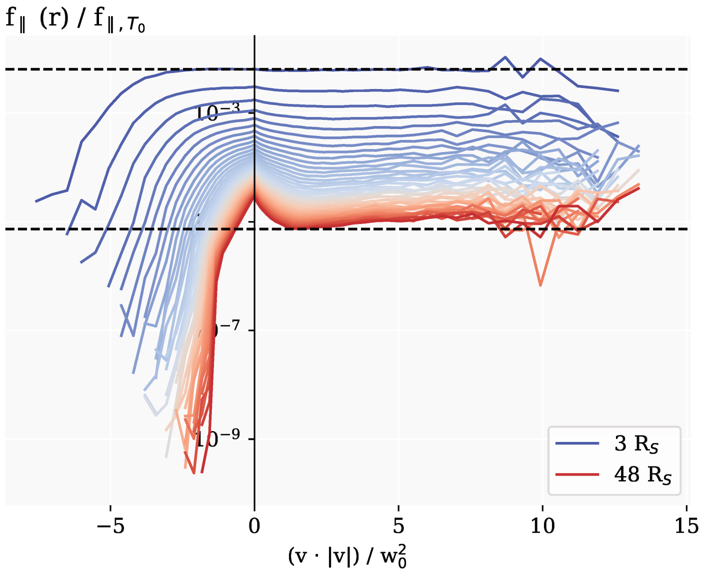

Figure 12. Electron VDFs, integrated along the ⊥ direction ($f_{\parallel}$), for different radial bins, normalised with a Maxwellian VDF with the temperature $T_{e,bot}$. X-axis represents velocity (v) multiplied with its absolute value in the units of square of thermal velocity of the electron VDF at the bottom boundary (w_0^2). Radial distance is presented in colour spanning from blue closer to the Sun to red at the top boundary. Presented data is from the run MC, the same figures from runs HC and LC can be found in Appendix B.

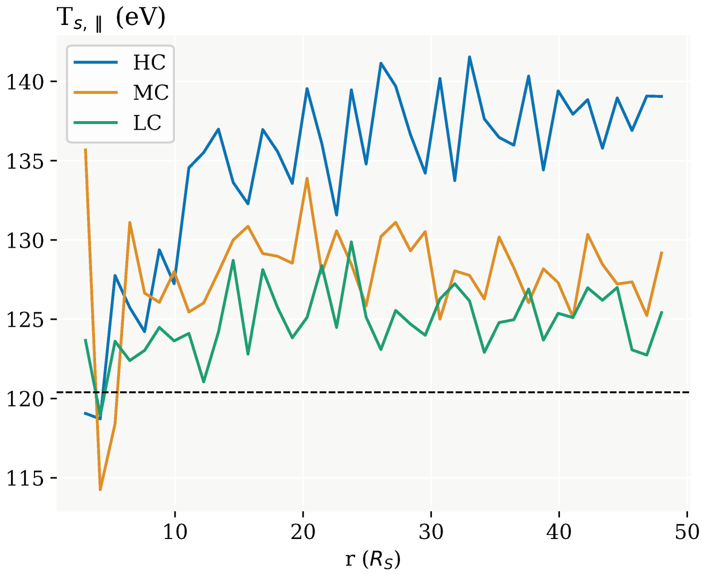

Figure 13. Evolution of $T_{\parallel}$ over radial distance for the simulation runs HC, MC, and LC. The dashed black line shows the temperature of the Maxwellian set at the bottom boundary.

bottom boundary ($f_{0,Maxw}$):

$$l = \frac{\int f_i(v_\parallel, v_\perp) dv_\perp}{\int f_{0,Maxw}(v_\parallel, v_\perp) dv_\perp}, \tag{17}$$

where index i is the number of the radial bin. This technique was used to verify the exospheric prediction, which says that $f_\parallel$ should, in absence of collisions and wave-particle interactions, remain unchanged in the exosphere, and carry the information about the shape of the VDF at the exobase to farther radial distances. If $T_{s,\parallel}$ remains unchanged from the bottom boundary the presented normalisation results in a horizontal line, as found for the VDF in the first radial bin (blue colour). Decreasing curves denote temperatures smaller than $T_{e,bot}$, which can be seen for farther radial distances (red colour) at low electron energies and represent the electron core population. Increasing curves appearing at strahl electron energies indicate that the $T_{s,\parallel}$ slightly increases with radial distances. Fig. 12 includes values from the run MC, while plots for runs HC and LC are added in Appendix B.

The same result was obtained by fitting $f_\parallel$ with a 1D Maxwellian to obtain $T_{s,\parallel}$ (see Fig. 13). The increase in $T_{s,\parallel}$ is the largest for the most collisional run A, at radial distance of 35 R_S by 15% exceeding the initial $T_{e,bot}$. The smallest increase was found in run C, amounting to 3%.

6 Discussion

6.1 Modelled and observed solar wind

The used kinetic solar wind model does not capture all the physics of the solar wind. Most importantly it does not account for electro-magnetic (EM) wave activity, or the Parker spiral, non-radial, magnetic field. It assumes spherically geometric radial expansion to reconstruct a 3-dimensions in space from its 1-dimensional simulation domain. However, it allows us to focus on electron kinetic physics on the global solar wind scales. Using this model we are able to quantify the contribution of the kinetic electron behaviour, under the influence of gravity and Coulomb collisions, in the solar wind dynamics. As the resulting electron VDFs are not far from the observed ones, we can speculate that the recognised differences between the modelled and observed VDF are the result of the physical mechanisms not included in our simulation, like EM waves or non-radial magnetic field.

The simulation run A presents the solar wind arising solely from the hot Maxwellian solar corona with a temperature of 2 MK (172 eV). This temperature is higher than value 0.79 MK reported above the surface for the coronal holes (David et al., 1998; Cranmer, 2002), but an upper limit temperature related to the edges of coronal holes in the recent study by Berčič et al. (2020) inferring the temperature of the coronal electrons from the strahl electrons measured by PSP. The estimated density at 1 R_S in the simulation is about one order of magnitude lower than that reported for the coronal holes, measured by multi-frequency radio imaging (Mercier & Chambe, 2015). Due to their small mass, the contribution of electrons to the total mass flux of the solar wind is very small, however, the high velocities they reach, and their subsonic behaviour have an important role in the solar wind acceleration. In comparison to the heavier protons, electrons evaporate from the Sun faster, which requires an existence of large-scale electric field ensuring the plasma quasi-neutrality (Lemaire & Scherer, 1971). This electric field is referred to as the *ambipolar* electric field (E), and is self-consistently obtained in the simulation. It is responsible for acceleration of the solar wind protons to the supersonic velocity at 4 R_S, and to the terminal velocity of 206 km/s. Even though the modelled corona is somewhat hotter than measured, the obtained terminal velocity is still about a third smaller than frequently observed velocities of $\sim$ 300 km/s during the first two encounters of the PSP (Kasper et al., 2019). We conclude that the ambipolar electric field is an important driver of the solar wind acceleration, but can alone not produce the terminal velocities observed in the solar wind. A significant contribution could be due to the heat and momentum transfer from electro-magnetic wave activity and turbulence (Tu & Marsch, 1997, 2001). At the same time, the shape of the coronal particle VDFs has an important effect on the solar wind acceleration. For example, fast solar wind can be produced by the exospheric solar wind models assuming a Kappa electron VDF in the solar corona (Maksimovic et al., 1997; Lamy et al., 2003) even including the effect of binary particle collisions Zouganelis et al. (2005). Moreover, several evidence seem to indicate that the coronal plasma is not in a thermal equilibrium. Strong temperature anisotropies were observed in the VDFs of coronal ions (e.g. Kohl et al., 1998). Different temperatures and thermal anisotropies in the proton distribution function can have a strong effect on the velocity of the resulting solar wind. However, the study how the solar wind terminal velocity depends on the bottom boundary parameters is out of the scope of the current work.

Our obtained electron VDF are very similar to the ones measured during the first two encounters of PSP (Halekas et al., 2019). The observed core electron temperatures, between 30 and 40 eV, are slightly lower than the modelled ones at 35 R_S. The density estimated for the simulation run MC corresponds well to an average density observed ($\sim 300 cm^-3$), while the densities in runs HC and LC reach the high and low extremes, respectively (see Tab. 2). However, as shown in Sec. 3.1.1, the determination of physical unit density from the model is not simple and some errors can be expected. We assume an accuracy up to an order of magnitude on the obtained absolute value, and pay more attention to the relative values between the simulation runs. The biggest difference between the modelled and observed VDFs is that halo electron component is not present in the modelled one. This leads us to believe that the halo is an outcome of phenomena not included in the kinetic model and we can rule out the Coulomb collisions, and ambipolar electric field as possible halo generation mechanisms.

6.2 Ambipolar electric field

The electric field in the solar wind is responsible for the energy transfer from electrons to protons, modifying the the fluid properties of the solar wind, like velocity and temperature, as well as the kinetic properties of electron VDF. Its cumulative effects explain the two-component form of electron VDF in the exospheric models (Jockers, 1970; Lemaire & Scherer, 1971). The total electric potential exerted on them by protons (through E) creates a potential well, at each radial distance separating electron VDF in two regimes. Electrons with anti-sunward velocities high enough to climb out of the potential well can escape and form the strahl. Electrons with anti-sunward velocities lower than that are ballistic. After they use all their energy they start falling back, forming the sunward directed part of electron VDF, symmetrical about v = 0 in Sun's resting frame. The ballistic population represents the electron core. In exospheric models the separation velocity (v_ϕ, Eq. 11) defines two boundaries in electron VDF. In the anti-sunward direction it separates the core and the strahl population, and in the sunward direction it defines the largest possible electron speed, referred to as the electron cutoff.

The behaviour of a fully ionised gas under the influence of an electric field of arbitrary magnitude was studied by (Dreicer, 1959, 1960). He defined a parameter relating electric field strength to the collisionality, which is after him referred to as the *Dreicer electric field* (E_D, Eq. 13). In a homogeneous plasma, an electric field of 0.43 E_D, causes electrons to drift with respect to the ions, with a velocity equal to their thermal velocity. For $E > E_D$, electrons efficiently gain energy in a process called *runaway*. This scenario, characterised by large electric currents, was observed in the fusion laboratory experiments. Scudder (1996) generalised the Dreicer's work to make it applicable to the solar wind, where zero current condition appears to be fulfilled despite the presence of ambipolar electric field (E) of the order of E_D. Analytically calculated E at the solar wind critical point was shown to be between 0.6 and 2 E_D. Following the work of Fuchs et al. (1986), he defines a boundary velocity (v_D, Eq. 14), separating the electron velocity space into a region where E is overdamped by collisions, and a region where E is underdamped.

In the series of articles by Scudder (2019a, 2019b, 2019c), the author develops a Steady Electron Runaway Model (SERM) of the solar wind, based on the presence of E. In this model, all the suprathermal electrons, moving towards or away from the Sun, are a consequence of the runaway mechanism. The expected electron VDF is shown in Scudder (2019b) - Fig. 4, where the boundary between the core and the suprathermal electrons in both parallel directions is v_D.

Two different solar wind models, provide two separation velocities. v_ϕ predicted by the exospheric models describes the effects of the electric potential, thus the cumulative effects of E. v_D from SERM model is a result of the local effects of E. v_ϕ in our simulations corresponds the cutoff velocity over all the simulation domain, while the strahl break point is well described by v_D. This is clearly visible in the least collisional run LC, where v_D is much lower than v_ϕ (see Fig. 8 (d)). In the anti-sunward direction v_ϕ still describes the properties of the core population, it marks the velocity at which the core electron flux strongly decreases.

We note that the sunward directed portion of the electron VDF had to be defined at the top boundary and was assumed to be Maxwellian. Any non-Maxwellian features injected at the top boundary are in the model propagated towards the Sun, accordingly with the separation velocity v_D. An example of a simulation run with a non-Maxwellian top boundary condition is shown in Appendix C. The feature is damped by collisions for velocities below v_D, and persists for velocities above this speed.

In the solar wind non-Maxwellian features could be produced locally through field-particle interactions, and be propagated towards the Sun. Another mechanism producing a bump in the sunward direction could be the focusing of the strahl in cases where $v_\phi > v_D$. When this condition is fulfilled, part of the strahl electrons has energy bellow the electric potential energy required to escape the Sun. This means that these electrons reach their maximal radial distance and then start falling back towards Sun. As the anti-sunward portion of the VDF below v_ϕ is non-Maxwellian, this could translate into a non-Maxwellian sunward potion as well.

6.3 Strahl electron focusing

High energy, anti-sunward moving strahl electrons are able to escape the collisional core and focus around the radial magnetic field. In a collisionless approximation, a simple model conserving magnetic moment and electron energy (Berčič et al. (2019) - Eq. 6), describes the evolution of electron VDF from the exobase, where the focusing begins, to the measuring point. Additional required input parameter is the potential difference between these two points in space ($\Delta\phi$).

The focusing taking place in the simulation accounts for two additional physical effects, compared to the simple collisionless model described above. The first difference is that the exobase is not limited to a single radial distance, and accounts for so called *multi-exobase* phenomena. In the simulations the strahl starts to form gradually, from the highest energy electrons, which are first able to avoid Coulomb collisions and focus, to the lower energy electrons following the decrease of v_D with radial distance. Therefore, strahl electrons with different energies have different exobase locations.

However, v_D gradient is the highest close to the Sun, therefore the exobases of the majority of strahl electrons lie within a relatively small radial distance. From Figs. 9, A1, and A2 we conclude that majority of the strahl is formed within $\sim 20\ R_S$. A second phenomena included in the kinetic model are the Coulomb collisions which can, despite the Coulomb cross-section decrease with v^4, have some effect on the strahl electrons.

The results in Fig. 11, show that the high energy strahl electrons are not affected by Coulomb collisions, as the same PAW values are found for the simulation runs HC, MC, and LC. For the low energy strahl electrons the effect of collisionality is reflected in the shape of the decreasing PAW with electron energy. In a collisionless model and in the least collisional simulation run LC, the transition between low strahl PAWs and core PAWs reaching over 180^o (only PAW below 180^o are shown in Fig. 11) is abrupt. While the collisions in run HC make this transition gradual and smooth, comparing better with the PAWs observed by PSP.

PAWs obtained from a single-exobase collisionless model with the exobase of 3 R_S do not compare well with PAWs measured for the collisionless, high-energy electrons in all three simulation runs, as well starting from 3 R_S. This difference is accounted to the multi-exobase phenomena. Furthermore, we found that exobase in the simple model needs to be shifted to 10 R_S, to correspond to the collisionless part of the strahl obtained by simulations BiCoP.

PAWs measured during the first two encounters of PSP, shown by Berčič et al. (2020) for the low electron beta solar wind, still appear from 10 to 20^o wider than PAWs obtained in the most collisional simulation run HC. Since the gradual transition between core and strahl electrons is very similar to our simulation result we conclude that the difference is not a consequence of Coulomb collisions. We suggest that broader strahls observed by PSP are a result of the non-radial magnetic field topology not captured by our kinetic model, or a consequence of the measurement technique, integrating electron VDF over time periods with varying magnetic field angle. In fact, in-situ measured PAWs for energies above 300 eV were found to be between 10 and 15^o larger for the instances during which the standard deviation of B was above 10 nT, than when it was below that value (Berčič et al., 2020).

The wider strahls observed could also result from scattering by EM fluctuations, however, due to the monotonic decreasing relation between strahl PAW and energy, some of scattering mechanisms can be ruled out. Scattering through a resonance with a whistler wave, for example, is expected to produce a peak in PAW at the resonant electron energy (Behar et al., 2020). And an electron VDF relaxation mechanism giving energy to a whistler wave would first scatter the higher energy strahl electrons, which would result in an increasing trend between PAW and energy (Verscharen et al., 2019).

The simple, single-exobase focusing model does not affect the parallel profile of the electron distribution function, therefore preserving its shape from the solar corona to the measuring point (Feldman et al., 1975). This argument was used by Berčič et al. (2020), who use the strahl parallel temperature ($T_{s,\|}$, Eq. 16) measured by the PSP, to make a zero order estimation of the electron temperature in the solar corona. Surprisingly, $T_{s,\|}$ was found to increase with radial distance in our simulation runs. The smallest increase was found for the least collisional run LC amounting to only 3 %, while the $T_{s,\|}$ in the most collisional run HC increased for 15 %. Due to the correlation between the percentage of increase in $T_{s,\|}$ and the collisionality of the system, we believe the effective heating of the strahl electrons is caused by Coulomb collisions.

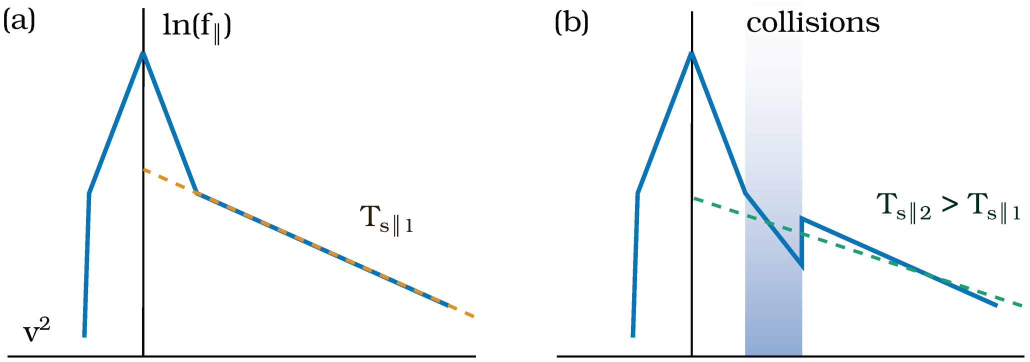

Figure 14. An illustration of how Coulomb collisions can increase $T_{s,\|}$. (a) Collisionless case, (b) collisions decrease the temperature of only lowest energy strahl electrons, which results in the increase of the total effective $T_{s,\|}$.

With a schematics in Fig. 14, we propose a physical mechanism which could result in an increase of $T_{s,\|}$ with radial distance. The parallel cut through electron VDF is illustrated with straight lines in the logarithmic parameter space, representing Maxwellians with different temperatures. Fig. 14 (a) shows the core and the strahl for a collisionless case, where a yellow dashed line represents the fit giving $T_{s,\|}$. The same VDF cut is shown in Fig. 14 (b) for a collisional case, where the lowest strahl energies are affected by Coulomb collisions. In the region marked with blue, the strahl electrons are cooled down by collisions, however, when fitting to the whole strahl energy range (green dashed line), the obtained temperature is higher than the one obtained for the collisionless case (a). In the simulation this mechanism, exaggerated in the schematics, is continuous, reshaping the the parallel cut through the strahl VDF over the radial distance. The strahl parallel profiles obtained by the kinetic model are well represented by a Maxwellian, however, it is not obvious why a mechanism described above would preserve a Maxwellian shape.

Comparing the simulation results with the observations shown by Berčič et al. (2020), we believe that most of the solar wind observed during the first two encounters of PSP best corresponds to the simulation runs HC or MC. Therefore the presented $T_{s,\|}$ (Berčič et al. (2020) - Figs. 6 and 7) probably overestimates the temperature of coronal electrons. In the simulation runs HC and MC at the distance of $\sim$ 35 R_S, $T_{s,\|}$ is overestimated by 15 % and 8 %, respectively. Applying this correction to the observed $T_{s,\|}$ with a mean value of 96 eV, we obtain the mean temperature of coronal electrons between 83 an 89 eV.

7 Conclusions

We presented results of a kinetic model of the solar wind accounting for binary Coulomb collisions (BiCoP), simulating the solar wind acceleration region (1 - 45 R_S). The model does not include EM waves and non-radial magnetic fields. Nevertheless it can produce a solar wind, accelerated only through the ambipolar electric field (E), rising from the difference in the pressure gradients between electrons and protons. High coronal temperatures were assumed, leading to the terminal solar wind velocities approximately a third smaller than the ones reported by PSP. We conclude that, while E is responsible for a big part of solar wind terminal velocity, it is not the only solar wind acceleration mechanism.

The self-consistently obtained E in our model was found to be on the order of the Dreicer electric field (E_D). We analysed the effects it has on electron VDF. The cumulative effects of E were predicted by exospheric solar wind models, and the separation velocity v_ϕ correlates well with the electron sunward cutoff velocity. Similarly, v_ϕ describes an upper velocity limit for the core population in the anti-sunward direction. The local effects of E on the VDF were described by the Steady Electron Runaway Model (SERM) (Scudder, 2019b) predicting a separation of electron velocity space into two regions separated by v_D: an overdamped region, where collisions are frequent enough to overdamp the electric force and preserve a Maxwellian VDF, and an underdamped region, where electrons can be accelerated by E and departures from a Maxwellian VDF can be found. In our obtained VDFs v_D represents well the strahl break point velocity.

Strahl focusing in the kinetic model is compared to the simple, single-exobase collisionless focusing model. We find that at the distance of 34 R_S, energies above 250 eV are not affected by Coulomb collisions. Pitch-angle widths are observed to be larger than the ones obtained from a simple focusing model, and this difference is accounted to the multi-exobase phenomena. For energies below 250 eV Coulomb collisions are able to scatter the strahl electrons and change the dependence of PAW on electron energy.

In the collisionless approximation the strahl parallel temperature ($T_{s,\|}$) is independent of radial distance. However, $T_{s,\|}$ in our simulation runs was found to be larger than the temperature set at the bottom boundary, and the increase to be correlated to the collisionality of the system. We presented a raw idea of how scattering of the low energy strahl electrons by Coulomb collisions in the solar wind acceleration region could affect $T_{s,\|}$.

Appendix A Radial evolution of the parallel cuts through electron VDF for simulation runs HC and LC

Appendix B $f_\|$ normalised to the Maxwellian at the bottom boundary for simulation runs HC and LC

Appendix C Simulation run with a non-Maxwellian top boundary condition

With slices through electron VDFs at different radial distances we demonstrate the propagation of the non-Maxwellian feature produced in the sunward portion of the electron VDF at the top boundary. The parameters used for the presented run are gathered in Table C1. In this simulation run, v_D (black dashed line in Fig. C1) separates the over-, and underdamped parts of the VDF in both directions. In the antisunward direction it marks the beginning of the strahl component, as already shown for runs HC, MC, and LC. In the sunward direction v_D follows the beginning of the feature propagating towards the Sun, separating electron VDF into Maxwellian and non-Maxwellian parts.

Acknowledgments

References

Behar, E., Sahraoui, F., & Berčič, L. (2020). Resonant whistler-electron interactions: Mms observations vs. test-particle simulation. *arXive*, *submitted*.

Berčič, L., Maksimović, M., Landi, S., & Matteini, L. (2019). Scattering of strahl electrons in the solar wind between 0.3 and 1 au: Helios observations. *Monthly Notices of the Royal Astronomical Society*, *486*(3), 3404–3414. doi: 10.1093/

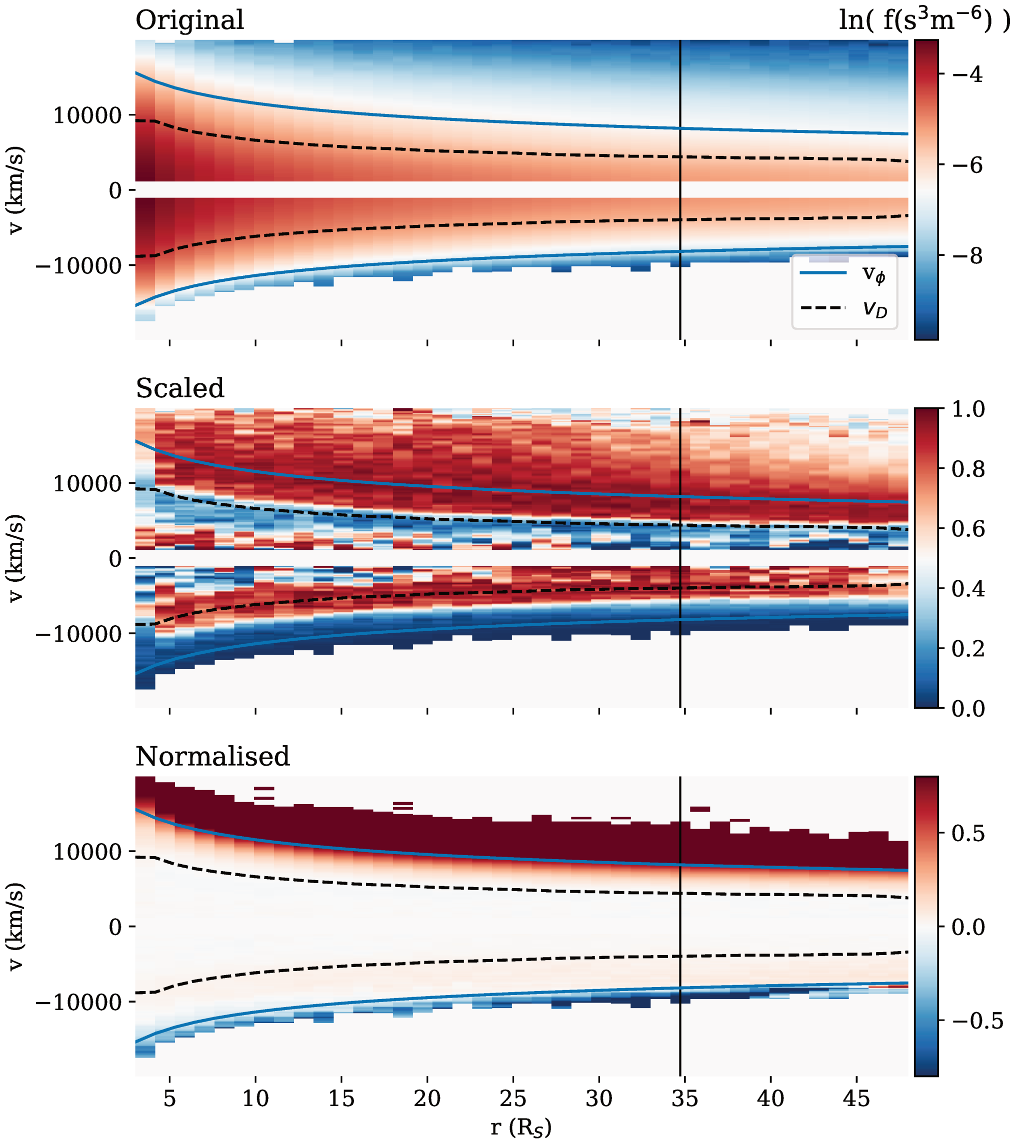

Figure A1. Parallel cuts through electron VDF plotted with respect to the radial distance in original (top), scaled (middle), and normalised (bottom) representation for the simulation run HC. v_ϕ and v_D are marked with blue and black lines. A black vertical line denotes the radial distance of the VDFs shown in Fig. **??** (left).

mnras/stz1007

Berčič, L., Larson, D., Whittlesey, P., Maksimović, M., Badman, S. T., Landi, S., . . . Stevens, M. L. (2020, April). Coronal Electron Temperature Inferred from the Strahl Electrons in the Inner Heliosphere: Parker Solar Probe and Helios Observations. , *892*(2), 88. doi: 10.3847/1538-4357/ab7b7a

Brasseur, G., & Lemaire, J. (1977, February). Fitting of hydrodynamic and kinetic solar wind models. , *25*(2), 201-203. doi: 10.1016/0032-0633(77)90028-9

Chamberlain, J. W. (1960, January). Interplanetary Gas.II. Expansion of a Model Solar Corona. , *131*, 47. doi: 10.1086/146805

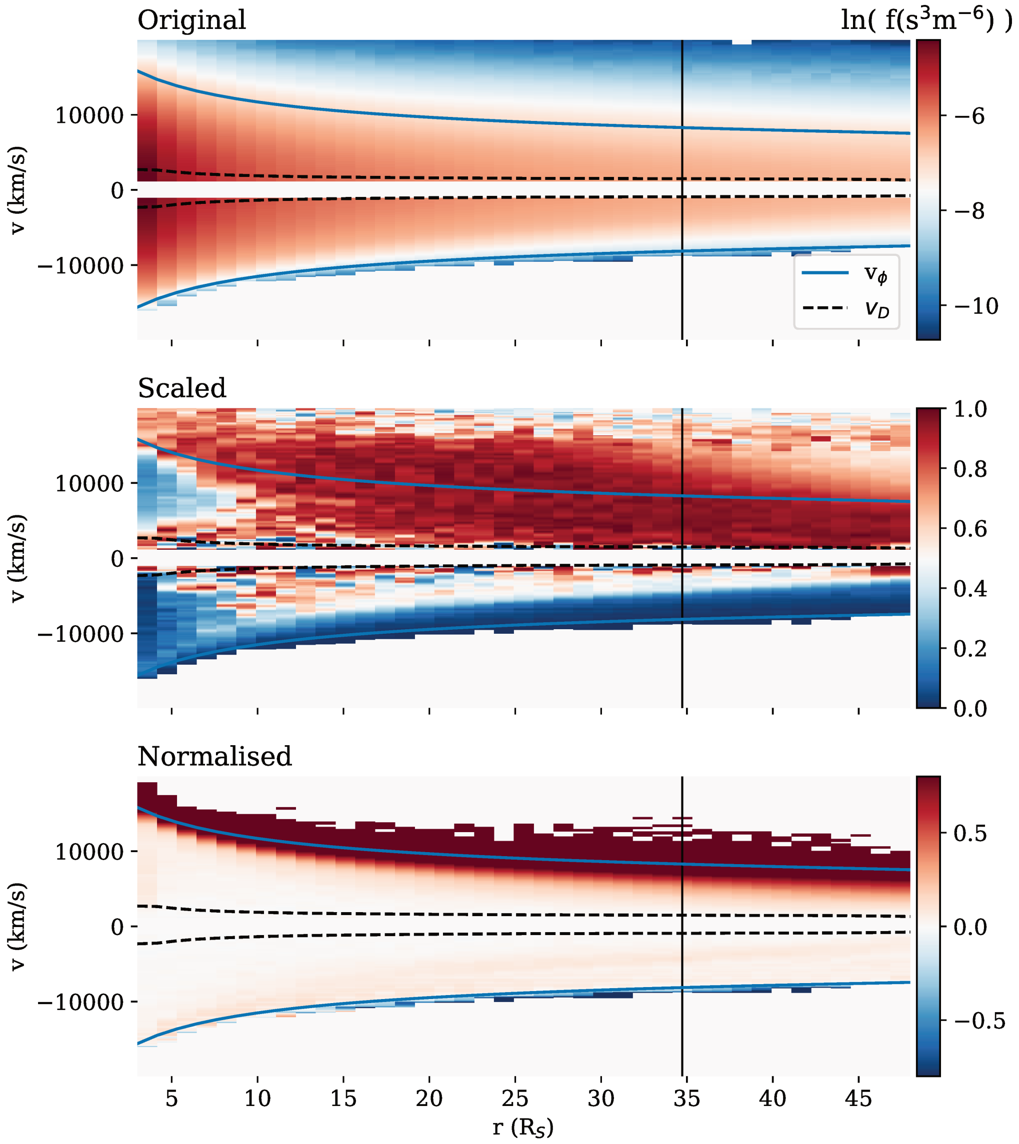

Figure A2. Parallel cuts through electron VDF plotted with respect to the radial distance in original (top), scaled (middle), and normalised (bottom) representation for the simulation run LC. v_ϕ and v_D are marked with blue and black lines. A black vertical line denotes the radial distance of the VDFs shown in Fig. **??** (right).

Cranmer, S. (2002). Coronal holes and the solar wind. *COSPAR Colloquia Series*(January), 1–10. Retrieved from `http://www.sciencedirect.com/science/article/pii/S0964274902800038` doi: 10.1016/S0964-2749(02)80003-8

David, C., Gabriel, A. H., Bely-Dubau, F., Fludra, A., Lemaire, P., & Wilhelm, K. (1998). Measurement of the electron temperature gradient in a solar coronal hole. *Astronomy and Astrophysics*, *336*(3), 90–94.

Dreicer, H. (1959, July). Electron and Ion Runaway in a Fully Ionized Gas. I. *Physical Review*, *115*(2), 238-249. doi: 10.1103/PhysRev.115.238

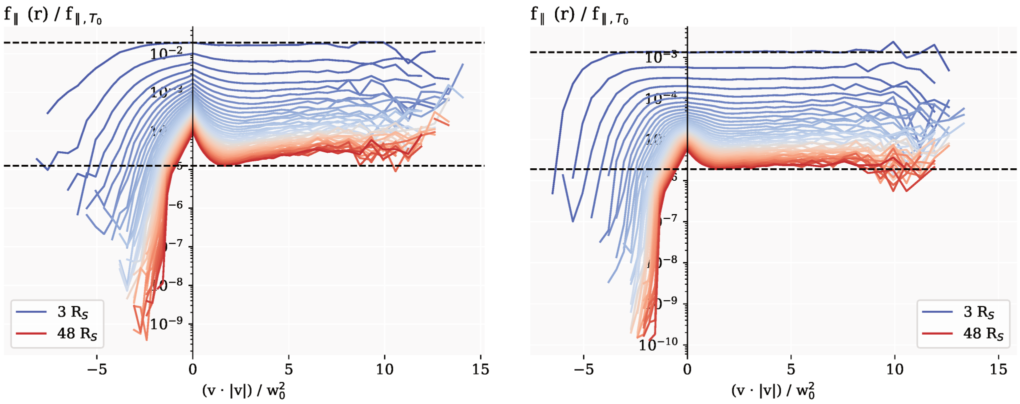

Figure B1. Electron VDFs, integrated along the ⊥ direction ($f_\parallel$), for different radial bins, normalised with a Maxwellian VDF with the temperature $T_{e,bot}$. X-axis represents velocity (v) multiplied with its absolute value in the units of square of thermal velocity of the electron VDF at the bottom boundary (w_0^2). Radial distance is presented in colour spanning from blue closer to the Sun to red at the top boundary. Presented data is from the run HC (left) and run LC (right).

Table C1. Presented simulation runs and their crucial input parameters.

Parameters	Unit	non-Maxw.
N		22500
v_C	$v_{th,0}$	0.3
$T_{e,p,bot}$	10^6 K	1
$T_{e,top}$	10^6 K	0.4
g_0		0.0177
r	R_S	4 - 49
v_{bot}	km/s	77
v_{top}	km/s	171

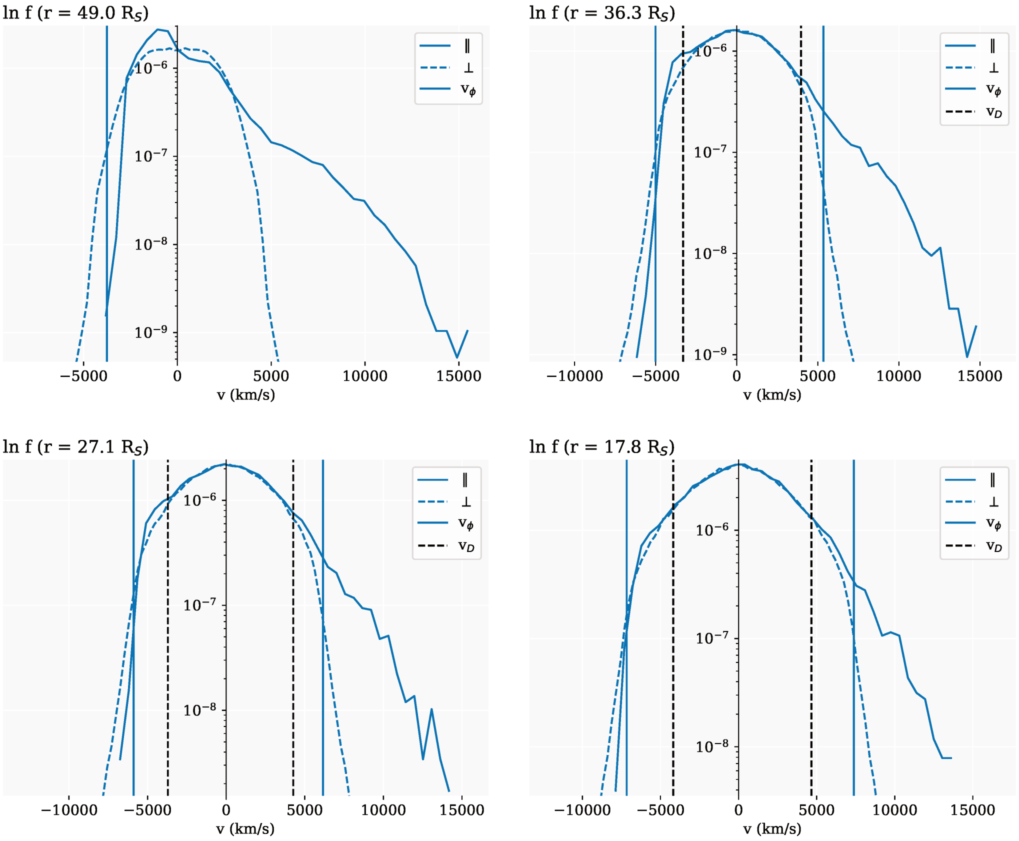

Figure C1. Parallel and perpendicular cuts through electron VDF, at different radial distances (marked in the title of each plot) for the simulation run with a non-Maxwellian top boundary condition. The electric potential velocity (v_ϕ) and the Dreicer velocity (v_D) are marked with blue and black lines.

Dreicer, H. (1960, January). Electron and Ion Runaway in a Fully Ionized Gas. II. *Physical Review*, *117*(2), 329-342. doi: 10.1103/PhysRev.117.329

Feldman, W. C., Asbridge, J. R., Bame, S. J., Montgomery, M. D., & Gary, S. P. (1975). Solar wind electrons. *Journal of Geophysical Research.* doi: 10.1029/JA080i031p04181

Fox, N. J., Velli, M. C., Bale, S. D., Decker, R., Driesman, A., Howard, R. A., ... Szabo, A. (2016). The Solar Probe Plus Mission: Humanity's First Visit to Our Star. *Space Science Reviews*, *204*(1-4), 7–48. Retrieved from `http://dx.doi.org/10.1007/s11214-015-0211-6` doi: 10.1007/s11214-015-0211-6

Fuchs, V., Cairns, R. A., Lashmore-Davies, C. N., & Shoucri, M. M. (1986, September). Velocity-space structure of runaway electrons. *Physics of Fluids*, *29*(9), 2931-2936. doi: 10.1063/1.865493

Graham, G. A., Rae, I. J., Owen, C. J., Walsh, A. P., Arridge, C. S., Gilbert, L., ... Waite, J. H. (2017). The evolution of solar wind strahl with heliospheric distance. *Journal of Geophysical Research: Space Physics*, *122*(4), 3858–3874. doi: 10.1002/2016JA023656

Halekas, J. S., Whittlesey, P., Larson, D. E., Mcginnis, D., Maksimovic, M., Berthomier, M., ... Malaspina, D. M. (2019). Electrons in the Young Solar Wind: First Results from Parker Solar Probe. *Astrophysical Journal.*

Hammond, C. M., Feldman, W. C., McComas, D. J., Phillips, J. L., & Forsyth, R. J. (1996). Variation of electron-strahl width in the high-speed solar wind: ULYSSES observations. *Astronomy and Astrophysics*, *316*, 350–354. Retrieved from `http://ukads.nottingham.ac.uk/abs/1996A{\&}A...316..350H`

Hefti, S., Zurbuchen, T. H., Fisk, L. A., Gloeckler, G., Larson, D., & Lin, R. P. (1999). The transition from slow to fast solar wind: Charge state composition and electron observations. *AIP Conference Proceedings*, 471, 495. doi: 10.1063/1.58682

Horaites, K., Boldyrev, S., & Medvedev, M. V. (2019). Electron strahl and halo formation in the solar wind. *Monthly Notices of the Royal Astronomical Society*, *484*(2), 2474–2481. doi: 10.1093/mnras/sty3504

Horaites, K., Boldyrev, S., Wilson, L. B., Viñas, A. F., & Merka, J. (2018). Kinetic theory and fast wind observations of the electron strahl. *Monthly Notices of the Royal Astronomical Society*, *474*(1), 115–127. doi: 10.1093/MNRAS/STX2555

Jockers, K. (1970). Solar Wind Models Based on Exospheric Theory. *\aap*, *6*, 219. Retrieved from `https://ui.adsabs.harvard.edu/abs/1970A{\&}A.....6..219J`

Kajdič, P., Alexandrova, O., Maksimovic, M., Lacombe, C., & Fazakerley, A. N. (2016). Suprathermal Electron Strahl Widths in the Presence of Narrow-Band Whistler Waves in the Solar Wind. *The Astrophysical Journal*, *833*(2), 172. Retrieved from `http://stacks.iop.org/0004-637X/833/i=2/a=172?key=crossref.6e0cb686c031c19378090937228000f2` doi: 10.3847/1538-4357/833/2/172

Kasper, J. C., Bale, S. D., Belcher, J. W., Berthomier, M., Case, A. W., Chandran, B. D. G., ... Schwadron, N. A. (2019). Alfvénic velocity spikes and rotational flows in the near-Sun solar wind. (July). doi: 10.1038/s41586-019-1813-z

Kohl, J. L., Noci, G., Antonucci, E., Tondello, G., Huber, M. C. E., Cranmer, S. R., ... Suleiman, R. M. (1998, July). UVCS/SOHO Empirical Determinations of Anisotropic Velocity Distributions in the Solar Corona. , *501*(1), L127-L131. doi: 10.1086/311434

Krishna Jagarlamudi, V. (2020, April). Whistler waves. *Journal of Geophysical Reserch.* doi: 10.1093/inprep

Lamy, H., Pierrard, V., Maksimovic, M., & Lemaire, J. F. (2003, Jan). A kinetic exospheric model of the solar wind with a nonmonotonic potential energy for the protons. *Journal of Geophysical Research (Space Physics)*, *108*(A1), 1047.

doi: 10.1029/2002JA009487

Landi, S., Matteini, L., & Pantellini, F. (2012). On the competition between radial expansion and coulomb collisions in shaping the electron velocity distribution function: Kinetic simulations. *Astrophysical Journal*, *760*(2). doi: 10.1088/0004-637X/760/2/143

Landi, S., Matteini, L., & Pantellini, F. (2014). Electron heat flux in the solar wind: Are we observing the collisional limit in the 1 AU data? *Astrophysical Journal Letters*, *790*(1), 1–5. doi: 10.1088/2041-8205/790/1/L12

Landi, S., & Pantellini, F. (2001). On the temperature profile and heat flux in the solar corona: Kinetic simulations. *Astronomy & Astrophysics*, *372*, 686–701. doi: 10.1051/0004-6361:20010552

Landi, S., & Pantellini, F. (2003). Kinetic simulations of the solar wind from the subsonic to the supersonic regime. *Astronomy and Astrophysics*, *400*, 769–778. doi: 10.1051/0004-6361:20021822

Landi, S., Pantellini, F., & Matteini, L. (2010). Radial evolution of the electron velocity distribution in the heliosphere: Role of collisions. *AIP Conference Proceedings*, *1216*(1), 218-222. Retrieved from `https://aip.scitation.org/doi/abs/10.1063/1.3395841` doi: 10.1063/1.3395841

Lemaire, J., & Scherer, M. (1970). Model of the polar ion-exosphere. *Planetary and Space Science*, *18*(1), 103 - 120. Retrieved from `http://www.sciencedirect.com/science/article/pii/003206337090070X` doi: https://doi.org/10.1016/0032-0633(70)90070-X

Lemaire, J., & Scherer, M. (1971). Kinetic models of the solar wind. *Journal of Geophysical Research*, *76*, 7479–. doi: 10.1029/JA076i031p07479

MacNeil, A. R., Owen, C. J., & Wicks, R. T. (2017). Tests for coronal electron temperature signatures in suprathermal electron populations at 1 AU. *Annales Geophysicae*, *35*(6), 1275–1291. doi: 10.5194/angeo-35-1275-2017

Macneil, A. R., Owens, M. J., Lockwood, M., Štverák, Š., & Owen, C. J. (2020, Jan). Radial Evolution of Sunward Strahl Electrons in the Inner Heliosphere. , *295*(2), 16. doi: 10.1007/s11207-019-1579-3

Maksimovic, M., Pierrard, V., & Lemaire, J. F. (1997, August). A kinetic model of the solar wind with Kappa distribution functions in the corona. , *324*, 725-734.

Maksimovic, M., Zouganelis, I., Chaufray, J. Y., Issautier, K., Scime, E. E., Littleton, J. E., . . . Elliott, H. (2005). Radial evolution of the electron distribution functions in the fast solar wind between 0.3 and 1.5 AU. *Journal of Geophysical Research: Space Physics*, *110*(A9), 1–9. doi: 10.1029/2005JA011119

Mercier, C., & Chambe, G. (2015, November). Electron density and temperature in the solar corona from multifrequency radio imaging. , *583*, A101. doi: 10.1051/0004-6361/201425540

Pagel, C., Gary, S. P., de Koning, C. A., Skoug, R. M., & Steinberg, J. T. (2007). Scattering of suprathermal electrons in the solar wind: ACE observations. *Journal of Geophysical Research*, *112*(A4), 1–11. Retrieved from `http://www.agu.org/pubs/crossref/2007/2006JA011967.shtml` doi: 10.1029/2006JA011967

Pannekoek, A. (1922, July). Ionization in stellar atmospheres (Errata: 2 24). , *1*, 107.

Parker, E. N. (1958, November). Dynamics of the Interplanetary Gas and Magnetic Fields. *The Astrophysical Journal*, *128*, 664. doi: 10.1086/146579

Pierrard, V., Maksimovic, M., & Lemaire, J. (1999, August). Electron velocity distribution functions from the solar wind to the corona. , *104*(A8), 17021-17032. doi: 10.1029/1999JA900169

Pilipp, W. G., Miggenrieder, H., Montgomery, M. D., Mühlhäuser, K. H., Rosenbauer, H., & Schwenn, R. (1987). Characteristics of electron velocity distribution functions in the solar wind derived from the Helios Plasma Experiment.

Journal of Geophysical Research, *92*(A2), 1075. Retrieved from `http://doi.wiley.com/10.1029/JA092iA02p01075` doi: 10.1029/JA092iA02p01075

Rosseland, S. (1924, June). Electrical state of a star. , *84*, 720-728. doi: 10.1093/mnras/84.9.720

Saito, S., & Gary, P. S. (2007). All whistlers are not created equally: Scattering of strahl electrons in the solar wind via particle-in-cell simulations. *Geophysical Research Letters*, *34*(1), 1–5. doi: 10.1029/2006GL028173

Salem, C., Hubert, D., Lacombe, C., Bale, S. D., Mangeney, A., Larson, D. E., & Lin, R. P. (2003, March). Electron Properties and Coulomb Collisions in the Solar Wind at 1 AU: Wind Observations. , *585*(2), 1147-1157. doi: 10.1086/346185

Scudder, J. D. (1996, June). Dreicer order ambipolar electric fields at Parker's steady state solar wind sonic critical point. , *101*(A6), 13461-13472. doi: 10.1029/96JA00189

Scudder, J. D. (2019a, November). The Long-standing Closure Crisis in Coronal Plasmas. , *885*(2), 148. doi: 10.3847/1538-4357/ab48e0

Scudder, J. D. (2019b, November). Steady Electron Runaway Model SERM: Astrophysical Alternative for the Maxwellian Assumption. , *885*(2), 138. doi: 10.3847/1538-4357/ab4882

Scudder, J. D. (2019c, September). The Thermal Force in Astrophysical Plasmas: Current Free Coulomb Friction. , *882*(2), 146. doi: 10.3847/1538-4357/ab3348

Štverák, Š., Maksimovic, M., Trávníček, P. M., Marsch, E., Fazakerley, A. N., & Scime, E. E. (2009). Radial evolution of nonthermal electron populations in the low-latitude solar wind: Helios, Cluster, and Ulysses Observations. *Journal of Geophysical Research: Space Physics*, *114*(5), 1–15. doi: 10.1029/2008JA013883

Tao, J., Wang, L., Zong, Q., Li, G., Salem, C. S., Wimmer-Schweingruber, R. F., … Bale, S. D. (2016, Mar). Quiet-time Suprathermal (~0.1-1.5 keV) Electrons in the Solar Wind. , *820*(1), 22. doi: 10.3847/0004-637X/820/1/22

Tu, C. Y., & Marsch, E. (1997, April). Two-Fluid Model for Heating of the Solar Corona and Acceleration of the Solar Wind by High-Frequency Alfven Waves. , *171*(2), 363-391. doi: 10.1023/A:1004968327196

Tu, C. Y., & Marsch, E. (2001, May). On cyclotron wave heating and acceleration of solar wind ions in the outer corona. , *106*(A5), 8233-8252. doi: 10.1029/2000JA000024

Verscharen, D., Chandran, B. D. G., Jeong, S.-Y., Salem, C. S., Pulupa, M. P., & Bale, S. D. (2019, December). Self-induced Scattering of Strahl Electrons in the Solar Wind. , *886*(2), 136. doi: 10.3847/1538-4357/ab4c30

Vocks, C., Salem, C., Lin, R. P., & Mann, G. (2005). Electron Halo and Strahl Formation in the Solar Wind by Resonant Interaction with Whistler Waves. *The Astrophysical Journal*, *627*(1), 540–549. Retrieved from `http://stacks.iop.org/0004-637X/627/i=1/a=540` doi: 10.1086/430119

Štverák, Š., Trávníček, P., Maksimovic, M., Marsch, E., Fazakerley, A. N., & Scime, E. E. (2008, Mar). Electron temperature anisotropy constraints in the solar wind. *Journal of Geophysical Research (Space Physics)*, *113*(A3), A03103. doi: 10.1029/2007JA012733

Wilson, I., Lynn B., Chen, L.-J., Wang, S., Schwartz, S. J., Turner, D. L., Stevens, M. L., … Goodrich, K. A. (2019a, Dec). Electron Energy Partition across Interplanetary Shocks. II. Statistics. , *245*(2), 24. doi: 10.3847/1538-4365/ab5445

Wilson, I., Lynn B., Chen, L.-J., Wang, S., Schwartz, S. J., Turner, D. L., Stevens, M. L., … Goodrich, K. A. (2019b, Jul). Electron Energy Partition across Interplanetary Shocks. I. Methodology and Data Product. , *243*(1), 8. doi: 10.3847/1538-4365/ab22bd

Zouganelis, I., Maksimovic, M., Meyer-Vernet, N., Lamy, H., & Issautier, K. (2004). A transonic collisionless model of the solar wind. *The Astrophysical Journal*, *606*, 542–554. Retrieved from `http://arxiv.org/abs/astro-ph/0402358` doi: 10.1086/382866

Zouganelis, I., Meyer-Vernet, N., Landi, S., Maksimovic, M., & Pantellini, F. (2005, June). Acceleration of Weakly Collisional Solar-Type Winds. , *626*(2), L117-L120. doi: 10.1086/431904

BIBLIOGRAPHY

Abramowitz, M. and I. A. Stegun (1972). *Handbook of Mathematical Functions*.

Agapitov, O. V. et al. (Mar. 2020). "Sunward-propagating Whistler Waves Collocated with Localized Magnetic Field Holes in the Solar Wind: Parker Solar Probe Observations at 35.7 R Radii." In: *The Astrophysical Journal Letters* 891.1, L20, p. L20. DOI: `10.3847/2041-8213/ab799c`. arXiv: `2002.09837 [astro-ph.SR]`.

Bale, S. D. et al. (2019). "Highly structured slow solar wind emerging from an equatorial coronal hole." In: *Nature* July. ISSN: 14764687. DOI: `10.1038/s41586-019-1818-7`. URL: `http://dx.doi.org/10.1038/s41586-019-1818-7`.

Behar, E., F. Sahraoui, and L. Berčič (2020). "Resonant whistler-electron interactions: MMS observations vs. test-particle simulation." In: *Journal of Geophysical Research: Space Physics*. DOI: `10.1029/2020JA028040`.

Brasseur, G. and J. Lemaire (Feb. 1977). "Fitting of hydrodynamic and kinetic solar wind models." In: *Planetary and Space Science* 25.2, pp. 201–203. DOI: `10.1016/0032-0633(77)90028-9`.

Bruno, R. and B. Bavassano (Sept. 1997). "On the winding of the IMF spiral for slow and fast wind within the inner heliosphere." In: *Geophysical Research Letters* 24.18, pp. 2267–2270. DOI: `10.1029/97GL02183`.

Chamberlain, Joseph W. (Jan. 1960). "Interplanetary Gas.II. Expansion of a Model Solar Corona." In: *The Astrophysical Journal* 131, p. 47. DOI: `10.1086/146805`.

Chandran, B. D. G., D. Verscharen, E. Quataert, J. C. Kasper, P. A. Isenberg, and S. Bourouaine (Oct. 2013). "Stochastic Heating, Differential Flow, and the Alpha-to-proton Temperature Ratio in the Solar Wind." In: *The Astrophysical Journal* 776.1, 45, p. 45. DOI: `10.1088/0004-637X/776/1/45`. arXiv: `1307.8090 [astro-ph.SR]`.

Chen, C. H. K., T. S. Horbury, A. A. Schekochihin, R. T. Wicks, O. Alexandrova, and J. Mitchell (June 2010). "Anisotropy of Solar Wind Turbulence between Ion and Electron Scales." In: *Physical Review Letters* 104.25, 255002, p. 255002. DOI: `10.1103/PhysRevLett.104.255002`. arXiv: `1002.2539 [physics.space-ph]`.

Chen, W. M., C. S. Lai, H. E. Lin, and W. C. Lin (Jan. 1972). "Collisionless solar wind in the spiral magnetic field." In: *Journal of Geophysical Research* 77.1, p. 1. DOI: `10.1029/JA077i001p00001`.

Cranmer, Steven R. (Aug. 2002). "Coronal Holes and the High-Speed Solar Wind." In: *Space Science Reviews* 101.3, pp. 229–294.

David, C., A. H. Gabriel, F. Bely-Dubau, A. Fludra, P. Lemaire, and K. Wilhelm (1998). "Measurement of the electron temperature gradient in a solar coronal hole." In: *Astronomy and Astrophysics* 336.3, pp. 90–94. ISSN: 00046361.

Dreicer, H. (July 1959). "Electron and Ion Runaway in a Fully Ionized Gas. I." In: *Physical Review D (Applied Physics)* 115.2, pp. 238–249. DOI: 10.1103/PhysRev.115.238.

Dzifčáková, Elena, Alena Zemanová, Jaroslav Dudík, and Šimon Mackovjak (Feb. 2018). "Spectroscopic Diagnostics of the Non-Maxwellian κ-distributions Using SDO/EVE Observations of the 2012 March 7 X-class Flare." In: *The Astrophysical Journal* 853.2, 158, p. 158. DOI: 10.3847/1538-4357/aaa426. arXiv: 1801.02936 [astro-ph.SR].

Feldman, W. C., J. R. Asbridge, S. J. Bame, M. D. Montgomery, and S. P. Gary (1975). "Solar wind electrons." In: *Journal of Geophysical Research*. ISSN: 01480227. DOI: 10.1029/JA080i031p04181.

Graham, G. A. et al. (2017). "The evolution of solar wind strahl with heliospheric distance." In: *Journal of Geophysical Research: Space Physics* 122.4, pp. 3858–3874. ISSN: 21699402. DOI: 10.1002/2016JA023656.

Gringauz, K. I., V. G. Kurt, V. I. Moroz, and I. S. Shklovskii (Jan. 1960). "Results of Observations of Charged Particles Observed Out to R = 100, 000 km, with the Aid of Charged-Particle Traps on Soviet Space Rockets." In: *Astronomicheskii Zhurnal* 37, p. 716.

Hahn, M., E. Landi, and D. W. Savin (Aug. 2011). "Differential Emission Measure Analysis of a Polar Coronal Hole during the Solar Minimum in 2007." In: *The Astrophysical Journal* 736.2, 101, p. 101. DOI: 10.1088/0004-637X/736/2/101.

Halekas, J S et al. (2019). "Electrons in the Young Solar Wind: First Results from Parker Solar Probe." In: *The Astrophysical Journal*. arXiv: arXiv:1912.02216v1.

Hammond, C. M., W. C. Feldman, D. J. McComas, J. L. Phillips, and R. J. Forsyth (1996). "Variation of electron-strahl width in the high-speed solar wind: ULYSSES observations." In: *Astronomy and Astrophysics* 316, pp. 350–354. ISSN: 0004-6361. URL: http://ukads.nottingham.ac.uk/abs/1996A{\&}A...316..350H.

Horaites, Konstantinos, Stanislav Boldyrev, and Mikhail V. Medvedev (2019). "Electron strahl and halo formation in the solar wind." In: *Monthly Notices of the Royal Astronomical Society* 484.2, pp. 2474–2481. ISSN: 13652966. DOI: 10.1093/mnras/sty3504. arXiv: 1811.01098.

Horaites, Konstantinos, Stanislav Boldyrev, Lynn B. Wilson, Adolfo F. Viñas, and Jan Merka (2018). "Kinetic theory and fast wind observations of the electron strahl." In: *Monthly Notices of the Royal Astronomical Society* 474.1, pp. 115–127. ISSN: 13652966. DOI: 10.1093/MNRAS/STX2555. arXiv: 1706.03464.

Howard, R. A. et al. (Dec. 2019). “Near-Sun observations of an F-corona decrease and K-corona fine structure.” In: *Nature* 576.7786, pp. 232–236. DOI: 10.1038/s41586-019-1807-x.

Jagarlamudi, Vamsee Krishna, Olga Alexandrova, Laura Berčič, Thierry Dudok de Wit, Vladimir Krasnoselskikh, Milan Maksimovic, and Štěpán Štverák (July 2020). “Whistler Waves and Electron Properties in the Inner Heliosphere: Helios Observations.” In: *The Astrophysical Journal* 897.2, 118, p. 118. DOI: 10.3847/1538-4357/ab94a1.

Jockers, K. (1970). “Solar Wind Models Based on Exospheric Theory.” In: *Astronomy and Astrophysics* 6, p. 219. URL: https://ui.adsabs.harvard.edu/abs/1970A{\&}A.....6..219J.

Kajdič, P., O. Alexandrova, M. Maksimovic, C. Lacombe, and A. N. Fazakerley (2016). “Suprathermal Electron Strahl Widths in the Presence of Narrow-Band Whistler Waves in the Solar Wind.” In: *The Astrophysical Journal* 833.2, p. 172. ISSN: 1538-4357. DOI: 10.3847/1538-4357/833/2/172. URL: http://stacks.iop.org/0004-637X/833/i=2/a=172?key=crossref.6e0cb686c031c19378090937228000f2.

Kasper, J. C., A. J. Lazarus, and S. P. Gary (Dec. 2008). “Hot Solar-Wind Helium: Direct Evidence for Local Heating by Alfvén-Cyclotron Dissipation.” In: *Physical Review Letters* 101.26, 261103, p. 261103. DOI: 10.1103/PhysRevLett.101.261103.

Kasper, J. C. et al. (Dec. 2019). “Alfvénic velocity spikes and rotational flows in the near-Sun solar wind.” In: *Nature* 576.7786, pp. 228–231. DOI: 10.1038/s41586-019-1813-z.

Lacombe, C., O. Alexandrova, L. Matteini, O. Santolík, N. Cornilleau-Wehrlin, A. Mangeney, Y. de Conchy, and M. Maksimovic (Nov. 2014). “Whistler Mode Waves and the Electron Heat Flux in the Solar Wind: Cluster Observations.” In: *The Astrophysical Journal* 796.1, 5, p. 5. DOI: 10.1088/0004-637X/796/1/5. arXiv: 1410.6187 [astro-ph.SR].

Lamy, H., V. Pierrard, M. Maksimovic, and J. F. Lemaire (2003). “A kinetic exospheric model of the solar wind with a nonmonotonic potential energy for the protons.” In: *Journal of Geophysical Research: Space Physics* 108.A1, 1047, p. 1047. DOI: 10.1029/2002JA009487.

Landi, S., L. Matteini, and F. Pantellini (2012). “On the competition between radial expansion and coulomb collisions in shaping the electron velocity distribution function: Kinetic simulations.” In: *The Astrophysical Journal* 760.2. ISSN: 15384357. DOI: 10.1088/0004-637X/760/2/143.

— (2014). “Electron heat flux in the solar wind: Are we observing the collisional limit in the 1 AU data?” In: *The Astrophysical Journal Letters* 790.1, pp. 1–5. ISSN: 20418213. DOI: 10.1088/2041-8205/790/1/L12.

Landi, S. and F. Pantellini (2001). “On the temperature profile and heat flux in the solar corona: Kinetic simulations.” In: *Astronomy and Astrophysics* 372, pp. 686–701. DOI: 10.1051/0004-6361:20010552.

— (2003). “Kinetic simulations of the solar wind from the subsonic to the supersonic regime.” In: *Astronomy and Astrophysics* 400, pp. 769–778. ISSN: 0004-6361. DOI: 10.1051/0004-6361:20021822.

Landi, S., F. Pantellini, and L. Matteini (2010). “Radial Evolution of the Electron Velocity Distribution in the Heliosphere: Role of Collisions.” In: *AIP Conference Proceedings* 1216.1, pp. 218–222. DOI: 10.1063/1.3395841. eprint: https://aip.scitation.org/doi/pdf/10.1063/1.3395841. URL: https://aip.scitation.org/doi/abs/10.1063/1.3395841.

Lazar, M., V. Pierrard, S. M. Shaaban, H. Fichtner, and S. Poedts (June 2017). “Dual Maxwellian-Kappa modeling of the solar wind electrons: new clues on the temperature of Kappa populations.” In: *Astronomy and Astrophysics* 602, A44, A44. DOI: 10.1051/0004-6361/201630194. arXiv: 1703.01459 [physics.plasm-ph].

Lemaire, J. and M. Scherer (1970). “Model of the polar ion-exosphere.” In: *Planetary and Space Science* 18.1, pp. 103 –120. ISSN: 0032-0633. DOI: https://doi.org/10.1016/0032-0633(70)90070-X. URL: http://www.sciencedirect.com/science/article/pii/003206337090070X.

— (1971). “Kinetic models of the solar wind.” In: *Journal of Geophysical Research* 76, pp. 7479–. DOI: 10.1029/JA076i031p07479.

Levy, E. H. (June 1976). “The interplanetary magnetic field structure.” In: *Nature* 261.5559, pp. 394–395. DOI: 10.1038/261394a0.

Lie-Svendsen, Øystein, Viggo H. Hansteen, and Egil Leer (1997). “Kinetic electrons in high-speed solar wind streams: Formation of high-energy tails.” In: *Journal of Geophysical Research: Space Physics* 102.A3, pp. 4701–4718. DOI: 10.1029/96JA03632. eprint: https://agupubs.onlinelibrary.wiley.com/doi/pdf/10.1029/96JA03632. URL: https://agupubs.onlinelibrary.wiley.com/doi/abs/10.1029/96JA03632.

Livadiotis, G. and D. J. McComas (Dec. 2013). “Understanding kappa distributions in space physics.” In: *AGU Fall Meeting Abstracts*. Vol. 2013, SH33D–08.

Livadiotis, George (Sept. 2017). “Statistical origin and properties of kappa distributions.” In: *Journal of Physics Conference Series*. Vol. 900. Journal of Physics Conference Series, p. 012014. DOI: 10.1088/1742-6596/900/1/012014.

Macneil, Allan R., Mathew J. Owens, Mike Lockwood, Štěpán Štverák, and Christopher J. Owen (2020). “Radial Evolution of Sunward Strahl Electrons in the Inner Heliosphere.” In: *Solar Physics* 295.2, 16, p. 16. DOI: 10.1007/s11207-019-1579-3.

Maksimovic, M, V Pierrard, and J F Lemaire (1997a). "A kinetic model of the solar wind with Kappa distribution functions in the corona." In: *Astronomy and Astrophysics* 324, pp. 725–734. ISSN: 00046361.

Maksimovic, M. et al. (2005). "Radial evolution of the electron distribution functions in the fast solar wind between 0.3 and 1.5 AU." In: *Journal of Geophysical Research* 110.A9, pp. 1–9. ISSN: 21699402. DOI: `10.1029/2005JA011119`.

Maksimovic, M. et al. (Feb. 2020). "Anticorrelation between the Bulk Speed and the Electron Temperature in the Pristine Solar Wind: First Results from the Parker Solar Probe and Comparison with Helios." In: *The Astrophysical Journal, Supplement Series* 246.2, 62, p. 62. DOI: `10.3847/1538-4365/ab61fc`.

Maksimovic, Milan, Viviane Pierrard, and Pete Riley (1997b). "Ulysses electron distributions fitted with Kappa functions." In: *Geophysical Research Letters* 24.9, pp. 1151–1154. DOI: `10.1029/97GL00992`. eprint: `https://agupubs.onlinelibrary.wiley.com/doi/pdf/10.1029/97GL00992`. URL: `https://agupubs.onlinelibrary.wiley.com/doi/abs/10.1029/97GL00992`.

Malaspina, David M. et al. (Feb. 2020). "Plasma Waves near the Electron Cyclotron Frequency in the Near-Sun Solar Wind." In: *The Astrophysical Journal, Supplement Series* 246.2, 21, p. 21. DOI: `10.3847/1538-4365/ab4c3b`. arXiv: `1912.06793 [physics.space-ph]`.

Mariani, F., N. F. Ness, L. F. Burlaga, B. Bavassano, and U. Villante (Nov. 1978). "The large-scale structure of the interplanetary magnetic field between 1 and 0.3 AU during the primary mission of Helios 1." In: *Journal of Geophysical Research* 83.A11, pp. 5161–5166. DOI: `10.1029/JA083iA11p05161`.

Mariani, F., U. Villante, R. Bruno, B. Bavassano, and N. F. Ness (Sept. 1979). "An extended investigation of Helios 1 and 2 observations: the interplanetary magnetic field between 0.3 and 1 AU." In: *Solar Physics* 63.2, pp. 411–421. DOI: `10.1007/BF00174545`.

Marsch, E. and H. Goldstein (Dec. 1983). "The effects of Coulomb collisions on solar wind ion velocity distributions." In: *Journal of Geophysical Research* 88.A12, pp. 9933–9940. DOI: `10.1029/JA088iA12p09933`.

Marsch, E., W. G. Pilipp, K. M. Thieme, and H. Rosenbauer (June 1989). "Cooling of solar wind electrons inside 0.3 AU." In: *Journal of Geophysical Research* 94.A6, pp. 6893–6898. DOI: `10.1029/JA094iA06p06893`.

Marsch, E., R. Schwenn, H. Rosenbauer, K. H. Muehlhaeuser, W. Pilipp, and F. M. Neubauer (Jan. 1982). "Solar wind protons: Three-dimensional velocity distributions and derived plasma parameters measured between 0.3 and 1 AU." In: *Journal of Geophysical Research* 87.A1, pp. 52–72. DOI: `10.1029/JA087iA01p00052`.

Martinović, Mihailo M., Kristopher G. Klein, and Sofiane Bourouaine (July 2019). "Radial Evolution of Stochastic Heating in Low-β Solar Wind." In: *The Astrophysical Journal* 879.1, 43, p. 43. DOI: `10.3847/1538-4357/ab23f4`. arXiv: `1905.13355 [physics.space-ph]`.

McComas, D. J., B. L. Barraclough, H. O. Funsten, J. T. Gosling, E. Santiago-Muñoz, R. M. Skoug, B. E. Goldstein, M. Neugebauer, P. Riley, and A. Balogh (May 2000). "Solar wind observations over Ulysses' first full polar orbit." In: *Journal of Geophysical Research* 105.A5, pp. 10419–10434. DOI: `10.1029/1999JA000383`.

McComas, D. J. et al. (Jan. 1998). "Ulysses' return to the slow solar wind." In: *Geophysical Research Letters* 25.1, pp. 1–4. DOI: `10.1029/97GL03444`.

McComas, D. J. et al. (2019). "Probing the energetic particle environment near the Sun." In: *Nature* 576.June. ISSN: 14764687. DOI: `10.1038/s41586-019-1811-1`.

McComas, David J. (Sept. 2003). "The Three-Dimensional Structure of the Solar Wind Over the Solar Cycle." In: *Solar Wind Ten*. Ed. by Marco Velli, Roberto Bruno, Francesco Malara, and B. Bucci. Vol. 679. American Institute of Physics Conference Series, pp. 33–38. DOI: `10.1063/1.1618535`.

Mercier, C. and G. Chambe (Nov. 2015). "Electron density and temperature in the solar corona from multifrequency radio imaging." In: *Astronomy and Astrophysics* 583, A101, A101. DOI: `10.1051/0004-6361/201425540`.

Moncuquet, Michel et al. (Feb. 2020). "First In Situ Measurements of Electron Density and Temperature from Quasi-thermal Noise Spectroscopy with Parker Solar Probe/FIELDS." In: *The Astrophysical Journal, Supplement Series* 246.2, 44, p. 44. DOI: `10.3847/1538-4365/ab5a84`. arXiv: `1912.02518 [astro-ph.SR]`.

Neugebauer, M. (Jan. 1976). "The role of Coulomb collisions in limiting differential flow and temperature differences in the solar wind." In: *Journal of Geophysical Research* 81.1, p. 78. DOI: `10.1029/JA081i001p00078`.

Neugebauer, Marcia and Conway W. Snyder (Dec. 1962). "Solar Plasma Experiment." In: *Science* 138.3545, pp. 1095–1097. DOI: `10.1126/science.138.3545.1095-a`.

Pannekoek, A. (July 1922). "Ionization in stellar atmospheres (Errata: 2 24)." In: *Bulletin Astronomical Institute of the Netherlands* 1, p. 107.

Pantellini, Filippo G. E. (Jan. 2000). "A simple numerical model to simulate a gas in a constant gravitational field." In: *American Journal of Physics* 68.1, pp. 61–68. DOI: `10.1119/1.19374`.

Pantellini, Filippo and Simone Landi (June 2001). "A Simulation Method for Semicollisional Plasmas." In: *Astrophysics and Space Science* 277, pp. 149–152. DOI: `10.1023/A:1012213003182`.

Parker, E. N. (Nov. 1958). "Dynamics of the Interplanetary Gas and Magnetic Fields." In: *The Astrophysical Journal* 128, p. 664. DOI: `10.1086/146579`.

Phillips, J. L., S. J. Bame, W. C. Feldman, J. T. Gosling, C. M. Hammond, D. J. McComas, B. E. Goldstein, and M. Neugebauer (Aug. 1995). "ULYSSES solar wind plasma observations during the declining phase of solar cycle 22." In: *Advances in Space Research* 16.9, pp. 85–94. DOI: `10.1016/0273-1177(95)00318-9`.

Phillips, J. L. and J. T. Gosling (Apr. 1990). "Radial evolution of solar wind thermal electron distributions due to expansion and collisions." In: *Journal of Geophysical Research* 95.A4, pp. 4217–4228. DOI: `10.1029/JA095iA04p04217`.

Phillips, J. L., J. T. Gosling, D. J. McComas, S. J. Bame, S. P. Gary, and E. J. Smith (June 1989). "Anisotropic thermal electron distributions in the solar wind." In: *Journal of Geophysical Research* 94.A6, pp. 6563–6579. DOI: `10.1029/JA094iA06p06563`.

Pierrard, V., K. Issautier, N. Meyer-Vernet, and J. Lemaire (Jan. 2001). "Collisionless model of the solar wind in a spiral magnetic field." In: *Geophysical Research Letters* 28.2, pp. 223–226. DOI: `10.1029/2000GL011888`.

Pierrard, V. and J. Lemaire (Apr. 1996). "Lorentzian ion exosphere model." In: *Journal of Geophysical Research* 101.A4, pp. 7923–7934. DOI: `10.1029/95JA03802`.

Pierrard, V., M. Maksimovic, and J. Lemaire (Aug. 1999). "Electron velocity distribution functions from the solar wind to the corona." In: *Journal of Geophysical Research* 104.A8, pp. 17021–17032. DOI: `10.1029/1999JA900169`.

Pilipp, W. G., H. Miggenrieder, M. D. Montgomery, K. H. Mühlhäuser, H. Rosenbauer, and R. Schwenn (1987a). "Characteristics of electron velocity distribution functions in the solar wind derived from the Helios Plasma Experiment." In: *Journal of Geophysical Research* 92.A2, p. 1075. ISSN: 0148-0227. DOI: `10.1029/JA092iA02p01075`. URL: `http://doi.wiley.com/10.1029/JA092iA02p01075`.

Pilipp, W.G., H. Miggenrieder, M. D. Montgomery, K. H. Mühlhäuser, H. Rosenbauer, and R. Schwenn (Feb. 1987b). "Unusual electron distribution functions in the solar wind derived from the Helios plasma experiment: Double-strahl distributions and distributions with an extremely anisotropic core." In: *Journal of Geophysical Research* 92.A2, pp. 1093–1102. DOI: `10.1029/JA092iA02p01093`.

Rosenbluth, M. N. (Jan. 1965). "Microinstabilities." In: *Lectures presented at the Trieste Seminar on Plasma Physics*, p. 485.

Rosseland, S. (June 1924). "Electrical state of a star." In: *Monthly Notices of the Royal Astronomical Society* 84, pp. 720–728. DOI: `10.1093/mnras/84.9.720`.

Saito, Shinji and Peter S. Gary (2007). "All whistlers are not created equally: Scattering of strahl electrons in the solar wind via particle-in-cell simulations." In: *Geophysical Research Letters* 34.1, pp. 1–5. ISSN: 00948276. DOI: `10.1029/2006GL028173`.

Salem, C., D. Hubert, C. Lacombe, S. D. Bale, A. Mangeney, D. E. Larson, and R. P. Lin (Mar. 2003). "Electron Properties and Coulomb Collisions in the Solar Wind at 1 AU: Wind Observations." In: *The Astrophysical Journal* 585.2, pp. 1147–1157. DOI: `10.1086/346185`.

Saqri, Jonas, Astrid M. Veronig, Stephan G. Heinemann, Stefan J. Hofmeister, Manuela Temmer, Karin Dissauer, and Yang Su (Jan. 2020). "Differential Emission Measure Plasma Diagnostics of a Long-Lived Coronal Hole." In: *Solar Physics* 295.1, 6, p. 6. DOI: `10.1007/s11207-019-1570-z`. arXiv: `2001.02259 [astro-ph.SR]`.

Scudder, J. D. (Nov. 2019). "Steady Electron Runaway Model SERM: Astrophysical Alternative for the Maxwellian Assumption." In: *The Astrophysical Journal* 885.2, 138, p. 138. DOI: `10.3847/1538-4357/ab4882`.

Scudder, Jack D. (Oct. 1992a). "On the Causes of Temperature Change in Inhomogeneous Low-Density Astrophysical Plasmas." In: *The Astrophysical Journal* 398, p. 299. DOI: `10.1086/171858`.

— (Oct. 1992b). "Why All Stars Should Possess Circumstellar Temperature Inversions." In: *The Astrophysical Journal* 398, p. 319. DOI: `10.1086/171859`.

— (June 1996). "Dreicer order ambipolar electric fields at Parker's steady state solar wind sonic critical point." In: *Journal of Geophysical Research* 101.A6, pp. 13461–13472. DOI: `10.1029/96JA00189`.

Stansby, D., T. S. Horbury, C. H. K. Chen, and L. Matteini (Sept. 2016). "Experimental Determination of Whistler Wave Dispersion Relation in the Solar Wind." In: *The Astrophysical Journal Letters* 829.1, L16, p. L16. DOI: `10.3847/2041-8205/829/1/L16`. arXiv: `1609.03039 [physics.space-ph]`.

Stansby, D., L. Matteini, T. S. Horbury, D. Perrone, R. D'Amicis, and L. Berčič (Feb. 2020). "The origin of slow Alfvénic solar wind at solar minimum." In: *Monthly Notices of the Royal Astronomical Society* 492.1, pp. 39–44. DOI: `10.1093/mnras/stz3422`. arXiv: `1907.02646 [physics.space-ph]`.

Stone, E. C., A. C. Cummings, F. B. McDonald, B. C. Heikkila, N. Lal, and W. R. Webber (Sept. 2005). "Voyager 1 Explores the Termination Shock Region and the Heliosheath Beyond." In: *Science* 309.5743, pp. 2017–2020. DOI: `10.1126/science.1117684`.

Štverák, Štěpán, Milan Maksimovic, Pavel M. Trávníček, Eckart Marsch, Andrew N. Fazakerley, and Earl E. Scime (2009). "Radial evolution of nonthermal electron populations in the low-latitude solar wind: Helios, Cluster, and Ulysses Observations." In: *Journal of Geophysical Research: Space Physics* 114.5, pp. 1–15. ISSN: 21699402. DOI: `10.1029/2008JA013883`.

Štverák, Štěpán, Pavel M. Trávníček, and Petr Hellinger (2015). "Electron energetics in the expanding solar wind via Helios observations." In: *Journal of Geophysical Research: Space Physics* 120.10, pp. 8177–8193. ISSN: 21699402. DOI: 10.1002/2015JA021368.

Štverák, Štěpán, Pavel Trávníček, Milan Maksimovic, Eckart Marsch, Andrew N. Fazakerley, and Earl E. Scime (2008). "Electron temperature anisotropy constraints in the solar wind." In: *Journal of Geophysical Research: Space Physics* 113.A3, A03103, A03103. DOI: 10.1029/2007JA012733.

Tao, Jiawei, Linghua Wang, Qiugang Zong, Gang Li, Chadi S. Salem, Robert F. Wimmer-Schweingruber, Jiansen He, Chuanyi Tu, and Stuart D. Bale (2016). "Quiet-time Suprathermal (~0.1-1.5 keV) Electrons in the Solar Wind." In: *The Astrophysical Journal* 820.1, 22, p. 22. DOI: 10.3847/0004-637X/820/1/22.

Tong, Yuguang, Ivan Y. Vasko, Anton V. Artemyev, Stuart D. Bale, and Forrest S. Mozer (June 2019). "Statistical Study of Whistler Waves in the Solar Wind at 1 au." In: *The Astrophysical Journal* 878.1, 41, p. 41. DOI: 10.3847/1538-4357/ab1f05. arXiv: 1905.08958 [physics.space-ph].

Tsallis, Constantino (July 1988). "Possible generalization of Boltzmann-Gibbs statistics." In: *Journal of Statistical Physics* 52.1-2, pp. 479–487. DOI: 10.1007/BF01016429.

Verscharen, Daniel, Benjamin D. G. Chandran, Seong-Yeop Jeong, Chadi S. Salem, Marc P. Pulupa, and Stuart D. Bale (Dec. 2019a). "Self-induced Scattering of Strahl Electrons in the Solar Wind." In: *The Astrophysical Journal* 886.2, 136, p. 136. DOI: 10.3847/1538-4357/ab4c30. arXiv: 1906.02832 [physics.space-ph].

Verscharen, Daniel, Kristopher G. Klein, and Bennett A. Maruca (Dec. 2019b). "The multi-scale nature of the solar wind." In: *Living Reviews in Solar Physics* 16.1, 5, p. 5. DOI: 10.1007/s41116-019-0021-0. arXiv: 1902.03448 [physics.space-ph].

Vocks, C., C. Salem, R. P. Lin, and G. Mann (2005). "Electron Halo and Strahl Formation in the Solar Wind by Resonant Interaction with Whistler Waves." In: *The Astrophysical Journal* 627.1, pp. 540–549. ISSN: 0004-637X. DOI: 10.1086/430119. URL: http://stacks.iop.org/0004-637X/627/i=1/a=540.

Whittlesey, Phyllis L. et al. (Feb. 2020). "The Solar Probe ANalyzers—Electrons on the Parker Solar Probe." In: *The Astrophysical Journal, Supplement Series* 246.2, 74, p. 74. DOI: 10.3847/1538-4365/ab7370. arXiv: 2002.04080 [astro-ph.IM].

Wilson Lynn B., III et al. (2019a). "Electron Energy Partition across Interplanetary Shocks. I. Methodology and Data Product." In: *The Astrophysical Journal, Supplement Series* 243.1, 8, p. 8. DOI: 10.3847/1538-4365/ab22bd. arXiv: 1902.01476 [physics.space-ph].

— (2019b). "Electron Energy Partition across Interplanetary Shocks. II. Statistics." In: *The Astrophysical Journal, Supplement Series* 245.2, 24, p. 24. DOI: 10.3847/1538-4365/ab5445.

Zouganelis, I., M. Maksimovic, N. Meyer-Vernet, H. Lamy, and K. Issautier (2004). "A transonic collisionless model of the solar wind." In: *The Astrophysical Journal* 606, pp. 542–554. ISSN: 0004-637X. DOI: `10.1086/382866`. arXiv: `0402358 [astro-ph]`. URL: `http://arxiv.org/abs/astro-ph/0402358`.

Zouganelis, I., N. Meyer-Vernet, S. Landi, M. Maksimovic, and F. Pantellini (June 2005). "Acceleration of Weakly Collisional Solar-Type Winds." In: *The Astrophysical Journal Letters* 626.2, pp. L117–L120. DOI: `10.1086/431904`. arXiv: `astro-ph/0505324 [astro-ph]`.